



HAL
open science

Design and bottom-up fabrication of nanostructured photonic / plasmonic materials

Hanbin Zheng

► **To cite this version:**

Hanbin Zheng. Design and bottom-up fabrication of nanostructured photonic / plasmonic materials. Chemical Physics [physics.chem-ph]. Université de Bordeaux; Instituto superior técnico (Lisbonne), 2014. English. NNT : 2014BORD0255 . tel-01390199

HAL Id: tel-01390199

<https://theses.hal.science/tel-01390199>

Submitted on 1 Nov 2016

HAL is a multi-disciplinary open access archive for the deposit and dissemination of scientific research documents, whether they are published or not. The documents may come from teaching and research institutions in France or abroad, or from public or private research centers.

L'archive ouverte pluridisciplinaire **HAL**, est destinée au dépôt et à la diffusion de documents scientifiques de niveau recherche, publiés ou non, émanant des établissements d'enseignement et de recherche français ou étrangers, des laboratoires publics ou privés.

THÈSE EN COTUTELLE PRÉSENTÉE
POUR OBTENIR LE GRADE DE

DOCTEUR DE

**L'UNIVERSITÉ DE BORDEAUX
ET DE L'UNIVERSITE DE LISBONNE**

ÉCOLE DOCTORALE DES SCIENCES CHIMIQUES
SPÉCIALITÉ: PHYSICO-CHIMIE DE LA MATIÈRE CONDENSÉE

Par Hanbin, ZHENG

**DESIGN AND BOTTOM-UP FABRICATION OF
NANOSTRUCTURED PHOTONIC / PLASMONIC MATERIALS**

Sous la direction de : Serge, RAVAINÉ
(co-directeur : Rui M., ALMEIDA)

Soutenue le 24 November 2014

Membres du jury :

M. KUHN, Alexander
M. PLAIN, Jérôme
M. PEYRADE, David
M. ANDRE, Paulo S.
M. RAVAINÉ, Serge
M. ALMEIDA, Rui M.
M. RIVERA, Thomas

Professeur, Bordeaux INP
Professeur, Université de Technologie de Troyes
Chargé de Recherche, CNRS
Associate Professor, Universidade de Lisboa
Professeur, Université de Bordeaux
Professor, Universidade de Lisboa
Research Project Manager, Orange Labs Network

President
Rapporteur
Rapporteur
Examineur
Directeur de thèse
Directeur de thèse
Invité

THÈSE EN COTUTELLE PRÉSENTÉE
POUR OBTENIR LE GRADE DE

DOCTEUR DE

**L'UNIVERSITÉ DE BORDEAUX
ET DE L'UNIVERSITE DE LISBONNE**

ÉCOLE DOCTORALE DES SCIENCES CHIMIQUES
SPÉCIALITÉ: PHYSICO-CHIMIE DE LA MATIÈRE CONDENSÉE

Par Hanbin, ZHENG

**DESIGN AND BOTTOM-UP FABRICATION OF
NANOSTRUCTURED PHOTONIC / PLASMONIC MATERIALS**

Sous la direction de : Serge, RAVAINÉ
(co-directeur : Rui M., ALMEIDA)

Soutenue le 24 November 2014

Membres du jury :

M. KUHN, Alexander
M. PLAIN, Jérôme
M. PEYRADE, David
M. ANDRE, Paulo S.
M. RAVAINÉ, Serge
M. ALMEIDA, Rui M.
M. RIVERA, Thomas

Professeur, Bordeaux INP
Professeur, Université de Technologie de Troyes
Chargé de Recherche, CNRS
Associate Professor, Universidade de Lisboa
Professeur, Université de Bordeaux
Professor, Universidade de Lisboa
Research Project Manager, Orange Labs Network

President
Rapporteur
Rapporteur
Examineur
Directeur de thèse
Directeur de thèse
Invité

To my family who have been so absolutely supportive of all my endeavours.

“An expert is one who knows more and more about less and less until he knows absolutely everything about nothing”

— Murphy’s Laws on Technology

ACKNOWLEDGEMENTS

It is with much emotions and thoughts as I consolidate and remember all the help and assistance that I have received, as well as all the fun and laughter I have shared over the last three years, during the entire course of my thesis work.

It is without a doubt that this piece of work could not have been possible without the joint efforts of the IDS FunMat Program Committee, Professor Serge Ravaine, Professor Rui M. Almeida, and Dr Thomas Rivera. I would especially like to extend my gratitude to Prof Ravaine for his guidance, support and ‘open-door’ policy of interaction during the time I have spent working in the CRPP. In addition, I also have to thank Prof Almeida and Dr Rivera for their collaboration and endorsement of this thesis work.

Furthermore, as this thesis work was mainly spread between the CRPP (Bordeaux) and ICEMS (Lisbon), I have been given a great opportunity to interact with a variety of people in the course of my work. Living in Bordeaux and Lisbon has been a very enriching experience; the people, the culture and especially the food have rarely been disappointing.

From CRPP, I want to thank Stéphane Reculosa and Béatrice Agricole for teaching me the basics of what I had to do when I just started (especially on the Langmuir-Blodgett technique). I also want to thank Isabelle Ly, for without her, this thesis would never be filled with the beautiful SEM images littered throughout. She has been most helpful and patient with my insatiable appetite for more sessions at the PLACAMAT, and for that I really appreciate all the assistance she has provided me despite her busy schedule of juggling work and the duties as a mother of three children. To Monsieur Renaud Vallée, I want to thank him for his help with the simulations described in this thesis and the few fruitful discussions we had. It has helped me understand more of the physics that is discussed in this work. I also have to thank Céline Leroy for her help in the DSSC project and reducing a little of my workload until her baby had to arrive. I want to thank Emmeline Feltrin for showing me how to work with PDMS. In addition, I have to thank the Master (Laura, Julien, Audrey) and undergraduate students (Remi, Antoine, Valentin) I had the chance to mentor and work with during my time in CRPP. They have proved very helpful in lightening my workload most of the time. To my various lunch buddies over the course of three years, Christos, Miguel, Noelia, Petra, Cintia, Yu, Fay, David, Carmen and Sergio, it has been a pleasure to have spent these downtime together over lunch. I also want to extend my thanks to all the people in MaFIC, the administrative, IT,

chemical and mechanical divisions for all the help I get every now and then on various technical issues.

From PLACAMAT (formerly CREMEM), I have to especially thank Elisabeth Sellier and Michel Martineau for their assistance rendered whenever there were problems with the SEM. From IMS, I want to acknowledge the guidance and assistance I received from Mamatimin Abbas and Said Karim Shah in fabricating the solid state DSSC devices. From IST, I want to thank Luis M. Fortes for showing me the ropes of the work that was to be done over in Lisbon. Furthermore, I want to thank Sahendra, Liliana, Gonçalo, Bruno, Carole, Jaroslav, Tomin, Joao and Alex, who form the wonderful and friendly group of people who I shared the office together in IST. From Orange Labs network, I want to thank the then-stagiare Claire-Eline Bres for helping me with the measurements when I was there. I also want to acknowledge all the other IDS-FunMat participants (especially the ones who spent time in Bordeaux; Natacha, Deniz, Mercedes, Mathilde, Mariel, Maryna) who have been or are still in the program for sharing part of this experience with me.

Finally, I want to thank my family and friends back home in Singapore for supporting me in spirit since I left back in 2009 for my Masters in Europe and continued on with my PhD till now. Thank you all for your encouragements and words of advice.

“No matter how much time passes, no matter what takes place in the interim, there are some things we can never assign to oblivion, memories we can never rub away.”

— Haruki Murakami

RESUME DE THESE EN FRANÇAIS

Dans les domaines de la photonique et de la plasmonique, la capacité à manipuler les ondes électromagnétiques dans le domaine du visible requiert des matériaux fonctionnels ayant des caractéristiques structurales qui sont inférieures ou égales à la longueur d'onde de la lumière. En outre, les propriétés optiques d'un dispositif sont fortement liées au choix de la nature et de la structure du ou des matériaux constitutifs. Ceci a des retombées directes dans de nombreux domaines d'applications tels que les guides d'ondes [1], les circuits photoniques [2] et les biocapteurs [3].

Dans la nature, des matériaux photoniques peuvent être trouvés, par exemple, dans les ailes de certains papillons [4] et les opales (Figure A) [5]. Pour recréer artificiellement des matériaux similaires, c'est-à-dire présentant une structuration périodique, les scientifiques ont principalement utilisé des techniques dites « top-down », telles que la lithographie électronique [6], la photolithographie [7] et la lithographie par faisceau d'ions focalisé (FIB) [8]. Une autre voie consiste à tirer profit de l'auto-assemblage d'entités colloïdales pouvant conduire à la formation de structures ordonnées à grande échelle présentant une structure répétitive, qui peut être facilement modulée via le choix des briques utilisées [9]. Par exemple, en combinant l'utilisation de moules colloïdaux avec une technique telle que l'électrodéposition, il est possible de fabriquer des matériaux plasmoniques nanostructurés qui sont des répliques inverses du moule utilisé [10]-[17].

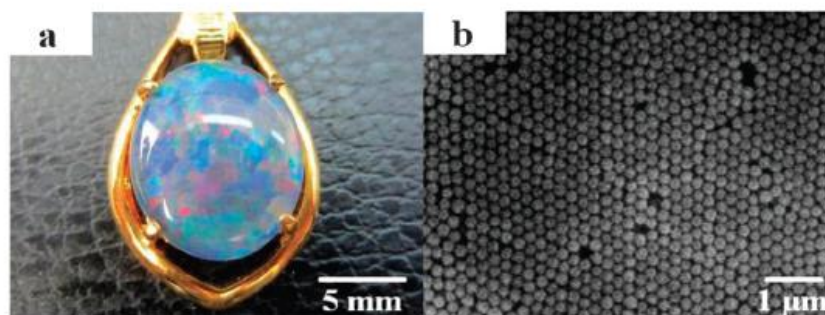


Figure A. (a) Photographie d'une opale naturelle. (b) Image de microscopie électronique à balayage (MEB) illustrant la structure périodique d'une opale.

L'objectif de cette thèse est de concevoir et de développer des voies de fabrication de matériaux photoniques et plasmoniques nanostructurés, basées sur l'auto-assemblage de particules colloïdales. Des cristaux colloïdaux bi- et tridimensionnels ont été réalisés par deux techniques différentes et ont été utilisés comme moules pour fabriquer (1) des opales inverses de dioxyde de titane; (2) des films nanostructurés d'or; (3) des réseaux organisés de nanopiliers d'or et (4) des métamatériaux de type « fishnet ».

Dans le chapitre 1, les concepts généraux permettant d'appréhender les travaux réalisés au cours de cette thèse sont présentés. Ainsi, des notions théoriques relatives à la photonique et à la plasmonique sont exposées et les principales approches « top-down » et « bottom-up » permettant la réalisation de systèmes photoniques et plasmoniques sont également décrites.

Dans le chapitre 2, nous détaillons les travaux que nous avons entrepris dédiés à l'incorporation d'une opale inverse de TiO_2 dans une cellule à colorant « tout solide » afin d'améliorer le piégeage de la lumière et d'améliorer l'efficacité de la cellule. Dans un premier temps, nous démontrons qu'il est possible de contrôler l'épaisseur de l'opale inverse via l'empilement « une à une » de couches de particules de polystyrène sur un substrat (Figure B), suivi de l'infiltration des interstices entre les particules à l'aide d'un précurseur organo-minéral.

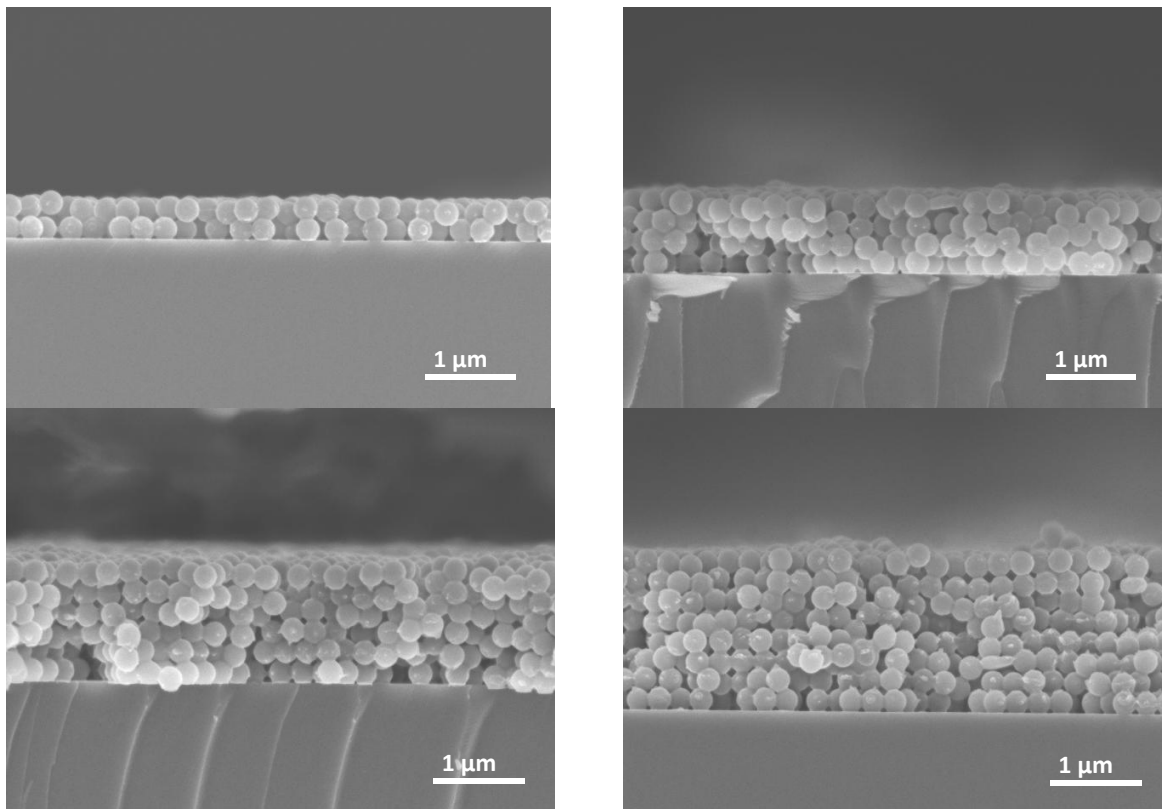


Figure B. Images MEB de cristaux colloïdaux constitués de 2, 4, 6, et 8 couches de particules de polystyrène de 260 nm de diamètre.

L'étude des propriétés optiques des structures photoniques réalisées a permis de révéler que la position de la bande interdite pouvait être modulée en variant la taille des particules utilisées, ce qui est particulièrement important dans le but de faire coïncider la position de la bande interdite de l'opale inverse avec celle du pic d'absorption du colorant utilisé. Nous avons également mis en évidence qu'il existe une épaisseur optimale pour l'opale inverse, pour laquelle l'efficacité de la cellule solaire est maximale.

Dans le chapitre 3, nous montrons qu'il est possible d'électrodéposer de l'or au sein des interstices existants entre des billes de polystyrène organisées sous la forme d'une monocouche compacte. L'ajustement du temps d'électrodéposition permet de contrôler très finement l'épaisseur du dépôt d'or (Figure C).

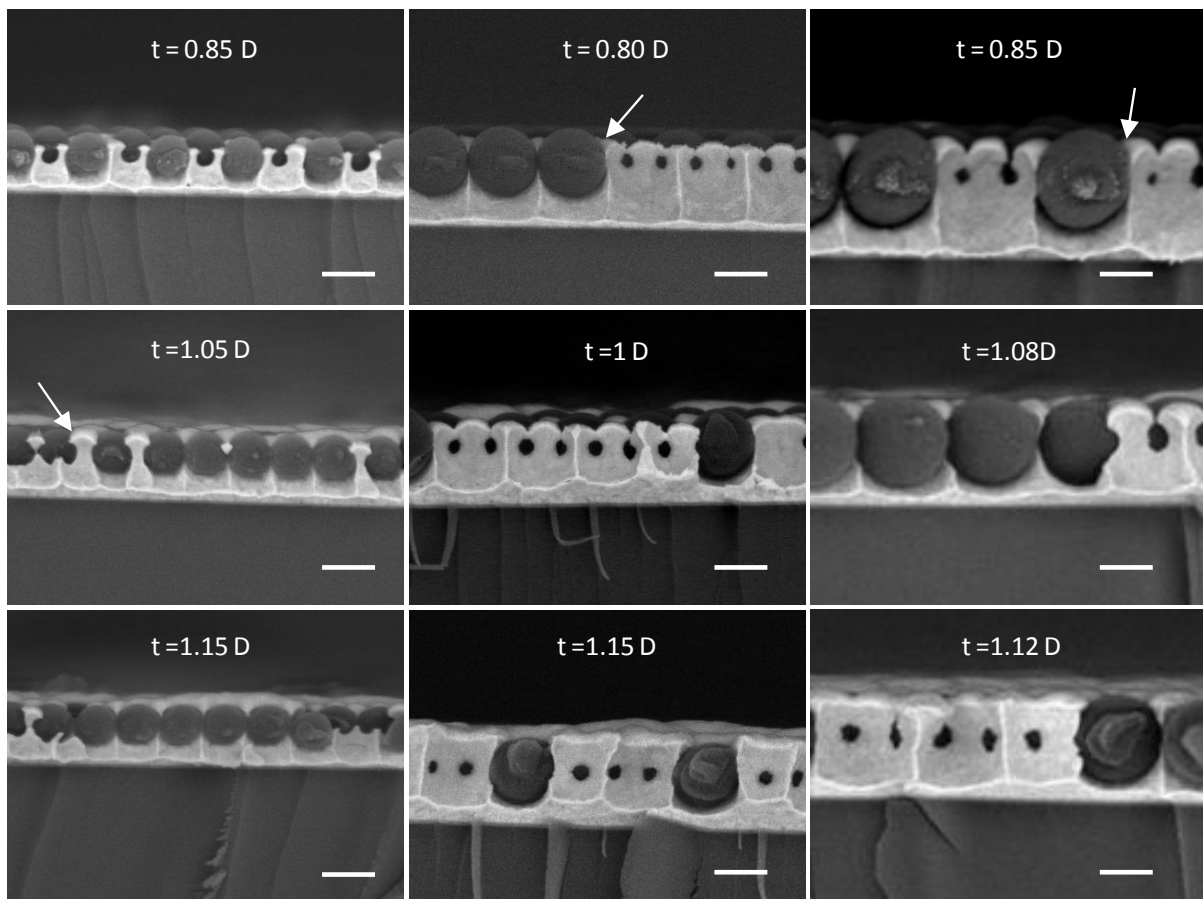


Figure C. Images MEB de dépôts d'or de différentes épaisseurs (t) électrodéposés à travers une monocouche de particules de polystyrène de diamètre D égal à : 260 nm (gauche), 430 nm (centre) et 595 nm (droite). Barre d'échelle : 300 nm.

L'étude des propriétés optiques de ces dépôts a permis de mettre en évidence une absorption de la lumière omnidirectionnelle pour différentes tailles de particules. Lorsque les billes de polymère sont éliminées, ce qui conduit à la formation d'un film d'or contenant un réseau

périodique de trous, l'absorption est décalée vers le bleu et est légèrement diminuée. Des dépôts d'or micro- et nanostructurés présentant une structure fractale ont également été fabriqués par électrodéposition. Nous avons là encore étudié les propriétés optiques de ces films et avons montré qu'ils présentent une réflexion spéculaire inférieure à 1% dans la plage de longueur d'onde allant de 250 nm à 2500 nm, ce qui en fait d'excellents candidats pour des dispositifs tels que des capteurs en milieu extrême.

Dans le chapitre 4, nous présentons nos travaux dédiés à la fabrication de réseau de nanopiliers d'or à partir de monocouches de billes de polystyrène préalablement frittées (Figure D).

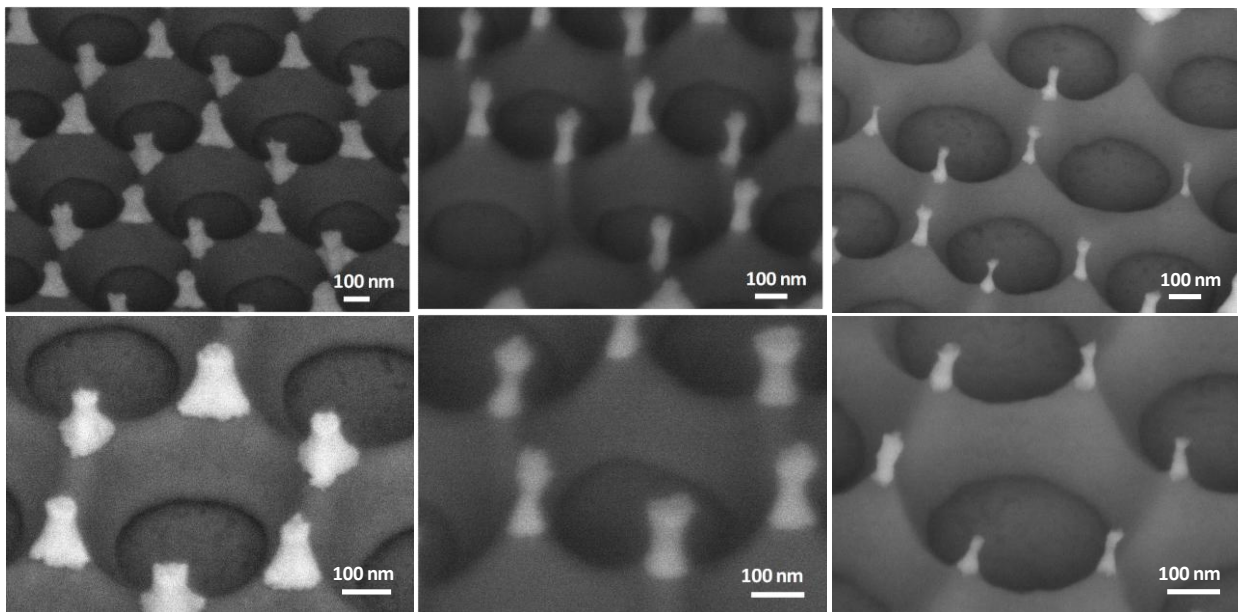


Figure D. Images MEB de nanopiliers d'or électrodéposés à travers une monocouche de particules de polystyrène de 595 nm de diamètre préalablement frittées à 110°C durant 6 (gauche), 7 (centre) et 8 minutes (droite).

En faisant varier de manière contrôlée le temps d'électrodéposition, nous avons pu faire varier la morphologie des nanopiliers. En particulier, nous avons cherché à minimiser la distance entre les extrémités triangulaires de ceux-ci, dans le but de créer des « points chauds » pouvant conduire à des effets d'exaltation de la diffusion Raman exaltée de surface (SERS). Toutefois, aucun effet notable de la distance sur la réponse Raman n'a été observé. Nous avons aussi utilisé tiré profit de la formation d'une couche de nickel sacrificielle par voie électrolytique pour transférer les nanopiliers d'or au sein d'un film transparent de polydiméthylsiloxane (PDMS). Les échantillons obtenus ont été caractérisés optiquement et nous avons pu montrer que les spectres d'absorption présentent des pics dont la position et l'intensité varient en fonction de la morphologie des nanopiliers et de leur interdistance. En

particulier, une augmentation de la hauteur des piliers induit un décalage vers le bleu des pics d'absorption. Les résultats expérimentaux obtenus sont en bon accord avec ceux issus de simulations réalisées par FDTD.

Le chapitre 5 est consacré à la fabrication de métamatériaux de type « fishnet » par électrodéposition séquentielle d'or et de nickel au sein d'une monocouche de billes de polystyrène préalablement rognées. Là encore, le contrôle du temps d'électrodéposition permet un contrôle précis des épaisseurs de chaque couche de métal déposée (Figure E). La dissolution sélective ultérieure des couches sacrificielles de nickel permet d'obtenir des métamatériaux de plusieurs cm^2 , constitués d'une couche d'air emprisonnés entre deux couches d'or.

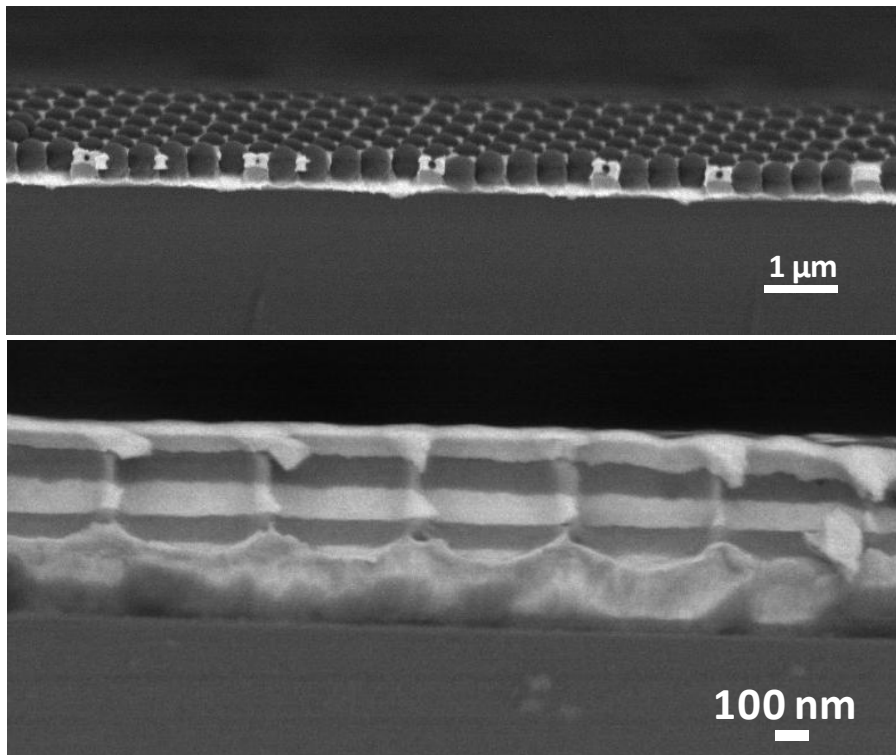


Figure E. Images MEB de dépôts nickel-or (haut) et nickel-or-nickel (bas) électrodéposés à travers une monocouche de particules de polystyrène de 430 nm de diamètre.

REFERENCES

- [1] F. Di Stasio, M. Cucini, L. Berti, D. Comoretto, A. Abboto, L. Bellotto, N. Manfredi, and C. Marinzi, "Tuning optical properties of opal photonic crystals by structural defects engineering," *J. Eur. Opt. Soc. Rapid Publ.*, vol. 4, p. 09033, Jun. 2009.
- [2] E. Ozbay, "Plasmonics: merging photonics and electronics at nanoscale dimensions.," *Science*, vol. 311, no. 5758, pp. 189–93, Jan. 2006.
- [3] J. Homola, "Present and future of surface plasmon resonance biosensors.," *Anal. Bioanal. Chem.*, vol. 377, no. 3, pp. 528–39, Oct. 2003.
- [4] M. Kolle, P. M. Salgard-Cunha, M. R. J. Scherer, F. Huang, P. Vukusic, S. Mahajan, J. J. Baumberg, and U. Steiner, "Mimicking the colourful wing scale structure of the *Papilio blumei* butterfly.," *Nat. Nanotechnol.*, vol. 5, no. 7, pp. 511–5, Jul. 2010.
- [5] J. V. Sanders, "Colour of precious opal," *Nature*, vol. 204, no. 4964, p. 1151, 1964.
- [6] N. A. Hatab, C.-H. Hsueh, A. L. Gaddis, S. T. Retterer, J.-H. Li, G. Eres, Z. Zhang, and B. Gu, "Free-standing optical gold bowtie nanoantenna with variable gap size for enhanced Raman spectroscopy.," *Nano Lett.*, vol. 8, pp. 4952–4955, Nov. 2010.
- [7] V. Linder, B. D. Gates, D. Ryan, B. A. Parviz, and G. M. Whitesides, "Water-soluble sacrificial layers for surface micromachining.," *Small*, vol. 1, no. 7, pp. 730–6, Jul. 2005.
- [8] J. Valentine, S. Zhang, T. Zentgraf, E. Ulin-Avila, D. A. Genov, G. Bartal, and X. Zhang, "Three-dimensional optical metamaterial with a negative refractive index.," *Nature*, vol. 455, no. 7211, pp. 376–9, Sep. 2008.
- [9] F. Li, D. P. Josephson, and A. Stein, "Colloidal assembly: the road from particles to colloidal molecules and crystals.," *Angew. Chem. Int. Ed. Engl.*, vol. 50, no. 2, pp. 360–88, Jan. 2011.
- [10] P. N. Bartlett, P. R. Birkin, M. A. Ghanem, and C.-S. Toh, "Electrochemical syntheses of highly ordered macroporous conducting polymers grown around self-assembled colloidal templates," *J. Mater. Chem.*, vol. 11, no. 3, pp. 849–853, 2001.
- [11] P. N. Bartlett, J. J. Baumberg, P. R. Birkin, M. A. Ghanem, and M. C. Netti, "Highly ordered macroporous gold and platinum films formed by electrochemical deposition through templates assembled from submicron diameter monodisperse polystyrene spheres," *Chem. Mater.*, vol. 14, no. 5, pp. 2199–2208, May 2002.
- [12] P. N. Bartlett, J. J. Baumberg, S. Coyle, and M. E. Abdelsalam, "Optical properties of nanostructured metal films," *Faraday Discuss.*, vol. 125, p. 117, 2004.
- [13] R. Szamocki, S. Reculosa, S. Ravaine, P. N. Bartlett, A. Kuhn, and R. Hempelmann, "Tailored mesostructuring and biofunctionalization of gold for increased electroactivity.," *Angew. Chem. Int. Ed. Engl.*, vol. 45, no. 8, pp. 1317–21, Feb. 2006.

- [14] S. Reculosa, M. Heim, F. Gao, N. Mano, S. Ravaine, and A. Kuhn, “Design of catalytically active cylindrical and macroporous gold microelectrodes,” *Adv. Funct. Mater.*, vol. 21, no. 4, pp. 691–698, Feb. 2011.
- [15] M. Heim, S. Reculosa, S. Ravaine, and A. Kuhn, “Engineering of complex macroporous materials through controlled electrodeposition in colloidal superstructures,” *Adv. Funct. Mater.*, vol. 22, no. 3, pp. 538–545, Feb. 2012.
- [16] M. E. Abdelsalam, P. N. Bartlett, T. Kelf, and J. Baumberg, “Wetting of regularly structured gold surfaces,” *Langmuir*, vol. 21, no. 5, pp. 1753–7, Mar. 2005.
- [17] M. E. Abdelsalam, P. N. Bartlett, J. J. Baumberg, S. Cintra, T. A. Kelf, and A. E. Russell, “Electrochemical SERS at a structured gold surface,” *Electrochem. commun.*, vol. 7, no. 7, pp. 740–744, Jul. 2005.

TABLE OF CONTENTS

Acknowledgements	i
Résumé de thèse en Français.....	iii
References	viii
Table of Contents	xi
Introduction	1
Motivation	1
Scope and Aim of Thesis.....	2
Outline of Thesis	3
References	4
Chapter 1: Bibliography Review.....	7
General Introduction	9
1. Photonics	10
1.1 Photonic Crystals	11
1.2 Photonic Bandgaps.....	15
2. Plasmonics.....	17
2.1 Surface plasmon polaritons.....	17
2.2 Localized surface plasmon resonance.....	20
3. Fabrication methods	23
3.1 Top-down approaches	24
3.2 Bottom-up approaches	27
3.2.1 Colloidal assembly	27
3.2.3 Colloidal lithography.....	33
References	36

Chapter 2: Efficiency Enhancement of Solid State Dye Sensitized Solar Cells (DSSC) by the Incorporation of Light Trapping Photonic Crystal Structures	41
1. Introduction	43
2. Deposition of the colloidal crystal (Opal) templates.....	48
2.1 Vertical deposition of colloidal crystals.....	48
2.2 Stacking of closed packed PS monolayers packed on a water surface	54
2.3 Comparison between the two assembly methods	58
3. Incorporation of inverse opals (IO) of TiO ₂ into solid state DSSCs	58
3.1 Evaluation of Cell Performance (The first series)	62
3.2 Evaluation of Cell Performance (The second series).....	66
4. Conclusion.....	69
References	70
Chapter 3: Fabrication of Nanostructured Gold Surfaces with Unique Optical Properties by Electrodeposition.....	73
1. Introduction	75
2. Electrodeposition of Gold into Colloidal Templates.....	78
3. Quasi Total Omnidirectional Absorption in Micro-/Nano-structured Gold Surfaces...	82
3.1 Context of the study	82
3.2 Templated gold films electrodeposited through a close-packed monolayer of polystyrene beads.....	83
3.3 Non-templated electrodeposition of micro/nanotextured gold films	89
4. Conclusion.....	96
References	97
Chapter 4: Bottom-up Design of Two Dimensional Plasmonic Nanopillar Arrays.....	101
1. Introduction	103
2. Fabrication of nanopillar arrays	108
2.1 Modification of pore shape and size of the colloidal crystal templates	108
2.2 Electrodeposition of gold nanopillar arrays	110

2.2.1	Tuning the inter-distance between triangular tips of pillars by controlling the electrodeposition depth.	111
2.2.2	Surface enhanced Raman signal (SERS) measurements.....	113
2.3	Electrodeposition of nickel and gold into the colloidal templates.....	114
2.4	Transfer of electrodeposited gold pillars onto a transparent substrate.....	123
2.5	Stretching of the gold nanopillar arrays embedded in PDMS	128
3.	Conclusion.....	130
	References	132
Chapter 5: Bottom-up Design of Fishnet Metamaterials by Colloidal Lithography.....		135
1.	Introduction	137
2.	Preparation of non-closed packed monolayers of PS beads.....	142
3.	Sequential electrodeposition of metals.....	145
4.	Dissolution of sacrificial nickel layers	151
5.	Transferring the fishnet onto a transparent substrate	153
5.1	Transfer of fishnet structures onto PDMS	153
5.2	Transfer of fishnet structures onto water and re-scooping them out.....	156
6.	Conclusion.....	157
	References	159
Overall Conclusion and Perspectives		161
Annex 1. Synthesis of Silica and Polystyrene beads.....		165
A.	Synthesis of silica beads by the Stöber process.....	165
	Temperature dependent one step synthesis of silica nanoparticles.....	165
	Seeded Growth of Silica Nanoparticles	167
B.	Synthesis of polystyrene beads by emulsion polymerization	170
Annex 2. Preparation of Colloidal Crystals		173
A.	Vertical deposition technique	173
B.	Self-assembly of closed packed monolayer on water surface	174

C. Langmuir-Blodgett Technique	176
Annex 3. Fabrication of Solid State DSSCs	179
A. Preparation of fluorine-doped tin oxide (FTO) glass slides	179
B. Preparation of Compact TiO ₂ Layer	179
C. Preparation of Porous TiO ₂ Layer	180
D. Fabrication of inverse opal TiO ₂ by the vacuum infiltration method.....	181
E. Incorporation of dye and hole transport layer	182
F. Completing the solid state DSSC	183
Annex 4. Electrodeposition of Metals	185
A. Preparation of substrates.....	185
B. Electrodeposition of gold (Au)	187
C. Electrodeposition of nickel (Ni)	187
Annex 5. Fabrication of gold nanopillar structures in PDMS	189
Annex 6. Characterization of fabricated samples.....	193
References	194

INTRODUCTION

MOTIVATION

Nanotechnology has opened up a whole new realm of science that we are only beginning to discover, and this drive towards smaller devices has been largely due to the electronics industry. In the field of photonics and plasmonics, the ability to manipulate electromagnetic waves in the visible regime requires functional materials with features that are smaller or equal to the wavelength of light. The choice of material and structure has a direct effect on the resulting optical properties of the device. This can be translated into applications such as waveguides [1], photonic circuits [2] and biosensors [3]. In addition, plasmonic nanostructured materials have the ability to enhance certain optical processes, for example, surface enhanced Raman scattering (SERS) [4] and surface enhanced fluorescence (SEF) [5].

Naturally occurring photonic materials can be found for instance, in the wings of butterflies [6] and opals [7]. To artificially recreate similar nanostructured materials with repetitive features, scientists have mainly been dependent on top-down lithographic techniques such as electron beam lithography [8], photolithography [9] and focused ion beam (FIB) [10]. An alternative route is to make use of the self-assembly of tiny building units that when assembled can give rise to a large scale ordered repetitive structure that can be easily tuned by changing the building blocks used. Colloidal assembly [11] is a viable option in this respect, as it makes use of simple colloidal particles that self-assemble and organize themselves giving rise to ordered nanostructures that can be used as templates for subsequent processing steps. For instance, combining the use of colloidal templates with a technique such as electrodeposition, allows the fabrication of unique nanostructured materials that take the form of the inverse shape of the template used [12]. When metals such as gold or silver are involved, it is possible to create nanostructured plasmonic materials/surfaces via the combination of electrodeposition through the self-assembled colloidal templates [13], [14]. The combination of such techniques allows for the design of simple yet versatile processing routes to create novel functional nanostructured materials that can be further investigated [15]–[19].

SCOPE AND AIM OF THESIS

The subject of this thesis is to investigate and develop process routes to fabricate photonic and plasmonic nanostructured materials mainly via the bottom-up self-assembly of colloidal particles as a basis for creating nanostructured materials that exhibit photonic and/or plasmonic properties. There are two colloidal assembly techniques (Langmuir-Blodgett and self-assembly on water surface) utilized in this work, depending on the type of colloidal particles (silica or polystyrene particles) used. The colloidal crystals assembled can be either two- or three-dimensional. Finally, the processes to infiltrate the colloidal templates, which act as a mask, to fabricate (1) inverse opals of titanium dioxide; (2) templated and non templated nanostructured gold films; (3) arrays of plasmonic gold nano-antennas and (4) metamaterial fishnet structures, are developed and optimized.

The application of these structures in devices varies widely from; (1) enhancing the light extraction/cell efficiency in dye sensitized solar cells (for inverse opal titanium dioxide), (2) total quasi omnidirectional absorption of light in nanostructured gold surfaces (for gold films containing a closed packed monolayer of voids or dielectric material), and anti-reflective surfaces (for non templated nanostructured gold films); (3) enhancing the signal response of surface enhanced Raman spectroscopy (SERS) measurements (plasmonic gold nano-antenna array); to (4) novel metamaterials (fishnet structures).

The overall objective is to develop highly reliable, reproducible, bottom-up self-assembly based, simple and economical synthetic routes that can be used to fabricate the various high quality nanostructures on an extended scale through colloidal engineering which can offer an alternative to conventional top-down techniques that generally require expensive and bulky equipment.

OUTLINE OF THESIS

Chapter 1: Relevant photonic and plasmonic theories are described and an introduction to several well established bottom-up self-assembly techniques available today.

Chapter 2: The development of solid state dye sensitized solar cells incorporating inverse opal TiO₂ light trapping layers is presented, and the resulting cell efficiencies are reported.

Chapter 3: The fabrication of nanostructured gold surfaces via electrodeposition onto templated and non templated gold-coated glass substrate is described, and the optical characterizations of the fabricated surfaces are discussed.

Chapter 4: The fabrication of gold nano-antenna arrays via electrodeposition of nickel and gold into modified colloidal crystal templates is described, followed by the removal and transfer of the gold nano-antenna array into a transparent medium. Optical characterizations and preliminary surface enhanced Raman spectroscopy (SERS) measurements are presented.

Chapter 5: The fabrication of fishnet nanostructured materials by a combination of colloidal templating and electrodeposition is presented, and the problems encountered are listed.

Annexes: Details of all the experimental procedures are provided.

REFERENCES

- [1] F. Di Stasio, M. Cucini, L. Berti, D. Comoretto, A. Abboto, L. Bellotto, N. Manfredi, and C. Marinzi, "Tuning optical properties of opal photonic crystals by structural defects engineering," *J. Eur. Opt. Soc. Rapid Publ.*, vol. 4, p. 09033, Jun. 2009.
- [2] E. Ozbay, "Plasmonics: merging photonics and electronics at nanoscale dimensions.," *Science*, vol. 311, no. 5758, pp. 189–93, Jan. 2006.
- [3] J. Homola, "Present and future of surface plasmon resonance biosensors.," *Anal. Bioanal. Chem.*, vol. 377, no. 3, pp. 528–39, Oct. 2003.
- [4] M. D. Sonntag, J. M. Klingsporn, A. B. Zrimsek, B. Sharma, L. K. Ruvuna, and R. P. Van Duyne, "Molecular plasmonics for nanoscale spectroscopy.," *Chem. Soc. Rev.*, vol. 43, no. 4, pp. 1230–47, Feb. 2014.
- [5] E. Fort and S. Grésillon, "Surface enhanced fluorescence," *J. Phys. D. Appl. Phys.*, vol. 41, no. 1, p. 013001, Jan. 2008.
- [6] M. Kolle, P. M. Salgard-Cunha, M. R. J. Scherer, F. Huang, P. Vukusic, S. Mahajan, J. J. Baumberg, and U. Steiner, "Mimicking the colourful wing scale structure of the *Papilio blumei* butterfly.," *Nat. Nanotechnol.*, vol. 5, no. 7, pp. 511–5, Jul. 2010.
- [7] J. V. Sanders, "Colour of precious opal," *Nature*, vol. 204, no. 4964, p. 1151, 1964.
- [8] N. A. Hatab, C.-H. Hsueh, A. L. Gaddis, S. T. Retterer, J.-H. Li, G. Eres, Z. Zhang, and B. Gu, "Free-standing optical gold bowtie nanoantenna with variable gap size for enhanced Raman spectroscopy.," *Nano Lett.*, vol. 8, pp. 4952–4955, Nov. 2010.
- [9] V. Linder, B. D. Gates, D. Ryan, B. A. Parviz, and G. M. Whitesides, "Water-soluble sacrificial layers for surface micromachining.," *Small*, vol. 1, no. 7, pp. 730–6, Jul. 2005.
- [10] J. Valentine, S. Zhang, T. Zentgraf, E. Ulin-Avila, D. A. Genov, G. Bartal, and X. Zhang, "Three-dimensional optical metamaterial with a negative refractive index.," *Nature*, vol. 455, no. 7211, pp. 376–9, Sep. 2008.
- [11] F. Li, D. P. Josephson, and A. Stein, "Colloidal assembly: the road from particles to colloidal molecules and crystals.," *Angew. Chem. Int. Ed. Engl.*, vol. 50, no. 2, pp. 360–88, Jan. 2011.
- [12] P. N. Bartlett, P. R. Birkin, M. A. Ghanem, and C.-S. Toh, "Electrochemical syntheses of highly ordered macroporous conducting polymers grown around self-assembled colloidal templates," *J. Mater. Chem.*, vol. 11, no. 3, pp. 849–853, 2001.
- [13] P. N. Bartlett, J. J. Baumberg, P. R. Birkin, M. A. Ghanem, and M. C. Netti, "Highly ordered macroporous gold and platinum films formed by electrochemical deposition through templates assembled from submicron diameter monodisperse polystyrene spheres," *Chem. Mater.*, vol. 14, no. 5, pp. 2199–2208, May 2002.

- [14] P. N. Bartlett, J. J. Baumberg, S. Coyle, and M. E. Abdelsalam, "Optical properties of nanostructured metal films," *Faraday Discuss.*, vol. 125, p. 117, 2004.
- [15] R. Szamocki, S. Reculosa, S. Ravaine, P. N. Bartlett, A. Kuhn, and R. Hempelmann, "Tailored mesostructuring and biofunctionalization of gold for increased electroactivity.," *Angew. Chem. Int. Ed. Engl.*, vol. 45, no. 8, pp. 1317–21, Feb. 2006.
- [16] S. Reculosa, M. Heim, F. Gao, N. Mano, S. Ravaine, and A. Kuhn, "Design of catalytically active cylindrical and macroporous gold microelectrodes," *Adv. Funct. Mater.*, vol. 21, no. 4, pp. 691–698, Feb. 2011.
- [17] M. Heim, S. Reculosa, S. Ravaine, and A. Kuhn, "Engineering of complex macroporous materials through controlled electrodeposition in colloidal superstructures," *Adv. Funct. Mater.*, vol. 22, no. 3, pp. 538–545, Feb. 2012.
- [18] M. E. Abdelsalam, P. N. Bartlett, T. Kelf, and J. Baumberg, "Wetting of regularly structured gold surfaces.," *Langmuir*, vol. 21, no. 5, pp. 1753–7, Mar. 2005.
- [19] M. E. Abdelsalam, P. N. Bartlett, J. J. Baumberg, S. Cintra, T. A. Kelf, and A. E. Russell, "Electrochemical SERS at a structured gold surface," *Electrochem. commun.*, vol. 7, no. 7, pp. 740–744, Jul. 2005.

CHAPTER 1: BIBLIOGRAPHY REVIEW

GENERAL INTRODUCTION

The building, manipulating, and characterizing of optically active nanostructures are both related to the fields of nanophotonics and plasmonics. By investigating the fabrication techniques and resulting material properties, we can aim to design new capabilities in instrumentation for the nanoscale, chemical and biomedical sensing, disease treatment, enhanced solar cells and lighting, information and communications technologies, and many other applications.

The basic concepts of photonics and plasmonics has been known for the last 40 to 50 years, but it is only in the last decade where they have really attracted attention from the scientific community based on discoveries in nanoscience. Since the 1960s, photonic materials and devices have played a pervasive role in communications, energy conversion, and sensing. Nanophotonics, or photonics at the nanoscale, can be defined as “the science and engineering of light-matter interactions that take place on wavelength and subwavelength scales where the physical, chemical, or structural nature of natural or artificial nanostructure matter controls the interactions” [1]. In the next decade, nanophotonic structures and devices hold promise in reducing the energies of device operations, enhancing the spatial resolution for imaging, creating new sensors with increased sensitivity and specificity, and creating densely integrated information systems with lower power dissipation,

The aim of plasmonics is to exploit the unique optical properties of metallic nanostructures to enable routing and active manipulation of light at the nanoscale [2], [3]. It has only been slightly more than a decade that the young field of plasmonics has rapidly gained momentum, and it is envisioned to allow for the study of exciting new fundamental science as well as possible groundbreaking real-life applications in the areas of ultrahigh-resolution imaging and patterning, control of optical processes with extraordinary spatial and frequency precision, and targeted medical therapy. In addition, plasmonics can provide a bridge between classical electronics and photonics, thereby enabling the creation of next generation systems that comprise of both plasmonic and electronic devices exhibiting the best qualities of both photonics and electronics for computation and communication at high speed, broad bandwidth, and low power dissipation

Advances in the fabrication of optical structures at the nanoscale and improved control of materials properties have allowed researchers to demonstrate and realize the potential of nanophotonics and plasmonics, and they provide a strong motivation to continue the investigations in these fields which could further the understanding about the nature of light-matter interactions [4].

In the following sections, we will first touch on the topic of photonics with particular focus on the photonic crystals and discuss the underlying principles that gives them their unique optical properties. Following that, we will introduce the topic of plasmonics, and the various phenomena that make plasmonics such an interesting topic to investigate. Finally, we will make short overview of the current technologies available and used for the fabrication of photonic and plasmonics materials and devices.

1. PHOTONICS

Photonics is a term coined in analogy with electronics, which reflects the growing tie between optics and electronics forged by the increasing role that semiconductor materials and devices play in optical systems. Electronics involves the control of electric-charge flow (in vacuum or in matter), while photonics involves the control of photons (in free space or in matter). These two disciplines overlap each other since electrons often control the flow of photons and, on the other hand, photons can also control the flow of electrons. In addition, the term photonics reflects the importance of the photon nature of light in describing the operation of many optical devices [5].

Broadly speaking, photonics encompasses the generation of coherent light by lasers, and incoherent light by luminescence sources such as light-emitting diodes; the transmission of light in free space, through conventional optical components such as lenses, apertures, and imaging systems, and through waveguides such as optical fibers; modulation, switching, and scanning of light by the use of electrically, acoustically, or optically controlled devices; the amplification and frequency conversion of light by the use of wave interactions in nonlinear materials and the detection of light [5].

1.1 PHOTONIC CRYSTALS

One of the interesting materials that have been discovered in the field of photonics is the photonic crystal. It was as early as 1887 when Lord Rayleigh studied a one dimensional (1D) photonic crystal and observed the existence of high reflectivity over a narrow range of wavelengths known as the stop-band [6]. Today, these 1D structures, known as Bragg mirrors, are used extensively in light emitting diodes to improve light extraction and purity, in solar cells to enhance efficiency and in lasers to optimize their performance. Beyond 1D photonic crystals, there are also more complex two (2D) and three dimensional (3D) photonic crystals. In 1987, Yablonovitch [7] and John [8] theoretically predicted that high refractive index contrast (i.e; $n > 2.9$) 3D photonic crystals were capable of possessing an omnidirectional photonic bandgap, forbidding light propagation for all directions and all polarizations. Figure 1 shows a simple illustration of the different types of photonic crystals.

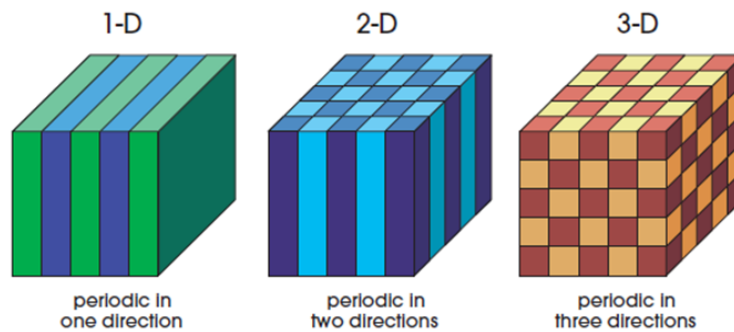


Figure 1. Simple illustrations of one, two and three dimensional photonic crystals. The different colors represent different dielectric constants. The periodicity of the dielectric material along one or more axes is the defining feature of a photonic crystal[9].

A crystal, as we all know, is a periodic arrangement of atoms and molecules. The pattern with which atoms or molecules are repeated in space is the crystal lattice. The conduction properties of a crystal are determined by the constituents of the crystals as well as the geometry of the lattice, which presents a periodic potential to an electron passing through it. According to quantum mechanics, electrons travel as waves in a conducting crystal, and only the waves that meet a certain criteria can propagate through a periodic potential without scattering (in the absence of defects and impurities). At the same time, the lattice also prohibits the propagation of other waves, and this is referred to as gaps in the energy band structure of the crystal. Energy bandgaps forbid the propagation of electrons with certain energies and directions. A complete bandgap occurs when there is a strong lattice potential

and the gap can cover all possible propagation directions. An example is the energy band gap between the valence and conducting bands in semiconductors.

A similar analogy can be said about photonic crystals. In the case of photonic crystals (Figure 1), the ‘atoms or molecules’ are replaced by macroscopic materials with differing dielectric constants, and the periodic potential is replaced with a periodic dielectric function (i.e. a periodic index of refraction). When the difference in dielectric constants is sufficiently large, and there is minimal absorption of light, then the refractions and reflections of light from all the various interfaces can result in a similar phenomenon for photons (light modes) that the atomic potential produces for electrons. Thus, a photonic crystal, a low loss periodic dielectric medium, can in theory provide a means of optical control and manipulation [9].

To understand how photonic crystals possess their unique optical properties, we first have to look at the interaction and propagation of light with a material. Using the macroscopic Maxwell’s equations, we derive the following [6], [9],

$$\nabla \cdot \mathbf{D} = \rho \quad \text{Equation 1}$$

$$\nabla \cdot \mathbf{B} = 0 \quad \text{Equation 2}$$

$$\nabla \times \mathbf{E} = -\frac{\partial}{\partial t} \mathbf{B} \quad \text{Equation 3}$$

$$\nabla \times \mathbf{H} = -\frac{\partial}{\partial t} \mathbf{D} + \mathbf{j} \quad \text{Equation 4}$$

Along with the constituent materials equations,

$$\mathbf{D} = \varepsilon_0 \mathbf{E} + \mathbf{P} \quad \text{Equation 5}$$

$$\mathbf{B} = \mu_0 (\mathbf{H} + \mathbf{M}) \quad \text{Equation 6}$$

Here, \mathbf{D} is the electric displacement, \mathbf{B} is the magnetic induction, \mathbf{E} is the electric field, \mathbf{H} is the magnetic field, ρ is the free charge density, \mathbf{j} is the free current density, \mathbf{P} is the polarization, \mathbf{M} is the magnetization, ε_0 is the permittivity constant in a vacuum and μ_0 the permeability constant in a vacuum.

By assuming that the materials are isotropic and only considering the case of linear optics, the equations (5 and 6) can be simplified to

$$\mathbf{D} = \varepsilon_0 \varepsilon \mathbf{E} \quad \text{Equation 7}$$

$$\mathbf{B} = \mu_0 \mu \mathbf{H} \quad \text{Equation 8}$$

From here, we obtain the master equations (7 and 8) which describe the propagation of the electric and magnetic fields. Further simplification of the equations can be made by assuming that there is no material dispersion and the materials are transparent (i.e. in the absence of free charges and free currents), which implies that $\rho = j = 0$. Hence, the Maxwell equations (Equations 1 to 4) become

$$\nabla \cdot \mathbf{H}(\mathbf{r}, t) = 0 \quad \text{Equation 9}$$

$$\nabla \cdot \varepsilon(\mathbf{r}) \mathbf{E}(\mathbf{r}, t) = 0 \quad \text{Equation 10}$$

$$\nabla \times \mathbf{H}(\mathbf{r}, t) - \varepsilon_0 \varepsilon(\mathbf{r}) \frac{\partial \mathbf{E}(\mathbf{r}, t)}{\partial t} = 0 \quad \text{Equation 11}$$

$$\nabla \times \mathbf{E}(\mathbf{r}, t) + \mu_0 \frac{\partial \mathbf{H}(\mathbf{r}, t)}{\partial t} = 0 \quad \text{Equation 12}$$

Mathematically the following can be rewritten as

$$\mathbf{H}(\mathbf{r}, t) = \mathbf{H}(\mathbf{r}) e^{-i\omega t} \quad \text{Equation 13}$$

$$\mathbf{E}(\mathbf{r}, t) = \mathbf{E}(\mathbf{r}) e^{-i\omega t} \quad \text{Equation 14}$$

For a specific frequency, the equations governing the mode profiles can be found by inserting equations 13 and 14 into equations 9 to 12. Thus,

$$\nabla \cdot \mathbf{H}(\mathbf{r}) = 0 \quad \text{Equation 15}$$

$$\nabla \cdot \varepsilon(\mathbf{r}) \mathbf{E}(\mathbf{r}) = 0 \quad \text{Equation 16}$$

$$\nabla \times \mathbf{H}(\mathbf{r}) + i\omega \varepsilon_0 \varepsilon(\mathbf{r}) \mathbf{E}(\mathbf{r}) = 0 \quad \text{Equation 17}$$

$$\nabla \times \mathbf{E}(\mathbf{r}) - i\omega \mu_0 \mathbf{H}(\mathbf{r}) = 0 \quad \text{Equation 18}$$

The master equation for the propagation of the magnetic field can now be solved by the elimination $\mathbf{E}(\mathbf{r})$ to yield an eigenvalue equation,

$$\nabla \times \left(\frac{1}{\varepsilon(\mathbf{r})} \nabla \times \mathbf{H}(\mathbf{r}) \right) = \left(\frac{\omega}{c} \right)^2 \mathbf{H}(\mathbf{r}) \quad \text{Equation 19}$$

Here, the constants ε_0 and μ_0 can be combined to obtain the speed of light in vacuum, $c = 1/\sqrt{\varepsilon_0\mu_0}$. With a given structure $\varepsilon(\mathbf{r})$, we can now use the master equation to find the modes $\mathbf{H}(\mathbf{r})$ and the corresponding frequencies. $\mathbf{E}(\mathbf{r})$ can then be calculated by using either equations 17 or 18.

From equation 19, the optical values of the photonic crystal and its dispersion relation are represented on the right hand side by the eigenvalues. For homogeneous and isotropic materials, permittivity, ε , is independent of spatial coordinates, and hence can be described solely by the material properties.

With the introduction of a spatial dependence of materials properties by a periodic ordering, the eigenvalues can be controlled which allows for the modification of the optical properties of the material according to how it is distributed. For periodically arranged materials, there exists a translational symmetry which can be represented as,

$$\varepsilon(\mathbf{r}) = \varepsilon(\mathbf{r} + \mathbf{R}) \quad \text{Equation 20}$$

Here, \mathbf{R} is the lattice-translation vector, and the solutions of the master equation (19), will have the following form,

$$\mathbf{H}(\mathbf{r}) = h_k(\mathbf{r}) \exp(i\mathbf{k}\mathbf{r}) \quad \text{Equation 21}$$

Where

$$h_k(\mathbf{r}) = h_k(\mathbf{r} + \mathbf{R}) \quad \text{Equation 22}$$

This solution is also known as the Bloch function[10].

1.2 PHOTONIC BANDGAPS

If we assume that light is propagating in a homogeneous, isotropic material with a refractive index of n , the index of refraction and permittivity are related by the following equation,

$$n = \sqrt{\epsilon} \quad \text{Equation 23}$$

The dispersion relation that describes the optical properties of this material is as follows,

$$\omega = \frac{c_0}{n} |\mathbf{k}| \quad \text{Equation 24}$$

Here, c_0 is the speed of light in a vacuum, the wave vector $|\mathbf{k}| = k = 2\pi/\lambda$, where λ is the wavelength of light in a vacuum, and the photon energy E , is given by $E = \hbar\omega$. Forward propagation (positive k values) of the dispersion relation results in a straight line. Backward propagation (negative k values) also results in the same dispersion properties. The blue line in Figure 2 originating from the origin illustrates the dispersion relation of a single unit cell of a periodic structure with lattice constant a .

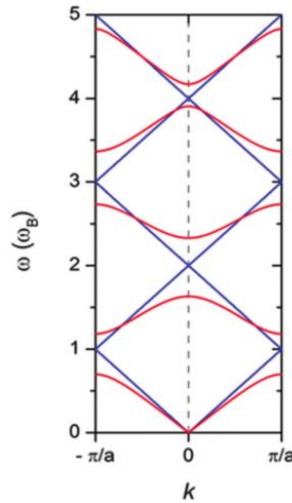


Figure 2. Light lines and the formation of a band gap. The calculations assume a material containing alternating slabs of 200 nm with refractive indices of 1.0 and 3.5. Blue lines represent the dispersion relation in an isotropic medium with artificial periodicity.[6]

By just considering the first Brillouin zone, (from $\mathbf{k} = -\pi/a$ to $\mathbf{k} = \pi/a$), it is observed that the dispersion lines of the forward and backward propagating waves cross at the frequency

$$\omega = \frac{c_0\pi}{\sqrt{\epsilon}a} \quad \text{Equation 25}$$

Bragg's Law provides the condition for a plane wave to be diffracted by a family of lattice planes according to the following equation

$$n\lambda = 2d\sin\theta \quad \text{Equation 26}$$

Here, d is the lattice spacing, θ is the angle between the wavevector of the incident plane wave and the lattice planes, λ is the wavelength and n is an integer corresponding to the order of the reflection. Even though it is generally used in crystallography calculations for X-rays, in the case of photonic crystals, the same rules can also be applied, but at optical wavelengths.

Assuming that the periodic structure is constructed with slabs of two alternating materials with different permittivity (similar to the sketch of the 1D photonic crystal shown in Figure 1), a forward propagating wave will be partially reflected at each interface between the two materials, resulting in both forward and backward travelling waves at the same time.

A standing wave, for frequencies that fulfill the Bragg condition, will then be formed due to the interference from both the forward and backward propagating waves.

The nodes and antinodes of the standing waves are either situated in the low refractive index and in the high refractive index material respectively or vice versa. The positions in between are forbidden. The electric field of the standing wave with nodes in the low index materials will mainly experience the high index material resulting in lower photon energy as described by equation 25. On the other hand, the other standing wave experiences a reduced effective index and will be found at higher photon energies. This difference in photon energies causes the opening of a gap in the dispersion relation which is known as the photonic bandgap. The lower energy band will be concentrated in the high index materials and is thus referred to as the "dielectric band", while the higher energy band will be concentrated in the low index materials and is commonly referred to as the "air band" (as it is usually composed of air). The red curves in Figure 2 illustrate the band structure described above. As a result of the band structure, no propagation within the photonic crystal is allowed for photons that have energies within the bandgap. Not only is it possible to obtain the fundamental bandgap, the higher order bandgaps can also be observed. Using Bragg's law (equation 26), the centre position of the bandgap can be calculated. Hence, the position of the bandgap can be shifted by either changing the properties of the materials and/or by changing the lattice constant. Modifying the low dielectric material mainly shifts the air band, while modifying the high dielectric

material mainly shifts the dielectric band. The width of the bandgap can thus be widened by increasing the difference between the dielectric constant of the two materials.

2. PLASMONICS

In the 1970s, one of the most significant discovered applications of plasmonics was the use of it in surface-enhanced Raman spectroscopy (SERS) [4]. It was not until the end of the 20th century and the beginning of the 21st century that the young field of plasmonics started to rapidly develop in new directions. This gain in momentum was spearheaded by the realization and successive demonstrations that metallic nanowires can guide light well below the seemingly unsurpassable diffraction limit [11], that metal films with nanoscale holes show extraordinarily high optical transmission [12], and that a simple thin film of metal can serve as an optical lens [13]. With the introduction of metamaterials (artificial optical materials with rationally designed geometries and arrangements of nanoscale building blocks.), plasmonic materials attracted even more attention as components incorporated into metamaterials.

While various advances have been made in the field of plasmonics, the most important ones have relied heavily on one key property of engineered metallic structures, and that is their unparalleled ability to concentrate light. Plasmonic structures and metamaterials consisting of deep-subwavelength building blocks enable light to be concentrated and actively manipulated in new ways. Even a simple spherical metallic nanoparticle can serve as a tiny antenna capable of capturing and concentrating light waves [4]. In the following sections, we will attempt to describe some of the plasmonic phenomena related to our work.

2.1 SURFACE PLASMON POLARITONS

Throw a rock into a pond and ripples will spread outwards across the surface. This is basically what happens when a photon hits the surface of a metal. However, the ripples in this case are made of electrons oscillating en masse and the wavelengths are measured in nanometers. These oscillations, known as surface plasmons, are able to pick up more light and carry it along the metal surface for considerable distances, akin to a “river of light” [14].

Following the pioneering work of Ritchie in the 1950s [15], surface plasmons have become widely recognized in the field of surface science. Surface plasmons are waves that propagate

along the surface of a conductor (usually a metal). Simply put, they are light waves trapped on the surface because of their interaction with the free electrons of the conductor, whereby the free electrons respond collectively by oscillating in resonance with the light wave. This resonant interaction between the electromagnetic field of light and the surface charge oscillation constitutes the surface plasmon and gives rise to its unique properties. Figure 3 illustrates the basics of surface plasmons.

There are two consequences that arise from the interaction between surface charges and the electromagnetic field constituting the surface plasmon [2].

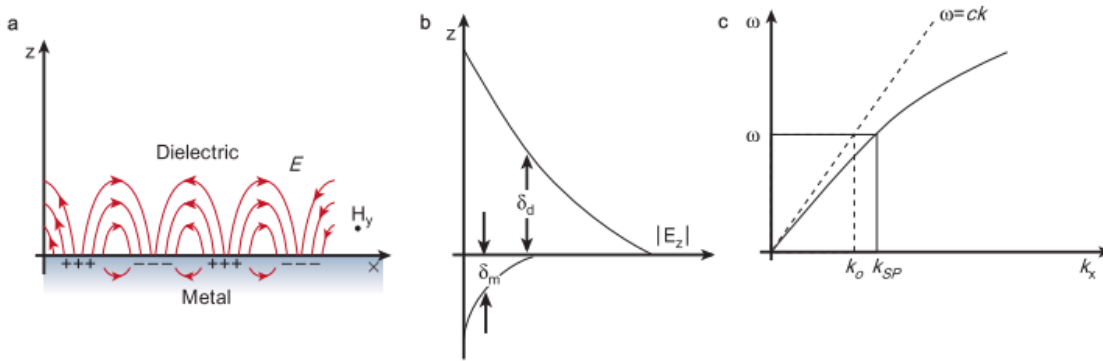


Figure 3. (a) Combined electromagnetic wave and surface charge character of a surface plasmon at the interface between a metal and dielectric material. (b) The field component of the perpendicular to the surface is enhanced near the surface and decays exponentially as it moves away from the surface. δ_d and δ_m are the decay lengths into the dielectric material and metal respectively. (c) Momentum mismatch between the surface plasmon mode and a free space photon of the same frequency [2].

The first consequence is that the momentum of the surface plasmon mode, $\hbar k_{sp}$, will be greater than that of a free space photon of the same frequency, $\hbar k_0$, where $k_0 = \omega/c$ is the free space wavevector. The surface plasmon dispersion relation (i.e. the frequency dependent surface plasmon wave vector, k_{sp}) can be obtained by solving the Maxwell's equations under the appropriate boundary conditions, resulting in

$$k_{sp} = k_0 \sqrt{\frac{\epsilon_d \epsilon_m}{\epsilon_d + \epsilon_m}} \quad \text{Equation 27}$$

Here, ϵ_d and ϵ_m are the frequency dependent permittivity of the dielectric and metal respectively and they must have opposite signs to allow the possibility of surface plasmons at the interface. For metals, this condition is satisfied as ϵ_m is both negative and complex.

The second consequence is that, unlike the propagating nature of surface plasmons along the surface, the field that is perpendicular to the surface decays exponentially with distance from the surface. This perpendicular field is the evanescent or near field, and is the result of the bound, non-radiative nature of surface plasmons which prevents power from propagating from the surface.

To generate surface plasmons using light, the momentum mismatch (which is associated with the binding of surface plasmons to the surface) between light and surface plasmons of the same frequency must be bridged. This can be achieved via three main techniques, which are (1) prism coupling to enhance momentum of incident light, (2) scattering from a topological defect on the surface and (3) making use of a periodic corrugation in the metal's surface.

From the optics point of view, surface plasmons are very attractive because of their ability to concentrate light and channel light using subwavelength structures. By making use of surface plasmons, periodically nanostructured metals have the potential of being used as photonic bandgap materials, in the form of photonic surfaces (Figure 4). When the effective wavelength of the surface plasmon mode is double the period of the nanostructure, scattering can lead to the formation of a surface plasmon standing wave and the opening of a surface plasmon stop band. When the surface is textured in both in plane directions, surface plasmon modes may be prevented from travelling in any in plane direction which leads to a full photonic band gap for surface plasmon modes [2].

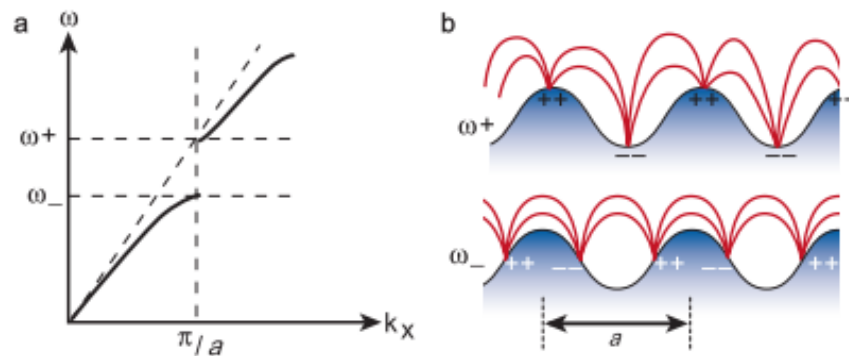


Figure 4. (a) Dispersion diagram showing the formation of a surface plasmon photonic bandgap on a periodically textured metal surface when the period, a , is equal to half the wavelength of the surface plasmon. Surface plasmon modes with frequencies between the band edges ω_+ and ω_- cannot propagate. (b) Illustration of the two surface plasmon standing wave solutions, each with the same wavelength. The upper frequency solution, ω_+ , is of higher energy because of greater the larger distance between surface charges and greater distortion of the field [2].

2.2 LOCALIZED SURFACE PLASMON RESONANCE

One of the oldest examples of man-made objects that incorporated noble metal (e.g. Au or Ag) nanoparticles was the Roman Lycurgus cup (Figure 5). The incorporation of the noble metal nanoparticles in the glass of the cup made it dichroic: it resembled jade with an opaque greenish-yellow hue under direct light, but becomes translucent ruby in color when light shines through it [16]. Today, we know that the light scattering brought about by the nanoparticles can be attributed to localized surface plasmons resonance (LSPR).

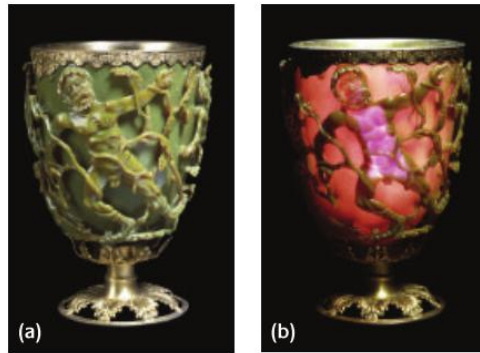


Figure 5. The Lycurgus Cup in (a) reflected and (b) transmitted light

Localized surface plasmon resonance is an optical phenomenon generated by a light wave trapped within conductive nanoparticles smaller than the wavelength of light. This interaction produces coherent localized plasmon oscillations (Figure 6) at a resonant frequency and intensity that is characteristic of the type of material, shape, size, size distribution and the surrounding environment [3], [17], [18].

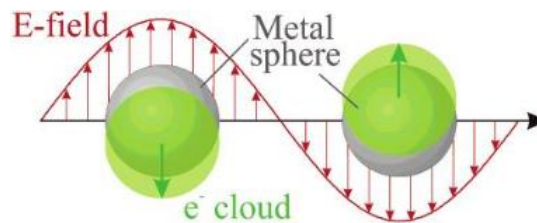


Figure 6. Schematics of the plasmon oscillation of a spherical metal nanoparticle showing the displacement of the conduction electron charge cloud relative to the nuclei [19].

Drude [20] introduced a simple model for the dielectric properties of metals, which describes the conduction electrons in metals as a classical diffusive electron gas. Mutual collision damp the electron motion at a rate of $1/\tau$, (where τ is the electron relaxation time of the free

electron gas), and when placed under an electric field, the electrons oscillate. From this model, a frequency dependent dielectric function $\varepsilon(\omega)$ of the Drude metal is described as follows,

$$\varepsilon(\omega) = \varepsilon_{\infty} - \frac{\omega_p^2}{\omega^2 + i\frac{\omega}{\tau}} \quad \text{Equation 28}$$

Here, ε_{∞} describes the contribution of the bound electrons to the polarizability, and the plasma frequency, ω_p , which describes the oscillation of the free electron plasma, is given by

$$\omega_p = \sqrt{\frac{n_e e^2}{\varepsilon_0 m_e}} \quad \text{Equation 29}$$

where n_e is the electron density of the metal, m_e is the effective mass of the conducting electrons, e is the electron charge, and ε_0 is the permittivity of vacuum,

Although the Drude model is able to accurately describe most of the dielectric properties of metals, it is still inadequate when dealing with optical frequencies and especially with noble metals because of the d-d transitions energy levels which give rise to the localized surface plasmon resonance in the visible range of the spectrum [17].

Metal nanostructures with dimensions in the range of the wavelength of light or below are able to support optical resonances. Mie Theory provides a solution to analytically treat the response of a metal particle (absorption or scattering) to an external electric field [21]. For small particles, where the dimensions are smaller than the wavelength ($d \ll \lambda$), the quasi static approximation can be used [22], and hence, the microscopic polarizability α of a small sphere with a radius r can be expressed as

$$\alpha(\omega) = 4\pi r^3 \frac{\varepsilon - \varepsilon_{med}}{\varepsilon + 2\varepsilon_{med}} \quad \text{Equation 30}$$

Here, ε and ε_{med} refer to the dielectric properties of the particle and the surrounding medium respectively. This function (equation 30), is also known as the Clausius-Mossotti relation, and is maximum for α when $\varepsilon = -2\varepsilon_{med}$. Since the dielectric function of a metal is dependent on frequency, the resonance condition can only be met for a distinct frequency that is determined by the material property as well as the dielectric function of the surrounding medium. For materials with a small imaginary part of ε , this resonance condition can be simplified to

$$Re[\varepsilon] = -2\varepsilon_{med} \quad \text{Equation 31}$$

This relationship is known as the Fröhlich condition and the associated mode (in an oscillating field) is the dipole surface plasmon of the metal nanoparticle. Equation 31 illustrates the direct relationship between the plasmon resonance frequency and the dielectric constant of the medium. It is exactly this unique property that makes metal nanoparticles ideal candidates for sensing applications to detect changes in its immediate environment.

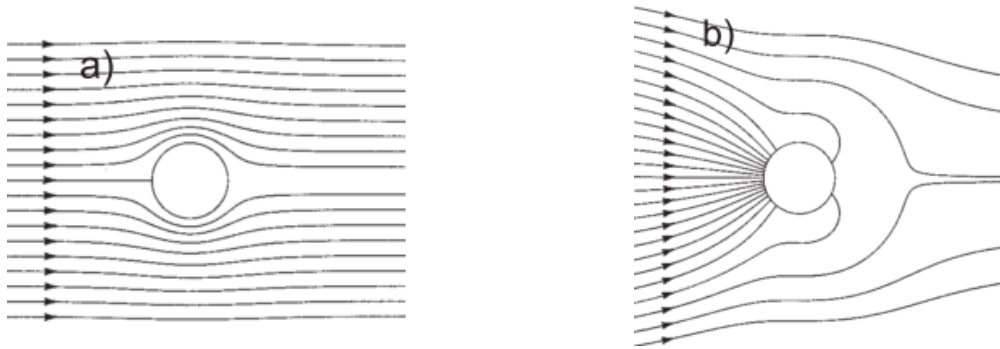


Figure 7. Energy flux (Poynting vector) around a metal nanoparticle (a) when excitation frequency is far from plasmon resonance and (b) at plasmon resonance frequency[3].

Simply put, when the frequency of light is far from the intrinsic plasmon resonance of the metal nanoparticle, the energy flow is only slightly disturbed (Figure 7a). However, at plasmon resonance frequency, the strong polarization of the particle draws the energy to itself (Figure 7b), resulting in a strong light scattering, the appearance of intense surface plasmon absorption bands and an enhancement in the local electric fields.

3. FABRICATION METHODS

The spike in the interest and research on the photonics over the last decade has led to a variety of applications related to photonics and plasmonics. This has been boosted by various factors, including the significant advances in computational design tools and their accessibility, the emergence of new nanofabrication techniques, and the realization of new optical and structural characterization methods. Undoubtedly, the most important factor has been the progress in the area of fabricating photonic and plasmonic devices that have dimensions on the order of or below the wavelength of light [4]. For example, in order for a photonic crystal to have applications in the visible or near infrared (NIR) regimes, they would need to have spatial modulations of the refractive index of a few hundred nanometers to one micron, since the working range of a photonic crystal is directly related to the spatial periodicity of the refractive index. Fabrication techniques at this scale have traditionally been an enormous challenge, and even with the current technology available and the introduction of new fabrication techniques, it still remains a challenge to discover a cost effective, reproducible, large scale and precise approach to fabricate such structures.

Fabrication of synthetic (i.e. man-made) photonic and plasmonic (nano)materials can be generally categorized by one of two approaches; top-down or bottom-up. Top-down approaches, such as lithography techniques using electrons, photons, atoms and ions as well as embossing and scanning tip methodologies, offer high precision to the final structure of the photonic crystal made. However, top-down approaches are generally expensive and require a longer time to fabricate the structures over a larger area because of the serial nature of the approach. In contrast, bottom-up approaches rely on the self-driven assembly of basic building blocks into ordered periodic structures that is generally faster, cheaper and on a larger scale than top down approaches. However, the control and precision in fabricating the structures may pale slightly when compared with top-down approaches. Nonetheless, the lower cost and ease of fabrication makes bottom-up approaches a viable and practical alternative that could rival top-down approaches.

In following sections, we will look at some of the different top-down and bottom-up nanofabrication techniques available today.

3.1 TOP-DOWN APPROACHES

Top-down fabrication of nanostructured materials is akin to sculpting from a block of stone. By starting with a defined base material, bits and parts of it are removed until the desired shape is created. In other words we start from the top of the blank material and work our way downwards, selectively removing material until we reach the base to attain the final nanostructure. Top-down approaches uses a variety of lithography techniques. Below, we will introduce a few of the more common techniques.

In conventional optical or photolithographic approaches, light is collimated through a quartz plate supporting a chromium coating to create patterns on a substrate spin-coated with a photoresist. The quartz plate serves as a mask and is placed in contact or close proximity to the resist-coated wafer. The photoresist can be either positive or negative. For a positive photoresist, the exposed regions will have a higher solubility than the protected regions after being illuminated. For a negative photoresist, the exposed regions of the material will become crosslinked after illumination; and hence, will have a lower solubility than the protected regions [23]. Thus, by exposing the illuminated photoresist to a suitable solvent after illumination; the lower solubility regions will be etched away, and a positive or negative pattern can be developed on it (depending on the type of photoresist used). Figure 8 shows an example of using a positive photoresist to pattern a substrate.

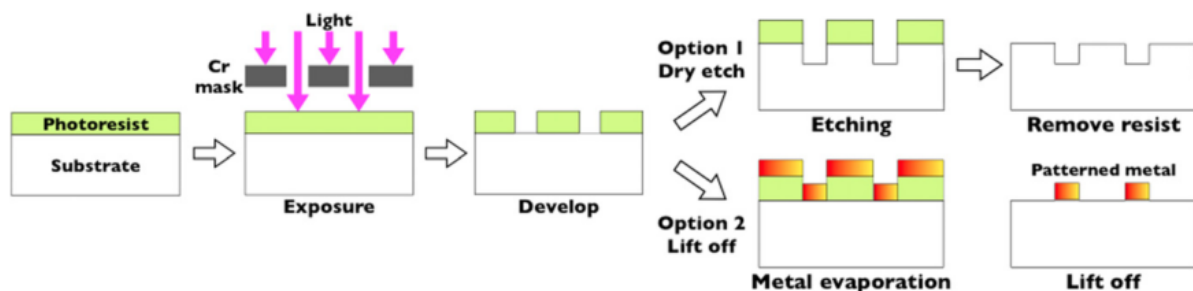


Figure 8. Schematics showing an example of optical lithography. A mask is first used to create a pattern on a photoresist (in this case a positive photoresist). Next, the patterned photoresist can be used to either pattern the substrate (option 1) or be used as a mask for metal evaporation onto the substrate (option 2) [24].

A cheaper alternative to conventional optical lithography is optical interferometric lithography. In this technique, coherent optical beams incident from different directions generate interference patterns in a photoresist without using any photomask or advanced exposure optics. While complex patterns are not possible with interferometric lithography, it is still a very practical option to make simple periodic structures, because of the reduced costs

and there is no requirement for an expensive photomask in the process. Furthermore, the patterning can be done with high throughput over a large area [24]. One major limitation of photolithographic techniques is that the final resolution of the structure is ultimately limited by the wavelength of the light used [23].

Another form of top-down mask-less lithography is electron beam (e-beam) lithography. It is considered superior over conventional photolithography as it is not limited by the diffraction limit of light that helps create features in the nanometer range (for conventional photolithography). It was first developed as a lithography method in the 1970s when researchers noticed that certain types of materials would be damaged under e-beam exposure [24]. E-beam lithography generates a latent pattern directly in an electron sensitive material by scanning with a focused, high energy electron beam. It is also a very popular method to make photomasks for photolithography. Figure 9 shows some typical structures fabricated by e-beam lithography.

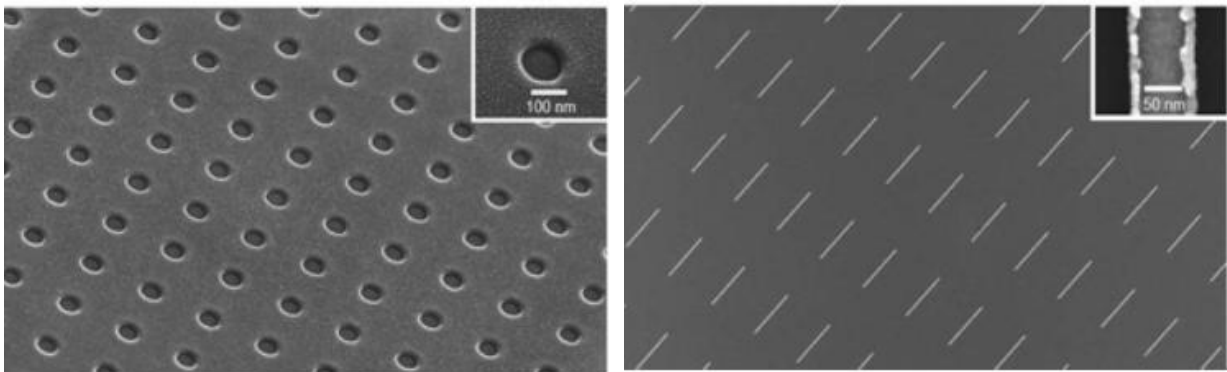


Figure 9. SEM images of nanostructures fabricated by e-beam lithography. An array of holes in PMMA (left). An array of gold nanorods fabricated by a liftoff process (right).

For the direct fabrication of metallic nanostructure, focused ion beam lithography (FIB) is used extensively. FIB offers an alternative method of nano-patterning compared with conventional methods that use a resist, exposure and development. The beam spot size can vary from 5 nm to a micron by using the appropriate equipment set up (column optics, ion source and beam current). Ga is widely used in FIB because of its low melting temperature (30 °C), low volatility and low vapor pressure [25]. FIB offers many advantages as a mask-free, high-resolution, direct-write nanofabrication tool with the ability to sputter, image, analyze and deposit. It also has the ability to create two- and three-dimensional patterns. However, similar to e-beam lithography, it is a serial lithography technique, which only

allows the patterning of one spot at a time. Hence, it is not practical for large-area patterning. One inherent problem arising from the use of FIB is the fact that Ga ions are implanted at atomic fractions of 1–50% near the sample surface as a result of the process, and this can lead to a degradation of the plasmonic properties of a patterned metal film [25].

Many interesting patterned materials have been made by top-down lithographic techniques. Using e-beam lithography, followed by e-beam evaporation and liftoff, Dolling et al. have, for instance, fabricated a double fishnet negative index metamaterial (NIM) that exhibits negative permittivity and permeability at 780 nm [26]. Similarly, Xiao et al. reported a negative index metamaterial (Figure 10) at around 580 nm [27]. Using FIB, Valentine et al. have experimentally demonstrated the first three dimensional optical NIM (Figure 11) made by stacking up multiple fishnet functional layers in 2008 [28].

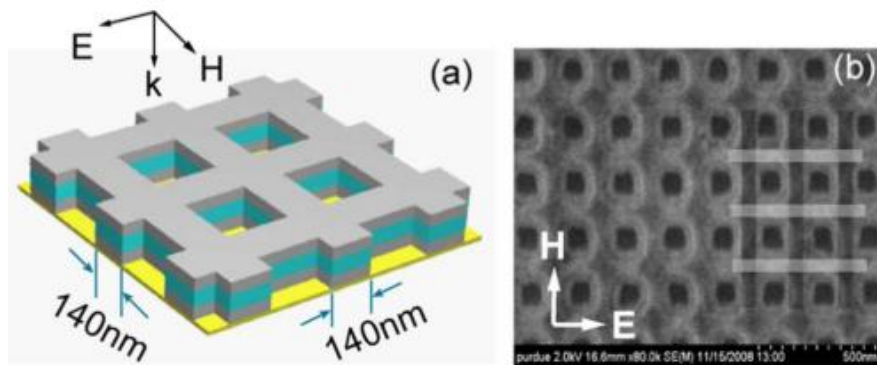


Figure 10. (a) Schematic of a fishnet metamaterial consisting of Al_2O_3 (10 nm), Ag (43 nm), Al_2O_3 (45 nm), Ag (43 nm), Al_2O_3 (10 nm). (b) Top view of an SEM image of the fabricated structure made by e-beam lithography [27].

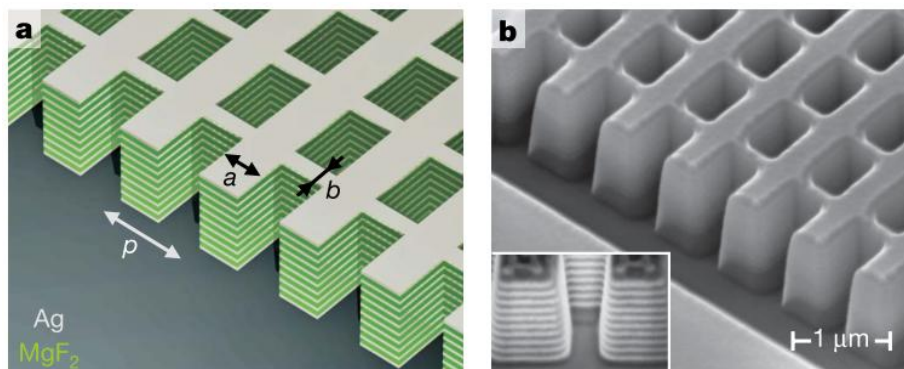


Figure 11. (a) Diagram of a 21-layer fishnet structure with a unit cell of $p=860$ nm, $a=565$ nm and $b=265$ nm. (b) SEM cross section image of the 21-layer fishnet structure made by FIB. The structure consists of alternating layers of 30 nm silver (Ag) and 50 nm magnesium fluoride (MgF_2), and the dimensions of the structure correspond to the diagram in (a).

3.2 BOTTOM-UP APPROACHES

Opals, butterfly wings, peacock feathers, etc., are naturally occurring examples of photonic colloidal crystal materials that exhibit iridescent colors due to the scattering and diffraction of light by random or periodic nanostructures. Such structures, which typically have features at the scale of the wavelength of light, interact strongly with light. Opal gems, in particular, are natural colloidal crystals created from the ordered deposition of spherical silica particles after a long period of siliceous sedimentation and compression under gravitational and hydrostatic forces [29], [30].

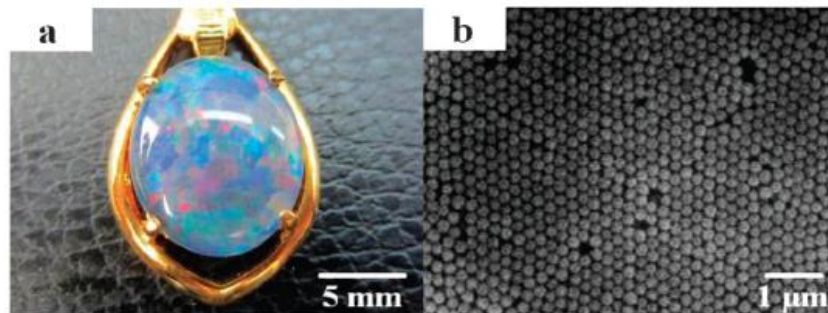


Figure 12. (a) Optical photograph of a gem opal. (b) SEM images of the packing inside the opal [29]

3.2.1 COLLOIDAL ASSEMBLY

Bottom-up approaches to make photonic colloidal crystals commonly make use of spherical beads as building blocks for self-assembly. Typically, these particles are either silica or polystyrene (PS) latex particles because of their ease of synthesis (see Annex 1).

The bottom-up assembly of a colloidal crystal is self-driven, implying that there are colloidal forces at work that brings the tiny building blocks together. In colloidal assembly, these forces are crucial and there are three types of forces that should be highlighted. The first type is the presence of intrinsic driving forces for ordering which could be the entropically favorable packing of monodisperse colloids into ordered arrays. For this, the monodispersity of the particles (i.e. size and shape homogeneity) is crucial. The second type to consider is the long range external forces, such as gravity or centrifugation, which act to bring the particles together. The third type is the repulsion forces between particles to prevent premature aggregation that could arise from Van der Waals forces. Electrostatic repulsions [31] by charge stabilization in polar solvents and steric repulsions [32] by solvated adsorbed layers are two examples for these kind of repulsion forces.

There are a variety of assembly methods available in literature[6], [29], [33], [34] for the fabrication of colloidal crystals depending on, the type of building blocks used, the resulting structure (two-dimensional monolayers or three-dimensional bulk crystals), and the application it is aimed at. Table 1 lists the common methods that are used to fabricate colloidal crystals.

The simplest and most basic method of direct assembly onto a substrate is by sedimentation, which is the process by which natural opals are formed as a result of gravity on the tiny individual particles that build the opal.

Another simple method is by drop casting. In this case where a drop of colloidal suspension is literally dropped onto the substrate surface and allowed to dry by evaporation. As water evaporates, the receding meniscus helps pull the particles together and they rearrange themselves in the lowest surface energy configuration. Temperature and humidity control, suspension concentration, choice of substrates are some of the factors that can be adjusted to obtain higher quality colloidal crystals.

Table 1 List of methods commonly used for colloidal assembly

Method	Remarks
Drop casting (Sedimentation) [35], [36]	<ul style="list-style-type: none"> • Simple but slow process. • Patches of colloidal crystals formed. • Difficult to control exact conditions
Vertical deposition [37]–[39]	<ul style="list-style-type: none"> • Requires very good control of evaporation conditions (i.e. temperature and humidity) for a good deposition. • Slow process (days). • Very good quality of colloidal crystals formed under the proper conditions • Gradient in the thickness of colloidal crystal formed
Centrifugation [40]	<ul style="list-style-type: none"> • Simple and fast process. • Generally big bulk colloidal crystals formed.
Spin-coating [41]–[43]	<ul style="list-style-type: none"> • Simple and fast process. • Monolayer formation possible. • Patches of small coating area of monolayers.
Dip-coating [44]–[46]	<ul style="list-style-type: none"> • Can control thickness of layers by the speed of withdrawal. • Gradient in layer thickness. [38]
Shear ordering [47]	<ul style="list-style-type: none"> • Requires very good control of process parameters • Slow process • Makes thin films
Langmuir-Blodgett [48][49]–[51]	<ul style="list-style-type: none"> • Monolayer compressed on water surface by mobile arms. • Monolayer transfer onto substrate. • Can be repeated to deposit multilayers exactly as desired. • Takes time for preparation of equipment and spreading of particles.
Direct assembly on water surface [52]–[54]	<ul style="list-style-type: none"> • Simple and fast process. • Good two dimensional closed pack array on water surface. • One monolayer at a time can be transferred. • Can be repeated to deposit multilayers exactly as desired.
Electrophoretic assembly [55]	<ul style="list-style-type: none"> • Simple and fast process • Can be used for patterning

The vertical deposition method (Figure 13) also involves evaporation of the liquid phase of a colloidal suspension to induce the convective assembly of a colloidal crystal onto a substrate. However, unlike drop casting where the substrate lays horizontal, the substrate is held vertically and partially submerged in a colloidal suspension. This method requires very good control of the deposition conditions and environment (suspension concentration, type of solvent, temperature, humidity, ground vibrations, wind, etc.), and long deposition time of a few days to allow for all the liquid (usually water) to evaporate. Any interruptions during the drying process will severely affect the quality of the colloidal crystal obtained. Nonetheless, if done correctly, very high quality of colloidal crystals can be obtained by this method.

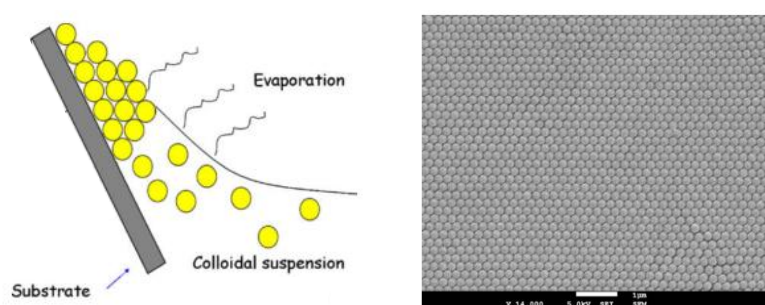


Figure 13. Schematic of convective self-assembly by vertical deposition and the SEM picture of an opal made of 235 nm polystyrene beads made by this method [38].

Centrifugation and spin coating are two methods that require the use of centrifugational forces to help compact the particles in a colloidal suspension. For centrifugation, the name speaks for itself. A colloidal suspension is placed in a centrifuge and spun at high speeds to compact the particles together. This results in bulk colloidal crystals that are of very good quality. Spin coating on the other hand, is used to make thin films or monolayers of colloidal crystals on planar substrates. However, as the force experienced by the suspension on different parts of the substrate is different, the resulting colloidal crystal films formed on the substrate varies according to the position from the rotation axis (as illustrated in Figure 14). The colloidal crystal films are usually patchy across the substrate.

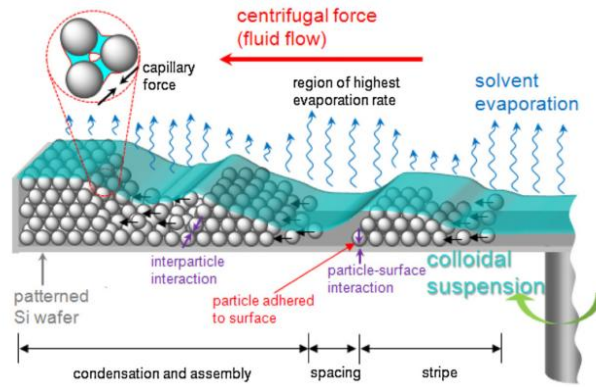


Figure 14. Schematic representation of particles and fluid flux on a substrate as it is rotated [41].

Dip coating (Figure 15, left) involves the controlled withdrawal of a substrate from a colloidal suspension. The substrate is vertically held on one end and first submerged into a colloidal suspension. It is then slowly pulled up from the suspension, and convective assembly takes place at the interface between the substrate surface and the air/liquid interface (the phenomenon is similar to vertical deposition). The thickness of the colloidal crystal deposited can be tuned by adjusting the speed of substrate withdrawal.

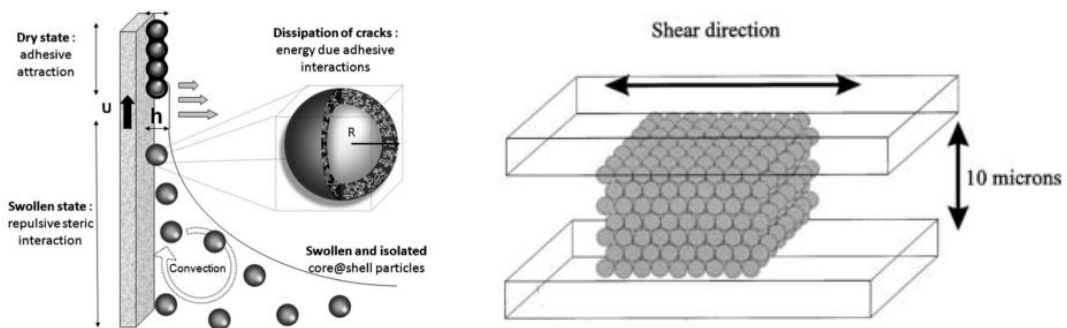


Figure 15. Schematics of (left) the dip coating process [46] and (right) by shear alignment [47].

Shear ordering (Figure 15, right) makes use of a narrow channel between two planes to confine and induce packing of the particles in a colloidal suspension by shear forces. This method is difficult to perform because of the complexity in maintaining a uniform shear force throughout the process.

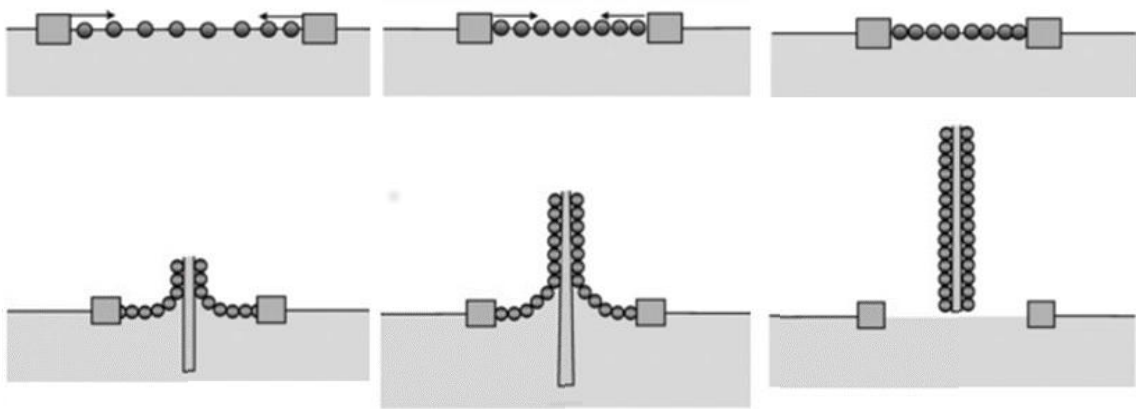


Figure 16. Schematic illustration of the Langmuir-Blodgett technique (adapted from [48]). (Top, from left to right) Packing of particles together on water surface by physically compressing them together using mobile barriers. (Bottom, from left to right) Transfer of a single layer of packed beads onto both sides of a substrate inserted and removed vertically from the trough.

The Langmuir-Blodgett (LB) technique is slightly different compared with the abovementioned methods. The previous methods involved the fabrication of colloidal crystals directly onto the substrates, while the Langmuir-Blodgett technique is a two-step process whereby a two dimensional colloidal crystal monolayer is first formed on a water surface before it is transferred onto the substrate (Figure 16). The monolayer of particles is formed by first spreading a colloidal suspension onto the surface of water and then followed by compacting the particles on the water surface by using mobile arms, while at the same time monitoring the surface pressure to determine when the monolayer is closed packed. This method offers a control of the colloidal crystal fabricated on the layer level (i.e. the transfer of monolayers can be repeated on the same substrate to stack the monolayers and make a colloidal crystal with a defined layer thickness).

The water surface transfer method is similar to the Langmuir-Blodgett technique in the sense that particles are spread on a water surface, but it differs in that, unlike the Langmuir-Blodgett technique, the particles self-organize into closed pack arrays by tuning the surface tension of water with surfactant, instead of physical compression using mobile arms (Figure 17). Since the particles self-organize, the resulting closed packed monolayers are usually of better quality than the Langmuir-Blodgett due to the nature of the formation. The monolayer can also be repeatedly stacked to make multilayered colloidal crystals.

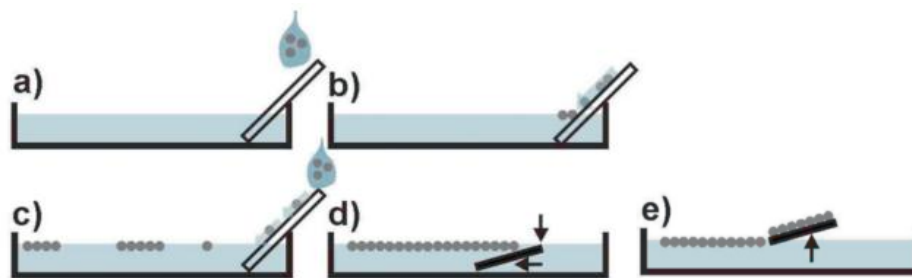


Figure 17. Schematic illustration of the water surface transfer method [52]. (a, b, c) Spreading of polystyrene beads onto a water surface by using a glass slide as tool to facilitate the process. (d, e) Transfer of self-assembled monolayers onto substrates by first immersing the substrates completely in the water phase and then positioning them under the monolayers and carefully lifting them out onto the substrate at an angle.

Electrophoretic assembly of colloidal crystals involves making use of colloidal particles with functional groups that induce a surface charge on them [55]. By applying an electric field across the colloidal suspension, the charged colloidal particles are displaced in an electric field towards an electrode of the opposite charge. This method can be used for particle positioning, separation, measurements of surface charge and for microfluidics.

3.2.3 COLLOIDAL LITHOGRAPHY

Colloidal lithography is a general term that refers to various surface patterning processes based on the use of colloidal crystals as templating masks. These colloidal masks can be used directly as deposited or subject to certain post-deposition treatment to alter and manipulate certain parameters of the template. This bottom-up masking methodology for surface patterning is gaining increasing attention because of its simplicity, low cost, the flexibility of extending on various planar and non-planar substrates with different surface chemistry, and the ease of scaling down the feature size below 100 nm [56].

The physical structure of a colloidal crystal deposited on a substrate can be altered by applying external forces to change the physical structure of the colloidal crystal. One method is by annealing. Controlled annealing refers to the use of heat to modify the structure of a polystyrene colloidal template. By exposing the polymer template to a temperature slightly above the glass transition temperature (T_g), it is possible to induce a slight fusing of the beads at the point at which they touch each. The beads are modified in terms of their shape by becoming gel like for a short period of time. Control of this sintering time is crucial to the

eventual pore dimensions and the shape of the beads which influence the overall shape of the colloidal crystal, and the subsequent material that is deposited through it. Kosiorek et al. demonstrated the use of microwave heating and microwave pulses to anneal polystyrene (PS) colloidal masks in a controlled fashion (Figure 18), which were subsequently used for the deposition of metals via metal evaporation [57].

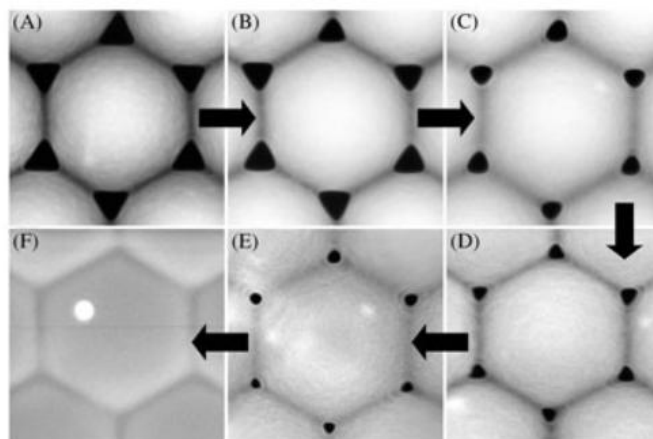


Figure 18. 540-nm PS latex mask annealed in 25 mL of water/EtOH/ acetone mixture by A) 1, B) 2, C) 4, D) 6, E) 7, and F) 10 microwave pulses [57].

Another way to modify the geometry of a colloidal crystal template is to make use of plasma etching. Most organic polymers can be plasma etched quickly and isotropically yielding only gaseous products. The etching of a colloidal crystal into a textured surface using a reactive ion beam was first reported by Deckmann and Dunsmuir in 1983 [58]. Today, this technique has become quite well established and is also known as nanospheres lithography (NSL). Ji et al. demonstrated a size-controllable NSL technique based on spin-coating of polystyrene nanospheres. The polystyrene nanospheres were used as a mask for the fabrication of nano-scale pillar structures on GaN, Al₂O₃, and Si substrates (Figure 19) via an inductively coupled plasma reactive ion etching process [59]. Choi et al. reported a colloidal lithographic approach to fabricating non spherical colloidal particle arrays by selective reactive ion etching of multilayered spherical colloidal particles [60]. Vogel et al. investigated the plasma etching conditions used to shrink the colloids in a close-packed monolayer to produce non close-packed monolayers with lattice spacing and symmetry reflecting the order of the initial close-packed monolayer [52]. Hanarp et al. made use of nanospheres lithography to fabricate short range ordered arrays of gold disks (Figure 20) with tunable localized surface plasmon resonances and studied their optical properties [61].

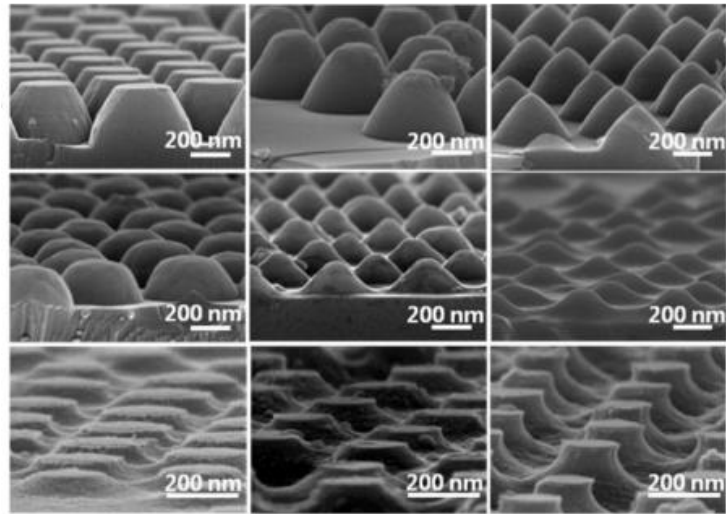


Figure 19. SEM Images of GaN (top), sapphire (middle) and silicon (bottom) substrates after inductively coupled plasma reactive ion etching [59].

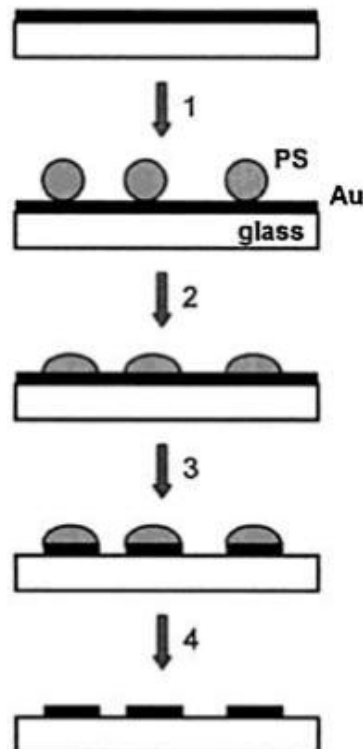


Figure 20. Nanofabrication of gold disks using colloidal lithography. (1) Polystyrene nanoparticles are adsorbed by polyelectrolyte self-assembly onto a glass slide pre-coated with 20 nm of Au. (2) Shape modification of the polystyrene particles by heat treatment on a hotplate, 106-120 °C. (3) Ar ion beam etching. (4) Removal of particle by UV/ ozone, leaving gold disks on a glass substrate [61].

REFERENCES

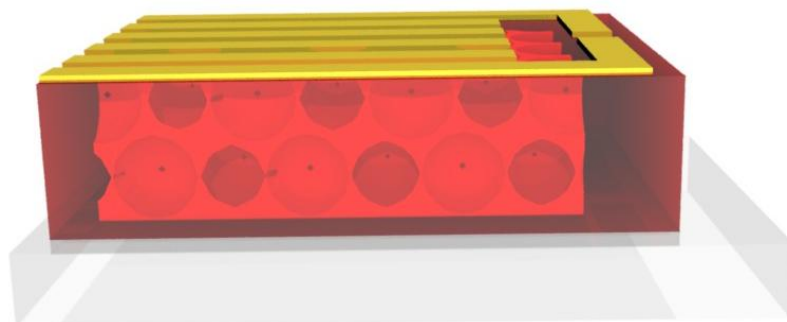
- [1] National Research Council, “Nanophotonics: Accessibility and Applicability,” National Academies Press, 2008.
- [2] W. L. Barnes, A. Dereux, and T. W. Ebbesen, “Surface plasmon subwavelength optics,” *Nature*, vol. 424, pp. 824–830, 2003.
- [3] S. A. Maier, M. L. Brongersma, P. G. Kik, S. Meltzer, A. A. G. Requicha, and H. A. Atwater, “Plasmonics - A Route to Nanoscale Optical Devices,” *Adv. Mater.*, vol. 13, no. 19, pp. 1501–1505, 2001.
- [4] E. L. Hu, M. Brongersma, and A. Baca, “Applications : Nanophotonics and Plasmonics,” 2008, pp. 318–340.
- [5] B. E. A. Saleh and M. C. Teich, *Fundamentals of Photonics*. 1991.
- [6] G. von Freymann, V. Kitaev, B. V Lotsch, and G. A. Ozin, “Bottom-up assembly of photonic crystals.,” *Chem. Soc. Rev.*, vol. 42, no. 7, pp. 2528–54, Apr. 2013.
- [7] E. Yablonovitch, “Inhibited spontaneous emission in solid-state physics and electronics,” *Phys. Rev. Lett.*, vol. 58, no. 20, pp. 2059–2062, 1987.
- [8] S. John, “Strong localisation of photons in certain disordered dielectric superlattices,” *Phys. Rev. Lett.*, vol. 58, no. 23, pp. 2486–2489, 1987.
- [9] J. D. Joannopoulos, S. G. Johnson, J. N. Winn, and R. D. Meade, *Photonic crystals - Molding the flow of light (Second edition)*. Princeton University Press, 2008.
- [10] F. Bloch, “Uber die Quantenmechanik der Elektronen in Kristallgittern,” *Zeitschrift fur Phys.*, vol. 52, no. 7–8, pp. 555–600, Jul. 1929.
- [11] J. Takahara, S. Yamagishi, H. Taki, a Morimoto, and T. Kobayashi, “Guiding of a one-dimensional optical beam with nanometer diameter.,” *Opt. Lett.*, vol. 22, no. 7, pp. 475–7, Apr. 1997.
- [12] T. W. Ebbesen, H. J. Lezec, H. F. Ghaemi, T. Thio, and P. A. Wolff, “Theory of extraordinary optical transmission through subwavelength hole arrays.,” *Nature*, vol. 391, pp. 667–669, Feb. 1998.
- [13] J. Pendry, “Negative refraction makes a perfect lens,” *Phys. Rev. Lett.*, vol. 85, no. 18, pp. 3966–9, Oct. 2000.
- [14] J. Heber, “Surfing the wave,” *Nature*, vol. 461, no. October, p. 720, 2009.
- [15] R. H. Ritchie, “Plasma losses by fast electrons in thin films,” *Phys. Rev.*, vol. 106, no. 5, pp. 874–881, 1956.
- [16] I. Freestone, N. Meeks, M. Sax, and C. Higgitt, “The Lycurgus Cup — A Roman nanotechnology,” *Gold Bull.*, vol. 40, no. 4, pp. 270–277, Dec. 2007.
- [17] E. Petryayeva and U. J. Krull, “Localized surface plasmon resonance: nanostructures, bioassays and biosensing--a review.,” *Anal. Chim. Acta*, vol. 706, no. 1, pp. 8–24, Nov. 2011.

- [18] E. Hutter and J. H. Fendler, "Exploitation of localized surface plasmon resonance," *Adv. Mater.*, vol. 16, no. 19, pp. 1685–1706, Oct. 2004.
- [19] K. L. Kelly, E. Coronado, L. Zhao, and G. C. Schatz, "The optical properties of metal nanoparticles: The influence of size, shape, and dielectric environment," *J. Phys. Chem. B*, no. 107, pp. 668–677, 2003.
- [20] P. Drude, "Zur Elektronentheorie der Metalle," *Ann. Phys.*, vol. 306, no. 3, pp. 566–613, 1900.
- [21] T. Wriedt, *The Mie Theory - (Chapter 2) Mie Theory: A Review*, vol. 169. Berlin, Heidelberg: Springer Berlin Heidelberg, 2012, pp. 53–71.
- [22] S. A. Maier, *Plasmonics : Fundamentals and Applications*. 2007.
- [23] A. Biswas, I. S. Bayer, A. S. Biris, T. Wang, E. Dervishi, and F. Faupel, "Advances in top-down and bottom-up surface nanofabrication: techniques, applications & future prospects," *Adv. Colloid Interface Sci.*, vol. 170, no. 1–2, pp. 2–27, Jan. 2012.
- [24] N. C. Lindquist, P. Nagpal, K. M. McPeak, D. J. Norris, and S.-H. Oh, "Engineering metallic nanostructures for plasmonics and nanophotonics.," *Reports Prog. Phys.*, vol. 75, no. 3, p. 036501, Mar. 2012.
- [25] C. A. Volkert and A. M. Minor, "Focused ion beam microscopy and micromachining," *MRS Bull.*, vol. 32, no. 05, pp. 389–399, Jan. 2007.
- [26] G. Dolling, M. Wegener, C. M. Soukoulis, and S. Linden, "Negative-index metamaterial at 780 nm wavelength.," *Opt. Lett.*, vol. 32, no. 1, pp. 53–5, Jan. 2007.
- [27] S. Xiao, U. K. Chettiar, A. V. Kildishev, V. P. Drachev, and V. M. Shalaev, "Yellow-light negative-index metamaterials.," *Opt. Lett.*, vol. 34, no. 22, pp. 3478–80, Nov. 2009.
- [28] J. Valentine, S. Zhang, T. Zentgraf, E. Ulin-Avila, D. a. Genov, G. Bartal, and X. Zhang, "Three-dimensional optical metamaterial with a negative refractive index.," *Nature*, vol. 455, no. 7211, pp. 376–9, Sep. 2008.
- [29] H. Cong, B. Yu, J. Tang, Z. Li, and X. Liu, "Current status and future developments in preparation and application of colloidal crystals.," *Chem. Soc. Rev.*, vol. 42, no. 19, pp. 7774–800, Oct. 2013.
- [30] J. V. Sanders, "Colour of precious opal," *Nature*, vol. 204, no. 4964, p. 1151, 1964.
- [31] D. A. Walker, B. Kowalczyk, M. O. de la Cruz, and B. A. Grzybowski, "Electrostatics at the nanoscale.," *Nanoscale*, vol. 3, no. 4, pp. 1316–44, Apr. 2011.
- [32] K. J. M. Bishop, C. E. Wilmer, S. Soh, and B. A. Grzybowski, "Nanoscale forces and their uses in self-assembly.," *Small*, vol. 5, no. 14, pp. 1600–30, Jul. 2009.
- [33] F. Li, D. P. Josephson, and A. Stein, "Colloidal assembly: the road from particles to colloidal molecules and crystals.," *Angew. Chem. Int. Ed. Engl.*, vol. 50, no. 2, pp. 360–88, Jan. 2011.
- [34] O. D. Velev and S. Gupta, "Materials fabricated by micro- and nanoparticle assembly - The challenging path from science to engineering," *Adv. Mater.*, vol. 21, pp. 1897–1905, May 2009.

- [35] K. E. Davis, W. B. Russel, and W. J. Glantschnig, "Disorder-to-order transition in settling suspensions of colloidal silica: X-ray measurements.," *Science*, vol. 245, no. 4917, pp. 507–510, Aug. 1989.
- [36] P. N. Pusey and W. van Meegen, "Phase behaviour of concentrated suspensions of nearly hard colloidal spheres," *Nature*, vol. 320, pp. 340–342, 1986.
- [37] Z. Zhou and X. S. Zhao, "Flow-controlled vertical deposition method for the fabrication of photonic crystals.," *Langmuir*, vol. 20, no. 4, pp. 1524–6, Feb. 2004.
- [38] L. M. Fortes, M. C. Gonçalves, and R. M. Almeida, "Processing optimization and optical properties of 3-D photonic crystals," *J. Non. Cryst. Solids*, vol. 355, no. 18–21, pp. 1189–1192, Jul. 2009.
- [39] L. M. Fortes, M. C. Gonçalves, and R. M. Almeida, "Flexible photonic crystals for strain sensing," *Opt. Mater. (Amst.)*, vol. 33, no. 3, pp. 408–412, Jan. 2011.
- [40] Y. Jiang, X. Yang, C. Wang, H. Li, F. Dong, B. Yang, K. Yu, and Q. Lin, "Centrifugation-induced water-tunable photonic colloidal crystals with narrow diffraction bandwidth and highly sensitive detection of SCN," *Appl. Mater. Interfaces*, vol. 5, pp. 1990–1996, 2013.
- [41] Y. G. Ko, D. H. Shin, G. S. Lee, and U. S. Choi, "Fabrication of colloidal crystals on hydrophilic/hydrophobic surface by spin-coating," *Colloids Surfaces A Physicochem. Eng. Asp.*, vol. 385, no. 1–3, pp. 188–194, Jul. 2011.
- [42] G. Arutinov, S. B. Brichtkin, and V. F. Razumov, "Self-Assembling of polystyrene microsphere monolayers by spin-coating," *Nanotechnologies Russ.*, vol. 5, no. 1, pp. 67–72, Mar. 2010.
- [43] A. B. D. Nandiyanto, T. Ogi, F. Iskandar, and K. Okuyama, "Highly ordered porous monolayer generation by dual-speed spin-coating with colloidal templates," *Chem. Eng. J.*, vol. 167, no. 1, pp. 409–415, Feb. 2011.
- [44] E. Armstrong, W. Khunsin, M. Osiak, M. Blömker, C. M. S. Torres, and C. O'Dwyer, "Ordered 2D colloidal photonic crystals on gold substrates by surfactant-assisted fast-rate dip coating.," *Small*, Mar. 2014.
- [45] Y.-H. Ye, T. S. Mayer, I.-C. Khoo, I. B. Divliansky, N. Abrams, and T. E. Mallouk, "Self-assembly of three-dimensional photonic-crystals with air-core line defects," *J. Mater. Chem.*, vol. 12, no. 12, pp. 3637–3639, Nov. 2002.
- [46] C. Deleuze, B. Sarrat, F. Ehrenfeld, S. Perquis, C. Derail, and L. Billon, "Photonic properties of hybrid colloidal crystals fabricated by a rapid dip-coating process.," *Phys. Chem. Chem. Phys.*, vol. 13, no. 22, pp. 10681–9, Jul. 2011.
- [47] R. Amos, J. Rarity, P. Tapster, T. Shepherd, and S. Kitson, "Fabrication of large-area face-centered-cubic hard-sphere colloidal crystals by shear alignment," *Phys. Rev. E*, vol. 61, no. 3, pp. 2929–2935, Mar. 2000.
- [48] J. Hur and Y.-Y. Won, "Fabrication of high-quality non-close-packed 2D colloid crystals by template-guided Langmuir–Blodgett particle deposition," *Soft Matter*, vol. 4, no. 6, p. 1261, 2008.

- [49] S. Reculosa and S. Ravaine, "Synthesis of colloidal crystals of controllable thickness through the Langmuir-Blodgett technique," *Chem. Mater.*, no. 15, pp. 598–605, 2003.
- [50] M. Heim, S. Reculosa, S. Ravaine, and A. Kuhn, "Engineering of Complex Macroporous Materials Through Controlled Electrodeposition in Colloidal Superstructures," *Adv. Funct. Mater.*, vol. 22, no. 3, pp. 538–545, Feb. 2012.
- [51] R. Szamocki, S. Reculosa, S. Ravaine, P. N. Bartlett, A. Kuhn, and R. Hempelmann, "Tailored mesostructuring and biofunctionalization of gold for increased electroactivity.," *Angew. Chem. Int. Ed. Engl.*, vol. 45, no. 8, pp. 1317–21, Feb. 2006.
- [52] N. Vogel, S. Goerres, K. Landfester, and C. K. Weiss, "A convenient method to produce close- and non-close-packed monolayers using direct assembly at the air-water interface and subsequent plasma-induced size reduction," *Macromol. Chem. Phys.*, vol. 212, no. 16, pp. 1719–1734, Aug. 2011.
- [53] Z. Lu and M. Zhou, "Fabrication of large scale two-dimensional colloidal crystal of polystyrene particles by an interfacial self-ordering process.," *J. Colloid Interface Sci.*, vol. 361, no. 2, pp. 429–35, Sep. 2011.
- [54] J. R. Oh, J. H. Moon, S. Yoon, C. R. Park, and Y. R. Do, "Fabrication of wafer-scale polystyrene photonic crystal multilayers via the layer-by-layer scooping transfer technique," *J. Mater. Chem.*, vol. 21, no. 37, p. 14167, 2011.
- [55] A. L. Rogach, N. A. Kotov, D. S. Koktysh, J. W. Ostrander, and G. A. Ragoisha, "Electrophoretic deposition of latex-based 3D colloidal photonic crystals: A technique for rapid production of high-quality opals," no. 16, pp. 2721–2726, 2000.
- [56] Y. Yu and G. Zhang, "Colloidal Lithography," in *Updates in Advanced Lithography*, S. Hosaka, Ed. InTech, 2013, pp. 3–34.
- [57] A. Kosiorek, W. Kandulski, H. Glaczynska, and M. Giersig, "Fabrication of nanoscale rings, dots, and rods by combining shadow nanosphere lithography and annealed polystyrene nanosphere masks.," *Small*, vol. 1, no. 4, pp. 439–44, Apr. 2005.
- [58] H. W. Deckman and J. H. Dunsmuir, "Applications of surface textures produced with natural lithography," *J. Vac. Sci. Technol. B*, vol. 1, no. 4, p. 1109, 1983.
- [59] W. Y. Ji, I. S. Jae, M. A. Ho, and G. K. Tae, "Fabrication of Nanometer-scale Pillar Structures by Using Nanosphere Lithography," *J. Korean Phys. Soc.*, vol. 58, no. 42, p. 994, Apr. 2011.
- [60] D.-G. Choi, H. K. Yu, S. G. Jang, and S.-M. Yang, "Colloidal lithographic nanopatterning via reactive ion etching.," *J. Am. Chem. Soc.*, vol. 126, no. 22, pp. 7019–25, Jun. 2004.
- [61] P. Hanarp, M. Ka, and D. S. Sutherland, "Optical properties of short range ordered arrays of nanometer gold disks prepared by colloidal lithography," no. ii, pp. 5768–5772, 2003.

**CHAPTER 2: EFFICIENCY ENHANCEMENT OF SOLID STATE
DYE SENSITIZED SOLAR CELLS (DSSC) BY THE
INCORPORATION OF LIGHT TRAPPING PHOTONIC
CRYSTAL STRUCTURES**



1. INTRODUCTION

Photovoltaics, the conversion of sunlight to electricity, is one of the most promising alternative clean energy technology for the future. Currently, in the commercial markets, crystalline Si solar cells dominate with a hefty 80% share, while the remaining 20% consists mostly of thin- film solar technology, such as CdTe and $\text{CuIn}_{1-x}\text{Ga}_x\text{Se}_2$ [1]. CdTe is an expensive indirect bandgap semiconductor material with high processing costs, and typically requires a 300 μm thick absorption layer. $\text{CuIn}_{1-x}\text{Ga}_x\text{Se}_2$ on the other hand, contains toxic elements which are not abundant on Earth. Even though $\text{CuIn}_{1-x}\text{Ga}_x\text{Se}_2$ is the best performing thin-film solar device, with an optimal efficiency of 20%, it is still more than 1.4 times as expensive as CdTe and amorphous Si devices. A promising alternative to these solid state devices is the dye sensitized solar cell (DSSC).

DSSCs are low cost and environmentally friendly alternatives to current existing photovoltaic technologies. The DSSC was first demonstrated by O'Regan and Grätzel in 1991 to be able to achieve a moderate efficiency [2]. Unlike classical semiconductor devices, where light is absorbed in the semiconductor layer, in a DSSC, the function of light absorption and charge carrier transport are separated. Figure 21 shows a simplified sketch of the electron flow in a DSSC.

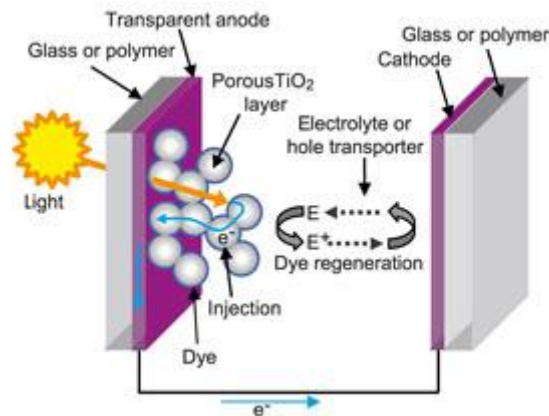


Figure 21. Schematic representation showing the various components and operating principle of the DSSC

In a DSSC, light is first absorbed by the dye molecules adsorbed onto a highly porous structure of TiO_2 nanoparticles. Following the dye excitation, electrons are injected into the conduction band of the semiconductor TiO_2 . The electrons injected into the TiO_2 nanoparticles are then transported to the front contact, which is usually a transparent

conductive oxide (TCO) layer. The dye is regenerated via a redox electrolyte, such as I^-/I_3^- which is in contact with a conductive back contact, which can also be a transparent TCO if backside illumination is desired.

The main issue with DSSC is the conversion efficiency and lifetime, which have to be extensively optimized. The conversion efficiency refers to the fraction of incident light that is converted to electrical energy, and the lifetime refers to how long the device can operate without significantly losing cell performance. In order to improve the efficiency and lifetime of the DSSCs, various aspects of the DSSCs have been studied. The use of different semiconductors [3], [4], dyes [5], ionic/hole conductors [1], [6], optical design [7] and the incorporation of nanostructures [8] and plasmonics [9] have demonstrated the complexity in optimizing of such a device. Recently, a DSSC that incorporated a porphyrin dye, SM315, was reported to achieved a power conversion efficiency of up to 13% by Mathew et al. [5].

Another promising method to improve the efficiency of a DSSC is by engineering optical nanostructures that can increase the pathlength of light within the cell, thereby increasing the probability of a photon being absorbed by the dye, resulting in an enhancement of the overall efficiency of the device. One possible structure that has the ability to “manipulate light” is a photonic crystal.

Previously mentioned in Chapter 1, photonic crystals (PCs) are materials that exhibit periodicities in their refractive index on the order of the wavelength of light. PCs, due to their structural arrangements, contain a photonic bandgap which can be described as forbidden frequencies where no electromagnetic modes may propagate. As such, they can be used to make materials with (i) only one allowed frequency mode, (ii) reflections in some directions, transmission in others, and (iii) trap light inside a material. Hence, the incorporation of a PC into a solar cell can provide many interesting possibilities for “photon management”, which include light bending, inhibition of spontaneous emission, and amplified photon absorption or emission [10].

In 2005, Mihi et al. theoretically investigated the effect of the presence of a photonic crystal on the optical absorption of dye-sensitized titanium oxide solar cells, and concluded that significant light absorption amplification over a wide spectral range occurred only in structures that combine the presence of a photonic crystal and a layer of nanocrystalline absorbing material. They also reported that the absorption enhancement occurs in resonant modes localized within the absorbing nanocrystalline coating rather than in the colloidal

crystal [11]. In 2006, Mihi et al. reported a theoretical analysis of the performance of a dye sensitized solar cell in which inverse titania opal multilayers and introduced in different configurations. They report that piling up different lattice constant crystals can lead to light harvesting enhancement in the whole dye absorption range [12].

In 2008, Lee et al. reported a quantitative comparison of the photo-activation spectra, short circuit current densities, and power conversion efficiencies of dye-sensitized solar cells (DSSCs) that contain bilayers of nanocrystalline (nc) TiO₂ and titania inverse opals [7]. They discovered that intimate physical contact between nc-TiO₂ and TiO₂ inverse opal layers is needed to achieve strong red enhancement in the action spectrum of bilayer DSSCs, and their findings are consistent with the model reported by Mihi-Miguez in 2005 [11].

In 2010, Guldin et al. demonstrated a material assembly route for the manufacture of DSSCs which incorporated a high-surface mesoporous layer to a three-dimensional photonic crystal fabricated by self-assembly [13]. An alternative way to incorporate photonic crystals into DSSCs was demonstrated by Mihi et al. in 2011 [10]. They described a general concept of transferring preformed 3D photonic crystals onto various substrates, by first fabricating three-dimensional inverse opal photonic crystals, and then embedding them in a polycarbonate matrix, before transferring them onto several different types of porous electrodes used in DSSCs. Figure 22 illustrates their process and resulting structures.

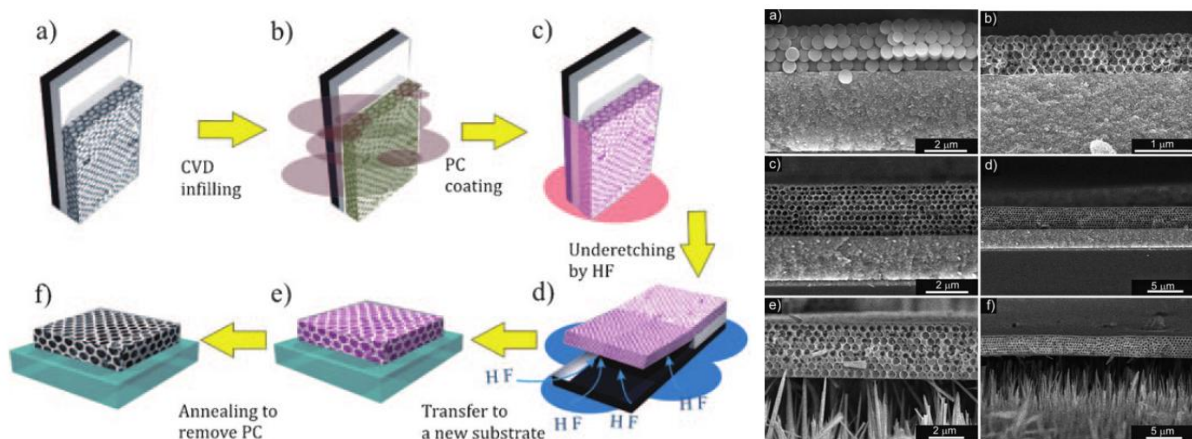


Figure 22. (left) Schematic of the process of fabrication and transfer of preformed photonic films. (Right) Cross sectional SEM images of (a) silica colloidal crystal, (b-f) various TiO₂ inverse opals fabricated [10].

While it has been theoretically and experimentally shown that the incorporation of photonic crystals into DSSCs are able to improve the efficiency of the device, there is still an inherent problem in DSSCs. Typical DSSCs suffer from durability problems (short lifetime) that result from the use of organic liquid electrolytes containing the iodide/tri-iodide redox couple. These iodine based liquid electrolytes can cause serious problems such as electrode corrosion and are susceptible to electrolyte leakage. One possible solution to treat this problem is to make use of solution processable p-type direct bandgap semiconductor for hole conduction instead of a liquid electrolyte [1]. Kim et al. reported an iodine free solid state DSSC with a 6.8% energy conversion efficiency made by carefully controlling the electrode/hole transport material (HTM) and nanocrystalline TiO₂/conductive glass interfaces while using the dye N719 [14].

The incorporation of inverse opals (IO) in a solid state DSSC (ssDSSC) was first reported in 2005 by Somani et al. [15]. They made use of evaporation induced self-assembly technique to fabricate the opal templates, and reported that direct comparison between the nanocrystalline TiO₂ and IO cells indicates that light conversion efficiency increased by at least one order of magnitude by using the IO TiO₂ films (Figure 23). In 2013, Hwang et al. presented a design in which a nanocrystal TiO₂ underlayer is integrated with an optically active porous three dimensional photonic crystals overlayer, and a sequential infiltration process is adopted to introduce additives to the solid electrolyte. They report an enhanced absorption in a specific spectral region, as well as improved efficiencies of the devices by as much as 32% when compared with a conventional DSSC. The opal template was made using vertical deposition and it was infiltrated by ALD [16].

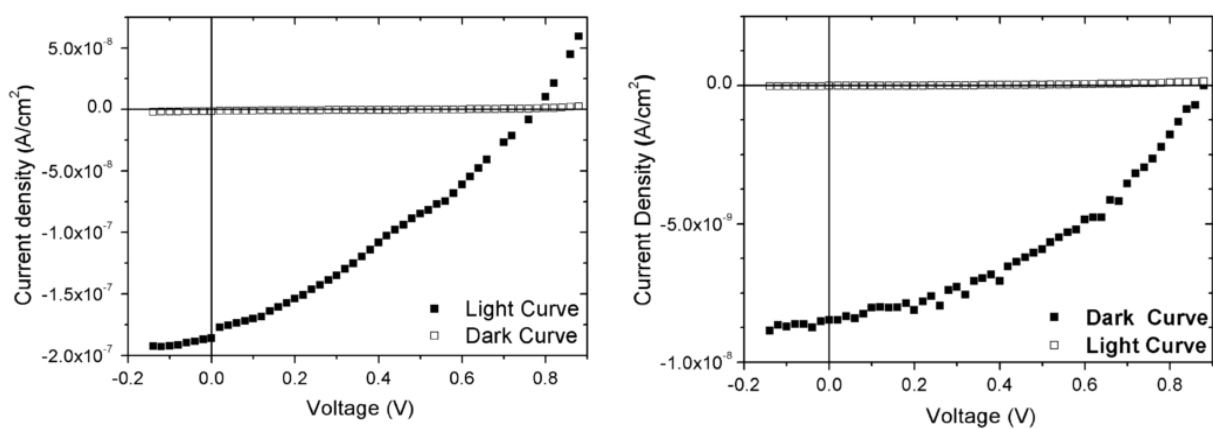


Figure 23. Current-Voltage (I-V) characteristics of a solid state DSSC (left) with an IO TiO₂ layer and (right) without an IO layer performed in the dark and under white light (simulated AM 1.5 illumination) [15].

The purpose of the current work described in this chapter is to fabricate a solid state DSSC with a controlled structure of the IO TiO_2 layer embedded within and investigate the corresponding efficiency enhancement (if any). To the best of our knowledge, there have been no reports on solid state DSSCs incorporated with photonic crystals that investigated the effects of varying the thickness of the photonic crystals on an individual layer level. All of the reported works have mainly made use of evaporation induced self-assembly methods (e.g. vertical deposition), which provides no real control on the thickness of the photonic crystals made. In addition, there is a gradient of the colloidal crystal thickness across the deposited surface due to changes in the suspension concentration as water evaporates. Furthermore, it is very difficult, if not impossible, to reproduce exactly a template of a consistent thickness each and every time by evaporation induced methods.

Hence, the aims of the experiments conducted were fourfold. First, we needed to investigate the most appropriate route to fabricate the inverse opal of titanium dioxide, TiO_2 , that can be easily incorporated into a solid state DSSC. Second, we wanted to determine if there was any effect on photo-conversion efficiency (PCE) due to the addition of an inverse opal TiO_2 of just a few layers (two, four, six and eight layers) thick into the solid state DSSC. Third, we wanted to investigate the effect on PCE due to the size of the inverse opal incorporated. Fourth, we wanted to determine if there was a relationship between the PCE and thickness of the inverse opal layers to identify an optimal thickness for the best PCE.

2. DEPOSITION OF THE COLLOIDAL CRYSTAL (OPAL) TEMPLATES

In order to deposit a colloidal crystal template by bottom up self-assembly, we had to first decide on the building blocks we wanted to use, which was mainly a choice between silica and polystyrene beads. In this respect, the choice was easy to make because of the foreseeable ease of removal of polystyrene beads as compared to silica after infiltration of the colloidal crystals.

For polystyrene beads, we investigated two methods of preparing the colloidal crystals. The first method was by vertical deposition, which is a method that has been well established to fabricate colloidal crystal structures. The second method was by packing monolayers of closed packed polystyrene beads on a water surface and then repeatedly stacking them up. The purpose of this investigation was to compare between the two methods, the ease of fabrication, the quality of the resultant colloidal crystals, as well as the tunability and reproducibility of the structures.

2.1 VERTICAL DEPOSITION OF COLLOIDAL CRYSTALS

The vertical deposition method is an evaporation induced technique to pack particles on the surface of the substrate as the meniscus of water recedes due to evaporation. It basically involved placing a substrate vertically, partially submerged in a suspension of monodisperse polystyrene (PS) beads of a fixed concentration for several days (usually more than 4 days) in an oven set at a fixed temperature and humidity. Both 250 nm and 595 nm PS beads were used in this test. The beads were synthesized by emulsion polymerization, and the details of the synthesis can be found in Annex 1. Experimental details on the vertical deposition method is detailed in Annex 2. Figure 24 shows a graphical illustration of the vertical deposition process.

Five different concentrations (0.01, 0.02, 0.05, 0.08 and 0.10 wt%) of PS (595 nm) suspensions (in water) were used to investigate the effects of PS suspension concentration on the quality of the colloidal crystal formed.

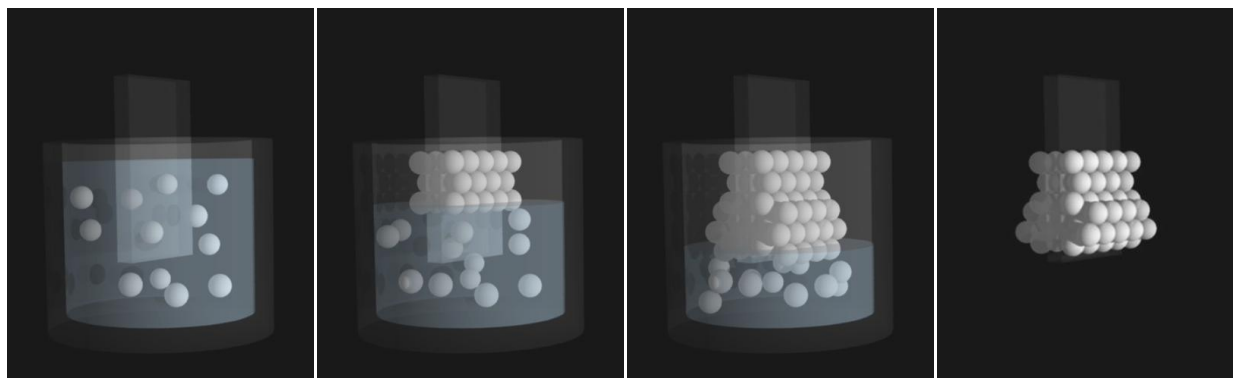


Figure 24. (from left to right) Schematic illustration of the vertical deposition process.

For the colloidal crystals that were made using 0.01 and 0.02 weight% (wt%) of PS (595 nm) suspension, the resulting quality of the self-assembled 3D colloidal crystal was not of a good quality as the assembled colloidal crystal on the substrate was patchy and streaky in appearance and only had localized regions where strips of good quality self-assembled colloidal crystal can be seen. However, for the colloidal crystal prepared with 0.05, 0.08 and 0.10 wt% of PS (595 nm) suspensions, very beautiful colloidal crystals that covered the entire immersed surface of the substrate were obtained. Figure 25 below shows an example of a self-assembled 3D photonic crystal made by vertical deposition from 0.08 wt% of PS (595 nm) suspension at 45°C and about 70% humidity.

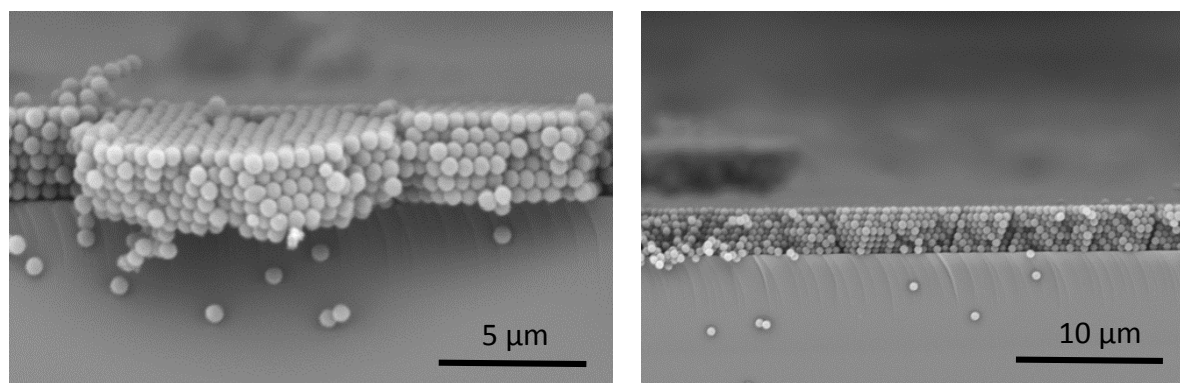


Figure 25. SEM side views of a 3D photonic crystal made from 595nm polystyrene beads.

The self-assembled colloidal crystals were shiny in appearance and generally uniform in color. There is also a noticeable gradient in the thickness of the colloidal crystal formed. The colloidal crystals appear thicker (more whitish) at the bottom than at the top where the colloidal crystals start depositing. Hence, we conclude that the low concentration of PS suspension (0.01 and 0.02 wt%) results in the poor quality of the colloidal crystal deposited

because of the following reason. When the concentration is low, only some particles (PS beads) will initially deposit at the interface of the meniscus and substrate surface. Thus, the colloidal crystals will grow regionally at the spots where the first particles are deposited. Due to the evaporation of water, these nucleated regions will grow vertically downwards, creating strips of colloidal crystals because there are insufficient particles in the solution to allow for a uniform deposition along the entire interface between the meniscus and the substrate. However, beyond a minimum ‘critical’ concentration (0.05 wt% in this case), there are sufficient particles to cover the entire interface, which allows for the uniform deposition of particles across the interface. In addition, because of the increase in PS suspension concentration as the meniscus recedes (due to the evaporation of water), the deposited colloidal crystal becomes thicker and appear whiter at the bottom of the vertically held substrate than at the start.

The reflectance and transmission data of the 3D colloidal crystals (opals) vertically deposited using 0.05, 0.08 and 0.10 wt% PS (595 nm) suspensions are shown in Figure 26. The measurements were taken in the middle of each sample at normal incidence to allow for a reasonable comparison of the data, and they were all made with respect to a blank reference substrate (i.e. no colloidal crystal deposited), which in this case, is glass.

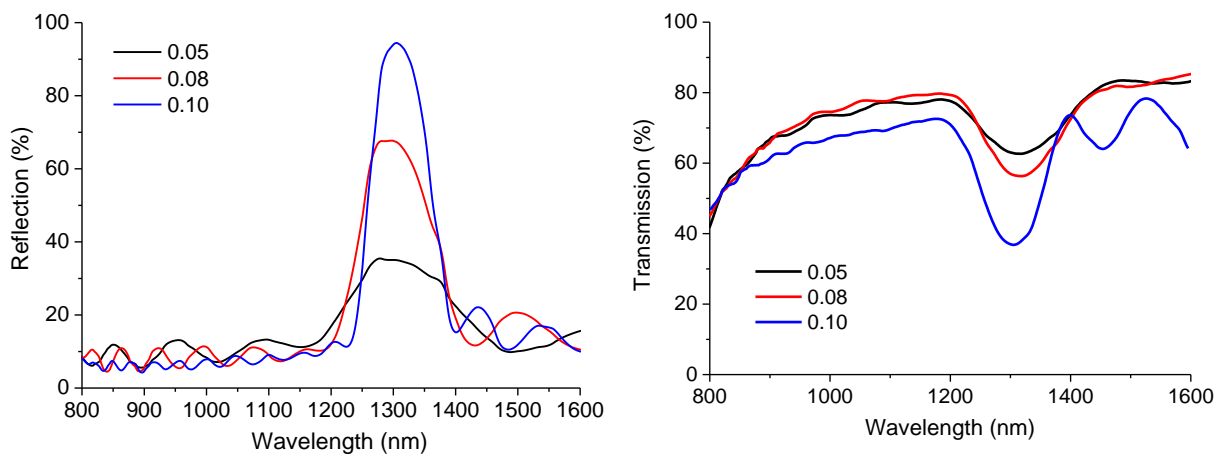


Figure 26. Reflection (left) and transmission (right) plots of direct opals made by vertical deposition with different concentrations of PS (595 nm) suspensions.

From the reflection and transmission plots in Figure 26, it can be seen that the intensity of the reflection and transmission spectra increases with increasing concentration of PS suspensions used for the vertical deposition process. This is due to the simple fact that the higher the concentration, the thicker the photonic crystal (opal) deposited and hence the stronger the

resulting Bragg's peak that corresponds to the size of the PS particles. The spectral positions of the stop bands for an opaline photonic crystal can be estimated by a modified version of Bragg's law, combined with Snell's law to account for the reduced angle with respect to the normal that light travels upon entering a medium of a higher refractive index as follows [17]:

$$\lambda = \frac{2d_{hkl}}{m} \sqrt{n_{avg}^2 - \sin^2\theta} \quad \text{Equation 32}$$

where λ is the wavelength of the stop band minimum (i.e. wavelength of the maximum reflected intensity), m is the order of Bragg diffraction, n_{avg} is the average refractive index of the photonic crystal, d is the distance between the planes (hkl) and θ is the angle measured from the normal to the planes. For measurements taken at normal incidence ($\theta = 0$), the equation can be further simplified as shown in Equation 2.

$$\lambda = \frac{2d_{hkl}}{m} n_{avg} \quad \text{Equation 33}$$

To calculate n_{avg} , a ratio of the refractive index of air and polystyrene and their corresponding refractive index is summed together as follows

$$n_{avg}^2 = \phi_{air} n_{air}^2 + (1 - \phi_{air}) n_{PS}^2 \quad \text{Equation 34}$$

ϕ_{air} represents the filling fraction of air and $(1 - \phi_{air})$ represents the filling fraction of polystyrene beads. In an ideal closed packed opaline structure of beads, ϕ_{air} has a value of 0.26. n_{air} and n_{PS} are the refractive indices of air ($n=1$) and polystyrene ($n=1.6$) respectively [18]. Thus we find that $n_{avg} = 1.46$.

Given that the beads are arranged in a cubic closed packed order, the relationship between the lattice constant, a , and the diameter of the beads, D is

$$a = \frac{2D}{\sqrt{2}} \quad \text{Equation 35}$$

For the colloidal crystals grown by assembly techniques, their (111) planes are oriented parallel to the substrate. Hence, for the plane (111), the relationship between d_{111} and lattice constant, a , is

$$\frac{1}{d_{111}^2} = \frac{3}{a^2} \quad \text{Equation 36}$$

Hence,

$$D = \sqrt{\frac{3}{2}} d \quad \text{Equation 37}$$

Vertical deposition was also done with a PS (250 nm) suspension to fabricate opaline photonic crystals made of 250 nm PS beads (experimental details in Annex 2). This was done to observe the effect of particle size on the position of the stop band. The resultant reflectance and transmission spectra obtained from an opaline photonic crystal made by vertical deposition of 250 nm and 595 nm PS particles (at 0.10 wt%) are shown in Figure 27. The theoretical Bragg's peak position was calculated to compare with the experimentally determined position of the Bragg's peak for the different samples prepared (Table 2).

Table 2. Comparison of the experimental and theoretical Bragg's peak position for the opals prepared.

Opal bead size (nm)	Experimental Bragg's peak position (nm)	Theoretical Bragg's peak position (nm)
595	1305	1418
250	526	596

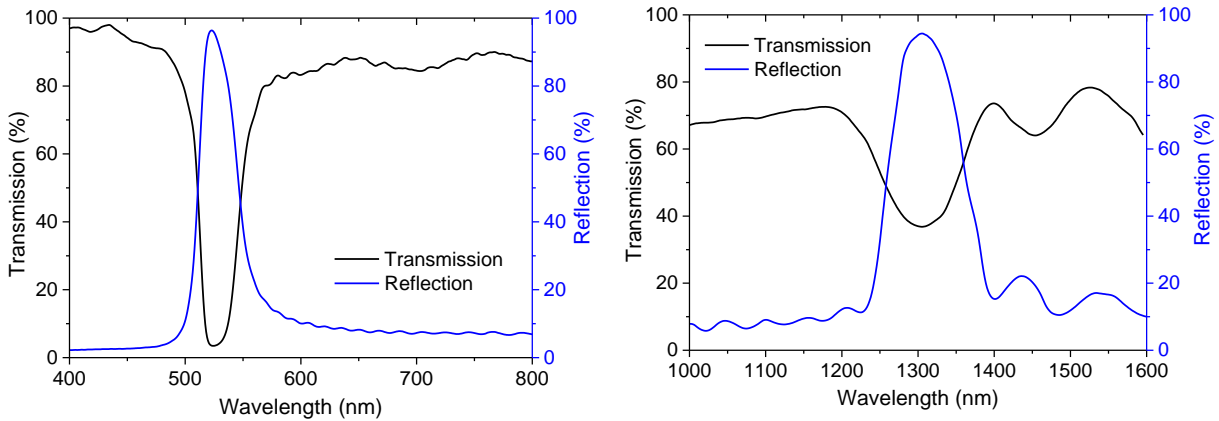


Figure 27. Reflection and transmission plots of direct opals made by vertical deposition with 250 nm (left) and 595 nm (right) PS particles.

It can be seen that the experimentally measured position of the stop bands are about 526 nm and 1305 nm for the opals made by PS (250 nm) and PS (595 nm) beads respectively. As expected according to Bragg's law, there is a shift towards shorter wavelengths (blue shift) as particle size decreases. Furthermore, it can be observed that the peaks are broader for the opals made from 595 nm PS particles when compared with the opals made from 250 nm particles. However, when compared with the calculated theoretical Bragg's peak position (using $n_{\text{avg}} = 1.46$), the experimental Bragg's peaks are all blue shifted compared with the theoretical Bragg's peaks. This could be due to the presence of defects in the opal due to the

presence of larger or smaller sized beads. This results in cracks or deformations leading to a decrease in the refractive index, n_{avg} , which blue shifts the Bragg's peak.

In addition, from the experimental data shown in Figure 26 and Figure 27, the occurrence of interference fringes in the reflectance spectrum can also be clearly observed, which indicates the quality of thin film photonic crystals [19]. These oscillations can be understood as Fabry-Pérot (FP) oscillations occurring due to the interference of the light reflected by opposite surfaces of the opal domains. Fabry-Pérot oscillations are a good indicator of the homogeneity of thickness and average refractive index of photonic crystals since they will vanish rapidly if the quality of the crystal is bad. The Fabry-Pérot oscillations appear different on both sides of the Bragg resonance showing a rapid decrease of the oscillation magnitude on the high-energy (i.e. shorter wavelength) side. The evolution of the amplitude of Fabry-Pérot oscillations can be explained by a rapid variation of the dielectric properties of the material in the vicinity of the photonic band gap [19].

Due to the presence of multiple reflecting surfaces, the interference that results from these different reflected light waves cause constructive or destructive interference (depending on their wavelength). Using these experimental FP fringes, it is possible to back-calculate and estimate the thickness of the respective colloidal crystals.

The FP fringes that we observe in the experimental spectra correspond to the local absorption maxima. This occurs when:

$$\frac{4n_{avg}\theta}{\lambda} = 2p + 1 \quad \text{Equation 38}$$

where p is an integer.

If we consider the two wavelengths where absorption is maximal, λ_p and λ_{p+m} , the following equations can be written

$$\frac{4n_{avg}\theta}{\lambda_p} = 2p + 1 \quad \text{Equation 39}$$

$$\frac{4n_{avg}\theta}{\lambda_{p+m}} = 2(p + m) + 1 = \frac{4n_{avg}\theta}{\lambda_p} + 2m \quad \text{Equation 40}$$

From here, we can establish the following relationship

$$m\lambda_p\lambda_{p+m} = 2n_{avg}(\lambda_p - \lambda_{p+m})\theta \quad \text{Equation 41}$$

In order to calculate the thickness of a colloidal crystal, we now have to plot $m\lambda_p\lambda_{p+m}$ against $(\lambda_p - \lambda_{p+m})$, and calculate the slope of the resulting line. From the gradient of the line, we can estimate the thickness of the colloidal crystal and hence, the corresponding number of layers of the colloidal crystal. The number of layers, N , can be calculated by the following equation

$$\theta = \left[1 + \left((N - 1) \times \sqrt{\frac{2}{3}} \right) \right] \times D \quad \text{Equation 42}$$

For the samples shown in Figure 26 and Figure 27, we have attempted to estimate the thickness of the samples (in terms of the number of layers) by making use of the Fabry-Pérot fringes. Table 3 shows the calculated thickness of the colloidal crystals from the experimental FP fringes.

Table 3. Estimated thickness of the colloidal crystals made by vertical deposition calculated from the FP fringes

Sample	PS 595 (0.05)	PS 595 (0.08)	PS 595(0.10)	PS 250 (0.10)
Number of layers	5	8	15	47

2.2 STACKING OF CLOSED PACKED PS MONOLAYERS PACKED ON A WATER SURFACE

The other approach that was used to assemble close packed layers of beads was done by spreading the PS beads and packing them on a water surface according to a procedure described by Vogel et al. [20] with some modifications. The experimental details adopted for this work can be found in Annex 2. Figure 28 shows a schematic illustration of the entire process to transfer one monolayer of closed packed PS beads onto a substrate and two photographs of 260 nm and 595 nm PS beads packed on a water surface.

In order to verify that the beads on the water surface are closed packed and is a single monolayer, after transferring the monolayers onto a glass substrate, SEM pictures of the cross section and top down views of the samples were taken (Figure 29).

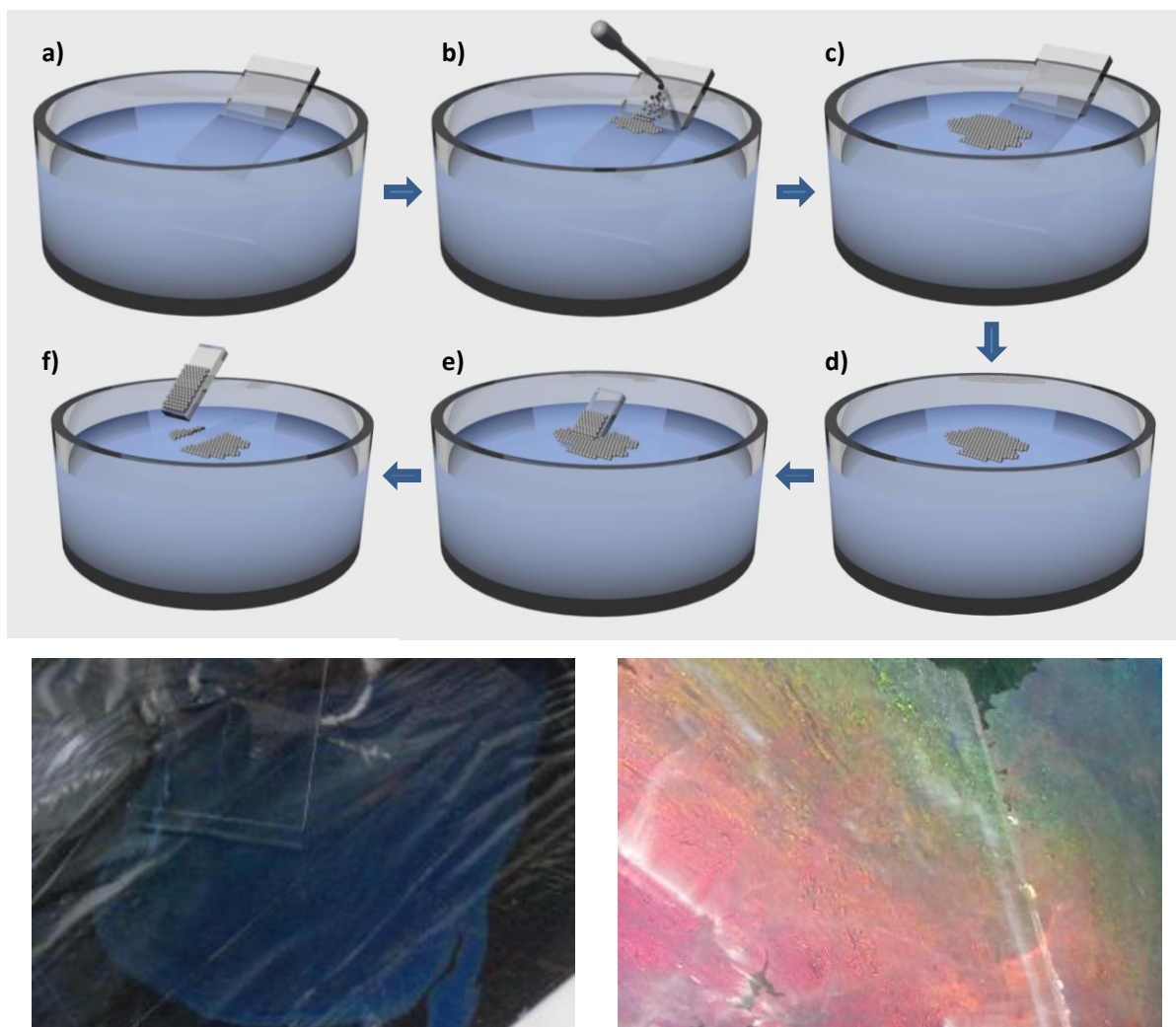


Figure 28. (top) Schematic illustration of the self-assembly and transfer of a monolayer of PS beads from the water surface onto a flat substrate. (a) Preparation of beaker with water and a glass slide is inserted at a 45° angle to the water surface. (b) Spreading of PS suspension. (c) PS beads self-assemble on water surface (d-f) transfer of self-assembled monolayers onto substrates. (Bottom) Self-assembled monolayers of (left) 260 nm and (right) 595 nm PS beads on a water surface.

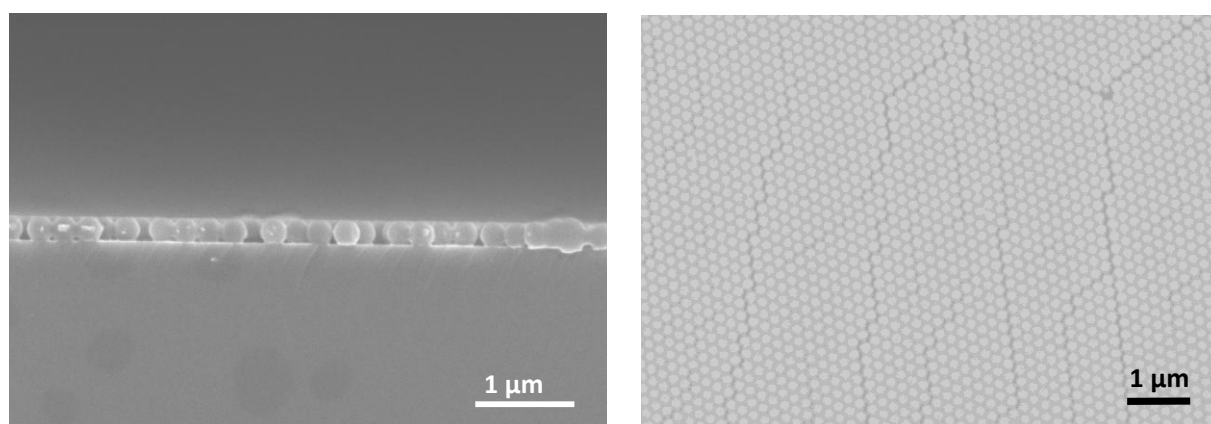


Figure 29. (left) Cross section and (right) top down SEM pictures of a monolayer of 260 nm polystyrene beads self-assembled on the water surface.

From Figure 29, it can be seen that only a single monolayer of closed packed polystyrene beads was transferred. The presence of slight cracks can be observed, and this can be attributed to the liftoff process where the monolayer is scooped onto a glass substrate that is manually held. Hence, slight shaking or jerks can cause little tiny cracks to appear. Overall, the quality of the deposited monolayer can still be considered to be well organized, as bright diffraction patterns can be observed very easily when the deposited substrates are tilted and viewed from an angle.

Having confirmed that it was possible to deposit only a single monolayer of closed packed particles onto a substrate with this technique, the next step was to experiment with the possibility of stacking individual close packed monolayers of polystyrene on each other. Hence, attempts were made to stack up to eight layers self-assembled monolayers on top of one another (exact experimental details can be found in Annex 2). A similar method had previously been reported by Oh et al. [21] that involved scooping layers of PS monolayers repeatedly from a water surface to get a 3D opaline structure. Figure 30 shows the SEM cross section pictures obtained after stacking two, four, six and eight layers of self-assembled PS 260 nm monolayers. The SEM pictures show that this method of stacking monolayers on top of each other provides control of the colloidal crystal deposited at the layer level. Furthermore, the deposition is uniform across the surface of the substrate. There is no gradient in the thickness of the deposited colloidal crystal across the surface. Similar samples were also made with 595 nm PS particles.

The optical reflectance and transmittance spectra of the stacked monolayers (measured at normal incidence with reference to a glass substrate) from one to eight layers were measured and the data obtained are presented in Figure 31.

From Figure 31, it can be clearly observed that there is a gradual increase in the intensity of the stop band as the thickness of the colloidal crystal increases with stacking of the monolayer. This is expected as the increase in layer thickness results in more interference to the incident light that strikes the photonic crystal. The transmission of light at the stop band (centered at 635 nm as expected according to Bragg's law) decreases and the corresponding reflection increases with increasing number of layers. From this result, it is demonstrated that it is possible to tune the intensity of the reflection and transmission of a 3D photonic crystal (made by bottom up self-assembly) by simply tailoring the exact number of layers desired.

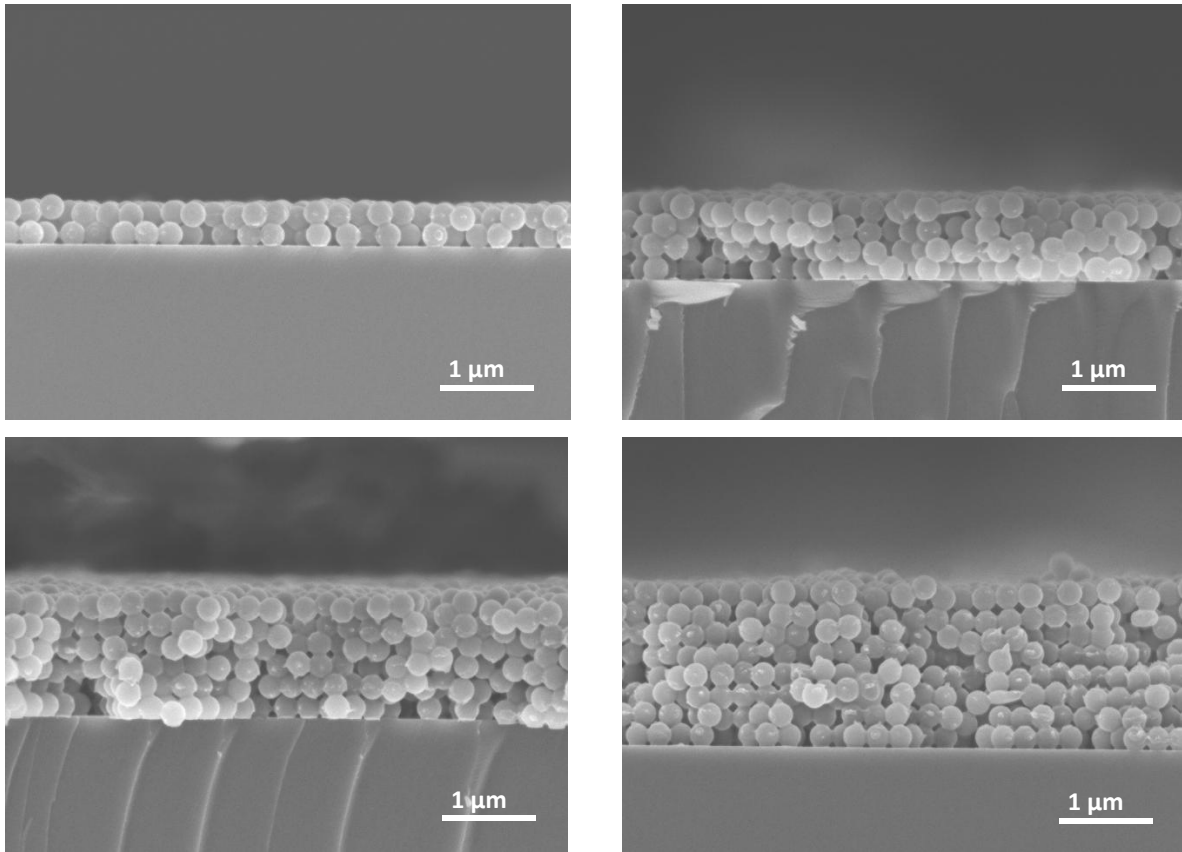


Figure 30. Cross section SEM pictures of two, four, six and eight layers of 260 nm PS beads made by repeatedly stacking individual monolayers on top of each other.

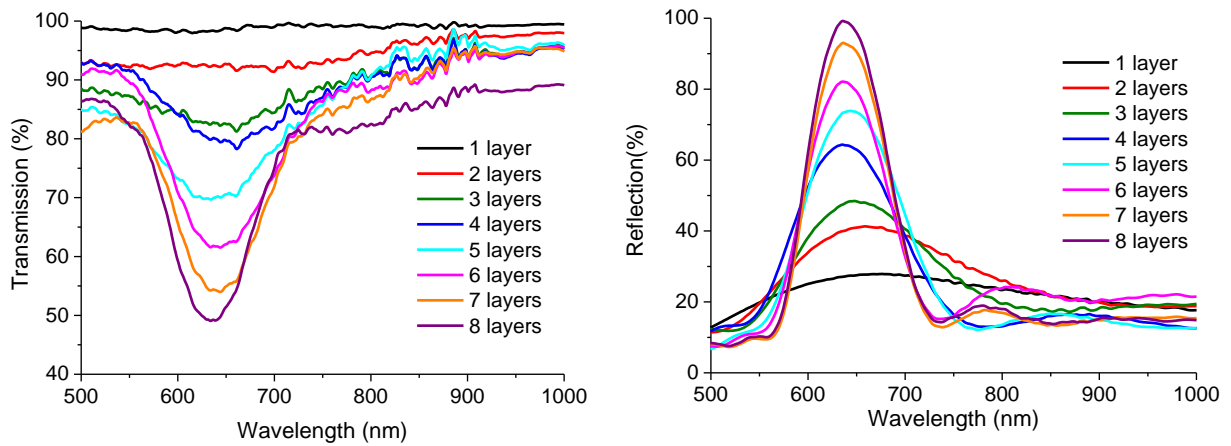


Figure 31. Transmission spectra (left) and reflection spectra (right) of photonic crystals made by the stacking of PS 260 nm monolayers via the water surface transfer technique.

2.3 COMPARISON BETWEEN THE TWO ASSEMBLY METHODS

Having tested out the two methods, vertical deposition and water surface self-assembly, it was determined that the water surface self-assembly method is better suited for the application that we desired due to the following reasons.

First and most importantly, by transferring individual monolayers and stacking them, this method provides a level of control in the thickness of the colloidal crystal – which exhibit a (2+1) structure and not a truly 3D one – that cannot be rivaled by the vertical deposition method. In addition, the deposited colloidal crystals do not exhibit a thickness gradient that is always present in vertically deposited colloidal crystals.

Furthermore, the time taken to transfer a single monolayer is only about a few hours (if all the substrate preparation steps are taken into account), while vertical deposition requires four days or more for a complete cycle. The amount of PS suspension used for each method is also significantly different. To vertically deposit a colloidal crystal requires a few milliliters (ml) of PS suspension, while to spread and stack a colloidal crystal of a similar thickness requires just a few hundreds of microliters (μl) of the same suspension.

3. INCORPORATION OF INVERSE OPALS (IO) OF TiO₂ INTO SOLID STATE DSSCs

In order to fabricate the solid state DSSCs incorporating the inverse opal structures, the first step was to coat the fluorine tin-doped oxide glass substrates with a thin compact and porous layer of TiO₂. This was done via a modified version of the protocol reported by Snaith et al. [22]. The exact procedure used to prepare the TiO₂ coated FTO substrates (used for the deposition of the three dimensional colloidal crystal templates) is described in Annex 3. Figure 32 shows a schematic illustration of the entire fabrication to make the solid state DSSC.

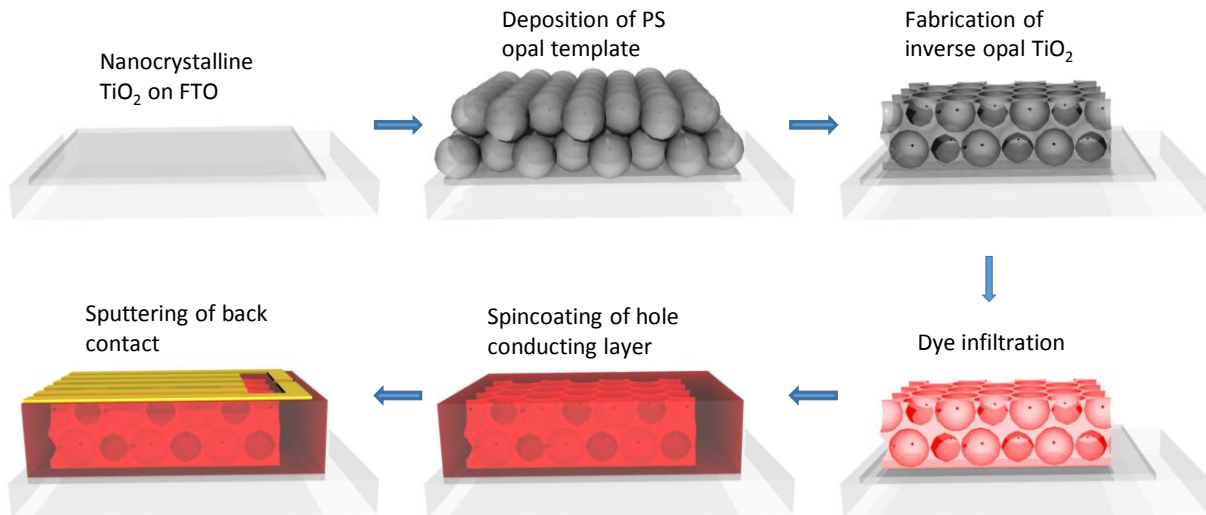


Figure 32. Schematic illustration of the solid state DSSC fabrication process

Once the FTO substrates were prepared with a thin layer of TiO₂, the opal templates were deposited onto these substrates by the water surface self-assembly method, and were stacked as desired. The next step was then to infiltrate the templates with TiO₂. For this step, we adopted a modified ‘sandwich vacuum infiltration’ procedure reported by Cai et al. [23]. The experimental details can be found in Annex 3. Briefly, a clean glass slide was placed on top of the 3D opal template and pressed together. Next, a part of it was immersed in a titania sol, which infiltrated the pores by capillary action. The substrates were then removed and left to dry. After drying, a simple calcination step (under air) was done to remove the PS particles and the inverse opal of TiO₂ is obtained. Figure 33 below shows the SEM pictures of the inverse opals fabricated from 3D opaline templates that consisted of 260 nm and 595 nm PS particles.

After calcination, it can be observed that the pores that are left after PS particles removal are now smaller than the original PS particles that served as the templates. This is due to the contraction of the TiO₂ during the calcination process. The average pore sizes of the inverse opal TiO₂ are 215 nm and 490 nm corresponding to the templates made using 260 nm and 595 nm PS particles respectively. The reduction of the inverse opal pore size from the original PS particle size is about 17% to 18%.

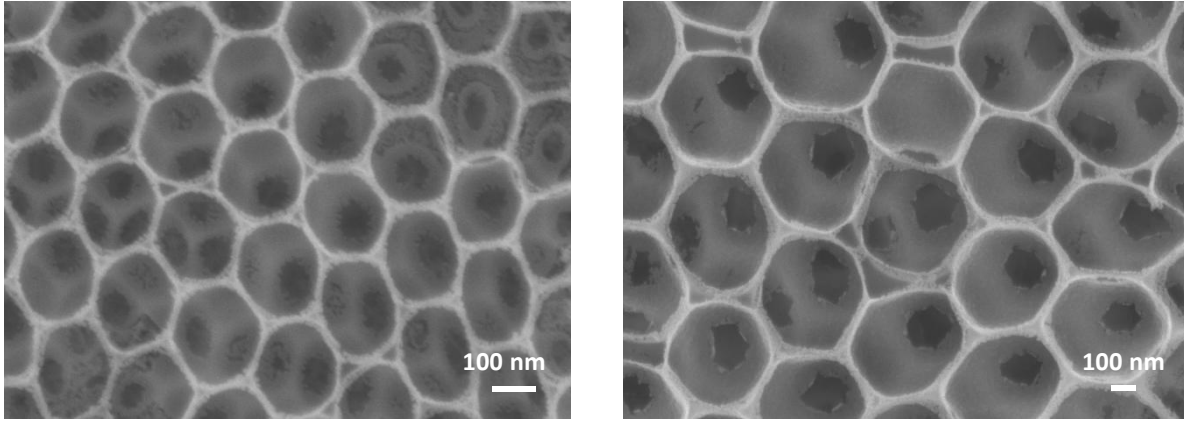


Figure 33. SEM images of the TiO₂ inverse opal formed from (left) 260 nm and (right) 595 nm PS opal templates

Due to this reduction in pore size and the change in the refractive index of the entire material, there is a significant change in the position of the stop band of the inverse opal when compared with the original opal template. Figure 34 shows the change in stop band position after fabricating the TiO₂ inverse opals.

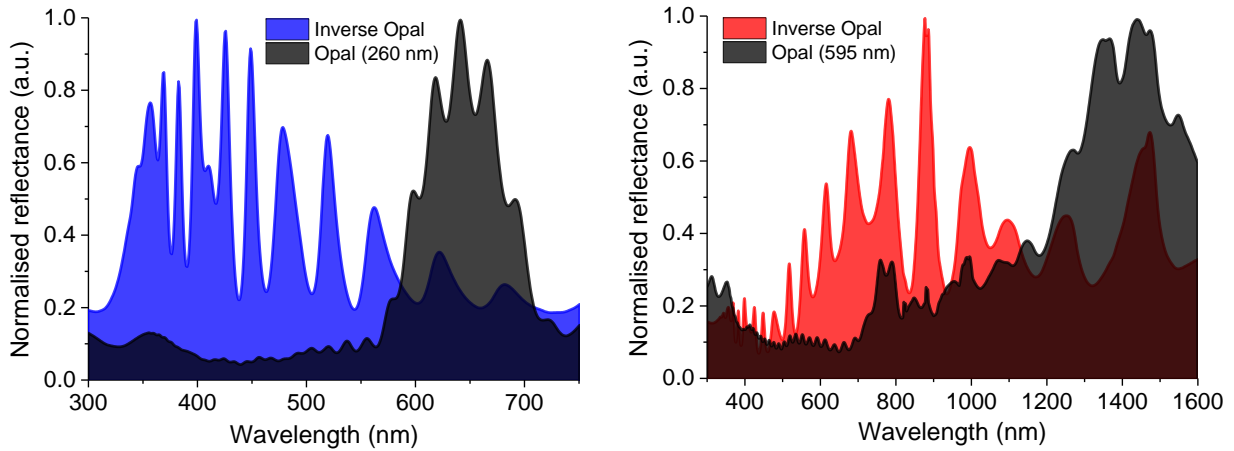


Figure 34. Normalized reflectance spectra of comparing the inverse opal fabricated and the original opal template for (left) 260 nm and (right) 595 nm PS particles

For the 3D opal templates made from 260 nm PS particles, the stop band position was at around 650 nm. After fabricating the TiO₂ inverse opal, the stop band shifted to around 410 nm. Similarly, for the 3D opal templates made from 595 nm particles, the stop band position was at around 1420 nm, but after fabricating the TiO₂ inverse opal, the stop band shifted to around 880 nm. This change in stop band position can be attributed to the change in average refractive index of the entire material, in which is now equal to:

$\sqrt{0.74 + 0.26n_{TiO_2}^2}$. Using

$n_{TiO_2} = 2.45$ [24], the calculated n_{avg} of the inverse opal structure is 1.52. Using Equation 2, we can theoretically calculate the new positions of the stop band of the titania inverse opals which correspond to 512 nm and 1168 nm for the inverse opals made with 260 nm and 595 nm PS particles respectively. The calculated values are red shifted compared with the experimental values (ca. 425 nm and 825 nm for the 260 nm and 595 nm PS particles respectively) obtained by measurements. The difference can be readily explained by the presences of cracks that appear during the sintering process of the titania inverse opals. These cracks occur due to the contraction of TiO_2 during the sintering process, and because of this, there are a lot of additional air pockets that are created in the IO structure. Figure 35 shows a large view of the TiO_2 inverse opal layer fabricated from both sizes of PS particles. The presence of all the cracks result in the lowering of the average refractive index of the entire structure due to the increased proportion of air contained within it.

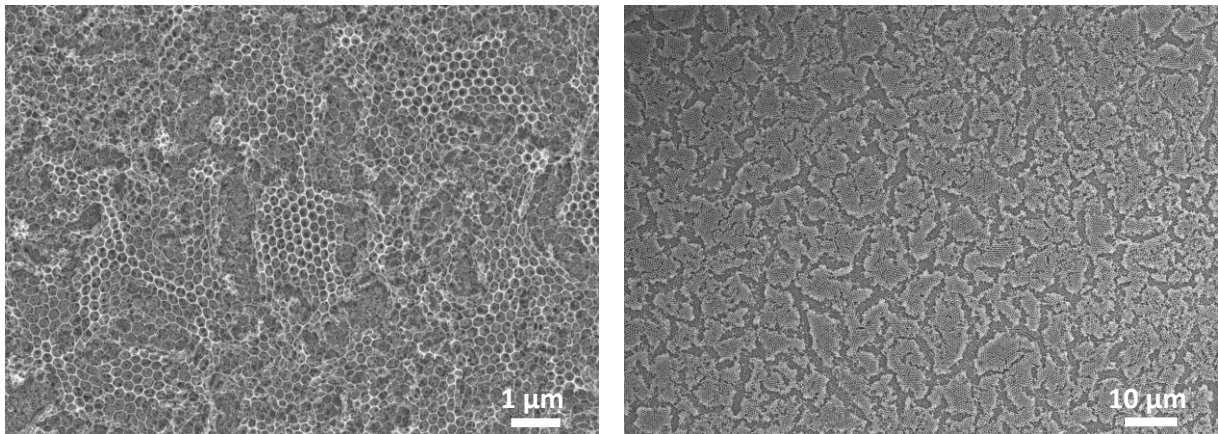


Figure 35. SEM images of the TiO_2 inverse opals made from PS particles of (left) 260 nm and (right) 595 nm.

We can also observe intense oscillations in the spectra measured for these samples prepared, and we attribute these observed oscillations to the complex collective interference of light waves resulting for the various reflecting surfaces available in the samples prepared. The interfaces that could contribute to the reflection of light are the glass/nanocrystalline (nc) TiO_2 , nc TiO_2 /IO, and the IO/air interfaces.

After preparing the TiO_2 inverse opals on the substrates, the substrates were soaked in the dye (D102) solution. The dye D102 (Figure 36) was used as it is a metal-free organic dye that has been reported to perform exceptionally as a sensitizer for solid state DSSCs [25]. Then, after a sufficient period time, the hole conducting material, spiro containing a lithium salt, is spin-

coated onto the dye soaked substrates. To complete the solid state DSSC; 50 nm of Ag and 50 nm of gold is sputtered onto the substrates to serve as back contacts. Figure 36 shows the structure of the dye and hole conductor used. Detailed experimental procedures for the whole process can be found in Annex 3.

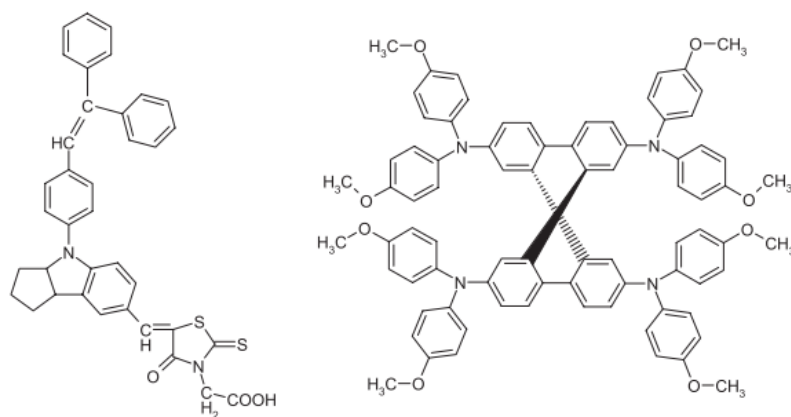


Figure 36. Structure of the (left) indoline dye molecule D102 and (right) spiro-OMeTAD {2,2',7,7'-tetrakis-(N,N-di-p-methoxyphenylamine)9,9'-spirobifluorene}

Two series of experiments were made to investigate the effect of having an inverse opal of TiO₂ layer. The first series involved making inverse opal of two and four layers thick of two different sizes (260 nm and 595 nm) to do a preliminary comparison on the effect of different pore sizes and layer thickness on the efficiency of the cell. Then, the pore size that resulted in better performance of the cell was put through a second series of experiments to determine the optimal thickness of the inverse opal layer.

3.1 EVALUATION OF CELL PERFORMANCE (THE FIRST SERIES)

The aims of the first series of solid state DSSCs made with the inverse opal structure was as follows:

1. To determine the best size of PS beads to use as starting materials for the 3D opal templates
2. To determine if there were any effect on cell efficiency due to the thickness of the inverse opal (IO) layer
3. To determine if the additional calcination step to fabricate the IO has any effect on the blank reference cells

Table 4 below lists the different specifications of each cell fabricated in the first series of experiments.

Table 4. List of experimental conditions for the different cells made in the first series.

Sample name	260/2	260/4	595/2	595/4	Blank ⁺	Blank (oven)
PS size (nm)	260	260	595	595	-	-
No. of layers	2	4	2	4	-	-
Oven	yes	yes	yes	yes	no	yes

⁺ Blank refers to fluorine tin-doped oxide glass substrate coated with a thin layer of ncTiO₂

The performance of the fabricated solid state DSSCs made in the above listed specifications were tested under a simulated set up in the Laboratoire de l'Intégration du Matériau au Système (IMS, Bordeaux), and the results are listed in Table 5. From the measured cell performance data of the fabricated solid state DSSCs, it can be seen that between the blank cells, the cells that were oven treated along with the inverse opal (IO) cells appear to have a slight increase in its efficiency, although the difference is not very significant.

Table 5. Measured cell performance data of the solid state DSSCs fabricated in the first series.

Sample	J _{sc} (mA/cm ²)	V _{oc} (V)	FF	PCE (%)
Blank	4.09	0.850	0.395	1.37
Blank (oven)	4.75	0.829	0.369	1.45
260/2	6.48	0.839	0.546	2.97
260/4	6.16	0.829	0.577	2.95
595/2	5.61	0.789	0.546	2.42
595/4	3.66	0.799	0.393	1.15

Comparing the blank cells, it appears that the PCE is very similar with only a slight increase of 0.08% observed after oven treatment. Between the inverse opal (IO) cells, it is evident that the IO cells prepared with the smaller PS 260 nm opal templates achieved a significant improvement in PCE when compared to both the blank cells and the IO cells prepared with

the PS 595 nm opal templates. Overall, with the exception of the 595/4 cell, the short circuit current (J_{sc}), fill factor (FF) and photo-conversion efficiency (PCE) increased for all the IO cells when compared with the blank cells. Figure 37 shows the comparison of the PCE between the different cell configurations.

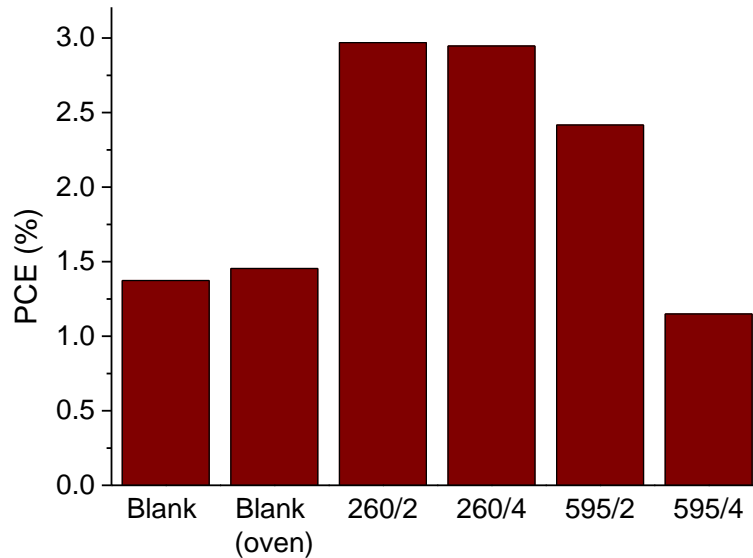


Figure 37. Comparison of the PCE between the different solid state DSSCs fabricated in the first series

From Figure 37, it is obvious that the IO TiO_2 structure incorporated in the solid state DSSCs does indeed have a significant effect on the performance of the cell. However, it is also observed that the IO made from PS 260 nm particles have a better effect on the efficiency of the cells as compared with the IO made from PS 595 nm particles. This difference can be attributed to the position of their respective stop bands and the absorption spectra of the dye D102. Figure 38 shows the comparison between the normalized absorption spectra of the dye D102 (used in the fabrication of these solid state DSSCs), and the normalized reflectance of the two different IO TiO_2 structures. By overlaying the absorption and reflection spectra, it can be clearly seen that the absorption of the dye D102 lies in the wavelength range of between 300 nm to 580 nm. This wavelength range coincides very well with the reflectance spectra of the IO TiO_2 structures made from PS 260 nm particles, which is from 320 nm to 500 nm. On the other hand, the reflection spectra of the IO TiO_2 made from PS 595 nm particles is broader, but lies in the wavelength range of 550 nm to 1200 nm. Thus, there is only very slight overlap with the absorption range of the dye D102. Hence, most of the light reflected by the PS 260 IO TiO_2 is able to be absorbed very well by the dye D102, while the light reflected by the PS 595 IO TiO_2 will mostly lie outside the absorption range of the dye

D102 and not be absorbed. This effect is clearly observed in the measured PCE results in Figure 37.

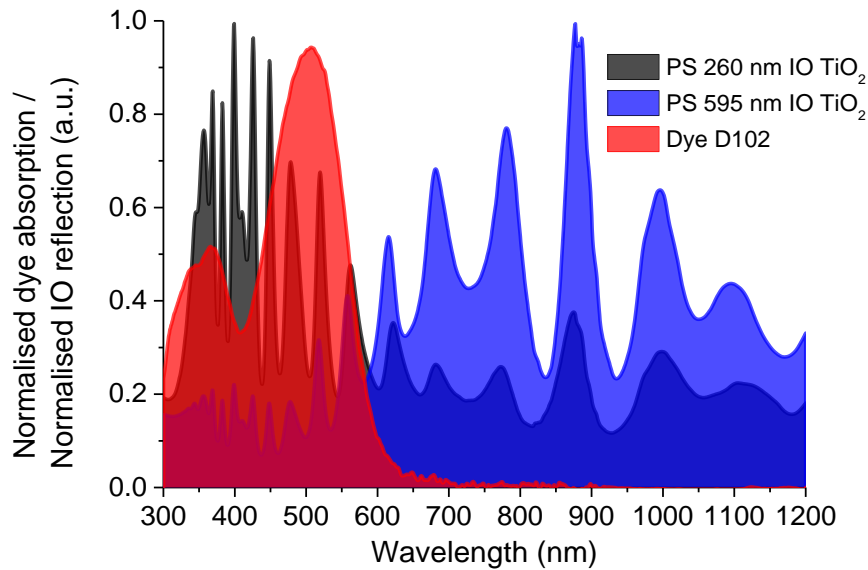


Figure 38. Absorption spectra of the dye D102 compared with the reflection spectra of the titania inverse opal structures.

It can also be seen from Figure 37 that there is still an increase in PCE when two layers of PS 595 IO TiO₂ is incorporated in the cell, but when the layer is doubled to four layers, there is a significant drop in PCE and it falls even lower than the blank reference cells. This suggests that there might a compromise between the thickness of the IO TiO₂ layer and the effective performance enhancement that can be achieved. Since the cells are solid state, they make use of a hole conducting medium (i.e. spiro with a Li salt). Unlike DSSCs containing liquid electrolytes, solid state DSSCs have to be thinner to account for the lower mobility of the holes. Hence, the increased thickness of the IO TiO₂ layer would reduce the current collected as it increases the possibility of recombination along the way. From the results, it appears that a four layer IO TiO₂ made from PS 595 nm particles, which is 1.7 μm^1 thick is detrimental to the cell performance. Hence, having identified the correct size of PS particles to use to fabricate the IO TiO₂ structures, the next series of test was done to determine if there was an optimal layer thickness of the IO TiO₂ structure that could be incorporated into the solid state DSSCs.

¹

$$\left(1 + 3\sqrt{\frac{2}{3}}\right) \times 0.490 = 1.7 \mu\text{m}$$

3.2 EVALUATION OF CELL PERFORMANCE (THE SECOND SERIES)

Similar to the first series, a new set of cells were fabricated including blanks cells with and without the IO calcination step. The cells made in the second series are listed in Table 6.

Table 6. List of experimental conditions for the different cells made in the second series.

Sample name	260/2	260/4	260/6	260/8	Blank	Blank (oven)
PS size (nm)	260	260	260	260	-	-
No. of layers	2	4	6	8	-	-
Oven	yes	yes	yes	yes	no	yes

The cells made in this series followed the protocols similar to that of the first series but with slight modifications to the spin-coating parameters (the experimental details are described in Annex 3). Their performances were measured in the same setup as before. Table 7 shows the measured results of the cells performances.

Table 7. Measured cell performance data of the solid state DSSCs fabricated in the second series.

Sample	J_{sc} (mA/cm ²)	V_{oc} (V)	FF	PCE (%)
Blank	6.78	0.631	0.485	2.07
Blank (oven)	7.11	0.790	0.486	2.73
260/2	7.25	0.78	0.510	2.88
260/4	9.74	0.780	0.460	3.50
260/6	9.73	0.780	0.560	4.25
260/8	8.34	0.780	0.493	3.21

From the results, it can be seen that the performance of the cells fabricated in the second series are generally better than those of the first series due to the optimization of the device preparation parameters. Comparing the data measured between the cells fabricated in this second series, we can see from Figure 39 that the short circuit current generally improves with increasing layer thickness of the IO TiO₂ up to a maximum of about 9.7 mA/cm² for the four and six layers IO TiO₂ and then drops to 8.3 mA/cm² for the eight layers of IO TiO₂ cell. Furthermore, it is also observed that the calcination step (to create the IO TiO₂ by burning off

the PS particles) has a beneficial effect of increasing the open circuit voltage of all the cells that were calcined as compared to the blank reference cell that was not treated with this step.

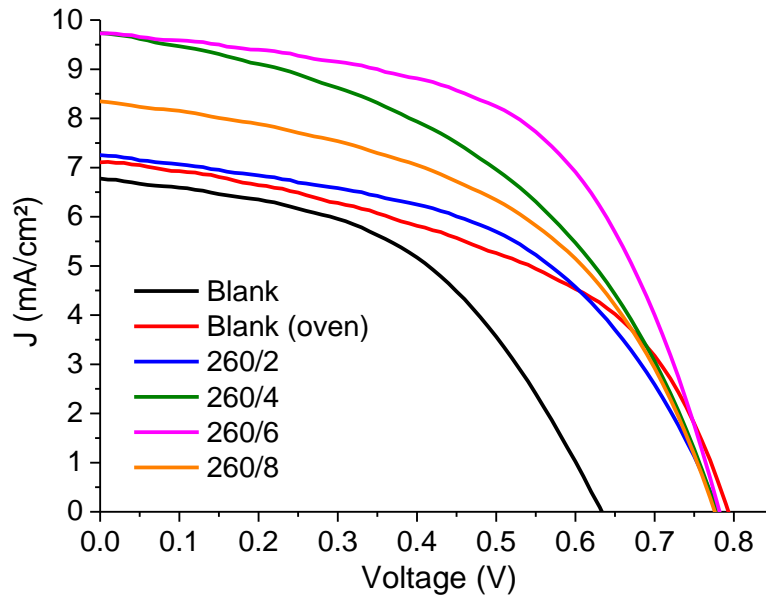


Figure 39. J-V characteristics of solid state DSSCs fabricated in the second series.

The increased V_{oc} for the cells that underwent the extra calcination step could probably be due to the increased crystallinity of the nanocrystalline TiO_2 layer. With increased crystallinity, there would be less defects in the nanocrystalline TiO_2 layer and hence less recombination sites that could affect the charge carriers. The J_{sc} can be observed to increase initially with addition of the IO TiO_2 up to six layers and then it decreases when an additional two layers are added (sample 260/8). The increase in J_{sc} can be attributed to the increased amount of light reflected back into the cell by the IO TiO_2 layer, which increases the amount of light absorbed by the dye and hence the amount of excited charge carriers available charge transport. This phenomenon is observed for cells fabricated with up to six layers of IO TiO_2 . However, when the layer thickness reaches eight layers, even though it is expected that the reflection intensity should be higher than the six layer cell, there is a decrease in J_{sc} . This decrease is most probably due to the increased distance that the charge carriers have to travel through the hole transport medium to the back contact for charge collection. With an increased distance to travel, there are more possibilities for recombination to occur which is detrimental to cell performance. Hence, it can be concluded that there is a compromise between the increased absorption (due to increased reflectance of the IO layer), and the thickness of the IO layer.

From the measured PCE data shown in Figure 40, it appears that having six layers of IO TiO₂ is optimal to the performance this set of solid state DSSCs fabricated.

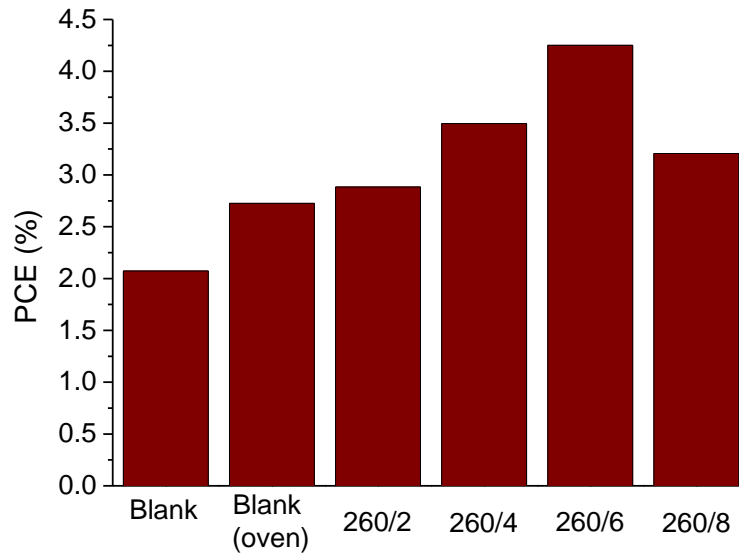


Figure 40. PCE comparison of the best performing cells of each series.

From Figure 40, it can be observed that treating the blank reference cells with an additional calcination step has a beneficial effect on the PCE, as it increases from 2.07% to 2.73%, which is about 35% increase in the PCE. With the addition of two, four, six and eight layers of IO TiO₂, the PCE is further increased to 2.88 %, 3.5 %, 4.25 % and 3.21 % respectively. This translates to an efficiency enhancement of 39 %, 69 %, 105% and 55 % in the PCE of the solid state DSSCs fabricated with two, four, six and eight layers of IO TiO₂ as compared with the blank reference cells without the IO structure.

4. CONCLUSION

The aim of this chapter was primarily to investigate the effect of incorporating an inverse opal (IO) titanium dioxide (TiO_2) structure in a solid state dye sensitized solar cell (ssDSSC). We set out to first determine the best route for the fabrication of the IO structure, and concluded that by stacking individual monolayers of polystyrene (PS) beads self-assembled on a water surface, we could tune the exact thickness of the opal structure that we intended to fabricate, and consequently the inverse opal structure as well.

Next, we have shown that by using different sizes of PS beads, we can tune the resultant pore sizes of the inverse opal and consequently adjust the position of the stop band that results from the structure. It was concluded that for the dye D102, the inverse opal TiO_2 structure with an average pore size of 215 nm (made from PS 260 nm beads), had the most compatible stop band position that coincided very well with the absorbance range of the dye.

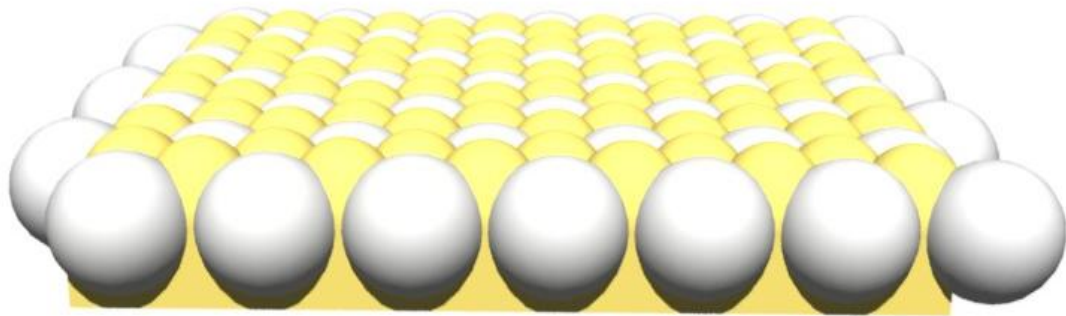
Finally, it was observed that while increasing the IO thickness can bring about greater reflectance and hence more absorption of light by the dye which results in better photoconversion efficiency (PCE), there is a limitation to the maximum thickness of the IO layer. This is because, by using a hole transport medium (HTM) in a solid state DSSC, the conductivity of holes are much lower than electrons (which are the charge carriers in typical DSSCs containing liquid electrolytes), hence, the successful collection of charge carriers with increased thickness of the HTM decreases beyond a certain thickness. Therefore, it is crucial to find a balance between the increased reflectance and the increased thickness of the IO to find an optimal configuration where the maximum PCE can be achieved. Through our series of experiments, it was determined that six layers of IO TiO_2 made from 260 nm PS beads achieved the best results with the dye D102. In the future, more work can be done to reproduce and these results. In addition, different dyes can also be experimented with different configurations of IO to determine the best dye/IO combination that can achieve the optimal cell efficiency.

REFERENCES

- [1] I. Chung, B. Lee, J. He, R. P. H. Chang, and M. G. Kanatzidis, "All-solid-state dye-sensitized solar cells with high efficiency.," *Nature*, vol. 485, no. 7399, pp. 486–9, May 2012.
- [2] B. O'Regan and M. Grätzel, "A low-cost, high-efficiency solar cell based on dye-sensitized colloidal TiO₂ films," *Nature*, vol. 353, no. 6346, pp. 737–740, Oct. 1991.
- [3] A. Facchetti and R. P. H. Chang, "Cross-linkable molecular hole-transporting semiconductor for solid-state dye-sensitized solar cells," 2014.
- [4] X. Xin, H.-Y. Liu, M. Ye, and Z. Lin, "Semiconductor hierarchically structured flower-like clusters for dye-sensitized solar cells with nearly 100% charge collection efficiency.," *Nanoscale*, vol. 5, no. 22, pp. 11220–6, Nov. 2013.
- [5] S. Mathew, A. Yella, P. Gao, R. Humphry-Baker, B. F. E. Curchod, N. Ashari-Astani, I. Tavernelli, U. Rothlisberger, M. K. Nazeeruddin, and M. Grätzel, "Dye-sensitized solar cells with 13% efficiency achieved through the molecular engineering of porphyrin sensitizers.," *Nat. Chem.*, vol. 6, no. 3, pp. 242–7, Mar. 2014.
- [6] W. Yuan, H. Zhao, H. Hu, S. Wang, and G. L. Baker, "Synthesis and characterization of the hole-conducting silica/polymer nanocomposites and application in solid-state dye-sensitized solar cell.," *ACS Appl. Mater. Interfaces*, vol. 5, no. 10, pp. 4155–61, May 2013.
- [7] S.-H. A. Lee, N. M. Abrams, P. G. Hoertz, G. D. Barber, L. I. Halaoui, and T. E. Mallouk, "Coupling of titania inverse opals to nanocrystalline titania layers in dye-sensitized solar cells.," *J. Phys. Chem. B*, vol. 112, no. 46, pp. 14415–21, Nov. 2008.
- [8] B. Lee, D.-K. Hwang, P. Guo, S.-T. Ho, D. B. Buchholtz, C.-Y. Wang, and R. P. H. Chang, "Materials, interfaces, and photon confinement in dye-sensitized solar cells.," *J. Phys. Chem. B*, vol. 114, no. 45, pp. 14582–91, Nov. 2010.
- [9] S. Pillai and M. A. Green, "Plasmonics for photovoltaic applications," *Sol. Energy Mater. Sol. Cells*, vol. 94, no. 9, pp. 1481–1486, Sep. 2010.
- [10] A. Mihi, C. Zhang, and P. V Braun, "Transfer of preformed three-dimensional photonic crystals onto dye-sensitized solar cells.," *Angew. Chem. Int. Ed. Engl.*, vol. 50, no. 25, pp. 5712–5, Jun. 2011.
- [11] A. Mihi and H. Míguez, "Origin of light-harvesting enhancement in colloidal-photonic-crystal-based dye-sensitized solar cells.," *J. Phys. Chem. B*, vol. 109, no. 33, pp. 15968–76, Aug. 2005.
- [12] A. Mihi, F. J. López-Alcaraz, and H. Míguez, "Full spectrum enhancement of the light harvesting efficiency of dye sensitized solar cells by including colloidal photonic crystal multilayers," *Appl. Phys. Lett.*, vol. 88, no. 19, p. 193110, 2006.
- [13] S. Guldin, S. Hüttner, M. Kolle, M. E. Welland, P. Müller-Buschbaum, R. H. Friend, U. Steiner, and N. Tétreault, "Dye-sensitized solar cell based on a three-dimensional photonic crystal.," *Nano Lett.*, vol. 10, no. 7, pp. 2303–9, Jul. 2010.
- [14] J. Kim, J. K. Koh, B. Kim, S. H. Ahn, H. Ahn, D. Y. Ryu, J. H. Kim, and E. Kim, "Enhanced performance of I₂-free solid-state dye-sensitized solar cells with conductive polymer up to 6.8%," *Adv. Funct. Mater.*, vol. 21, no. 24, pp. 4633–4639, Dec. 2011.

- [15] P. R. Somani, C. Dionigi, M. Murgia, D. Palles, P. Nozar, and G. Ruani, "Solid-state dye PV cells using inverse opal TiO₂ films," *Sol. Energy Mater. Sol. Cells*, vol. 87, no. 1–4, pp. 513–519, May 2005.
- [16] D.-K. Hwang, B. Lee, and D.-H. Kim, "Efficiency enhancement in solid dye-sensitized solar cell by three-dimensional photonic crystal," *RSC Adv.*, vol. 3, no. 9, p. 3017, 2013.
- [17] R. C. Schroden, M. Al-Daous, C. F. Blanford, and A. Stein, "Optical properties of inverse opal photonic crystals," *Chem. Mater.*, vol. 14, no. 8, pp. 3305–3315, Aug. 2002.
- [18] L. M. Fortes, M. C. Gonçalves, and R. M. Almeida, "Flexible photonic crystals for strain sensing," *Opt. Mater. (Amst.)*, vol. 33, no. 3, pp. 408–412, Jan. 2011.
- [19] T. Maka, D. N. Chigrin, S. G. Romanov, and C. M. S. Torres, "Three dimensional photonic crystals in the visible regime," *Prog. Electromagn. Res.*, vol. 41, pp. 307–335, 2003.
- [20] N. Vogel, S. Goerres, K. Landfester, and C. K. Weiss, "A convenient method to produce close- and non-close-packed monolayers using direct assembly at the air-water interface and subsequent plasma-induced size reduction," *Macromol. Chem. Phys.*, vol. 212, no. 16, pp. 1719–1734, Aug. 2011.
- [21] J. R. Oh, J. H. Moon, S. Yoon, C. R. Park, and Y. R. Do, "Fabrication of wafer-scale polystyrene photonic crystal multilayers via the layer-by-layer scooping transfer technique," *J. Mater. Chem.*, vol. 21, no. 37, p. 14167, 2011.
- [22] H. J. Snaith, R. Humphry-Baker, P. Chen, I. Cesar, S. M. Zakeeruddin, and M. Grätzel, "Charge collection and pore filling in solid-state dye-sensitized solar cells," *Nanotechnology*, vol. 19, no. 42, p. 424003, Oct. 2008.
- [23] Z. Cai, J. Teng, Z. Xiong, Y. Li, Q. Li, X. Lu, and X. S. Zhao, "Fabrication of TiO₂ binary inverse opals without overlayers via the sandwich-vacuum infiltration of precursor," *Langmuir*, vol. 27, no. 8, pp. 5157–64, Apr. 2011.
- [24] S. Lee, S. Rhee, and S. Oh, "Spectro-ellipsometric studies of sputtered amorphous titanium dioxide thin films: simultaneous determination of refractive index, extinction coefficient, and void distribution," *J. Korean Phys. Soc.*, vol. 34, no. 3, pp. 319–322, 1999.
- [25] L. Schmidt-Mende, U. Bach, R. Humphry-Baker, T. Horiuchi, H. Miura, S. Ito, S. Uchida, and M. Grätzel, "Organic dye for highly efficient solid-state dye-sensitized solar cells," *Adv. Mater.*, vol. 17, no. 7, pp. 813–815, Apr. 2005.

**CHAPTER 3: FABRICATION OF NANOSTRUCTURED GOLD
SURFACES WITH UNIQUE OPTICAL PROPERTIES BY
ELECTRODEPOSITION**



1. INTRODUCTION

Electrodeposition of a metal is a relatively simple process that makes use of an electrical current to reduce dissolved metal cations in an electrolytic bath into a metal on an electrode. The electrodeposition of gold can be traced back to the early work of Brugnatelli in 1805 [1]. The processes in the past were highly toxic as gold electrodeposition depended heavily on cyanide-based electrolytic baths [2]. Nowadays, in addition to cyanide based electrolytic baths, there are also cyanide-free Au(I) sulfite electrolytic baths for gold electrodeposition. However, the main issue with this complex (Au(I) sulfite) is that it is susceptible to disproportionation, forming Au(III) and metallic gold. Hence, the spontaneous decomposition of the complex that can occur in these baths has led to the use of proprietary stabilizing additives in commercial baths [1].

Electrodeposition is a very useful and versatile method that can be used to fabricate materials into arbitrary three-dimensional geometries, and this has led to its widespread adoption in nanotechnology [3]. Electrodeposition has three main attributes that make it very well suited for nano-, bio- and microtechnologies. Firstly, it can be used to grow functional material through complex 3D masks. Secondly, it can be performed near room temperature from water-based electrolytes. Thirdly, it can be scaled down to the deposition of a few atoms or up to large dimensions [2].

Braun and Wiltzius first reported in 1999, the replication of a colloidal crystal using electrodeposition, where both CdS and CdSe replicas were constructed with greater robustness and a higher index of refraction than had been achieved with other methods [4]. Wijnhoven et al. then successfully demonstrated (for the first time with a metal) in 2000, the patterning of macropores using electrodeposition to infiltrate the pores of polystyrene and silica colloidal templates with gold and subsequently removing the template to create artificial inverse opals of gold [5]. In the same year, Bartlett et al. reported the fabrication of highly ordered macroporous films of platinum, palladium and cobalt by electrodepositing these metals into the interstitial spaces of a template made by polystyrene latex spheres [6]. Due to the relative ease of the procedure, several similar works with other metals and materials were also reported in a short interval [3].

Having developed the method to make such templated metal structures, various studies were made to study their properties and possible applications. In 2004, Bartlett et al. made the first

systematic study of the normal incidence reflectance spectra as a function of the film thickness of nanostructured gold and platinum films templated by regular hexagonally closed packed monolayers [7]. In 2005, Abdelsalam et al. investigated the wetting properties of a metallic surface made by electrodeposition through a colloidal layer, and they showed for the first time that by simply changing the surface topography, it was possible to turn a hydrophilic gold surface into a hydrophobic one [8]. In 2007, Yu et al. demonstrated for the first time an electrochemical approach for fabricating high-quality metal inverse opals with complete control over, the structural openness (metal filling fraction). Using Ni electrodeposited into colloidal templates made of 2.2 μm PS beads, they showed that metal inverse opals modulate the absorption and thermal emission of the metal and only at high degrees of structural openness, these effects become 3D in nature [9].

Kelf et al. made a study on the localized and delocalized plasmons in a nanovoid structure made by colloidal templating and electrodeposition. They presented the dependence of the energies of both delocalized Bragg and localized Mie plasmons on the void geometry and provided theoretical models to explain their findings [10]. Various studies also investigated the surface enhanced raman scattering (SERS) effect brought about by such nanovoid structures [11]–[13].

Heim et al. showed in 2012 that by combining the Langmuir –Blodgett technique with electrodeposition, it was possible to integrate planar defects and well defined gradients in a colloidal crystal structure, and such a structure could be infiltrated using electrodeposition to obtain the inverse opal with a complex regulated structure after removal of the beads [14]. Recently in 2013, Pikul et al. made use of electrodeposition through a colloidal template to create interdigitated 3D nanoporous electrodes for lithium ion microbatteries [15].

While the use of templates combined with electrodeposition allows for a controlled structuring of the deposited material (which is the inverse geometry of the template used for electrodeposition), by simply changing certain electrodeposition conditions, it is also possible to electrodeposit complex structures of different geometries without the use of templates (although they are more randomly organized).

In the case of gold electrodeposition, El-Deab et al. showed that gold nanoparticles with different morphologies, such as nanocrystallites, perfect nanospheres, plumbs, and nanoaggregates can be electrodeposited on different substrates and the nature of the substrate

has a direct influence on the morphology, crystallinity, and consequently, the electrocatalytic activity of the Au nanoparticles electrodeposited on them [16]. Tian et al. reported a one-step, non-templated, low-cost electrochemical method for the growth of gold nanostructures with different shapes, such as pyramidal, rod-like, and spherical gold nanostructures, by manipulating the deposited potentials and concentrations of HAuCl_4 , which could be useful for the development of gold films that are potentially applicable to electrocatalysis, surface-enhanced Raman scattering (SERS), surface plasmon sensors (SPR), etc. [17].

Oyama et al. studied the cyclic voltammetric behavior of $[\text{AuCl}_4]^-$ at glassy carbon and gold electrodes in two different ionic liquids at room temperature. They found that the electrodeposition of Au nanoparticles was found to occur via disproportionation reactions, and that the potential-step electrolysis potential used in the electrodeposition process greatly influenced the size and morphology of the gold particles [18]. Sakai et al. electrodeposited various gold nanoparticles and nanostructures with different morphologies in the presence of L-cysteine on indium-doped tin oxide (ITO) substrates and characterized their optical properties. They reported that changes in deposition potential directly affected the geometry of electrodeposited gold and that prolonged electrodeposition led to dendritic gold structures [19].

Ren et al. presented a two-step process to electrodeposit a hierarchical cauliflower-like gold structure. They then modified the structure with fluoroalkylsilane which resulted in a superhydrophobic gold surface [20]. Elias et al. studied the role of adding gelatin during gold electrodeposition to create flail like structures of gold which exhibit a strong SERS effect [21]. Electrodeposited gold thin films with well controlled roughness, morphology and crystallographic orientation were also reported by the same team, and it was determined that the applied electrodeposition potential has a significant effect on the resultant morphology of gold [22]. They further mentioned that the roughness and size of the surface nanostructures affects both the electrocatalytical activity as well as the SERS scattering on such surface [22].

In this chapter, we have embarked on two different routes of gold electrodeposition. The first route, described in section 3.2 and 3.3 describes the electrodeposition of gold through a self-assembled colloidal crystal template, and how it is possible to control the electrodeposition depth to eventually fabricate nanostructured gold surface with exhibit omnidirectional absorption properties first predicted by Teperik et al. [23]. In section 3.4, a one-step template-

free electrodeposition of gold under different voltage conditions is investigated and the optical properties of the resulting broadband non-reflective rough gold surfaces are described.

2. ELECTRODEPOSITION OF GOLD INTO COLLOIDAL TEMPLATES

Electrodeposition is a useful tool that can be used to control very accurately the amount of material electrodeposited on a surface. Heim et al. described a way of controlling the thickness of a film electrodeposited through a multilayer colloidal crystal by monitoring the electrodeposition current under constant potential [14]. Due to the difference in cross sectional area as the material is electrodeposited through the colloidal crystal template, the electrodeposition current changes accordingly as well – larger cross-sectional area, larger electrodeposition current. Hence, it is possible to have a good estimate of the thickness of the electrodeposited material because of the periodic variation in the cross sectional area of the empty voids inside a colloidal crystal template. To verify this phenomena, a six layer colloidal crystal template made with 708 nm silica beads was fabricated using the Langmuir Blodgett (LB) technique (details in Annex 2), and gold was electrodeposited through the colloidal template (details in Annex 4). Figure 41 shows the change in current as gold is electrodeposited through a silica colloidal template made up of six layers of 708 nm silica beads

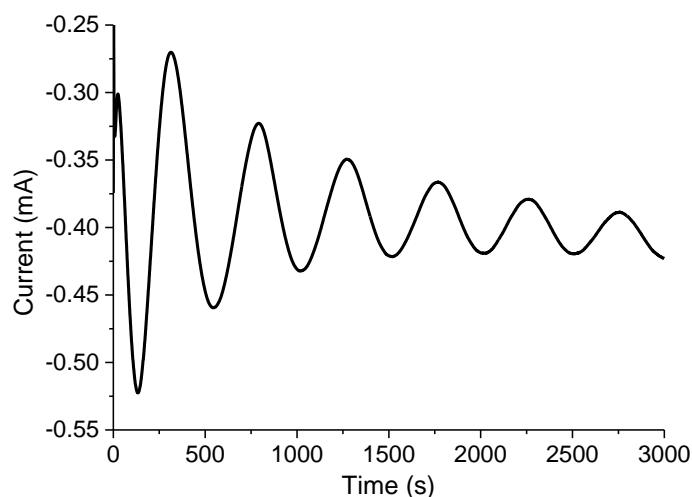


Figure 41. Potentiostatic electrodeposition curve of gold electrodeposited at -0.7V vs Ag/AgCl into a colloidal crystal template consisting of 6 layers of 708 nm silica beads

It can be seen from Figure 41 that there is an initial charging current from 0 to 135s, where the first maximum (most negative current value) of the current occurs. This first maximum

signals the point when electrodeposition is occurring across the entire available cross sectional area of the voids. Following this first maxima, there is a decrease in the absolute value of the current until 314s where the first minima (least negative current value) occurs. This decrease in the absolute value of the current indicates that gold is steadily electrodeposited in the voids and due to the nature of the template, there is a reduction in available deposition surface area as the silica beads are spherical. When the height of the electrodeposited gold is at half the diameter of the silica beads, the absolute value of the current is at a minimum (as available surface area for electrodeposition is at a minimum as well). Once the height of gold electrodeposited is above half of the diameter, the current starts to increase (in absolute value) again. This periodic oscillation in the current occurs as gold is electrodeposited through six layers of the colloidal crystal at a constant potential, and it can be observed that there are six minima and six maxima (excluding the first one) in the current versus time plot in Figure 41.

By determining the amount of time required to electrodeposit gold through one layer of beads, it is also possible to have a good estimate and control of the thickness of the gold within one layer of beads. This type of thickness control by monitoring the electrodeposited current has been described by Abdelsalam [11] previously. To validate the ability to electrodeposit gold according to the desired thickness we wanted in a colloidal templates, we first made a bilayer colloidal template using four different sizes of silica beads using the LB technique. Next, we electrodeposited gold into the templates up to the desired thickness corresponding to $\frac{1}{4}$, $\frac{1}{2}$, $\frac{3}{4}$ and 1 D, where D is the diameter of the silica beads used in the colloidal crystal template. The reason for using a bilayer template instead of a single monolayer in this set of experiments was to make it easier to identify the point when the height of the gold electrodeposited was about equal to the diameter of the silica beads. Figure 42 shows the SEM cross section views of gold electrodeposited through the bilayer colloidal template made of 1 μm silica beads, the SEM top view after silica bead removal and the graphical model of the simulated structure.

From Figure 42, we show that the resultant gold structure electrodeposited corresponds very well to the predicted structure that we intended to fabricate. This proves that it is possible to have a good control of the electrodeposition thickness of gold based on electrodeposition time by monitoring the electrodeposition current during the electrodeposition process.

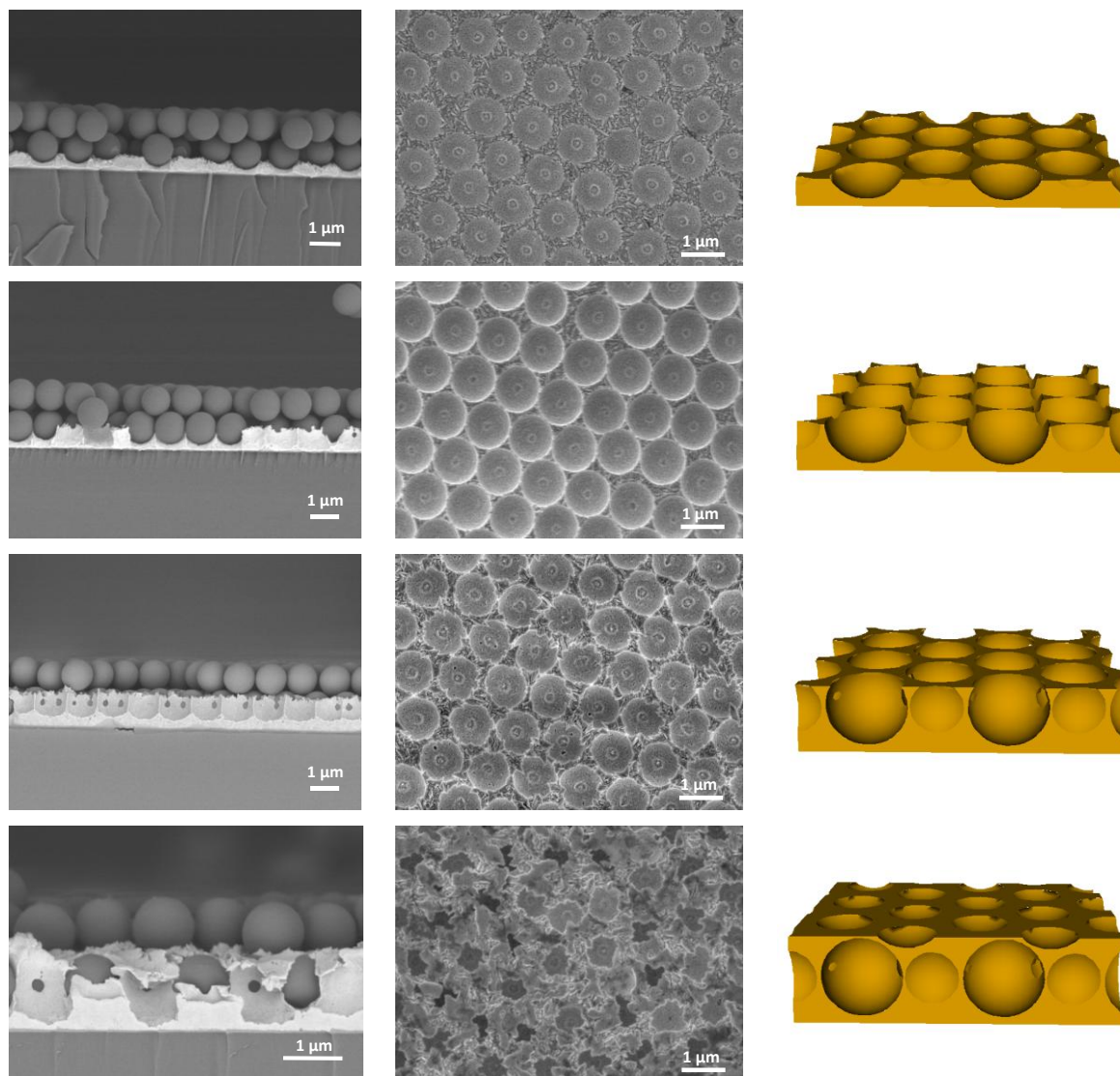


Figure 42. (From top to bottom) SEM pictures of gold electrodeposited into a bilayer of silica ($D = 1\mu\text{m}$) until the desired depths of $0.25D$, $0.5D$, $0.75D$ and $1D$. (Left) SEM cross section views of the various samples, (middle) SEM top views after silica bead removal, and (right) graphical illustration of the expected structures.

Having successfully electrodeposited the desired gold structures into colloidal crystal templates made of $1\mu\text{m}$ silica beads, we next wanted to reproduce the same results with smaller sized silica beads. Hence, similar experiments with bilayer templates of 708 nm , 480 nm and 285 nm silica beads were repeated and the final SEM cross sectional pictures are shown in Figure 43. From Figure 43, we can observe the various heights of gold electrodeposited into the various bilayer templates. The results confirm that this method is applicable to colloidal templates composed of smaller sized particles.

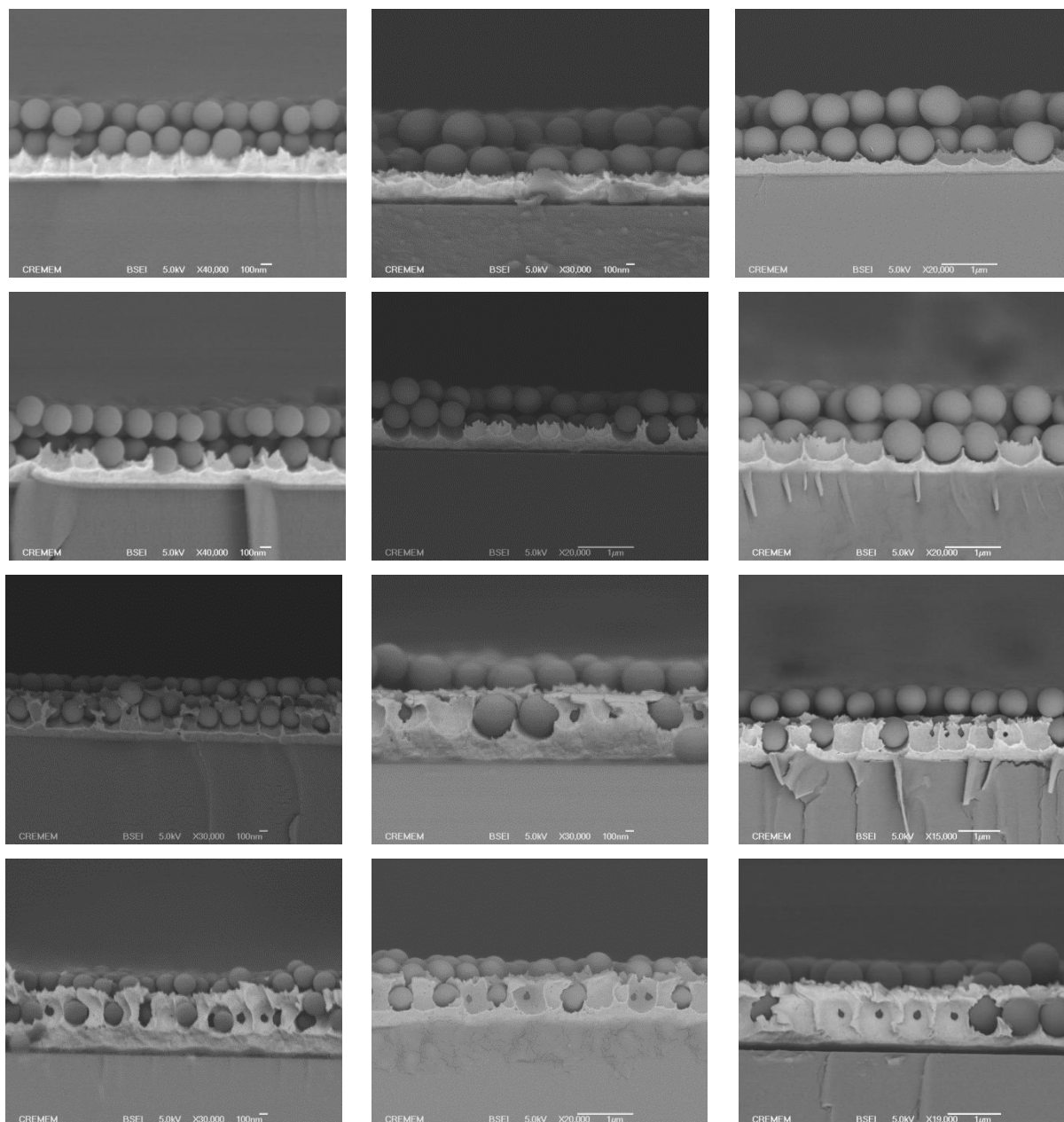


Figure 43. SEM side views of gold electrodeposited into bilayer template of silica of (from left to right) 285 nm, 480 nm and 708 nm at (from top to bottom) 0.25D, 0.5D, 0.75D and 1D. D refers to the diameter of the silica beads.

We have taken benefit of our ability to finely control both the thickness and the structure of the gold films to fabricate and optically characterize two types of omnidirectional absorptive nanostructure gold surfaces. The results that we obtained are discussed in the following sections.

3. QUASI TOTAL OMNIDIRECTIONAL ABSORPTION IN MICRO-/NANO-STRUCTURED GOLD SURFACES

3.1 CONTEXT OF THE STUDY

Nanostructured gold thin films have been reported to exhibit interesting optical properties, such as the total absorption of light, and the possibility of exhibiting zero specular reflection at certain wavelengths. The total absorption of light by a structured metal surface had been predicted and demonstrated as early as 1976, by Hutley and Maystre, on a single, gold coated, sinusoidal interference grating [24]. Hartman and Gaylord have reported that a gold surface-relief rectangular-groove grating exhibits nearly zero specular reflection in the blue region of the spectrum [25]. More recently, Kravets *et al.* [26] have demonstrated a blackbody-like behavior in a nanostructured gold layer fabricated by electron beam lithography, by recording a quasi-total absorption of p-polarized light from 240 nm to 550 nm. Efficient absorption of light on nanoscale metal-semiconductor gratings fabricated on a Bragg mirror has also been demonstrated by Collin *et al.* [27]. More recent work by Bonod *et al.* on lamellar metallic gratings has demonstrated that total absorption of light for any polarization is possible if there is only the zeroth propagating order [28]. However, the absorption of light on grating surfaces still remains heavily dependent on the incident angle. Furthermore, while textured gold surfaces exhibit a strong absorption of light for wavelengths spanning a few hundred nanometers, the challenge remains to achieve ideal anti-reflective properties over wide angles of incidence and broad wavelength regimes for large-area gold films.

In 2005, Teperik and Popov theoretically calculated that a nanoporous metallic film could exhibit total light absorption at plasma resonance when there is optimal coupling of the plasmons in the voids to external light, and this can occur when the voids are buried at a specific distance under the metal surface [29]. In porous metals, the lattice of voids beneath the metal surface has two roles [30]. First, it forms a coupling element which diffracts incident light into surface plasmon-polaritons. Secondly, localized Mie plasmons are excited in the spherical voids. Since void plasmons are radiative excitations, they can couple to light directly without any special coupling device. These localized void plasmons can also be brought into resonant interaction with the propagating surface plasmon-polaritons (SPPs) by tuning the structural parameters such as the diameter of the voids, and by filling them with dielectric materials.

It was further suggested that total omnidirectional absorption of light can be achieved in nanostructured metal surfaces that sustain localized optical excitations [23]. These nanoporous metal surfaces can simultaneously support delocalized SPPs and localized void plasmons, where the localized void plasmons are responsible for the omnidirectional absorption of light. It was demonstrated that almost total absorption of light can indeed be achieved with a lattice of voids just beneath the surface, and theoretically predicted that omnidirectional absorption is possible for a wide angle range (up to 40°). This range of angles can be further increased if the voids were filled with a dielectric medium (e.g. silica) because a dielectric medium can bring down the plasmon void energy to a region that it does not interact with the delocalized SPPs.

A separate work by Bonod and Popov mentioned that total light absorption by buried metal cavities can occur without the aid of surface plasmons under TM polarization due to the role of cavity resonance [31]. It stated that while an opening of the cavity is required to couple incident light into the cavity resonance, the opening has to be closed enough to sustain cavity resonance.

In this chapter, we studied the optical properties of two types of textured gold surfaces, templated and non templated gold surfaces fabricated by an electrodeposition process. The study on the first type of gold surface (in section 3.2) involved fabricating a series of nanostructured gold surfaces with a layer of buried closed packed voids/spheres to experimentally investigate the effect of tuning the cavity size, the cavity medium as well as the polarization of incident light on the phenomenon of omnidirectional total light absorption on such surfaces. The study on the second type of surface (in section 3.3) involved fabricating a series of randomly textured gold deposits by a simple, one step, non-templated electrodeposition process onto a smooth gold surface. We investigated the effect of tuning the applied electrodeposition voltage and time on the morphology and resulting reflectivity of the gold surfaces.

3.2 TEMPLATED GOLD FILMS ELECTRODEPOSITED THROUGH A CLOSE-PACKED MONOLAYER OF POLYSTYRENE BEADS

Self-assembled monolayers of polystyrene beads were first transferred onto a smooth gold coated glass substrate in a method similar to that described in section 2 (details in Annex 2),

and were then used as templates for the electrodeposition of gold into the porous space between the PS beads. Exact experimental details can be found in Annex 4.

It has been reported that a prerequisite of total light absorption by nanostructured gold surfaces is that the metal thickness must be adjusted in such a way that the radiative decay rate of the localized plasmons equals the rate associated with its dissipation [23]. Previously, we have described that it is easy for us to accurately control the thickness of a metallic deposit in a colloidal template by following the local minima/maxima of the current density, which can be attributed to the periodic variation of the electroactive surface area of the growth front during the gold deposition. Figure 44 shows SEM side views of gold films of well-controlled thickness, t , electrodeposited through a monolayer of polystyrene (PS) beads with a diameter, D , of 260 nm, 430 nm or 595 nm.

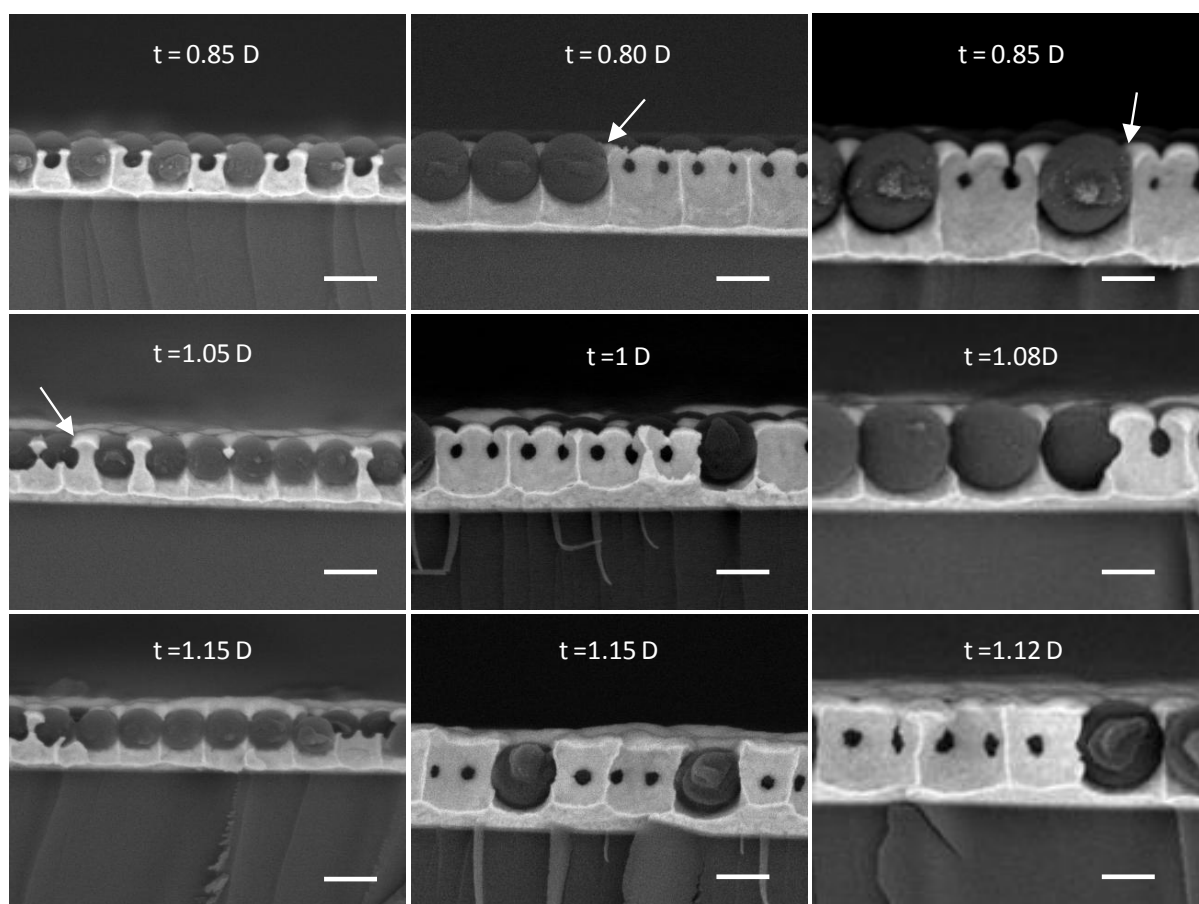


Figure 44. SEM side views of the gold deposits with various thicknesses grown through a monolayer of 260 nm (left), 430 nm (middle) or 595 nm (right) polystyrene (PS) beads. Scale bar: 300 nm.

It can be seen that the deposits are uniform over large distances, illustrating the homogeneity of the electrodeposition process. Another observed feature is that the film growth was slower

near the edges in contact with the PS spheres, possibly due to diffusion constraints. This results in ‘billowing’ of the metal film between the spheres, illustrated in Figure 45 (indicated by arrows in Figure 44).

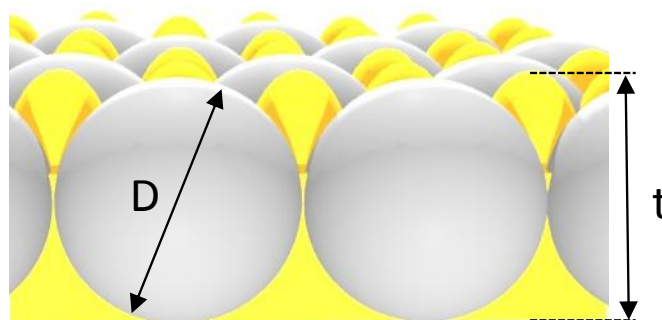


Figure 45. Sketch of the nanostructured gold surfaces, consisting of a monolayer of close-packed PS beads or voids of diameter D infiltrated with gold to a thickness t .

Optical characterization of the gold films

The absorption ($A=1-R$) spectra of the nanostructured gold surfaces for normal incidence of light are shown in Figure 46. Interestingly, the spectra exhibit multiple main peaks (up to 4 for the 595 nm PS template) with an intensity value higher than 90 %. These peaks correspond to the high-order plasma resonances, which can be observed here because of the reduction of their frequencies – which normally fall within the interband absorption spectra of gold – due to the presence of the PS beads, as demonstrated theoretically by Teperik *et al.* [29]. For $D = 260$ nm, almost total light absorption (ca. 98%) is observed at the wavelength of the fundamental Mie plasmon mode, *i.e.* 850 nm for an optimum value of t , found to be equal to 1.02 D . For the films prepared using the 430 nm (595 nm) PS spheres as template, 93 % (95%) of light is absorbed at 1020 nm (1305nm) when $t = 1.05 D$. When the film thickness exceeds the optimum value, the resonant absorption peak shifts towards lower wavelength and decreases in intensity.

We have simulated the optical spectra of the gold structures by the FDTD method, taking into account the billowing of the metal film between the PS beads (refer to Annex 4). Figure 46 shows a nice matching between the positions of the predicted (dashed lines) and measured (solid lines) fundamental plasma resonance peaks, while the band intensities differ slightly, probably due to a non-optimised design of the ellipsoidal caps which represent the billowing of the metal between the PS spheres.

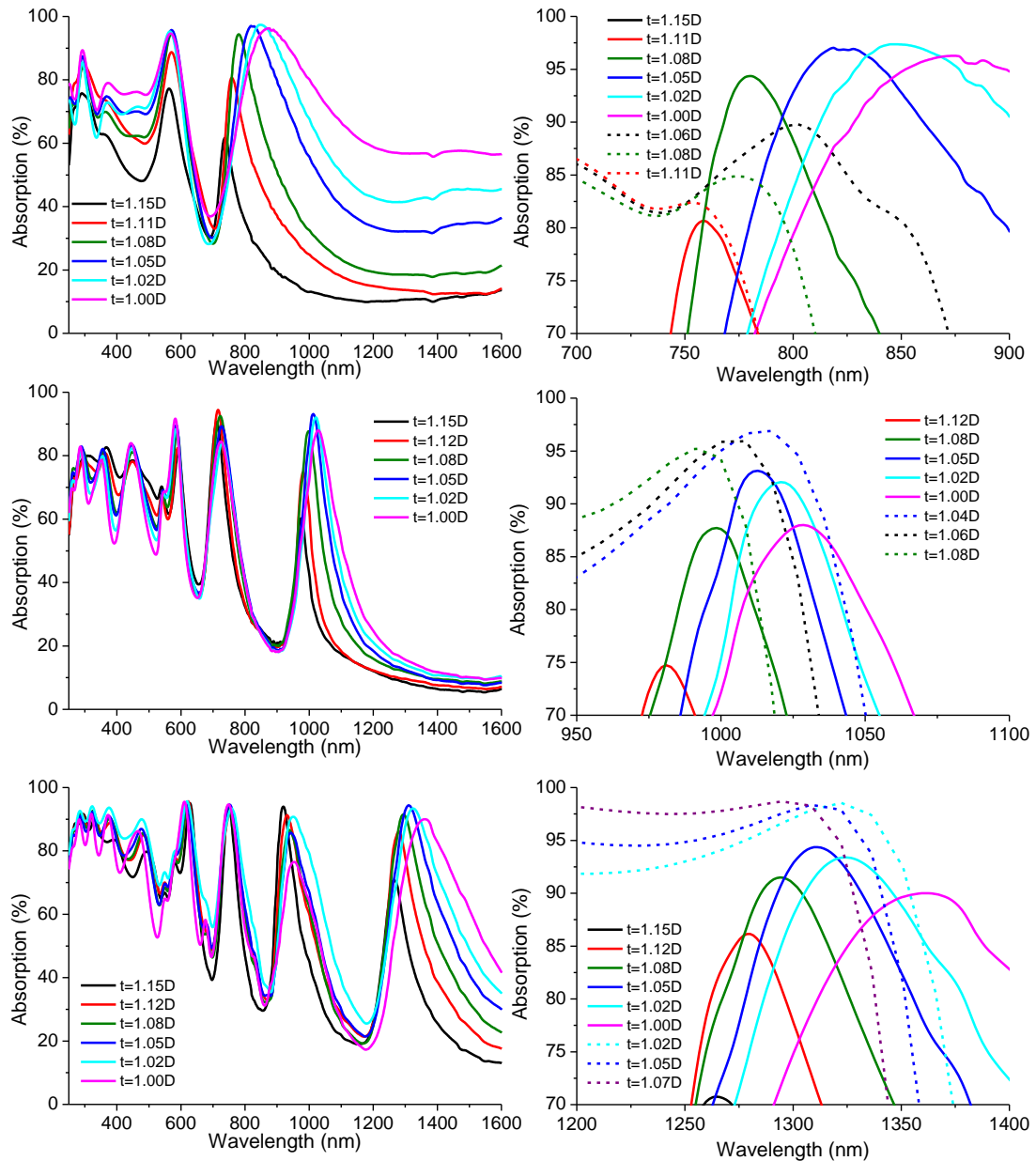


Figure 46. Measured (solid lines) and calculated (dashed lines) absorption spectra of gold films of different thicknesses grown through a monolayer of 260 nm (top), 430 nm (middle) or 595 nm (bottom) PS beads under normal incidence.

After dissolution of the PS template, porous gold surfaces containing a lattice of interconnected voids were obtained. Figure 47 shows SEM top views of the porous gold films, evidencing their uniformity over large areas and the existence of an aperture on the top of the films even when t is larger than D , which is a consequence of the ‘billowing’ of the metal film between the spheres.

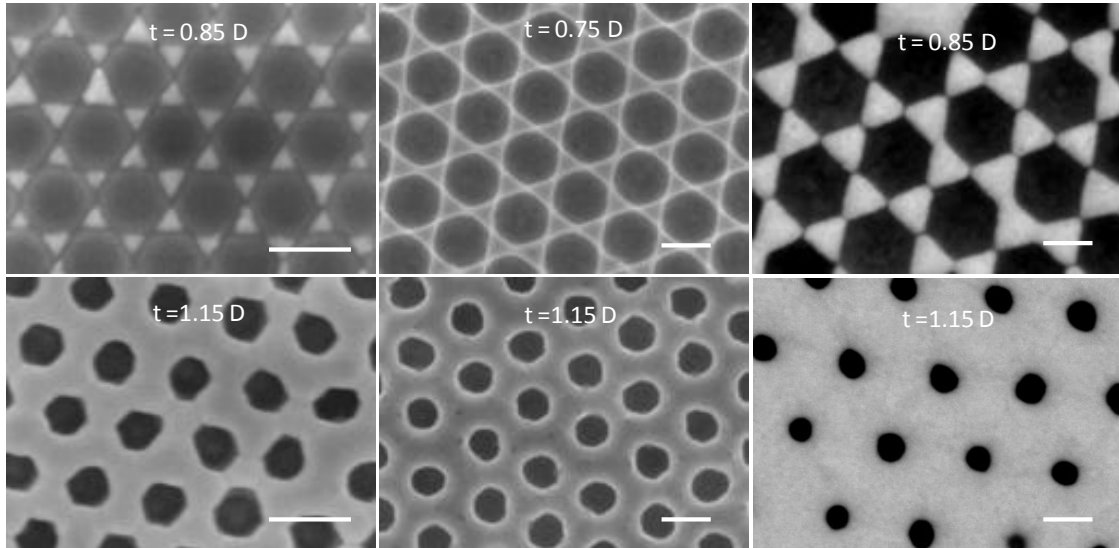


Figure 47. SEM top views of the porous gold films with various thicknesses after the dissolution of the 260 nm (left), 430 nm (middle) or 595 nm (right) PS beads. Scale bar: 300 nm.

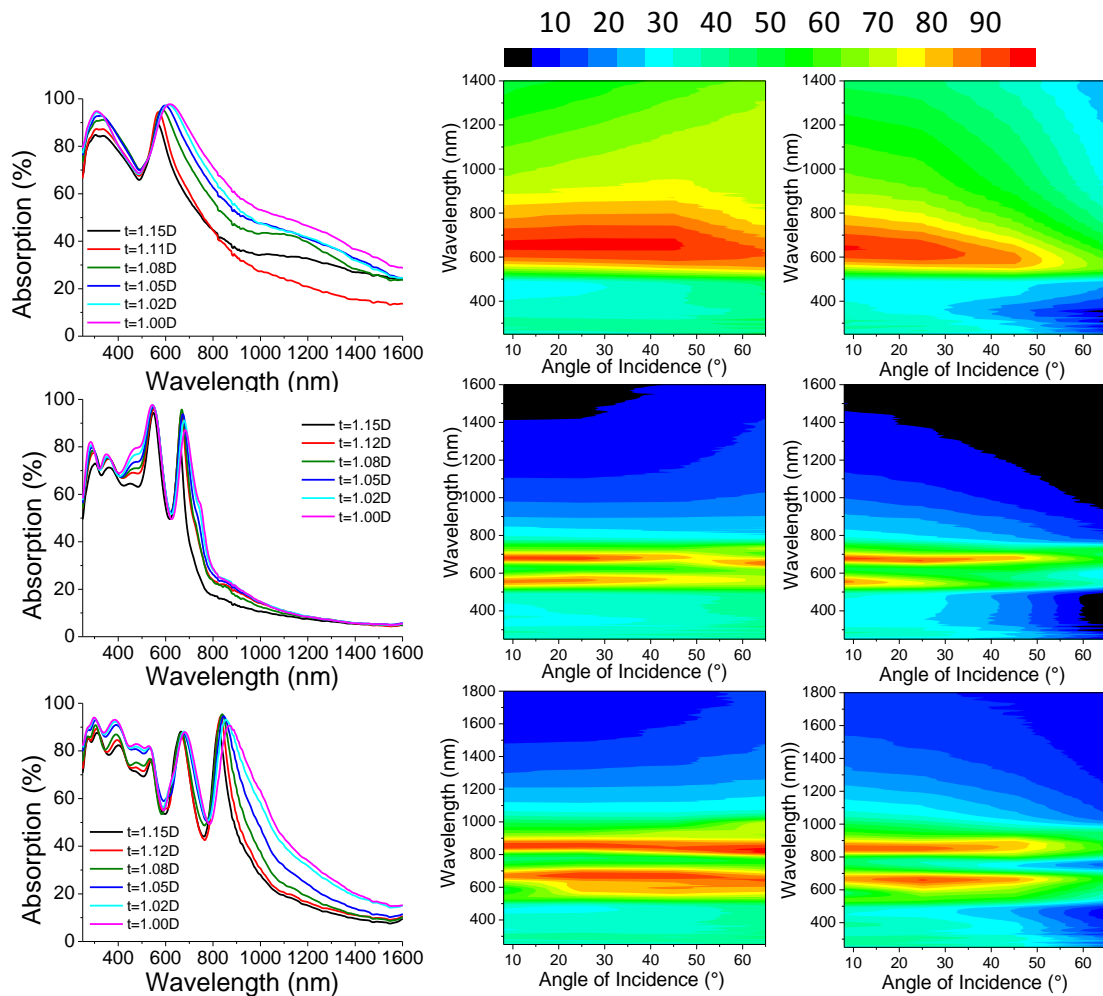


Figure 48. Experimental absorption spectra under normal incidence (left column) and incidence-angle dependence of absorption for p-polarized (center column) and s-polarized (right column) incident light of porous gold films with various thicknesses after the dissolution of the 260 nm (top), 430 nm (middle) or 595 nm (bottom) PS beads.

The optical spectra of the nanoporous gold films also exhibit a quasi total light absorption (Figure 48). For instance, when $D=260$ nm, 97% of the incident light is absorbed at 600 nm for $t = 1.05 D$, while 96 % of light is absorbed at 670 nm (840 nm) for $t=1.08 D$ when $D = 460$ nm (595 nm). As previously, the absorption peak decreases in intensity and shifts towards lower wavelength when t exceeds the optimum value. These results are in good agreement with those obtained by Teperik *et al.* [23]. As theoretically predicted by these authors [23], the near total light absorption of light by the nanoporous gold films persists over a large range of angles of incidence (AOI) for both s- and p-polarized incident light, as shown in Figure 48. For instance, more than 90% of the p-polarized incident light is absorbed for AOI values up to 45° when $D=260$ nm.

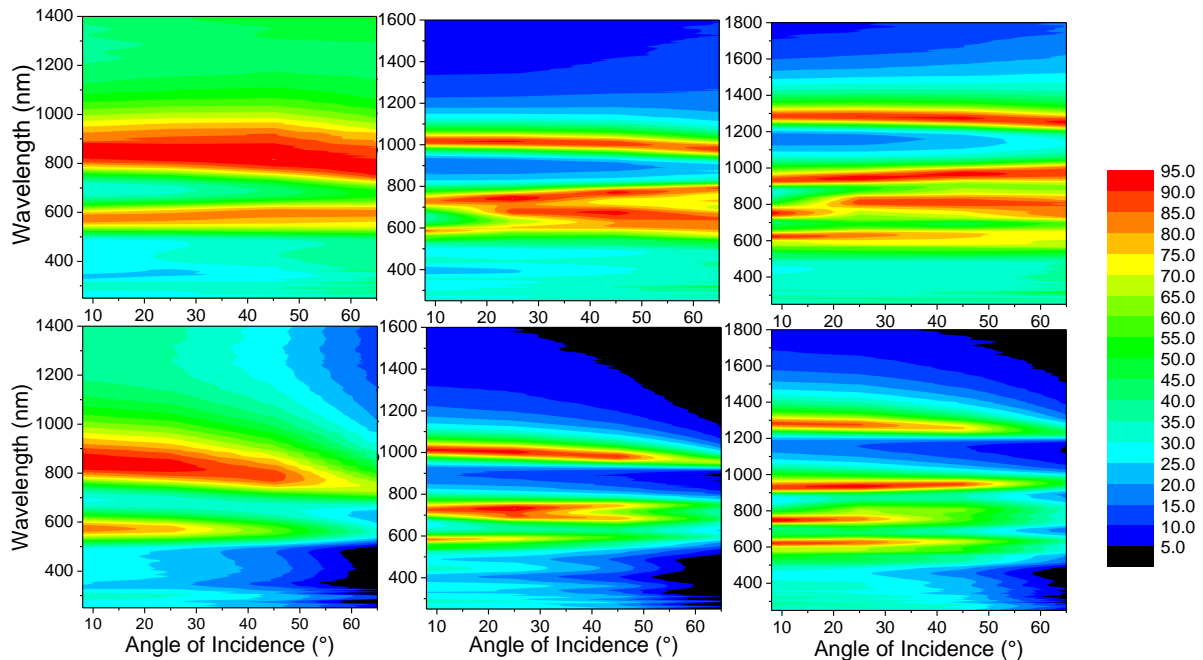


Figure 49. Incidence-angle dependence of absorption of gold films of different thicknesses containing a monolayer PS beads for p- (top) and s-polarized (bottom) incident light. $D=260$ nm (left), 460 nm (middle) and 595 nm (right).

Teperik *et al.* also suggested that this range of AOI can be further extended by infiltrating the voids with a dielectric medium so that the void plasmon is brought down in energy to a region where it does not interact with the delocalized SPPs. Figure 49 shows that this statement is experimentally verified for the gold films containing the PS beads, which absorb more than 90% of the p-polarized incident light for an AOI up to 65° , whatever the PS bead size.

To summarise, we have fabricated nanostructured gold films containing an embedded layer of spherical PS beads or voids by electrodeposition. Near total absorption of light at normal

incidence by gold films with an optimum thickness was experimentally and numerically demonstrated. We have shown that the gold films containing a monolayer of PS beads show light absorption larger than 90% for AOI values up to 65° , which makes the nanostructured gold films good candidates for low cost, high-efficiency absorber materials.

3.3 NON-TEMPLATED ELECTRODEPOSITION OF MICRO/NANOTEXTURED GOLD FILMS

The gold layers were fabricated onto gold-coated glass slides by potentiostatic electrodeposition (details in Annex 4). A commercially available plating solution containing brightener was used for all of the experiments and a constant potential versus Ag/AgCl reference electrode was applied in order to reduce the gold sulphite ions into metallic gold. The intensity of the faradaic current was then measured as a function of time.

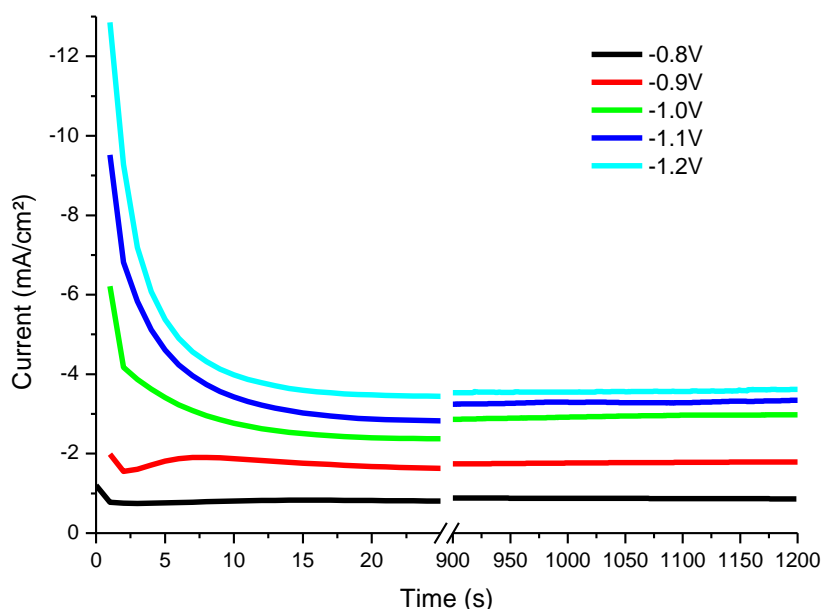


Figure 50. Chronoamperometric curves corresponding to the electrodeposition of gold at various applied potentials at room temperature.

In Figure 50, the chronoamperometric curves corresponding to the electrochemical growth of gold deposits at various applied potentials are shown. We can observe a maximum current density at the beginning, followed by a drastic fall until it reaches a plateau. This is a typical diffusion-controlled nucleation and subsequent growth of metallic electrodeposits, well described by Scharifker and Hills [32]. The maximum corresponds to the nucleation of metallic sites on the surface which is followed by the reduction of current corresponding with the three-dimensional growth of the films. The rise in current in each transient reflects the

electroactive area increases because either each independent nucleus grows in size and/or the number of nuclei increases. At this stage, a diffusion-controlled process directs the growth of the deposit and then the current falls at the final stage.

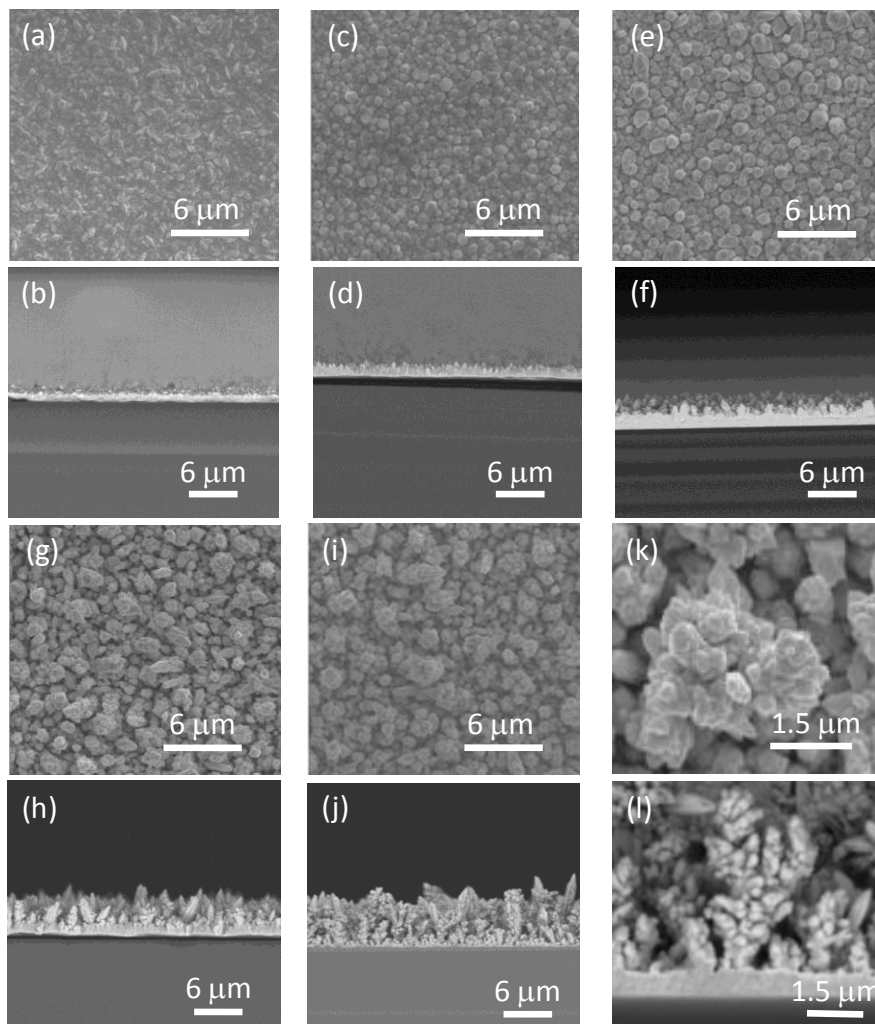


Figure 51. SEM top views and side views of the electrodeposited gold films at: (a-b) -0.8V, (c-d) -0.9V, (e-f) -1.0V, (g-h) -1.1V and (i-l) -1.2 V for 1200s.

Figure 51 shows that the morphology of the electrodeposited gold films is dependent on the applied voltage. At -0.8 V and -0.9 V, plate-like and scale-like microstructures can be observed, respectively. At -1.0 V, the surface appears rougher than before and grooves between the individual microstructures start to appear. At -1.1 V, the film roughness increases and some protrusions can be seen growing out randomly in all directions from the microstructures. At -1.2 V, the resulting deposit is the roughest, each dendritic microstructure resembling a bunch of Romanesco broccoli (see Figure 51). SEM side views show that both the thickness and the structure of the gold films are uniform over their whole surface. The

films' thickness and their deposition rate have been deduced from the SEM side views. Figure 52 shows that the films grow linearly with time, whatever the applied voltage. More negative the applied voltage, faster the deposition. It thus indicates that the formation of the dendrites is favoured at high deposition rate, as previously reported [33].

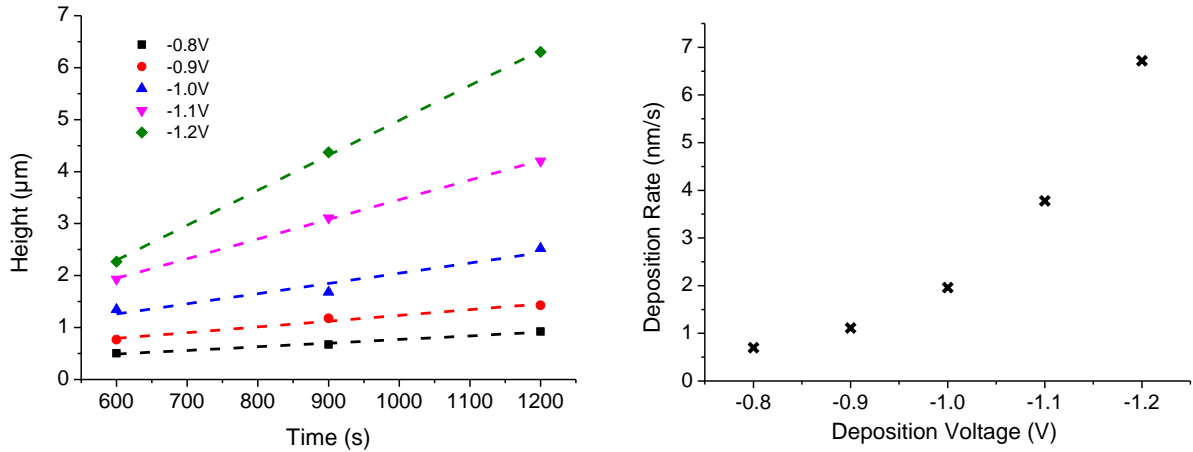


Figure 52 (left) Temporal evolution of the films' thickness; (right) Dependence of the deposition rate of the films on the applied voltage.

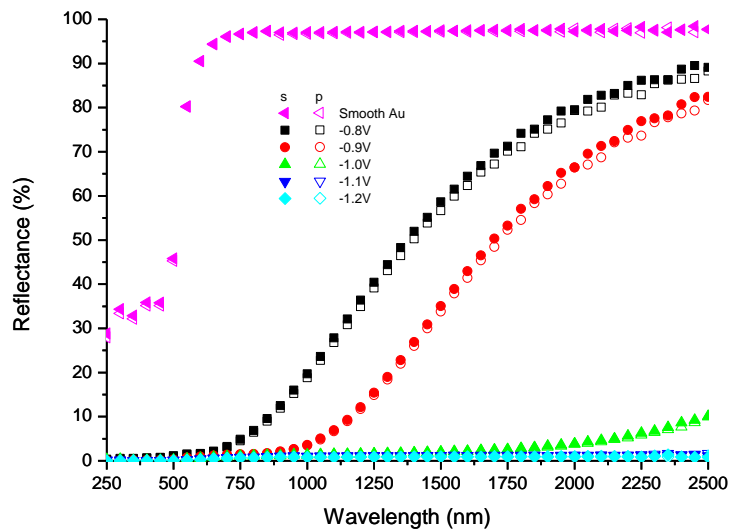


Figure 53. Comparison of the specular reflectance as a function of wavelength for a flat gold film and the textured gold films grown at various applied voltages for s- (solid symbols) and p-polarized (open symbols) incident beams and for 8° off-normal incidence.

Figure 53 shows the reflectance spectra of the corresponding gold films for s- (solid symbols) and p-polarized (open symbols) incident beams with an angle of incidence (AOI) of 8° off the surface normal. The reflectivity from a smooth gold surface is also shown. All the

nanostructured samples exhibit a reflectivity close to zero for both polarizations at the wavelength range of 200-600 nm. However, the difference in electrodeposition voltage has a noticeable effect on the reflectivity of the gold films for wavelengths extending into the infra red (IR) regime. The more negative the applied voltage, lower the reflectivity. The sample prepared at -1.2 V shows a reflectivity for near-normal incidence and both polarizations below 1 % until 2500 nm.

As illustrated in Figure 54, the electrodeposition time has a significant effect on the morphology of the gold deposits grown at -1.2 V vs Ag/AgCl. As already observed for the production of amorphous hydrogenated carbon films by chemical vapor deposition [34], a granular structure appears at short times with a characteristic length scale that grows in a disorderly fashion with further deposition.

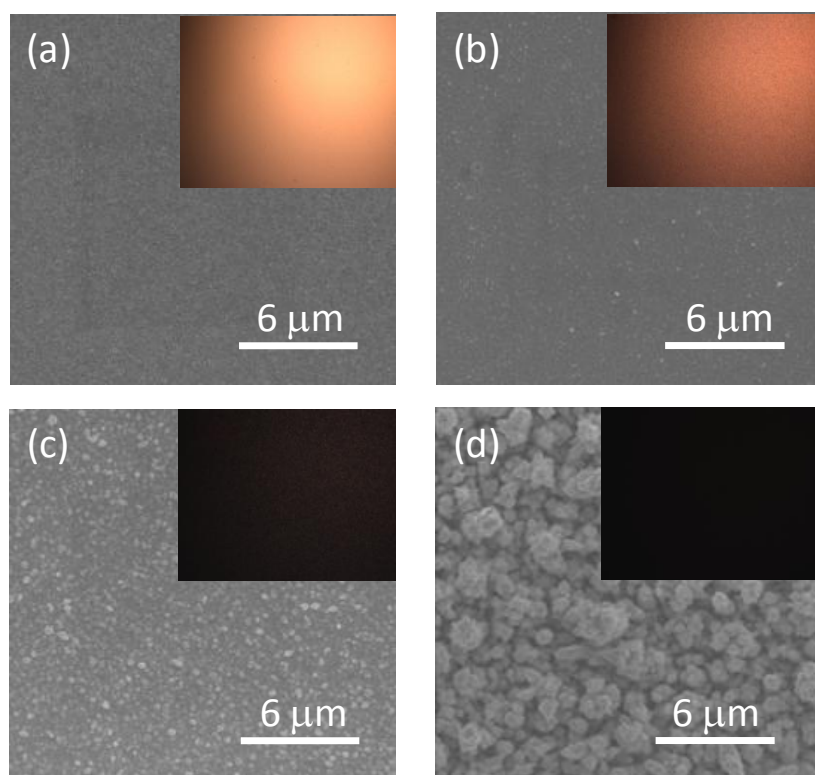


Figure 54. Optical photographs (insets) and SEM images of the electrodeposited gold films deposited at -1.2 V for: (a) 30, (b) 120, (c) 240 and (d) 1200 s.

Figure 54 also shows that the electrodeposition time has also a significant effect on the appearance of the gold deposits grown at -1.2 V. They become darker with time, which corresponds to the fractal growth of the romanesco broccoli-like microstructures. A similar trend was observed for gold films grown at other applied potentials. Figure 55 shows the

optical images of the electrodeposited gold films at various potentials and two different periods of time (600 s and 1200 s) for comparison.

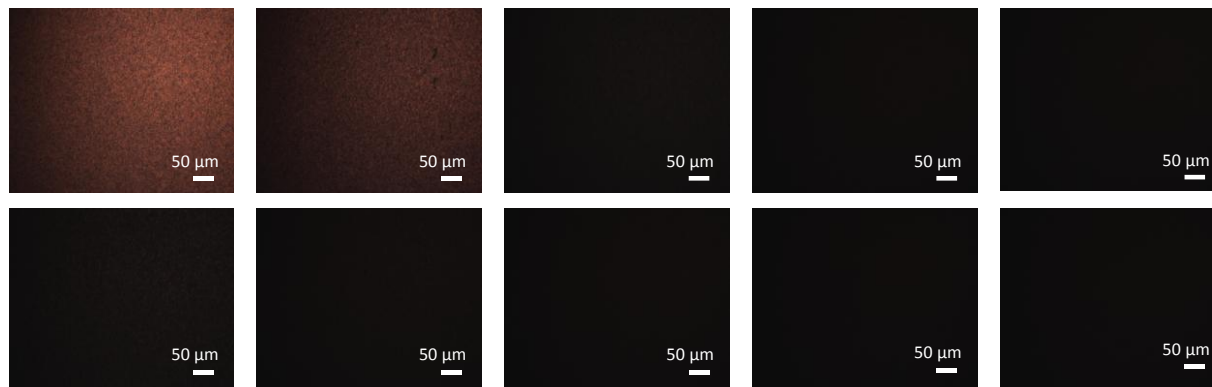


Figure 55. Comparison of the appearance of gold films at different potentials and time. (From left to right) Gold films electrodeposited at -0.8 V, -0.9 V, -1.0 V, -1.1 V and -1.2 V for (top) 600 s and (bottom) 1200 s.

The blackening of the films with time is also evidenced by Figure 56, which shows the influence of the electrodeposition time on the reflectance spectra of the gold films grown at -1.2 V for s- and p-polarized incident beams. The reflectivity of the gold films decreases as a function of time. It takes about 360s to reduce the reflectivity of the sample in the visible region to below 2%. Electrodeposition for an additional 240s further reduces the reflectivity of the sample for wavelengths up to 1600nm to below 5%. Samples electrodeposited for 900s exhibited similar reflectance as the samples electrodeposited for 1200s, which probably indicates the minimum reflectance that can be possibly attained by such a structure, as further deposition does not lead to any significant decrease in reflectance.

In order to perform as a good anti-reflector, the structure must show low reflectance over a wide range of AOI values, for both forms of light polarization. This is shown in Figure 57 for a textured gold film grown at -1.2 V for 1200s. The specular reflectance remains below 1% at AOI values between 8° and 65° off-normal for both s- and p-polarized light throughout the UV-VIS-Near infrared (NIR) region. Similar behaviour was observed for films deposited at lower applied voltages. The wide-angle and polarization independent anti-reflection properties of the gold films are probably due to their highly random nature, which induces multiple bounces of incident light on the fractal dendrites in all the directions of space. Moreover, by considering their structure, the gold films should exhibit a smooth gradient refractive-index profile made of multiple distinct regions, which has been reported to be a key

parameter to allow excellent anti-reflection properties in similar nanostructured silicon surfaces [35].

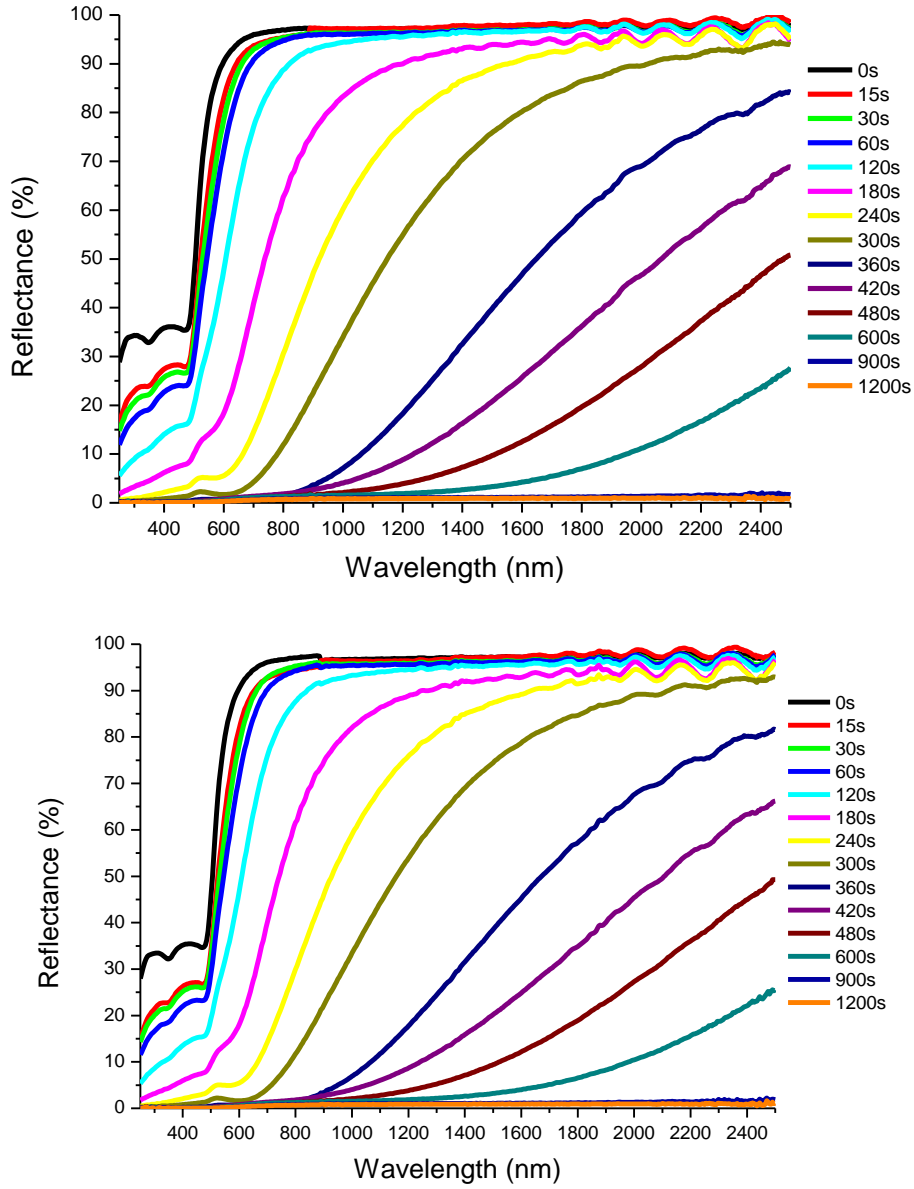


Figure 56. Electrodeposition time influence on the specular reflectance of a gold film grown at -1.2 V for an AOI of 8° and for (left) s- and (right) p-polarized incident beams, respectively.

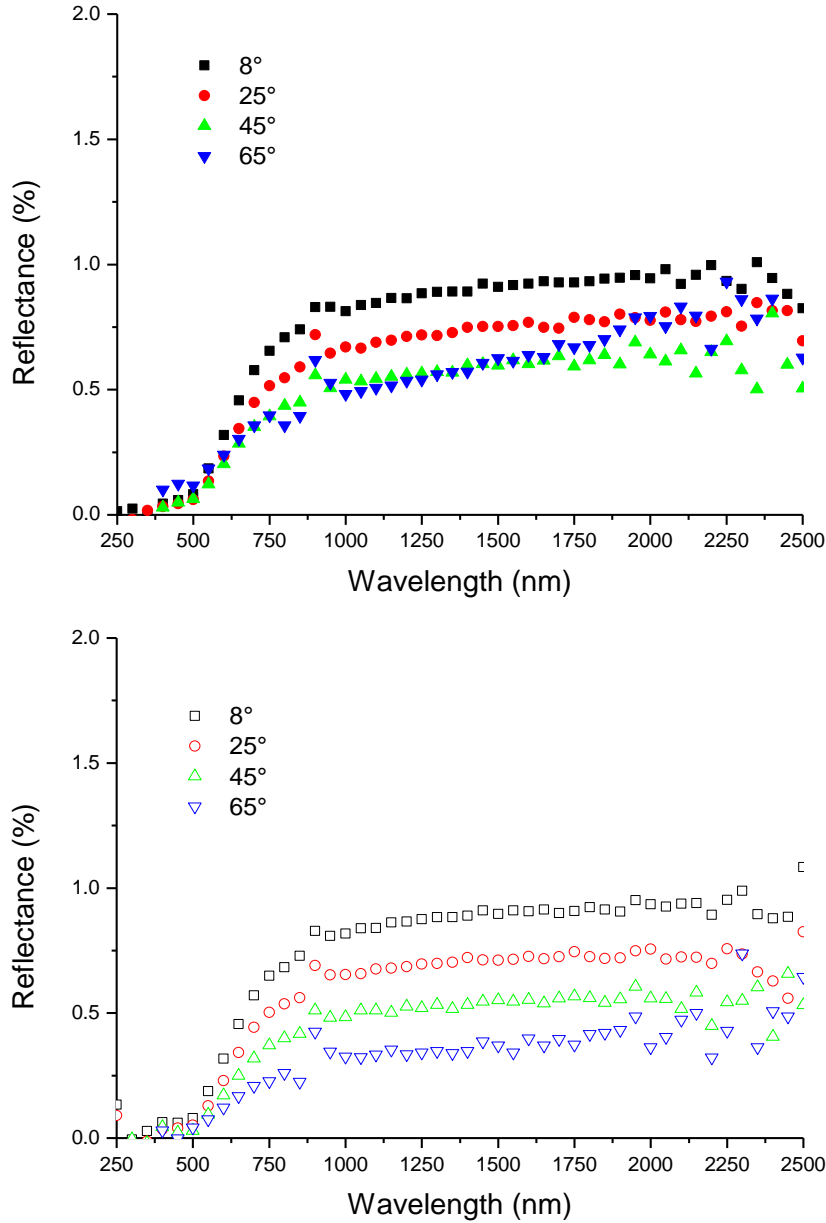


Figure 57. Specular reflectance of a gold film grown at -1.2 V for (top) s- and (bottom) p-polarized incident beams and for four AOI values.

In summary, we have developed an easy, one-step and template-free electrochemical method to fabricate nanostructured gold films with almost zero reflectance over the entire spectral range from the ultraviolet to the NIR. We have shown that the very low reflectivity achieved is slightly sensitive to the polarization and does not change significantly with the angle of incidence. This kind of nanostructured gold films has great potential for low cost, large area solar cell devices, photosensors or other technological applications which benefit from non-reflective coatings.

4. CONCLUSION

In this chapter, we have shown through the use of self-assembled colloidal templates that it is possible to monitor and control the amount of gold deposited into the porous space, and hence control the geometry of the electrodeposited gold structure to conform to that of the template structure. Optical characterisations of the fabricated structures confirm the existence of the omnidirectional absorption in gold thin films predicted by Teperik et al. [23]. This kind of plasmonic nanostructures exhibiting almost perfect absorption could be used with hot electron photodetectors to significantly enhance the hot electron transfer process [36]. Furthermore, the integration of such structures on silicon or other high index materials by suitable transferring methods, such as PDMS stamping, could also lead to the enhancement of the efficiencies of photovoltaic and photocatalytic devices.

In addition, through a simple investigation into the template free electrodeposition of gold, we have shown that by simply changing the deposition potential, we can induce a significant change to the resulting morphology of the gold electrodeposited. It is possible to electrodeposit smooth gold at small potentials and dramatically change the roughness by using higher electrodeposition potentials which directly affects the resulting optical properties of a gold surface. By optically characterising these gold surfaces, we discover that they exhibit very low reflectivity which is broadband and omnidirectional.

The optical properties of both the fabricated gold surfaces described in this chapter demonstrate the versatility of the electrodeposition technique to make structures of the same material but with radically different structures and resulting optical properties.

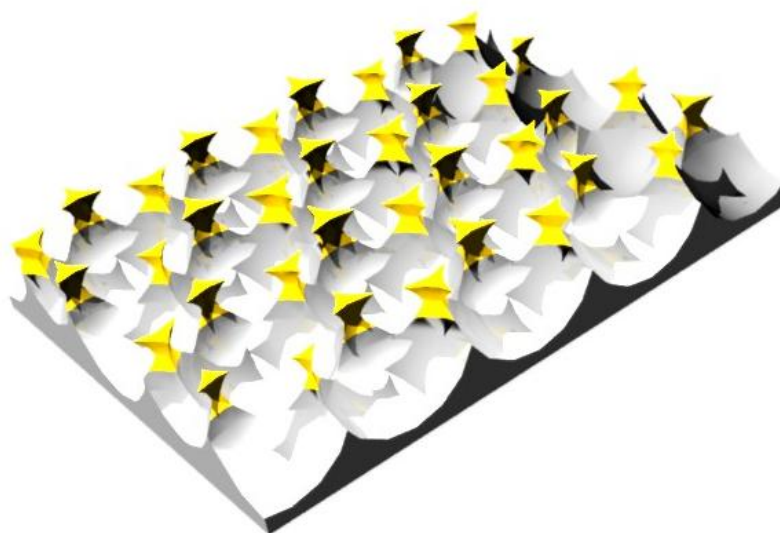
REFERENCES

- [1] P. A. Kohl, *Modern Electroplating - Chapter 4: Electrodeposition of gold*, Fifth Edit. John Wiley & Sons, Inc., 2010, pp. 115–130.
- [2] W. Shwarzacher, “Electrodeposition : A technology for the future,” *Electrochem. Soc. Interface*, vol. 15, no. 1, pp. 32–35, 2006.
- [3] P. V. Braun and P. Wiltzius, “Macroporous materials—electrochemically grown photonic crystals,” *Curr. Opin. Colloid Interface Sci.*, vol. 7, no. 1–2, pp. 116–123, Mar. 2002.
- [4] P. V Braun and P. Wiltzius, “Electrochemically grown photonic crystals,” *Nature*, vol. 402, pp. 603–604, 1999.
- [5] J. E. G. J. Wijnhoven, S. J. M. Zevenhuizen, M. a. Hendriks, D. Vanmaekelbergh, J. J. Kelly, and W. L. Vos, “Electrochemical assembly of ordered macropores in gold,” *Adv. Mater.*, vol. 12, no. 12, pp. 888–890, Jun. 2000.
- [6] P. N. Bartlett, P. R. Birkin, and M. a. Ghanem, “Electrochemical deposition of macroporous platinum, palladium and cobalt films using polystyrene latex sphere templates,” *Chem. Commun.*, no. 17, pp. 1671–1672, 2000.
- [7] P. N. Bartlett, J. J. Baumberg, S. Coyle, and M. E. Abdelsalam, “Optical properties of nanostructured metal films,” *Faraday Discuss.*, vol. 125, p. 117, 2004.
- [8] M. E. Abdelsalam, P. N. Bartlett, T. Kelf, and J. Baumberg, “Wetting of regularly structured gold surfaces,” *Langmuir*, vol. 21, no. 5, pp. 1753–7, Mar. 2005.
- [9] X. Yu, Y.-J. Lee, R. Furstenberg, J. O. White, and P. V. Braun, “Filling fraction dependent properties of inverse opal metallic photonic crystals,” *Adv. Mater.*, vol. 19, no. 13, pp. 1689–1692, Jul. 2007.
- [10] T. Kelf, Y. Sugawara, R. Cole, J. Baumberg, M. Abdelsalam, S. Cintra, S. Mahajan, a. Russell, and P. Bartlett, “Localized and delocalized plasmons in metallic nanovoids,” *Phys. Rev. B*, vol. 74, no. 24, p. 245415, Dec. 2006.
- [11] M. E. Abdelsalam, “Surface enhanced raman scattering of aromatic thiols adsorbed on nanostructured gold surfaces,” *Cent. Eur. J. Chem.*, vol. 7, no. 3, pp. 446–453, Jul. 2009.
- [12] R. M. Cole, S. Mahajan, P. N. Bartlett, and J. J. Baumberg, “Engineering SERS via absorption control in novel hybrid Ni/Au nanovoids,” *Opt. Express*, vol. 17, no. 16, pp. 13298–308, Aug. 2009.
- [13] M. E. Abdelsalam, P. N. Bartlett, J. J. Baumberg, S. Cintra, T. a. Kelf, and A. E. Russell, “Electrochemical SERS at a structured gold surface,” *Electrochem. commun.*, vol. 7, no. 7, pp. 740–744, Jul. 2005.

- [14] M. Heim, S. Reculosa, S. Ravaine, and A. Kuhn, "Engineering of complex macroporous materials through controlled electrodeposition in colloidal superstructures," *Adv. Funct. Mater.*, vol. 22, no. 3, pp. 538–545, Feb. 2012.
- [15] J. H. Pikul, H. Gang Zhang, J. Cho, P. V. Braun, and W. P. King, "High-power lithium ion microbatteries from interdigitated three-dimensional bicontinuous nanoporous electrodes," *Nat. Commun.*, vol. 4, p. 1732, Apr. 2013.
- [16] M. S. El-Deab, T. Sotomura, and T. Ohsaka, "Morphological selection of gold nanoparticles electrodeposited on various substrates," *J. Electrochem. Soc.*, vol. 152, no. 11, p. C730, 2005.
- [17] Y. Tian, H. Liu, G. Zhao, and T. Tatsuma, "Shape-controlled electrodeposition of gold nanostructures," pp. 23478–23481, 2006.
- [18] T. Oyama, T. Okajima, and T. Ohsaka, "Electrodeposition of gold at glassy carbon electrodes in room-temperature ionic liquids," *J. Electrochem. Soc.*, vol. 154, no. 6, p. D322, 2007.
- [19] N. Sakai, Y. Fujiwara, M. Arai, K. Yu, and T. Tatsuma, "Electrodeposition of gold nanoparticles on ITO: Control of morphology and plasmon resonance-based absorption and scattering," *J. Electroanal. Chem.*, vol. 628, no. 1–2, pp. 7–15, Apr. 2009.
- [20] H.-X. Ren, X.-J. Huang, O. Yarimaga, Y.-K. Choi, and N. Gu, "A cauliflower-like gold structure for superhydrophobicity.," *J. Colloid Interface Sci.*, vol. 334, no. 1, pp. 103–7, Jun. 2009.
- [21] J. Elias, P. Brodard, M. G. C. Vernooij, J. Michler, and L. Philippe, "Gold flails by electrochemical deposition: The role of gelatin," *Electrochim. Acta*, vol. 56, no. 3, pp. 1485–1489, Jan. 2011.
- [22] J. Elias, M. Gizowska, P. Brodard, R. Widmer, Y. Dehazan, T. Graule, J. Michler, and L. Philippe, "Electrodeposition of gold thin films with controlled morphologies and their applications in electrocatalysis and SERS.," *Nanotechnology*, vol. 23, no. 25, p. 255705, Jul. 2012.
- [23] T. V. Teperik, F. J. García de Abajo, A. G. Borisov, M. Abdelsalam, P. N. Bartlett, Y. Sugawara, and J. J. Baumberg, "Omnidirectional absorption in nanostructured metal surfaces," *Nat. Photonics*, vol. 2, no. 5, pp. 299–301, Apr. 2008.
- [24] M. C. Hutley and D. Maystre, "The total absorption of light by a diffraction grating," *Opt. Commun.*, vol. 19, no. 3, pp. 431–436, 1976.
- [25] N. F. Hartman and T. K. Gaylord, "Antireflection gold surface-relief gratings: experimental characteristics.," *Appl. Opt.*, vol. 27, no. 17, pp. 3738–43, Sep. 1988.
- [26] V. G. Kravets, F. Schedin, and a. N. Grigorenko, "Almost complete absorption of light in nanostructured metallic coatings: Blackbody behavior," *PIERS Online*, vol. 5, no. 4, pp. 397–400, 2009.

- [27] S. Collin, F. Pardo, R. Teissier, and J.-L. Pelouard, “Efficient light absorption in metal–semiconductor–metal nanostructures,” *Appl. Phys. Lett.*, vol. 85, no. 2, pp. 194–196, 2004.
- [28] N. Bonod, G. Tayeb, D. Maystre, S. Enoch, and E. Popov, “Total absorption of light by lamellar metallic gratings,” *Opt. Express*, vol. 16, no. 20, pp. 15431–8, Sep. 2008.
- [29] T. Teperik, V. Popov, and F. García de Abajo, “Void plasmons and total absorption of light in nanoporous metallic films,” *Phys. Rev. B*, vol. 71, no. 8, pp. 1–9, Feb. 2005.
- [30] T. V Teperik, V. V Popov, F. J. García de Abajo, M. Abdelsalam, P. N. Bartlett, T. A. Kelf, Y. Sugawara, and J. J. Baumberg, “Strong coupling of light to flat metals via a buried nanovoid lattice: the interplay of localized and free plasmons,” *Opt. Express*, vol. 14, no. 5, pp. 1965–72, Mar. 2006.
- [31] N. Bonod and E. Popov, “Total light absorption in a wide range of incidence by nanostructured metals without plasmons,” *Opt. Lett.*, vol. 33, no. 20, pp. 2398–400, Oct. 2008.
- [32] B. Scharifker and G. Hills, “Theoretical and experimental studies of multiple nucleation,” *Electrochim. Acta*, vol. 28, no. 7, pp. 879–889, 1983.
- [33] Y. Sawada, A. Dougherty, and J. P. Gollub, “Dendritic and fractal patterns in electrolytic deposits,” *Phys. Rev. Lett.*, vol. 56, no. 12, pp. 1260–1263, 1986.
- [34] M. Castro, R. Cuerno, M. Nicoli, L. Vázquez, and J. G. Buijnsters, “Universality of cauliflower-like fronts: from nanoscale thin films to macroscopic plants,” *New J. Phys.*, vol. 14, no. 10, p. 103039, Oct. 2012.
- [35] Y.-F. Huang, S. Chattopadhyay, Y.-J. Jen, C.-Y. Peng, T.-A. Liu, Y.-K. Hsu, C.-L. Pan, H.-C. Lo, C.-H. Hsu, Y.-H. Chang, C.-S. Lee, K.-H. Chen, and L.-C. Chen, “Improved broadband and quasi-omnidirectional anti-reflection properties with biomimetic silicon nanostructures,” *Nat. Nanotechnol.*, vol. 2, no. 12, pp. 770–4, Dec. 2007.
- [36] W. Li and J. Valentine, “Metamaterial perfect absorber based hot electron photodetection,” *Nano Lett.*, vol. 14, no. 6, pp. 3510–4, Jun. 2014.

CHAPTER 4: BOTTOM-UP DESIGN OF TWO DIMENSIONAL PLASMONIC NANOPILLAR ARRAYS



1. INTRODUCTION

Metallic nanostructures play an important role in many applications. In the emerging fields of plasmonics and nanophotonics, the ability to engineer metals on nanometric scales allows the fabrication of new devices and the study of exciting physics. Currently, gold and silver are the most commonly used materials in the field of plasmonics due to their plasmon resonances in the visible and near infra-red (NIR). In the case of silver, it exhibits the lowest losses of current materials in both the visible and NIR [1]. However, it is susceptible to corrosion from sulfur and chlorine species in the natural environment [2]. Gold is chemically stable in natural environments and exhibits the second lowest losses after silver, hence making it very well suited for plasmonic applications such as biosensors [3]. Other metals such as copper and aluminum have also shown promise as plasmonic materials but they each have unique advantages and disadvantages. Oxide-free copper displays plasmonic properties in the visible range but the surface of copper is readily oxidized. Hence, in an environment not exposed to air, copper could serve as a low cost alternative to gold as a plasmonic material [4]. Aluminum outperforms both gold and silver in the blue and UV regions as it displays a negative real permittivity at wavelengths less than 200nm with relatively low losses in this region. Gold and silver do not display the required negative real permittivity until approximately 327 nm and 207 nm, respectively [1].

Metallic nanostructures offer the possibility of subwavelength control and the manipulation of optical energy. While dielectric structures suffer from diffractive effects, metallic nanostructures that support surface plasmon polaritons (SPPs) offer a solution. Today, most of the fabrication techniques adopted to fabricate metallic nanostructures rely heavily on top down approaches such as electron-beam lithography ('write'), focused-ion-beam (FIB) lithography ('drill,' 'cut,' and 'solder'), nanoimprint ('stamp'), nano-molding and scanning-probe lithography ('rearranging the atoms') [5].

Tsai et al. fabricated arrays of gold nanopillars (Figure 58) and studied the effect of the size and spacing of these arrays on the spectral response of a P3HT: PCBM bulk heterojunction solar cell. They found that the patterned devices show a higher external quantum efficiency and that the corresponding resonance involves both localized particle plasmon excitation and multiple reflections/diffraction within the cavity formed by the electrodes [6].

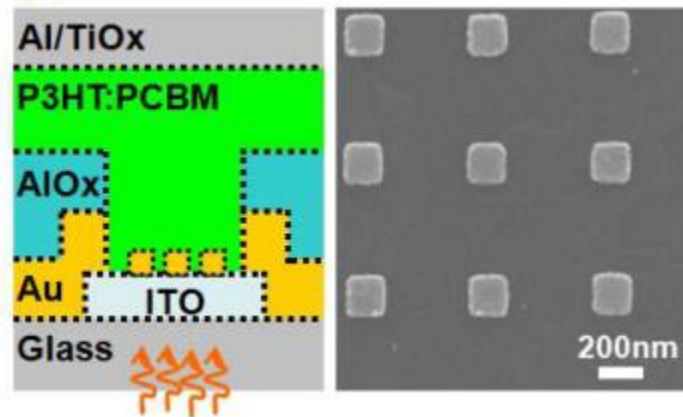


Figure 58. (left) Cross section schematic of nanopillar-patterned solar cell. (Right) SEM image of nanopillar arrays on ITO surface [6].

Nakamoto et al. reported a nanoimprint technique to create well-ordered metallic arrays of nanopillars in nanoholes which are made by fabricated magnetron sputtering into a plastic nanohole array over a large area. They showed that by controlling the sputtering time and initial hole design, they could adjust the pillar height and pillar-hole gap [7]. Hatab et al. described a new configuration of elevated gold bowtie nanoantenna arrays (Figure 59) with optimized array periodicity made by electron beam lithography which demonstrated large SERS enhancement factors exceeding 10^{11} [8].

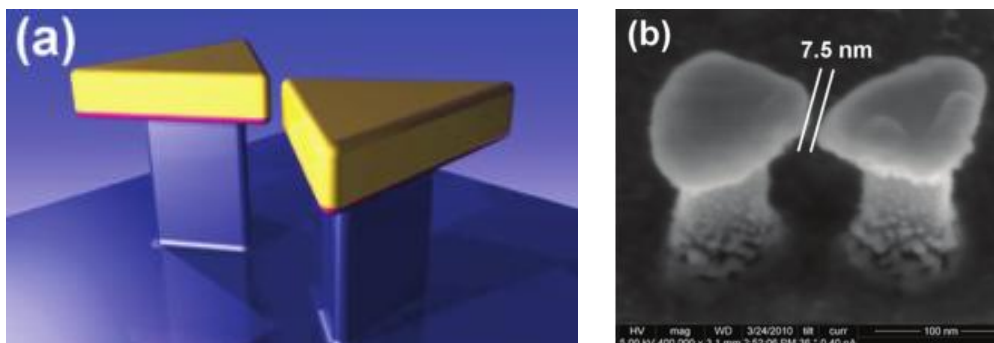


Figure 59. (a) Schematic illustration of elevated gold bowties on top of silicon posts etched into a Si wafer. (b) SEM image of a gold bowtie nanoantenna [8].

Chirumamilla et al. demonstrated that dimers of uniform, free-standing three dimensional star-shaped gold nanostructures are applicable for single / few molecules detection by SERS [9]. Cattoni et al. fabricated arrays of plasmonic nanocavities with very low volumes by soft UV nanoimprint lithography and demonstrated nearly perfect omnidirectional absorption for the fundamental mode of the cavity [10].

While the resolution, control and precision of nanostructures fabricated by top down approaches are of very high quality, the widespread use of such techniques are relatively limited due mainly to the costs and equipment associated with most top down fabrication techniques. Furthermore, due to the complexity of the equipment, the fabricated materials are usually small lab scale samples.

An alternative to creating nanostructures from the top down is to rely on the bottom up construction of these nanostructures. By using a combination of bottom-up and top down techniques, O'Carroll et al. demonstrated a process to create metal-polymer-metal dipole antennas that made use of template-directed sequential electrodeposition of gold and polythiophene into nanoporous alumina and the subsequent thermal evaporation of gold into the alumina template pores (Figure 60) [11].

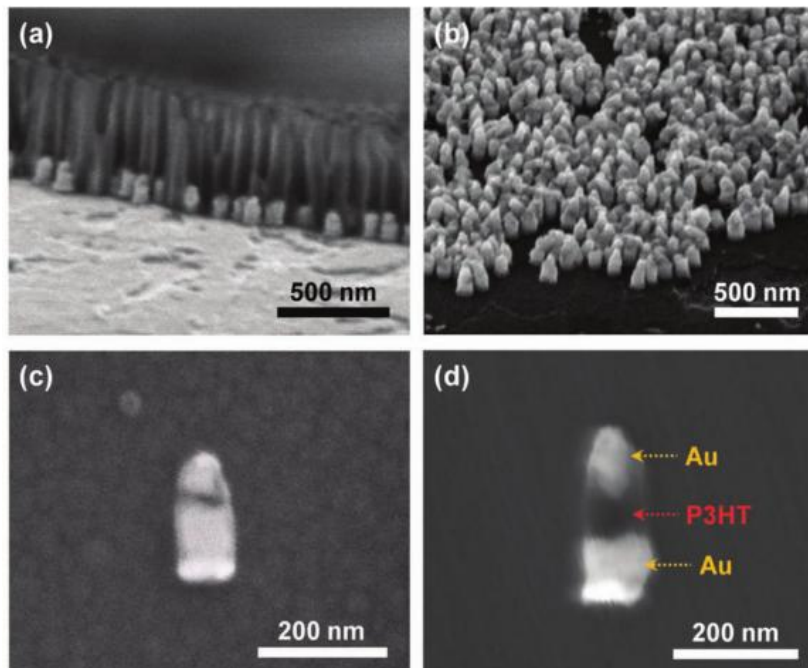


Figure 60. Cross-sectional SEM images of vertically oriented gold–P3HT– gold nanoantenna arrays a) in the alumina template and b) after alumina template removal (acquired at a 45 ° sample tilt). c,d): SEM images of single nanoantennas with different segment lengths (on gold and silicon substrates, respectively) [11].

Habouti et al. used home-made Si-supported anodized alumina thin film templates for the electrodeposition of large area self-standing silver and gold nanorod arrays. They report that both the nanorod spacing and morphology are responsible for the high electromagnetic enhancements at the nanorod tips [12]. Wolfrum et al. described a method which combined an imprint method with template-assisted electrodeposition to fabricate micro- and nanometer-

sized arrays of gold nanopillars at predefined positions on a silicon substrate. Both conventional photolithography and anisotropic silicon etching were used to prepare the stamps used for the imprint procedure. The feature size of the stamp determined the size of the nanopillar arrays [13]. Anandan et al. made use of electrodeposition to fabricate metallic nanopillar array structures and studied their application as electrodes in electrochemical-based biosensors. They report that the nanostructured electrode shows a 7-fold increase in sensitivity when compared with a flat electrode [14].

In this chapter, we describe an entirely bottom-up process route to fabricate arrays of plasmonic nanoantennas through the use of colloidal templating, electrodeposition and finally the transfer of the final gold nanopillars onto a transparent medium, such as polydimethylsiloxane (PDMS). We optically characterized the samples fabricated and compared them with simulated results. We also investigated the effect of stretching on the optical properties of the samples.

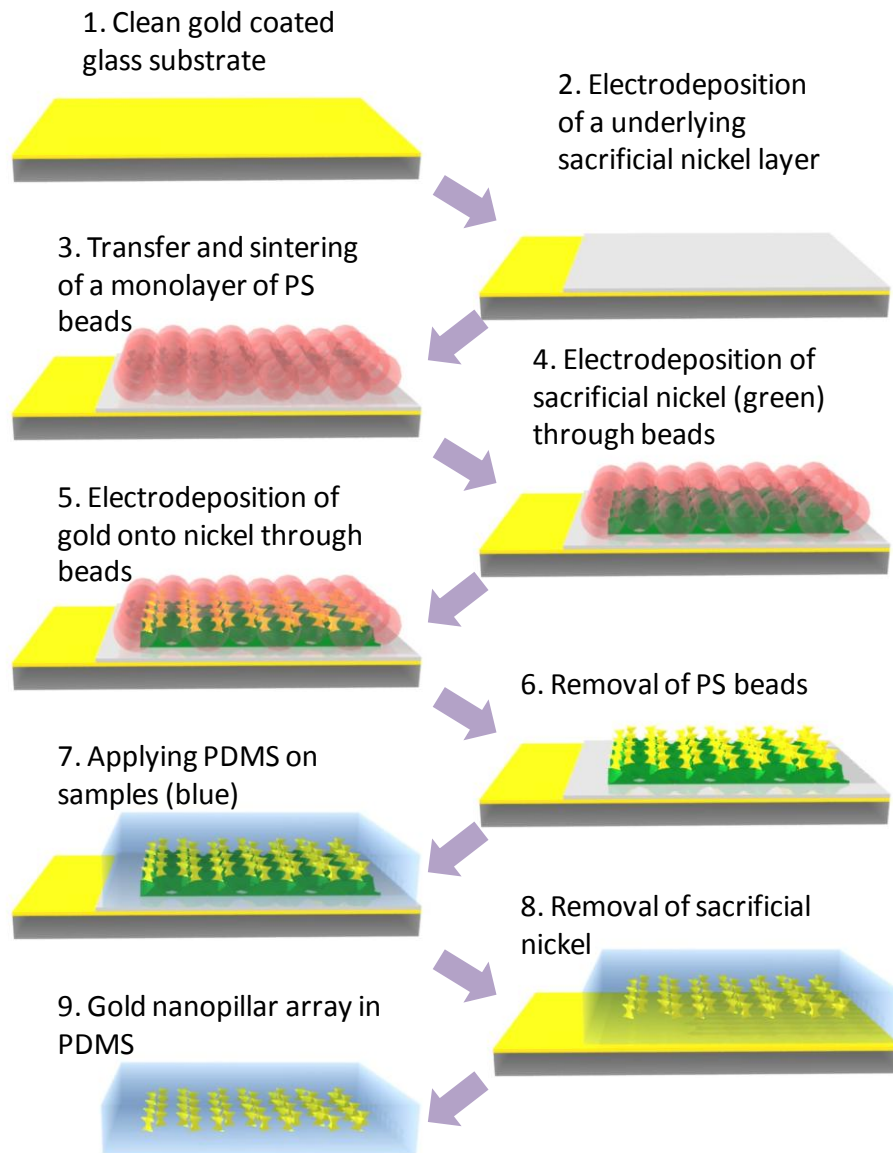


Figure 61. Step-by-step schematic illustration of the entire fabrication process of a 2D array gold nanopillars onto a transparent PDMS substrate.

2. FABRICATION OF NANOPILLAR ARRAYS

2.1 MODIFICATION OF PORE SHAPE AND SIZE OF THE COLLOIDAL CRYSTAL TEMPLATES

In Chapter 2, we have described the method to spread and self-assemble spherical polystyrene (PS) particles on the surface of water and successfully transfer the close packed monolayers onto a clean flat substrate. In this section, the same process was used to deposit the monolayers onto a nickel coated substrate (refer to Annex 2 for details). However, unlike the templates used in Chapters 2 and 3, the PS self-assembled monolayers in this work were modified by a simple sintering process before they could be used as templates for the subsequent steps. Figure 62 shows how the shapes of the PS particles and the pore size between the particles change when they are sintered for different times (from one to a few minutes) at a temperature (110°C) which is just slightly above the glass transition temperature of polystyrene of about 107°C [15].

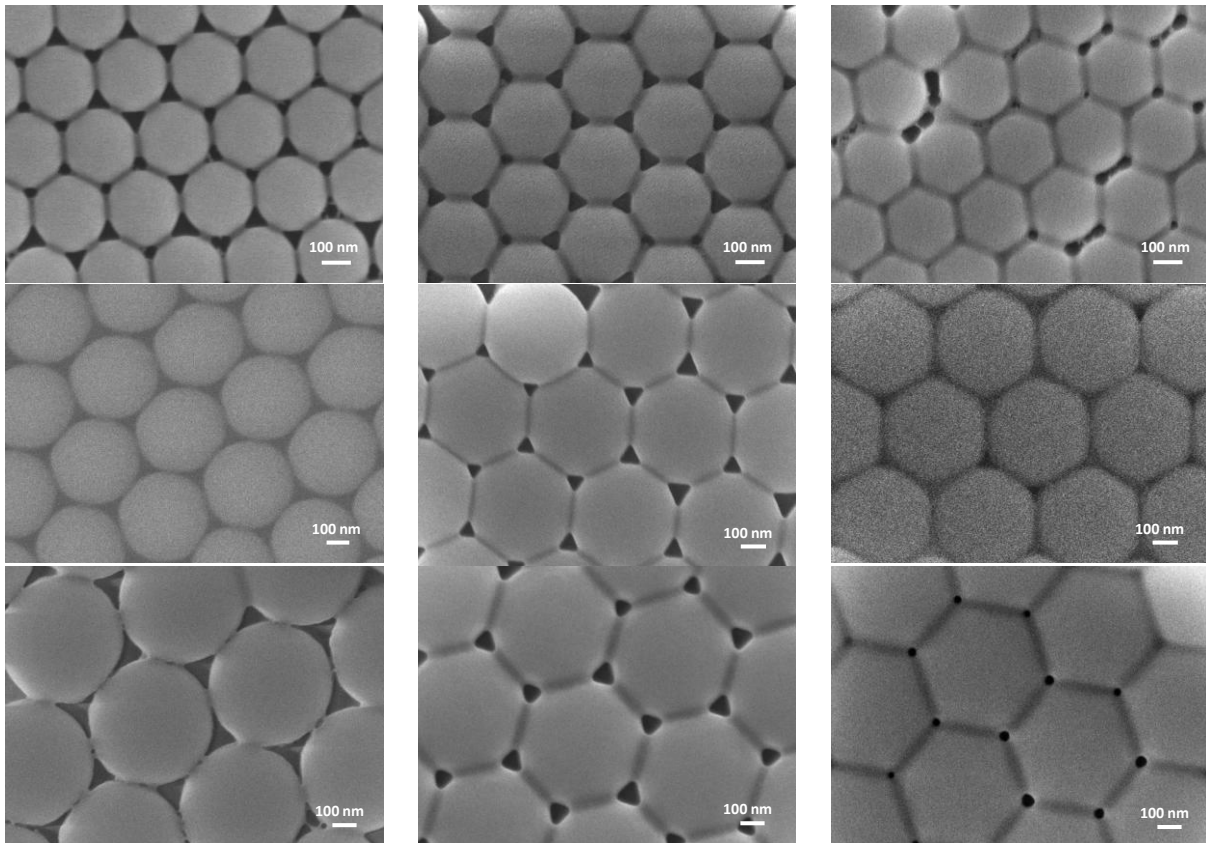


Figure 62 SEM views of a monolayer colloidal crystal. (Top, left to right) 260 nm PS beads after sintering under air in an oven at 110°C for 60 s, 120 s and 180 s. (Middle, left to right) 430 nm PS beads after sintering in an oven at 110°C for 330 s, 390 s and 450 s. (Bottom, left to right) 595 nm PS beads after sintering in an oven at 110°C for 360 s, 420 s and 480 s.

From the SEM images in Figure 62, we can observe that edges of the PS particles in contact with each other begin to fuse together as the monolayers are left in the oven at 110°C over a period of a few minutes. While this happens, the size of the pores are reduced and distinct triangular channels (seen from the top) are formed. Eventually, when the PS particles are exposed to the higher temperatures for a prolonged period of time, the contact area between the PS particles become maximum and all the pores are sealed. This phenomena happens for all the three bead sizes of PS particles tested. For the 260 nm, 430 nm and 595 nm PS particles, it takes approximately about 180 s, 450 s and 480 s respectively for most of the pores to fuse together at a temperature of 110°C. At this point, the PS monolayer cannot be used as a template for the subsequent steps.

Table 8 lists an estimate of the measured length of the edges of the triangular pores formed after sintering at 110°C for various sintering times.

Table 8 Edge length of triangular pores after sintering at 110 °C

PS size (nm)	Sintering time (s)	Triangular pore edge length (nm)	Variation of edge length (nm)
260	120	65	±8
430	390	70	±10
595	420	83	±11

2.2 ELECTRODEPOSITION OF GOLD NANOPILLAR ARRAYS

Hatab et al. demonstrated that a configuration of elevated gold bowtie nanoantenna arrays can show large SERS enhancement factors exceeding 10^{11} [8]. In this part of the work, our initial aim was to fabricate similar gold bowtie arrays using an electrodeposition process through a sintered monolayer of PS particles, and subsequently investigate the SERS effect on the fabricated samples. In Chapter 3, we have demonstrated that gold can be electrodeposited uniformly into a colloidal PS monolayer template. Here, to fabricate nanopillar arrays, the same electrodeposition technique is repeated on a sintered template with a narrower pore channel. Figure 63 shows the SEM side view of the electrodeposition of gold into a non-sintered and sintered monolayer template.

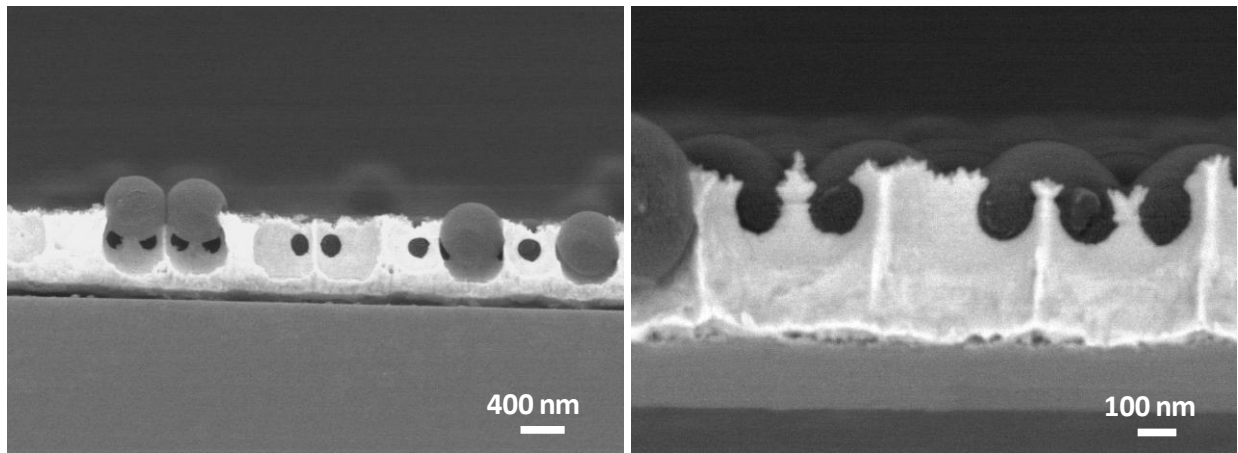


Figure 63. Cross sectional SEM images gold electrodeposited into a (left) non-sintered and (right) sintered monolayer template consisting of 430 nm PS particles (sintering time: 390 s).

From Figure 63, we can clearly see that the morphology of the electrodeposited gold is different due to the shape of pore channels before and after sintering. The prolonged sintering increases the contact area between adjacent PS beads resulting in a narrower pore channel available for the gold to be electrodeposited into. From the SEM image taken of the sintered monolayer template, we can clearly distinguish the pillar-like shapes that are replicated by the gold electrodeposited into it. Our aim here was to investigate if the changing of the distance between the tips of the adjacent gold nanopillars would have any significant effect on the SERS enhancement of the overall structure.

2.2.1 TUNING THE INTER-DISTANCE BETWEEN TRIANGULAR TIPS OF PILLARS BY CONTROLLING THE ELECTRODEPOSITION DEPTH.

By carefully estimating the relationship between deposition time and thickness, we could attempt to engineer the triangular tips of the gold pillars such that they are as close to each other as possible without contact. The interest in trying to reduce the inter-distance between the triangular tips is because of the possible strong electromagnetic field enhancements that could arise from the close proximity of the gold tips and thus to create “hot spots” [8]. Using PS monolayer templates made of 430 nm PS particles (sintered for 390 s), we attempted to demonstrate that it was possible to control inter-distance between the triangular tips by the electrodeposition. Gold was electrodeposited into the PS colloidal template up to a calculated desired thickness. Due to the nature of the shape of the pores, which are wider at the top and bottom but narrower in the middle (due to each pore being surrounded by three sintered pseudo-spherical PS particle), and the fact that the electrodeposited materials will conform exactly to the pore shape, we expected that there would be a particular range of electrodeposition depth that would allow for the triangular tips to be close but not touching. Hence, a series of experiments were made to electrodeposit gold up to a certain desired depth and the inter-distance between the tips was observed. Figure 64 shows the top down SEM images that were obtained for this series of experiments.

It can be observed that as the gold is electrodeposited past the narrowest part of the pore (corresponding to thickness = $0.5D$), the gold triangles start to grow outwards. Due to the shape of the pore channel, as more gold is electrodeposited, the surface area available for electrodeposition increases. It can be seen that when the electrodeposited depth is between $0.57D$ and $0.7D$, the gold triangles are not touching. However, when the depth reaches $0.75D$, we observe that the tips begin to touch and further electrodeposition beyond $0.75D$ is pointless. Table 9 gives the observed inter-distance between the gold tips of the electrodeposited gold.

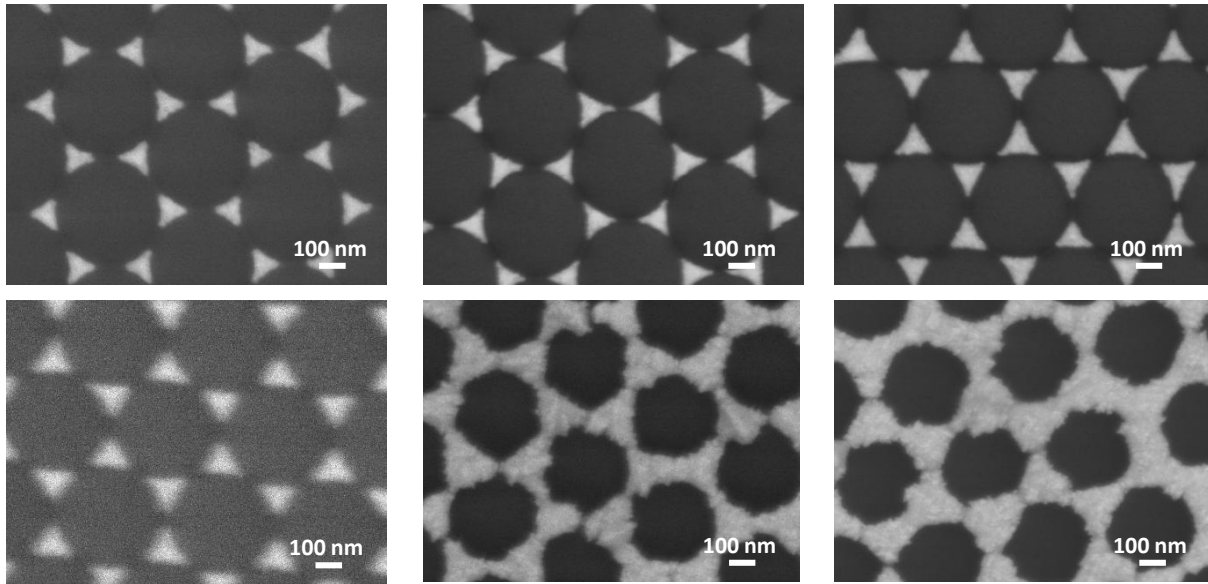


Figure 64. SEM top images showing the interdistance between the tips of the gold triangles at various deposition depths of (top left to right) $0.57D$, $0.62D$, $0.65D$ and (bottom left to right) $0.7D$, $0.75D$ and $0.85D$. D is the diameter of the PS particle used in the colloidal templates ($D=430$ nm).

Table 9. Observed inter-distance between gold triangular tips and respective depth of electrodeposition

Electrodeposited Depth (D)	0.57	0.62	0.65	0.7	0.75	0.85
Inter-distance between the tips (nm)	80 ± 6	67 ± 5	53 ± 5	33 ± 7	3 ± 3	0

By plotting the data in Table 9, we can visualize the relationship between the electrodeposition depth and the final inter-distance between the gold tips. Figure 65 shows the resulting plot of Table 9. From Figure 65, we can see that there is a decrease in the inter-distance between the gold tips as the electrodeposition thickness increases. This trend corresponds to what was observed in the SEM images in Figure 64. Figure 65 allows us to design nanostructures of gold with a desired inter-distance of the triangular tips.

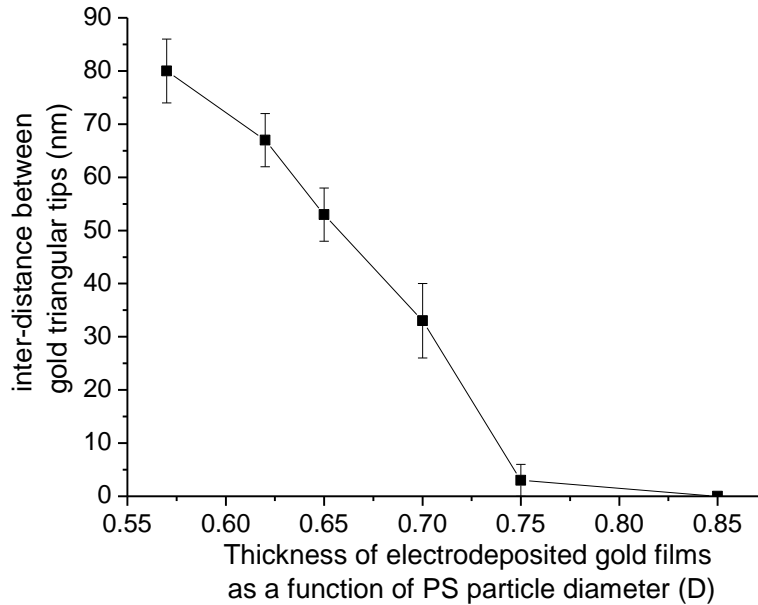


Figure 65. Relationship between electrodeposition thickness and inter-distance between the triangular gold tips.

2.2.2 SURFACE ENHANCED RAMAN SIGNAL (SERS) MEASUREMENTS

Based on the observations on the observations in Figure 65, we fabricated one series of gold nanopillar samples using a template consisting of 430 nm PS particles with a depth of $0.7D$, $0.72D$ and $0.74D$. This set of samples were investigated because we would like to determine if there are any interesting SERS properties that could arise from the decreasing of the inter-distance between the gold tips as we expected that such a decrease between the gold tips could lead to an enhancement of the local electromagnetic field which would correspondingly lead to an enhancement in the SERS effect [8]. The experiments were carried out in collaboration with the “Molecular Spectroscopy” team of the Institute of Molecular Sciences of Bordeaux and the following preliminary results were obtained.

The samples were immersed for 4 hours in a 10 mM ethanolic solution of benzenethiol, and subsequently rinsed copiously with absolute ethanol to remove free benzenethiol molecules that were not adsorbed on gold. Raman measurements were then made under irradiation at 568.2 nm, 647.0 nm and 752.0 nm. No signal could be detected at 568.2 nm, and the signal detected at 752.0 nm was significantly lower than the one obtained at 647.0 nm. The results of the Raman measurements are shown in Figure 66.

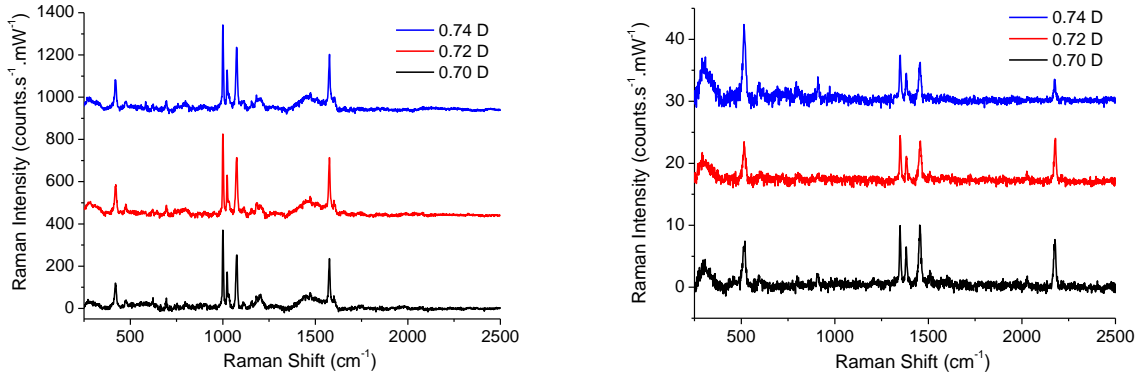


Figure 66. Raman spectra measured for 0.7 D, 0.72 D and 0.74 D gold nanopillar samples under (left) 647.0 and (right) 752.0 nm irradiation after subtracting the background. The blue and red lines are shifted along the y-axis for better viewing clarity.

From the measurements, we observe that no significant differences could be identified between the Raman spectra of the three samples 0.7D, 0.72D and 0.74D. Hence, this suggests that the SERS effect is mainly due to gold nanostructures themselves and, contrary to our expectation, it is not related to the progressive formation of hot spots when decreasing the gap between the triangular tips of the nanostructures. One possible reason for not observing the expected difference in SERS enhancements could be due to the fact that the gold nanopillars were connected to each at the bottom. To address this issue and investigate this possibility, we had to devise a method to ‘disconnect’ the individual pillars in the arrays. The option we derived with was to first electrodeposit a sacrificial metal layer before electrodepositing the gold and then subsequently dissolving the sacrificial layer to disconnect the gold nanopillars.

2.3 ELECTRODEPOSITION OF NICKEL AND GOLD INTO THE COLLOIDAL TEMPLATES

For the initial part of the work, we first investigated the process which relied on the sequential electrodeposition of nickel (as a sacrificial layer) followed by gold, such that the gold electrodeposited inside the porous space are symmetrical and positioned at a depth that is close to half the initial diameter of the PS particles (i.e. in the middle of the monolayer).

There were two major challenges to overcome in this process. First, we had to verify that the sequential electrodeposition of nickel and gold could be done uniformly into the colloidal monolayer template without any significant problems (i.e. the layers have to be smooth and even). Second, we had to devise a method or process that could reliably reproduce our intended nanostructures via electrodeposition of the metals into the monolayer templates.

The first challenge concerned the electrodeposition of nickel and gold into a colloidal monolayer template. We have already demonstrated that we could electrodeposit gold uniformly into the colloidal monolayer templates. However, some initial difficulties arose when we tried to sequentially electrodeposit nickel and then gold into similar monolayer templates. The first problem we encountered was that while we observed the electrodeposition of nickel on the substrate, it did not penetrate the template, but instead remained under the monolayer (Figure 67), resulting in the whole monolayer being pushed up as nickel was electrodeposited on the substrate.

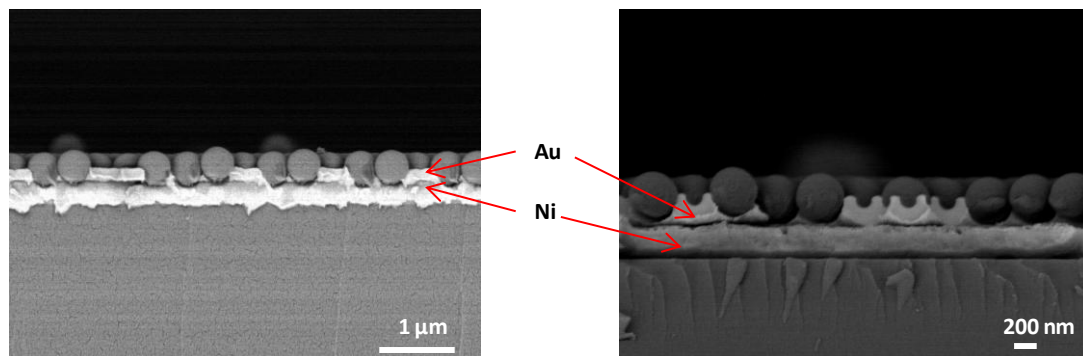


Figure 67. SEM cross sectional images showing two examples of nickel electrodeposited under a monolayer of 430 nm PS beads sintered for one minute

From Figure 67, we can observe that nickel is electrodeposited evenly across the substrate surface but under the polystyrene beads. We can also clearly see that the second layer of gold electrodeposited on the nickel layer does not exhibit the same problem. The gold layer can be clearly observed to penetrate the monolayer of PS beads, which is unlike the nickel layer. After several electrodeposition attempts with various samples, we realized that this problem was unique to samples that were only sintered for short durations of less than one minute. To better understand the reason behind this, we needed to investigate the electrodeposition rates for nickel and gold. Figure 68 shows an example of the electrodeposition curves of nickel and gold separately electrodeposited into two similar substrates with a monolayer of 598 nm PS beads up to a full depth of 1D (diameter of the PS particles).

From Figure 68, we can observe that the time taken for the electrodeposition of nickel and gold up to the same thickness is about 85 s and 460 s respectively. Furthermore, the electrodeposition current measured for nickel is about one order of magnitude larger than that for gold under constant potential electrodeposition conditions. From this, we can infer that the rate of nickel electrodeposition is a lot faster than that for gold, and the corresponding

physical growth of the nickel film is faster than the gold film. Judging from the SEM cross sectional views obtained (Figure 67), we can conclude that the rapid electrodeposition of nickel causes the PS beads to be pushed outwards as nickel is electrodeposited onto the substrate, while the slower electrodeposition rate of gold allows for the gradual electrodeposition of gold into the available pore spaces. Hence, the physical stability (i.e. adhesion) of the PS beads onto the substrate is crucial to determining whether the electrodeposited metal layers grow under or into the colloidal templates. Thus, we concluded that the templates have to be properly sintered before electrodeposition can be carried out. Figure 69 shows two examples of samples that were successfully electrodeposited with nickel and gold into the monolayer templates.

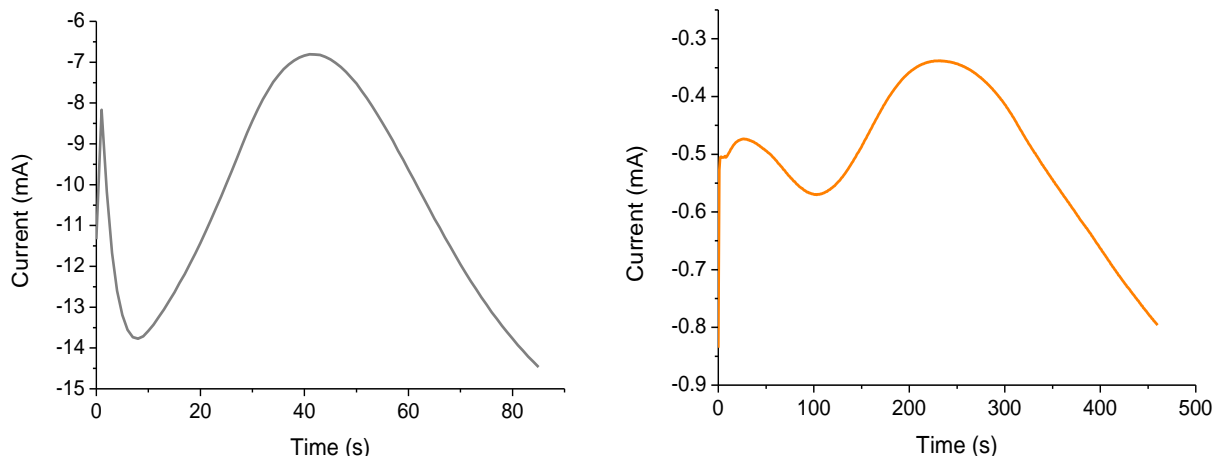


Figure 68. Current-time (I-t) plots of nickel (left) and gold (right) electrodeposited under constant potentials of -1.0 V and -0.7 V respectively into monolayer templates consisting of 598 nm PS beads sintered for 420 s.

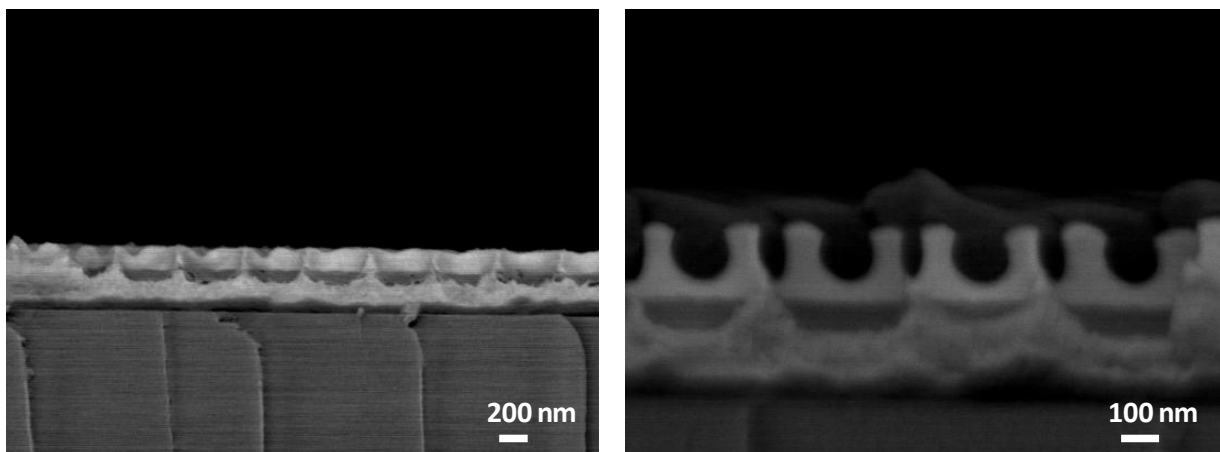


Figure 69. Sequential electrodeposition of nickel and gold into a monolayer of 430 nm PS beads sintered for (left) five minutes and (right) six minutes. PS particles have been removed to allow for better viewing of the electrodeposited metal layers under backscattered SEM.

From Figure 69, it is shown that by properly sintering the beads, we can overcome the problem of electrodepositing nickel under the entire monolayer. Furthermore, the difference in the morphology of the gold nanostructure electrodeposited into templates sintered for different durations can be distinctly observed between the different electrodeposited gold layers. For the electrodeposition of nickel and gold into the 430 nm PS template sintered for five minutes, no ‘pillar’ like structures are observed. On the other hand, for the electrodeposition of nickel and gold into the 430 nm PS template sintered for six minutes, we can readily see the distinct pillar like morphology that results from the shrinking of the pores between the PS monolayer particles. Figure 70 shows SEM images of other samples grown in sintered PS 430 nm monolayer templates after removal of the PS beads.

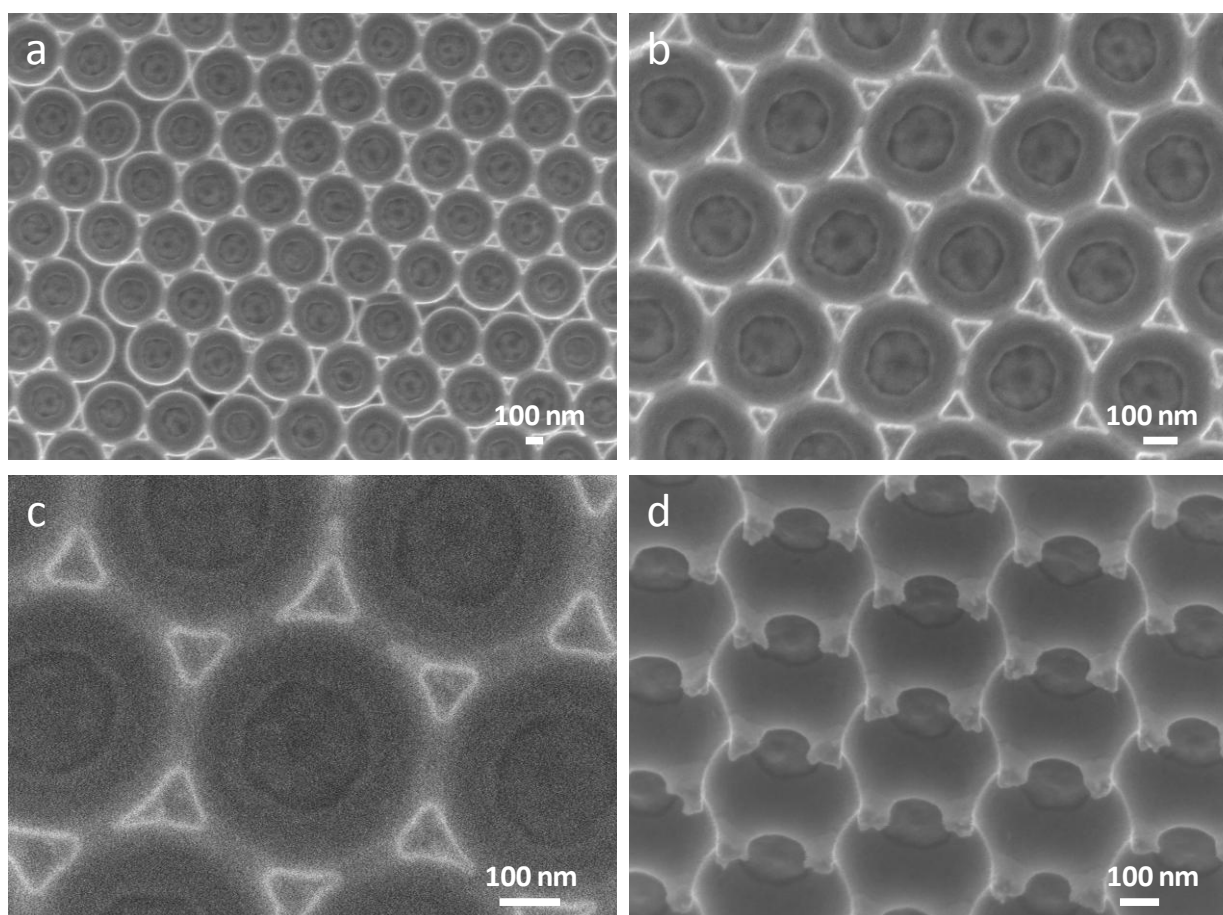


Figure 70. SEM images of nanopillar structures grown from PS 430 nm templates that were sintered for 390 s. (a, b and c) Top down SEM images taken at different magnifications. (d) Tilted (45 °) SEM image.

To better illustrate this point, we electrodeposited a series of samples into 595 nm PS monolayers sintered at different times to visualize the possible resultant morphologies of the

pillars electrodeposited as the pores became narrower with increased sintering time. Figure 71 shows examples the SEM images obtained from these samples.

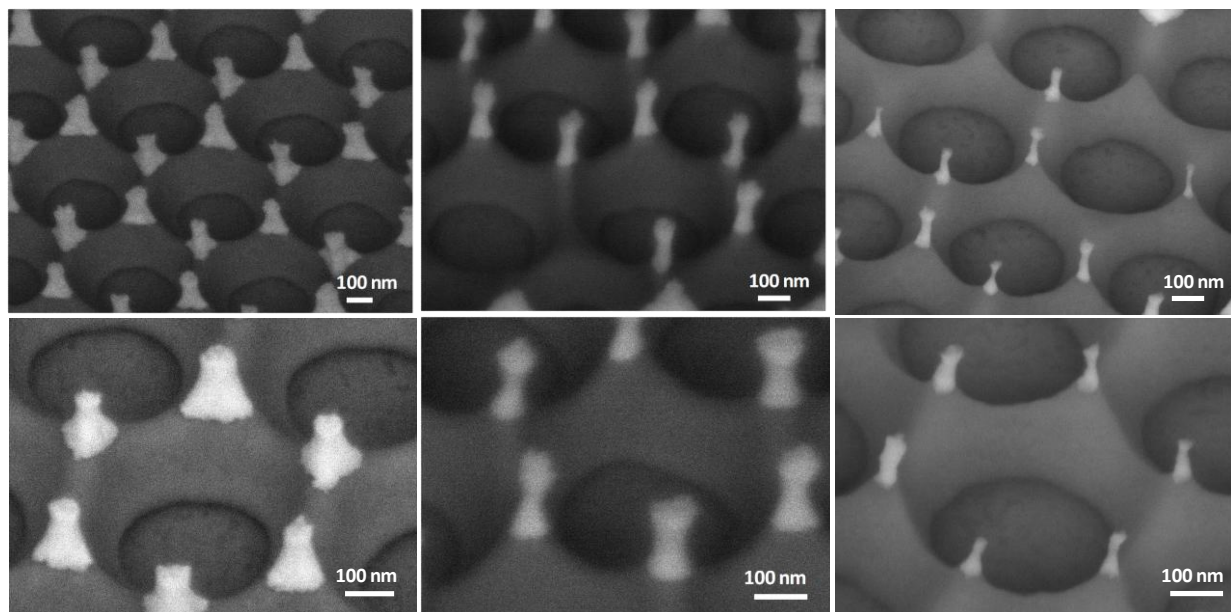


Figure 71. SEM images of electrodeposited gold nanopillar structures obtained by the sequential electrodeposition of nickel and gold into templates consisting of 595 nm PS monolayer templates sintered at 110°C for (left) six, (middle) seven and (right) eight minutes. The top and bottom rows are the samples imaged at low and high magnifications respectively. PS particles have been removed to allow for better viewing of the electrodeposited metal layers under backscattered SEM.

From Figure 71, we can see that nanopillars with a width as small as 15 nm can be obtained by using templates sintered for eight minutes. We can also observe the absence of some gold nanopillars on the surface which corresponds to the fused pores that can be observed on the colloidal template after sintering for eight minutes (refer to Figure 62)

In Chapter 3 we described that there was an observable change in the current profile during electrodeposition of a metal into a colloidal crystal template made of spherical particles. This method works well for the electrodeposition of a single metal layer into the colloidal monolayer template, and we can pretty accurately control the thickness of the electrodeposited metal. For the electrodeposition of more than one layer of metals, a similar approach can be adopted with slight adjustments to adapt to each desired configuration.

In order to have a relatively accurate control of the position of the electrodeposited nickel and gold layers (i.e. thickness of electrodeposited metal layers) in a colloidal monolayer template, it is necessary to first determine the time required to electrodeposit the metal to half the diameter of the particles (i.e. the time required to reach the first minima, minimum current in

absolute value, refer to chapter 3). Knowing the time it takes for the metal to be electrodeposited to a height that is half the diameter of the particles, we can then back calculate the time required for the electrodeposition of the metal to any desired depth. To simplify the calculations, the following assumptions were made:

1. The electrodeposition process was uniform across the surface of the substrate
2. The rate of electrodeposition was constant as each metal grew into the template (i.e. the change in deposition depth varied linearly with time)

From the cross sectional SEM images previously seen in Chapter 3, the first assumption can be considered to hold true as overall the height of the electrodeposited metal was constant across the samples with only slight discrepancies due to the billowing of the gold as it grows through the narrowest part of the pores.

For this part of the work, our aim was to fabricate gold nanopillars that were 1/3, 1/4, 1/5 and 1/6 of the respective PS particle diameters and positioned symmetrically in the middle of the colloidal template. By making use of the two assumptions above, the depth of the metal deposited into the templates during the experiments can be estimated using the simple calculation as listed in Table 10. Figure 72 shows an example of the current profile of nickel and gold as they are electrodeposited sequentially into the colloidal templates at constant potentials of -1.0 V and -0.7V respectively.

Table 10. Estimation of electrodeposition time for each metal

Desired height of gold pillars as a ratio of diameter of particles (D)	Time taken for Ni electrodeposition to reach first current minima (s)	Time taken for Au electrodeposition to reach first current minima (s)	Calculated Ni electrodeposition time (s)	Calculated Au electrodeposition time (s)
1/3	Experimentally determined for each batch, $t_{\frac{1}{2}Ni}$	Experimentally determined for each batch, $t_{\frac{1}{2}Au}$	$\frac{2}{3} \times t_{\frac{1}{2}Ni}$	$\frac{2}{3} \times t_{\frac{1}{2}Au}$
1/4			$\frac{3}{4} \times t_{\frac{1}{2}Ni}$	$\frac{1}{2} \times t_{\frac{1}{2}Au}$
1/5			$\frac{4}{5} \times t_{\frac{1}{2}Ni}$	$\frac{2}{5} \times t_{\frac{1}{2}Au}$
1/6			$\frac{5}{6} \times t_{\frac{1}{2}Ni}$	$\frac{1}{3} \times t_{\frac{1}{2}Au}$

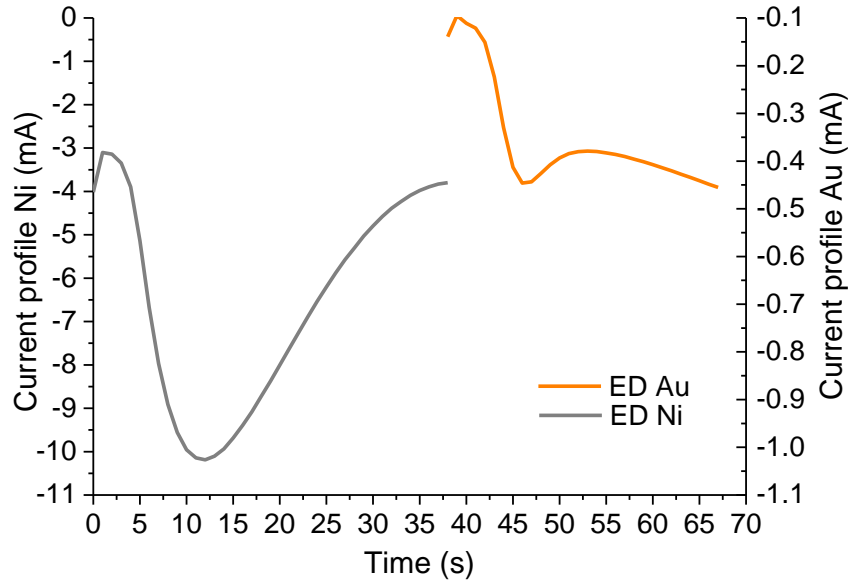


Figure 72. Electrodeposition current profiles of nickel and gold in a monolayer of 430 nm PS beads under constant potential of -1.0 V and -0.7 V respectively vs Ag/AgCl (saturated KCl).

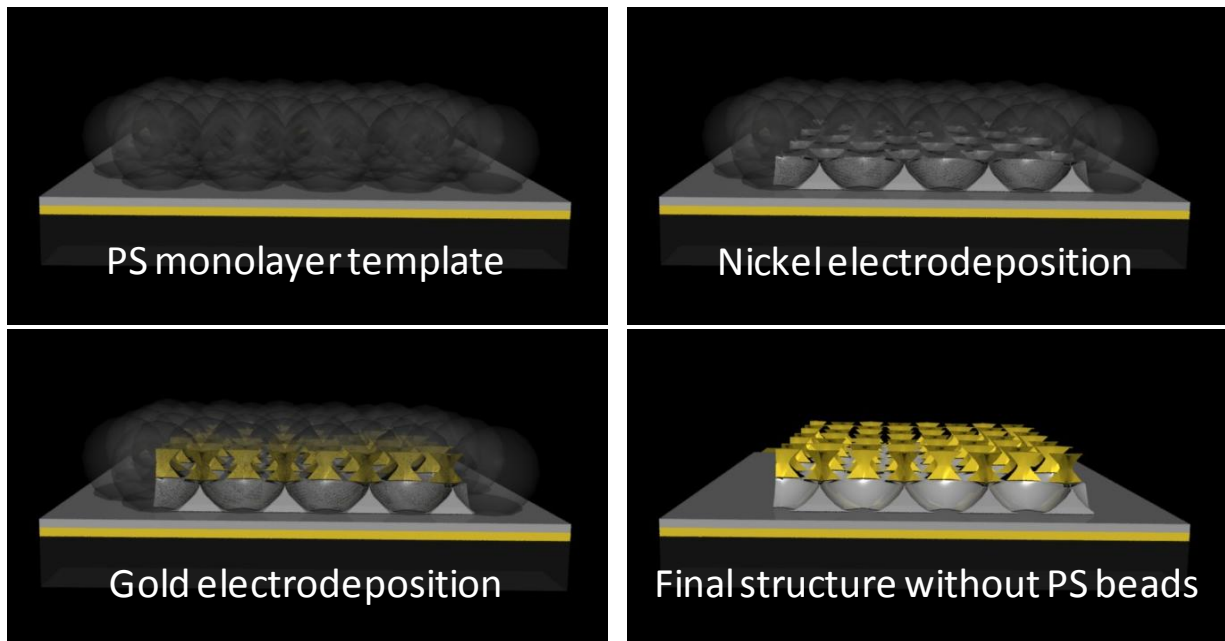


Figure 73. Schematic cross sectional illustration of the sequential electrodeposition of nickel and gold into a monolayer of PS beads to fabricate gold pillars symmetrically positioned in the middle of the PS template.

It can be observed from Figure 72 that the overall shape of the current profile obtained by the sequential electrodeposition of nickel and gold resembles that of the electrodeposition of a single metal into the template (see Figure 1 of chapter 3). By carefully calculating and adjusting the deposition time, it was possible to sequentially electrodeposit nickel and gold

according to our requirements. Figure 73 shows an illustration of the process of sequential electrodeposition of nickel and gold into a PS monolayer template to grow gold pillars of precise heights that are symmetrically positioned at the middle of the beads. Figure 74 shows an example of the cross sectional SEM images obtained of the electrodeposited structures after template removal.

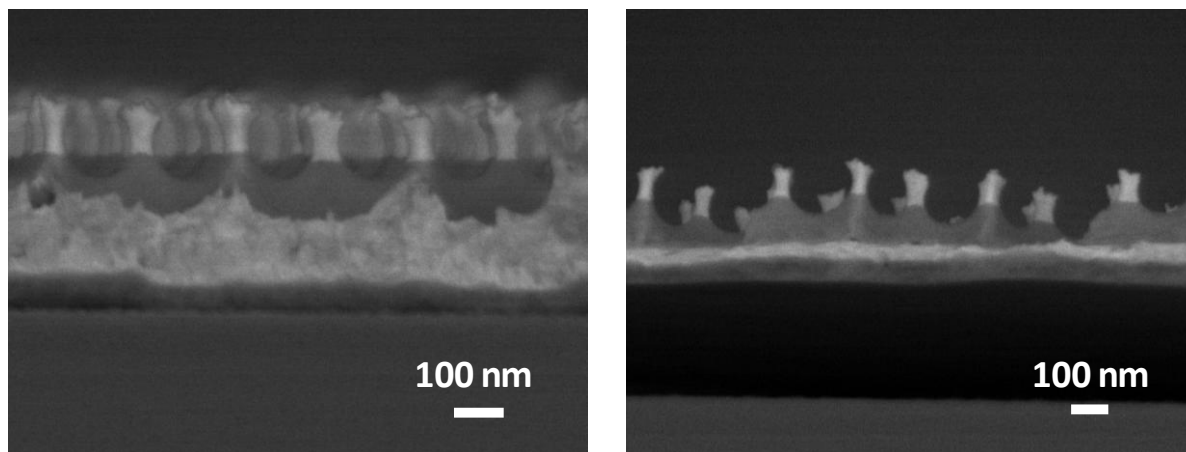


Figure 74. Sample cross sectional backscattered SEM images showing the morphology of the electrodeposited nickel and gold nanostructures after PS monolayer template removal.

It can be seen from Figure 74 that the final electrodeposited structure corresponds very closely with the illustrated sketch in Figure 73. We can observe that the electrodeposited structure is a replicate of the porous sections of the original PS colloidal template. From the backscattered SEM images, we can clearly distinguish the different nickel and gold electrodeposited into the template. It is observed that the electrodeposition is very uniform across the surface of the substrate and that the position of the gold electrodeposited is almost perfectly in the middle (i.e. at a depth of half the diameter of the PS template particles). This proves that it is valid to assume that the rate of electrodeposition of each metal was constant. The position of the gold on nickel gives the gold pillars a roughly symmetrical shape with a very regular spacing between them which conforms to the original arrangement of the pores from the PS colloidal templates. Here, we have shown that the method used to calculate the deposition time (shown in Table 10) is reliable and provides a good estimate and control for this type of electrodeposition process. Figure 75 shows one example of the electrodeposited structures obtained from each size of monolayer template.

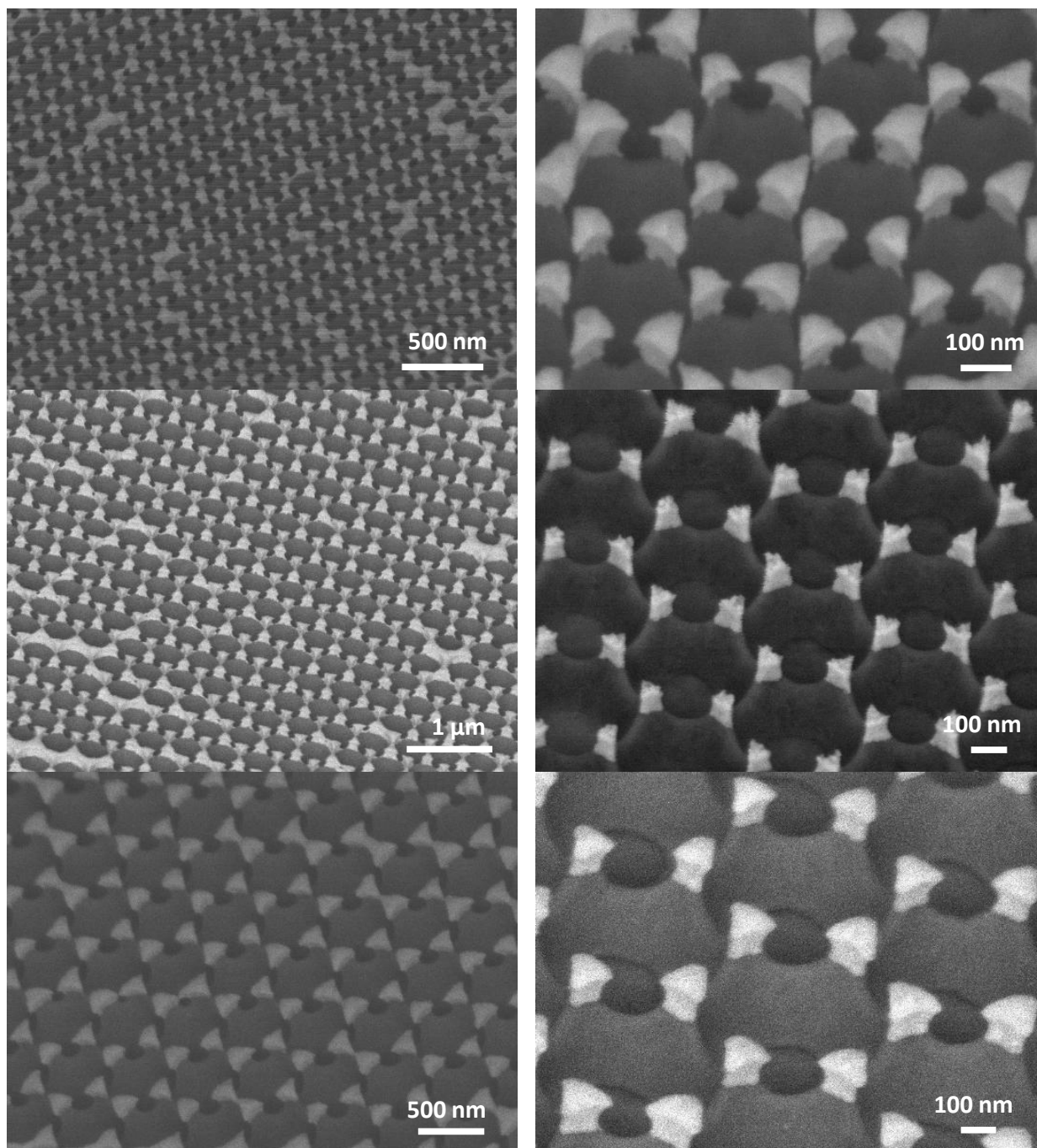


Figure 75. Tilted (45°) backscattered SEM images of the sequential electrodeposition of nickel and gold into (top) 260 nm, (middle) 430 nm and (bottom) 595 nm PS colloidal templates after template removal. (Left) low magnification view of the nanopillars arrays. (Right) High magnification views of the nanopillars arrays. The lighter coloured regions correspond to the electrodeposited gold and the darker regions correspond to the electrodeposited nickel.

From the low magnification SEM images, it can also be observed that there are regions on the electrodeposited samples where the gold pillars appear to be fused together. These regions correspond to the defects/cracks that exist in the original PS colloidal templates. The defects are a result of slight variations in the sizes of the PS particles, which causes tiny gaps to

appear when some PS particles are larger or smaller than the surrounding particles. Furthermore, the transfer of the monolayer of PS beads onto the substrate could result in 'invisible' cracks (to the naked eye). These defects tend to become evident only after the electrodeposition process.

In addition, by using the same calculation principle to estimate the thickness of the nickel and gold layers, it is also possible to adjust the positions of the gold layers along the pore channel to obtain other interesting morphologies. Figure 76 shows some of the different possible positions and morphologies of the electrodeposited gold layer that can be obtained by varying the electrodeposition thickness of the nickel base layer across the different monolayer PS templates.

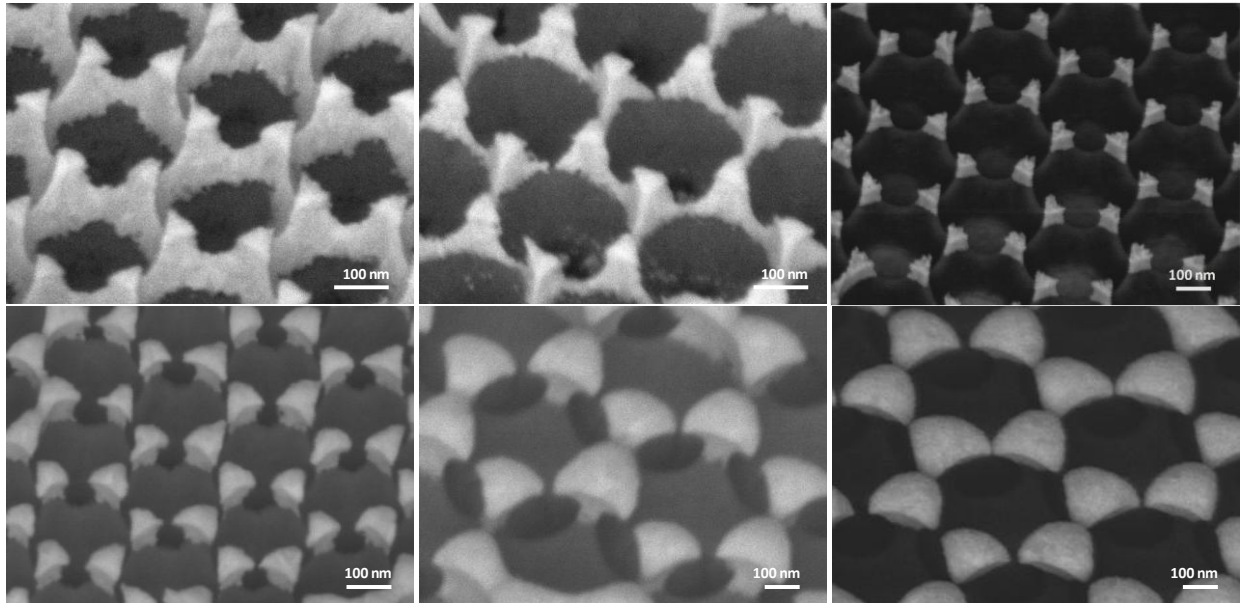


Figure 76. SEM images of images of the electrodeposited gold nanostructures as a result of increasing the electrodeposited nickel base layer. PS particles have been removed to allow for better viewing of the electrodeposited metal layers under backscattered SEM.

2.4 TRANSFER OF ELECTRODEPOSITED GOLD PILLARS ONTO A TRANSPARENT SUBSTRATE

Having successfully electrodeposited symmetrical gold nanopillar arrays onto a sacrificial nickel layer in PS colloidal templates, we now had to remove the gold nanopillar array from the conductive substrate and transfer it into a transparent medium to study their optical properties. We selected polydimethylsiloxane (PDMS) which is a chemically inert and durable transparent material. Briefly, the monomer and curing agent were mixed together and spread over the electrodeposited substrate (after removal of the PS colloidal template). Next,

the polymerization was initiated by heating the mixture and the sacrificial nickel layer was then dissolved in acid to leave the gold pillars embedded in the transparent PDMS matrix. The final PDMS samples with the gold nanopillars embedded are not only transparent and flexible, they also exhibit a good adhesion to smooth surfaces. The experimental details of this transfer step can be found in Annex 5. Figure 77 shows a photograph of an array of gold nanopillars before and after transferring onto PDMS, as well as the corresponding SEM image of the array in PDMS.

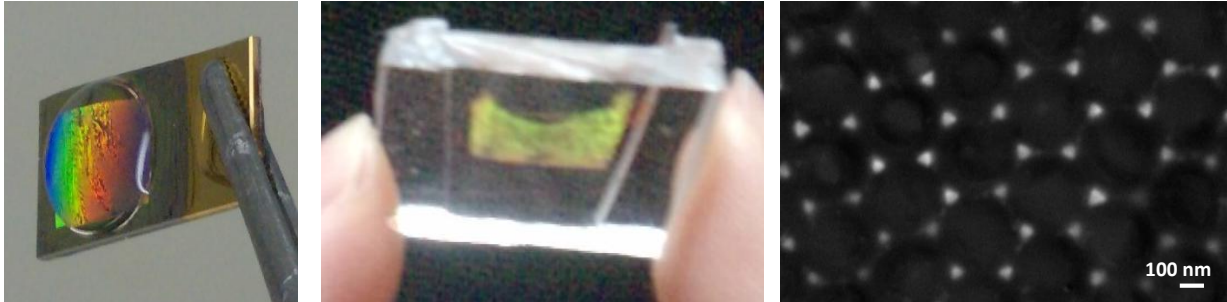


Figure 77. Photograph of an array of gold nanopillars (left) on a Ni coated gold substrate after electrodeposition, and (middle) after being transferred onto PDMS. (Right) SEM image of the gold nanopillar array in PDMS.

These transparent samples were then optically characterized. A series of corresponding optical simulations were also calculated using the same MEEP program as described in Chapter 3, with corresponding changes to the material parameters as described in the following sections. Table 11 shows the list of the samples prepared by electrodeposition before being transferred onto PDMS.

Table 11. List of electrodeposited samples transferred into PDMS

Particle size (nm)	260				430				595			
Ni electrodeposited depth (D) <i>First layer</i>	1/3	3/8	2/5	5/12	1/3	3/8	2/5	5/12	1/3	3/8	2/5	5/12
Au electrodeposited depth (D) <i>Second layer</i>	1/3	1/4	1/5	1/6	1/3	1/4	1/5	1/6	1/3	1/4	1/5	1/6

The measured transmission spectra obtained from the gold nanopillar arrays embedded in PDMS are shown in Figure 78, Figure 79 and Figure 80. In addition, the corresponding simulated spectra of these arrays are also represented next to the experimental spectra.

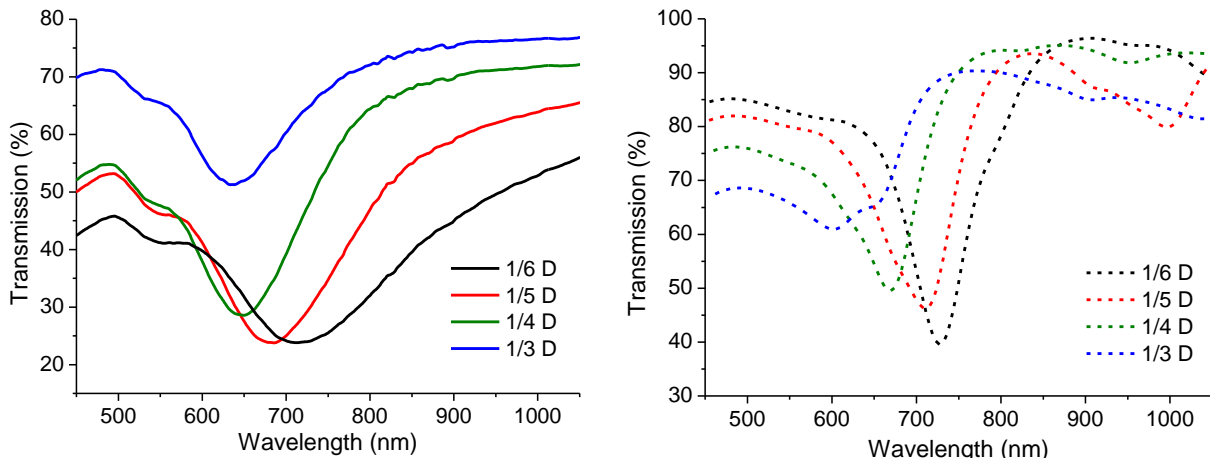


Figure 78. Transmission spectra of gold nanopillar array with different heights (fabricated from 260 nm PS colloidal template) embedded in PDMS. Experimental measurements (left) and simulated data (right).

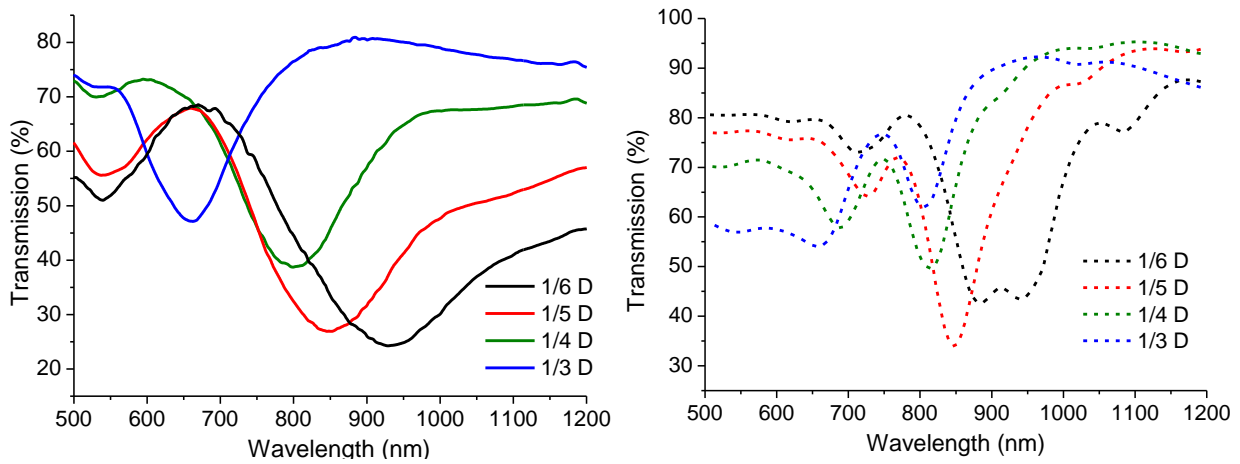


Figure 79. Transmission spectra of gold nanopillar array with different heights (fabricated from 430 nm PS colloidal template) embedded in PDMS. Experimental measurements (left) and simulated data (right).

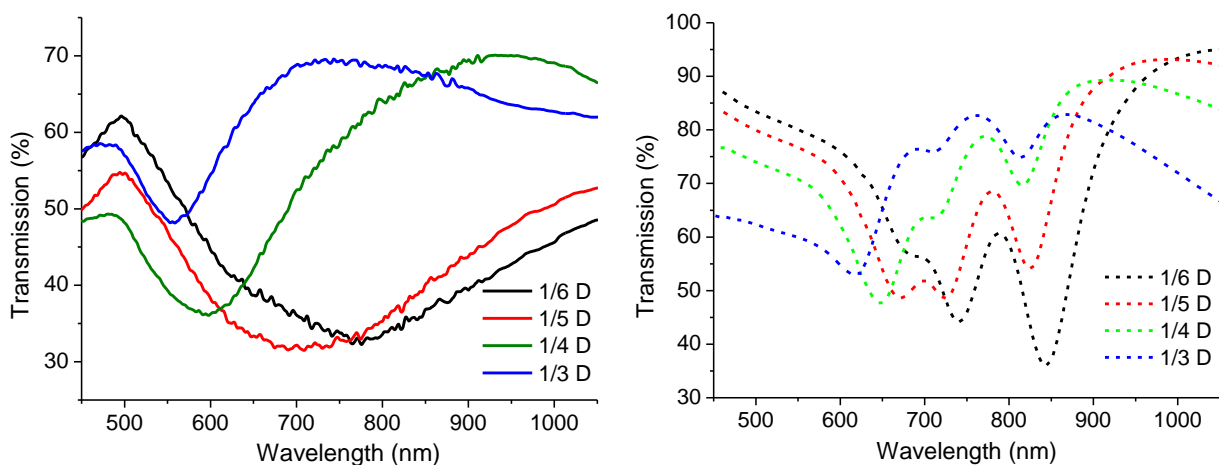


Figure 80. Transmission spectra of gold nanopillar array with different heights (fabricated from 595 nm PS colloidal template) embedded in PDMS. Experimental measurements (left) and simulated data (right).

From the measured experimental data of the gold nanopillars in PDMS, we can observe that for each particle size, as the gold nanopillars become longer, there is a blue shift in the main absorption peaks. For gold nanopillars fabricated from the PS 260 nm templates, the corresponding absorption peaks for the 1/6 D, 1/5 D, 1/4 D and 1/3 D samples are around 715 nm, 680 nm, 647 nm and 635 nm respectively. For gold nanopillars fabricated from the PS 430 nm templates, the corresponding absorption peaks for the 1/6 D, 1/5 D, 1/4 D and 1/3 D samples are around 930 nm, 846 nm, 799 nm and 662 nm respectively. For gold nanopillars fabricated from the PS 595 nm templates, the corresponding absorption peaks for the 1/6 D, 1/5 D, 1/4 D and 1/3 D samples are around 775 nm, 692 nm, 597 nm and 557 nm respectively.

We had initially expected to observe a red shift in the peak positions as the spacing between the gold nanopillars increased as a result of using templates made of larger PS beads, which is a typical observation. However, this was not observed in the case of our fabricated samples. While the general positions of the peaks red shifted as size of the template particles increased from 260 nm to 430 nm, the opposite trend was observed when the size of the template particles increased further from 430 nm to 595 nm. In order to explain our measured data, we looked towards the numerical simulations of the optical properties of our structures.

There were three main parameters investigated using the simulations, which were the size of the template particles, the height of the gold nanopillars (as a function of the diameter, D, of the PS particles) and the refractive index of the space between the gold nanopillars (i.e. the filling fraction of the voids left after removing the PS particles by PDMS). The size of the beads used in the simulations were the same size as the experiments, the length of the gold nanopillars were set in the same ratio as the experiments (i.e. 1/6 D, 1/5 D, 1/4 D and 1/3 D). The refractive index of the medium surrounding the gold nanopillar arrays were set at $n = 1.0$, 1.1, 1.2, 1.3 and 1.4, with $n=1.0$ corresponding to having no PDMS in the space around the gold nanopillars (filling fraction=0) and with $n=1.4$ corresponding to the situation where the space around the nanopillars is fully filled with PDMS (filling fraction=1).

By comparing the various sets of simulated data for each PS particle size consisting of the four ratios of gold nanopillar length with a set refractive index, n , of between 1.0 and 1.4, we found the best fit simulated set of spectra that matched very closely to our experimental measured results (shown in Figure 78, Figure 79 and Figure 80). It was determined that the main parameter that affected the absorption peak position was due to the refractive index of the surrounding medium. Figure 81 below illustrates an example of the effect of the refractive

index on the transmission spectra for one length ($1/5 D$) of gold nanopillar array fabricated from one size of PS beads (430 nm).

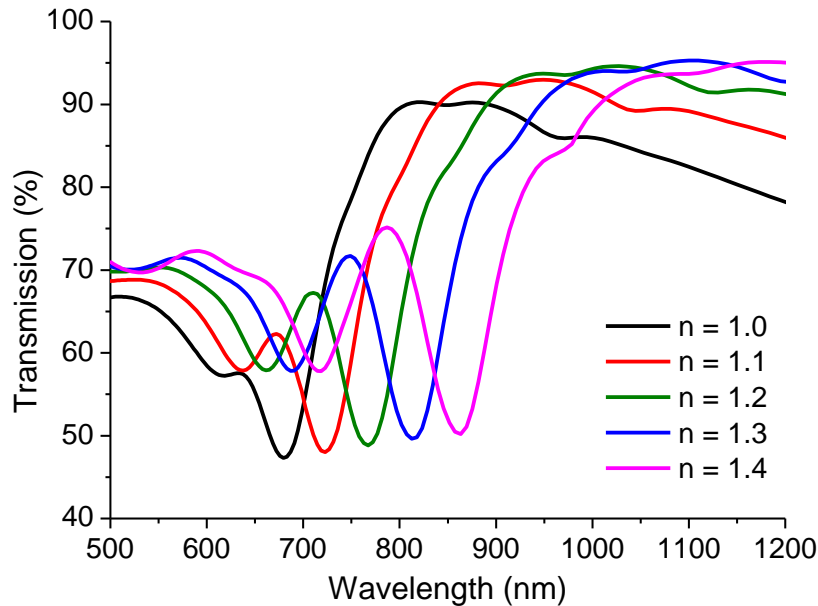


Figure 81. Simulated transmission spectra of gold nanopillar arrays fabricated from 430 nm PS monolayer template for a height of $1/5 D$ and for five different refractive indices of the surrounding medium.

From Figure 81, we observe that as the refractive index increases from 1.0 to 1.4, there is a significant red shift of the absorption peak from 679 nm to 863 nm. Based on the comparison of the simulated data with the experimental results, we concluded that for the gold nanopillars fabricated from 260 nm, 430 nm and 595 nm PS templates, the best fit simulations were obtained when the refractive index n was 1.0, 1.3 and 1.0 respectively. This finding suggests that a plausible explanation to explain the absorption peak position of the various fabricated PDMS samples is that the samples fabricated using the 430 nm PS monolayer templates were well filled with PDMS after bead removal, while 260 nm and 595 nm PS beads were not filled properly with PDMS after bead removal. Thus, this good or bad filling of the PDMS into the voids left after bead removal affects the effective refractive index of the material and also the resulting optical transmission spectra as well.

2.5 STRETCHING OF THE GOLD NANOPILLAR ARRAYS EMBEDDED IN PDMS

With the gold nanopillar arrays transferred into a PDMS layer, we wanted to investigate the effect of stress on the optical properties of the PDMS samples. Millyard et al. had previously reported that close packed monolayers of 20nm gold nanoparticles on elastic substrates exhibit active and reversible tuning of their plasmonic properties, due to plasmonic coupling effects at nanometer scale distances, which could potentially be used for developments of stretchable optical color filters and molecular sensors [16]. In light of this work, we performed a series of experiments to determine if there were any notable plasmonic effects that could be measured by stretching out PDMS samples containing the gold nanopillar arrays. For this investigation, one PDMS sample fabricated from PS particles of each size was selected and tested (i.e. the PDMS samples containing gold nanopillars that had lengths of $1/5D$). The PDMS samples were held firmly at two opposing ends using a homemade device and very slowly stretched in one direction. The samples were stretched for up to a maximum of 8 mm in one direction. The experimental optical transmission spectra of the stretched PDMS samples are shown in Figure 82, Figure 83 and Figure 84.

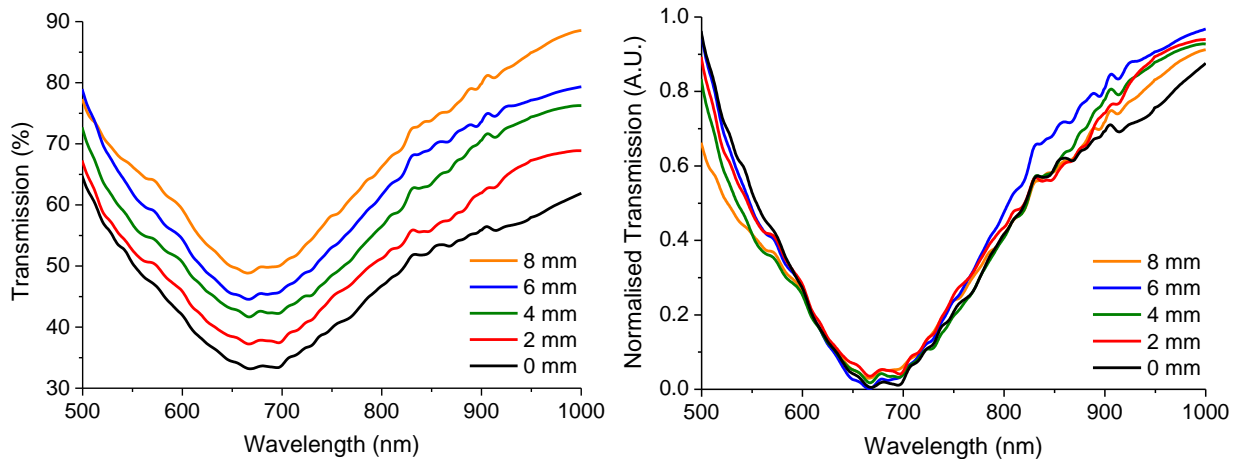


Figure 82. Transmission spectra of a PDMS sample containing a gold nanopillar array made from PS 260 nm particles under various stretching conditions.

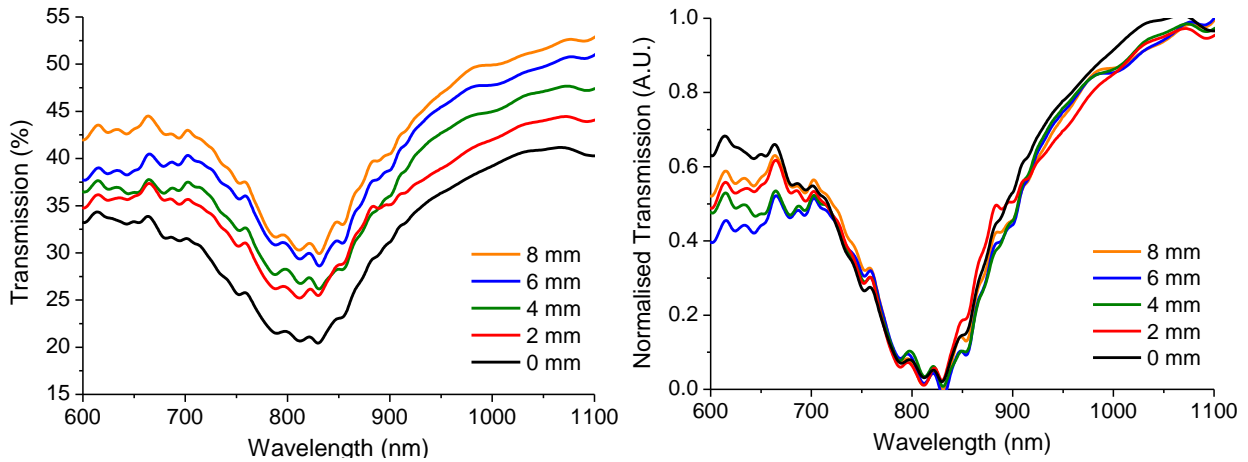


Figure 83. Transmission spectra of a PDMS sample containing a gold nanopillar array made from PS 430 nm particles under various stretching conditions.

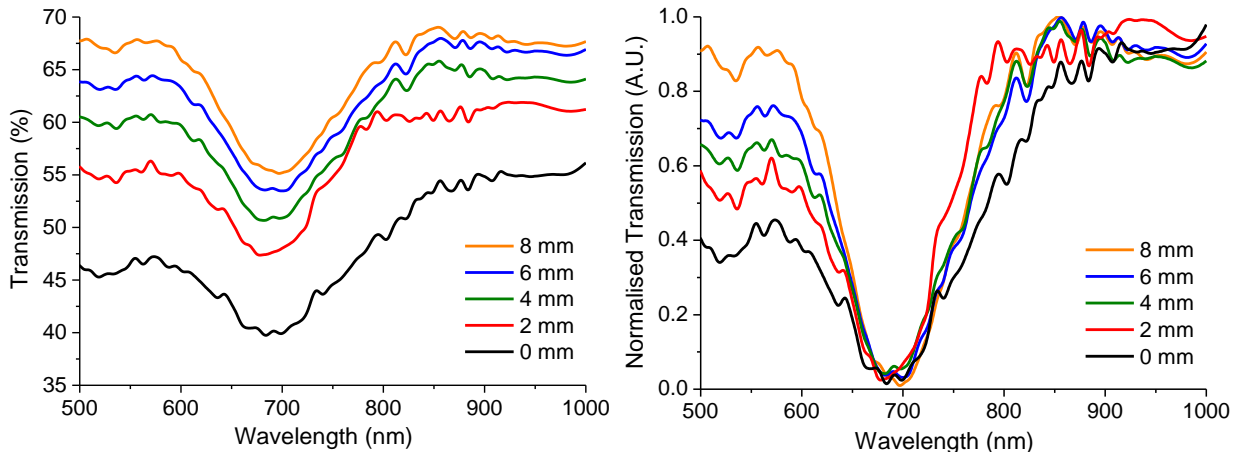


Figure 84. Transmission spectra of a PDMS sample containing a gold nanopillar array made from PS 595 nm particles under various stretching conditions.

From the measured transmission spectra of the samples, we can see that transmission increases as the stretching increases, probably due to the thinning of the PDMS samples as they are stretched. Nevertheless, from the raw measurements, it is hard to directly conclude if there were any shifts in the peak position. Hence, we normalized the data and the results show that there is no noticeable shift in the position of the absorption peaks that were observable by stretching the samples. This result indicates that the original spacing between the gold nanopillars were probably not sufficiently close enough to allow any plasmonic coupling between the nanopillars.

3. CONCLUSION

In this chapter, we set out to design an entirely bottom-up route to fabricate 2D arrays of plasmonic nanoantennas made of gold. We have investigated several different parameters to tune the template and control the shape of the gold nanopillars fabricated. The use of a simple sintering process has been shown to be effective in enabling us to adjust the pore dimensions of the colloidal template, regardless of the constituent PS particle size. We demonstrated that electrodeposition can be performed homogeneously across the sample surface and that it is possible to sequentially electrodeposit two different metals on top of one another and adjust their deposition depth. We showed it is possible to control to a certain extent, the distance between the triangular tips of the adjacent gold nanopillars, but this inter-tip distance has no significant effect on the SERS enhancement, which is most likely due to the gold nanostructures themselves.

By utilizing a sacrificial base metal layer of nickel, we have succeeded in transferring the gold nanopillars onto a transparent and flexible medium which is PDMS. Optical characterizations of the fabricated PDMS samples show that they exhibit absorption peaks that vary with the nanopillar distribution as well as the length of the nanopillars. Preliminary measurements taken after stretching the PDMS samples show that there is no noticeable shift in the peak positions as the PDMS samples are stretched. However, more measurements should be done with new samples to validate this further, and a better experimental set up should be developed for this purpose.

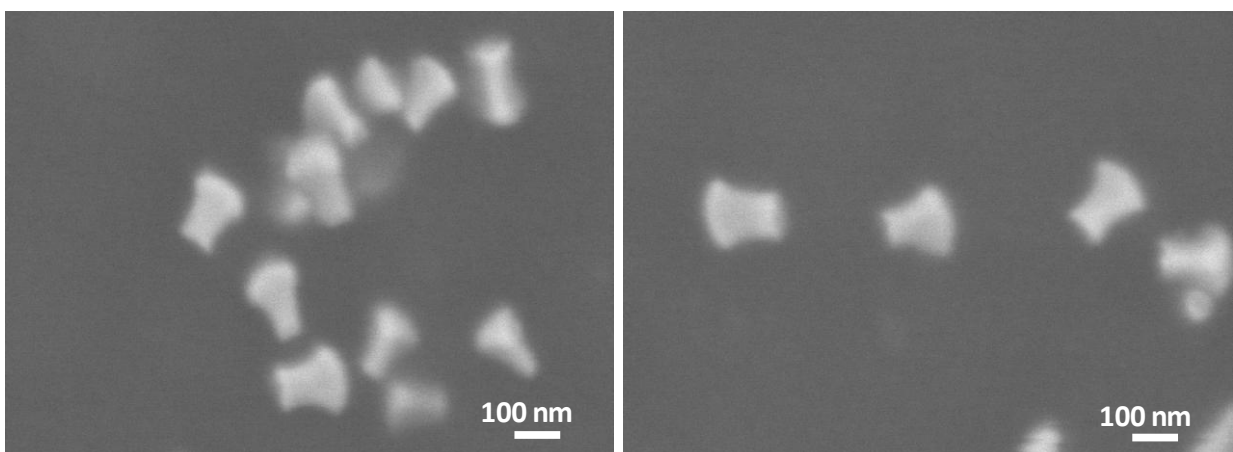


Figure 85. Examples of SEM images of gold nanopillars obtained after PS (595 nm) template removal and dissolution of the sacrificial nickel layer.

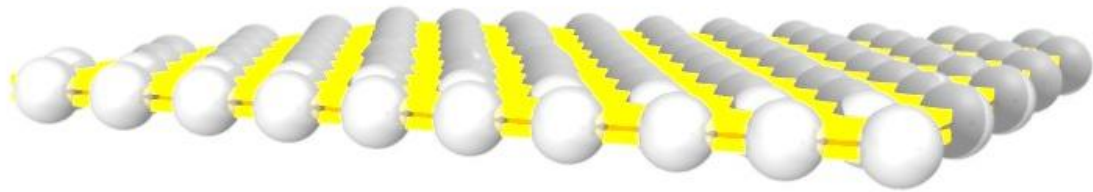
Further experiments to measure the SERS enhancement effect of the disconnected nanopillar arrays will be performed in the near future. In addition, possible future work can be done by studying the optical properties of the individual gold nanopillars (Figure 85) that can be obtained after the dissolution of the sacrificial nickel layer.

REFERENCES

- [1] P. R. West, S. Ishii, G. V. Naik, N. K. Emani, V. M. Shalaev, and A. Boltasseva, “Searching for better plasmonic materials,” *Laser Photon. Rev.*, vol. 4, no. 6, pp. 795–808, Nov. 2010.
- [2] T. E. Graedel, “Corrosion mechanisms for silver exposed to the atmosphere,” *J. Electrochem. Soc.*, vol. 139, no. 7, pp. 1963–1970, 1992.
- [3] J. Homola, “Present and future of surface plasmon resonance biosensors.,” *Anal. Bioanal. Chem.*, vol. 377, no. 3, pp. 528–39, Oct. 2003.
- [4] H. Gao, J. Henzie, M. H. Lee, and T. W. Odom, “Screening plasmonic materials using pyramidal gratings,” *Proc. Natl. Acad. Sci. U. S. A.*, vol. 105, no. 51, pp. 20146–51, Dec. 2008.
- [5] N. C. Lindquist, P. Nagpal, K. M. McPeak, D. J. Norris, and S.-H. Oh, “Engineering metallic nanostructures for plasmonics and nanophotonics.,” *Reports Prog. Phys.*, vol. 75, no. 3, p. 036501, Mar. 2012.
- [6] S. Tsai, M. Ballarotto, D. B. Romero, W. N. Herman, H. Kan, and R. J. Phaneuf, “Effect of gold nanopillar arrays on the absorption spectrum of a bulk heterojunction organic solar cell,” vol. 18, no. S4, pp. 416–420, 2010.
- [7] K. Nakamoto, R. Kurita, and O. Niwa, “Arrays of metallic nanopillars in holes for plasmonic devices,” pp. 1786–1788, 2011.
- [8] N. A. Hatab, C.-H. Hsueh, A. L. Gaddis, S. T. Retterer, J.-H. Li, G. Eres, Z. Zhang, and B. Gu, “Free-standing optical gold bowtie nanoantenna with variable gap size for enhanced Raman spectroscopy.,” *Nano Lett.*, vol. 8, pp. 4952–4955, Nov. 2010.
- [9] M. Chirumamilla, A. Toma, A. Gopalakrishnan, G. Das, R. P. Zaccaria, R. Krahné, E. Rondanina, M. Leoncini, C. Liberale, F. De Angelis, and E. Di Fabrizio, “3D nanostar dimers with a sub-10-nm gap for single-/few-molecule surface-enhanced raman scattering.,” *Adv. Mater.*, vol. 26, no. 15, pp. 2353–8, Apr. 2014.
- [10] A. Cattoni, P. Ghenuche, A.-M. Haghiri-Gosnet, D. Decanini, J. Chen, J.-L. Pelouard, and S. Collin, “ $\lambda/1000$ Plasmonic nanocavities for biosensing fabricated by soft UV nanoimprint lithography,” *Nano Lett.*, no. 11, pp. 3557–3563, Apr. 2011.
- [11] D. M. O’Carroll, J. S. Fakonas, D. M. Callahan, M. Schierhorn, and H. A. Atwater, “Metal-polymer-metal split-dipole nanoantennas.,” *Adv. Mater.*, vol. 24, no. 23, pp. OP136–42, Jun. 2012.
- [12] S. Habouti, M. Mátéfi-Tempfli, C.-H. Solterbeck, M. Es-Souni, S. Mátéfi-Tempfli, and M. Es-Souni, “Self-standing corrugated Ag and Au-nanorods for plasmonic applications,” *J. Mater. Chem.*, vol. 21, no. 17, p. 6269, 2011.
- [13] B. Wolfrum, Y. Mourzina, D. Mayer, D. Schwaab, and A. Offenhäusser, “Fabrication of large-scale patterned gold- nanopillar arrays on a silicon substrate using imprinted porous alumina templates,” *Small*, pp. 1256–1260, 2006.
- [14] V. Anandan and G. Zhang, “Nanopillar array structures for enhancing biosensing performance,” vol. 1, no. 1, pp. 73–79, 2006.

- [15] J. Rieger, “The glass transition temperature of polystyrene,” *J. Therm. Anal.*, vol. 46, pp. 965–972, 1996.
- [16] M. G. Millyard, F. Min Huang, R. White, E. Spigone, J. Kivioja, and J. J. Baumberg, “Stretch-induced plasmonic anisotropy of self-assembled gold nanoparticle mats,” *Appl. Phys. Lett.*, vol. 100, no. 7, p. 073101, 2012.

**CHAPTER 5: BOTTOM-UP DESIGN OF FISHNET
METAMATERIALS BY COLLOIDAL LITHOGRAPHY**



1. INTRODUCTION

Negative index materials (NIM) are materials that exhibit a negative index. To date, there are no known natural materials that exhibit the property of negative refraction. Hence, all known negative index materials are currently artificially engineered and manmade, and are otherwise known as metamaterials. Figure 86 illustrates how light travels through a material with a negative refractive index.

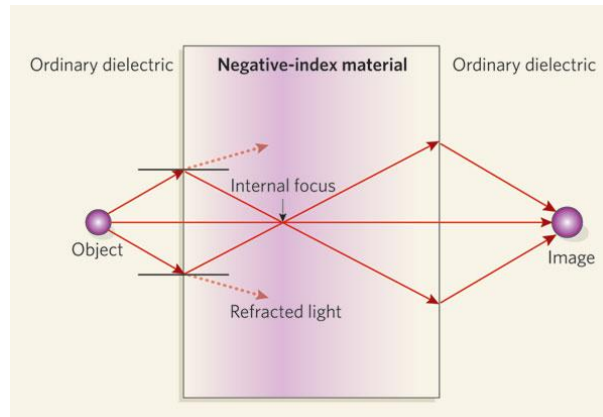


Figure 86. Light waves (arrows) from an external source will, at the interface between two materials of different refractive indices, bend towards or away from the normal to the interface (dotted arrows) but never beyond the normal. This limitation is overcome if one of the materials has a negative refractive index. The same thing happens at the second interface of the material, so it acts as a perfect lens, reproducing an image of an object. A conventional lens, which requires a curved surface, can never produce a perfect image because it will always fail to refocus the light that comes from the object in the form of decaying (evanescent) waves. Thus the image will not contain the information about the object carried by these waves [1].

The idea that a material can simultaneously have a negative permittivity and permeability leading to a negative refractive index was first proposed by Veselago in 1968 [2]. Slightly more than three decades later in 1999, Pendry et al. postulated that by creating ‘artificial atoms’ (i.e. artificially engineered, subwavelength structures), it was possible to construct artificial materials to exhibit an effective permittivity and permeability [3]. Shortly after, in 2001, Shelby et al. experimentally confirmed for the first time that a material can exhibit negative refractive index in the microwave regime by creating a composite material consisting of a two-dimensional array of repeated unit cells of copper strips and split ring resonators on interlocking strips of standard circuit board material [4]. Today, the development of metamaterials, is ranked as one of the top ten advances in materials science [5].

Negative index metamaterials (NIMs) are artificially tailored composites of dielectrics and noble metals (e.g. gold or silver). While NIMs have been demonstrated in the microwave

regime [4], it has been a challenge to design and engineer NIMs for optical frequencies. A commonly studied geometry in the visible and near-infrared (NIR) wavelength range is the fishnet structure which consists of a stack of metal-insulator-metal layers perforated by an array of holes. We can imagine a fishnet structure as a combination of two parts that allows the engineering of the permeability and permittivity separately [6]. The first part of the fishnet metamaterial are thick metallic strips oriented along the direction of magnetic field of the incoming light which are separated by a dielectric layer [Figure 87(a)]. This structure functions as an inductor and capacitor resonator wherein antisymmetric currents are created in the metal strips, giving rise to an induced magnetic polarization in the structure [Figure 87(e)]. This provides a magnetic response, or artificial permeability, that can achieve negative values near resonance. The second part consists of thin metallic wires oriented in the direction of the electric field of the incoming light [Figure 87(b)]. These wires function as a diluted metal with decreased plasma frequency, providing a negative effective permittivity that can be engineered separately from the permeability. The fishnet metamaterial is formed when both parts are combined and the negative permeability and permittivity can be engineered at a particular wavelength [Figure 87(c) and (d)].

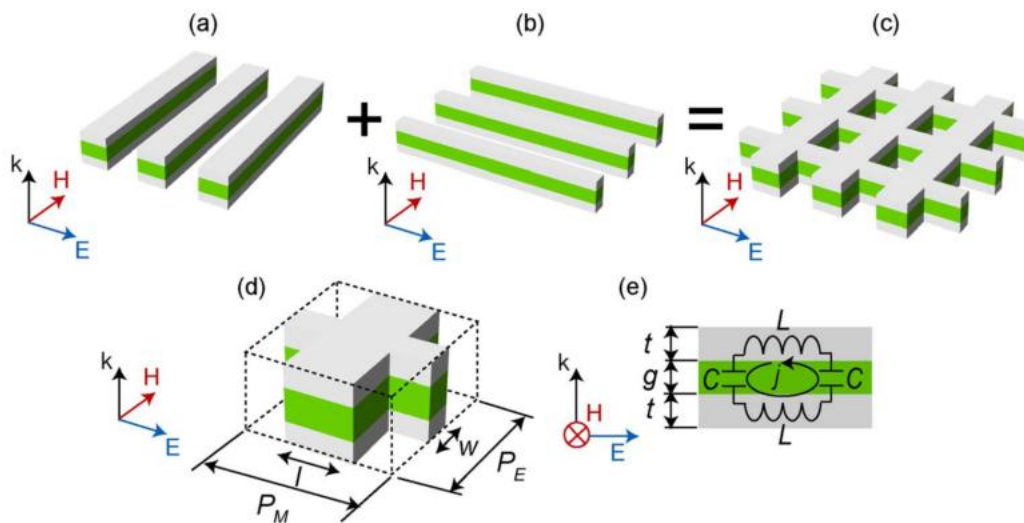


Figure 87. Schematic of a fishnet (metal (grey)-dielectric (green)-metal (grey)) metamaterial. (a) and (b) are schematics of the separate constituents of the metamaterial which provides the (a) magnetic and (b) electric response. (c) The complete fishnet structure. (d) Unit cell geometry of a metamaterial. (e) shows the inductor (L) - capacitor (C) circuit and current loop that form the magnetic response in the fishnet metamaterial [6].

Mary et al. presented a theory of the negative refractive index (NRI) response of double-fishnet structures by analyzing two very distinct frequency regimes. They describe double fishnet structures as holey plasmonic metamaterials, and that their electric permittivity is

governed by the cutoff frequency of the hole waveguide. They also state that the negative values of the magnetic permeability are associated with the excitation of gap surface plasmon polaritons (SPP) modes in the dielectric film [7].

By fabricating a single-negative negative index material (SNNIM) with a fishnet structure, Xiao et al. reported for the first time a material that demonstrated yellow light negative refractive index around the wavelength of 580 nm [8]. Other works have demonstrated materials that have negative indices close to the visible regime. Dolling et al. demonstrated a metamaterial with an effective real part of the index of refraction of -0.6 around 780 nm wavelength [9]. Similarly, Chettiar et al. fabricated a dual-band NIM sample with a period of 300 nm in both directions that exhibited double-negative effective properties in a 20 nm wavelength band around 810 nm [10]. Dolling et al. also investigated the propagation of femtosecond laser pulses through a metamaterial that has a negative index of refraction for wavelengths around 1.5 micrometers. They show that in direct pulse propagation experiments on negative-index metamaterials, the phase velocity and group velocity can be negative simultaneously [11]. Valentine et al. fabricated a three dimensional (3D) fishnet metamaterial by using focused ion-beam milling (FIB) on a multilayer metal-dielectric stacked material. They experimentally demonstrated the first (3D) optical NIM by directly measuring the angle of refraction from a prism made of cascaded fishnet metamaterial [12].

While the works mentioned above are all significant in the advancements of the studies on the physics of this field, a major drawback of most structures reported to date is that the fabrication involves expensive and low-throughput lithography steps (e.g. e-beam lithography, focused ion beam milling, etc.) which limits the potential usage of these metamaterials in large-scale applications. In light of this, Lodewijks et al. reported an alternative fabrication technique combining bottom up and top down approaches to create fishnet metamaterials. Their technique relies on nanospheres lithography (a bottom up process) and metal sputtering (a top down process) to create large-area double fishnet metamaterials consisting of a metal-insulator-metal layer stack perforated by a hexagonal array of holes (Figure 88) [13].

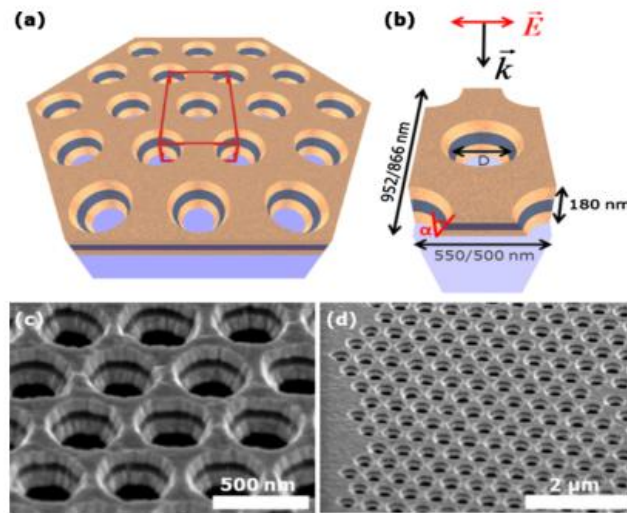


Figure 88. Schematic illustrations and SEM images of a fishnet sample made by nanosphere lithography [13].

In this chapter, we attempt to fabricate fishnet metamaterials consisting of two perforated layers of gold separated by a layer of dielectric in between the layers. Figure 89 show illustrations of the proposed design of the final fishnet metamaterial.

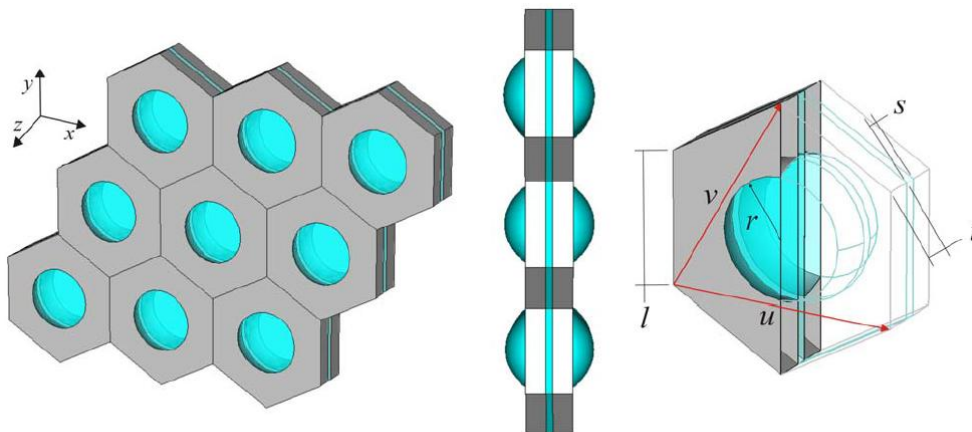


Figure 89. Illustration of the proposed fishnet design, where r is the radius of the spheres, t and s are the thickness of the gold and spacer layer respectively. u and v are the lattice vectors of the unit cell of the structure.

Our proposed fabrication route incorporates the techniques of self-assembly of colloidal templates, nanosphere lithography and electrodeposition (illustrated in Figure 90).

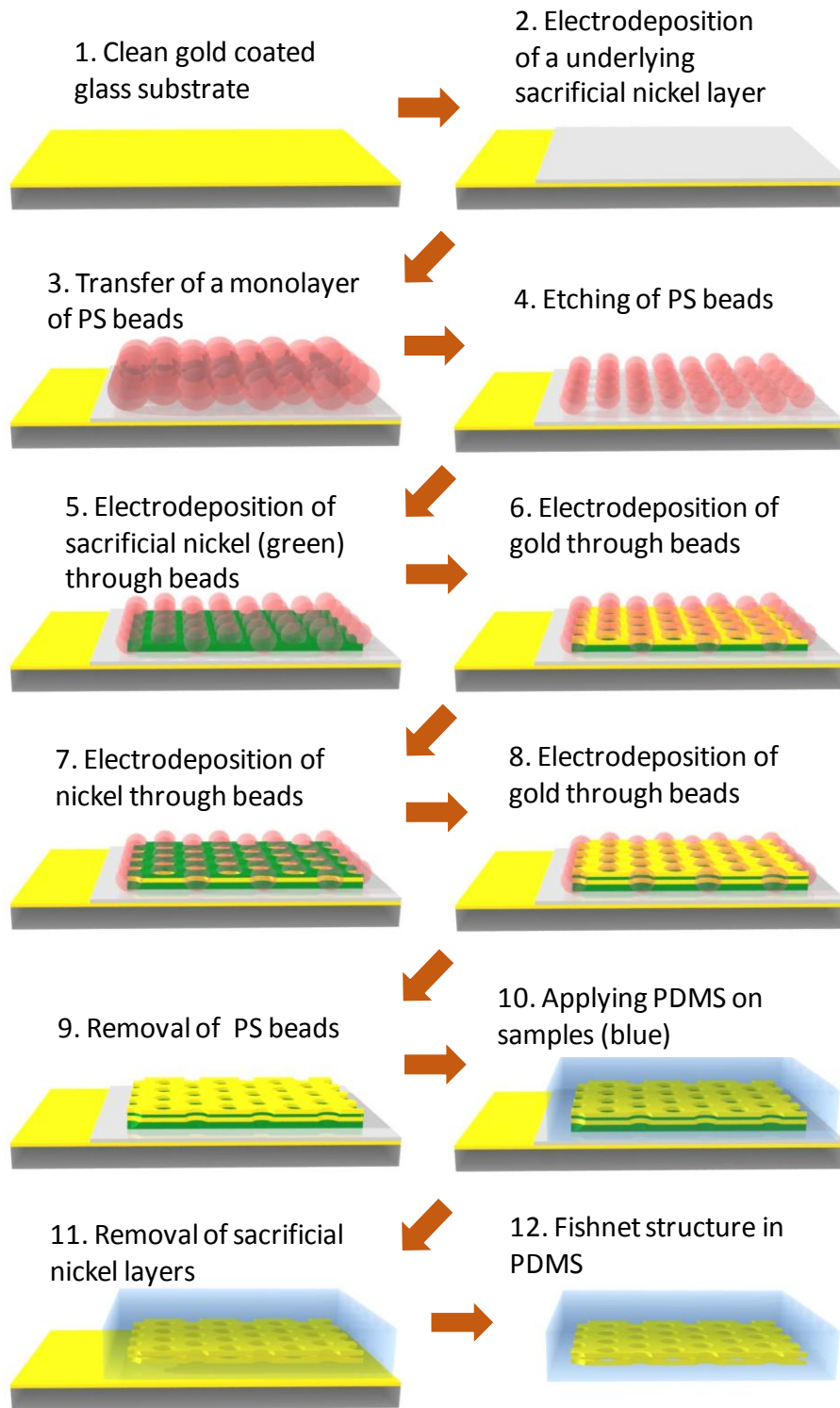


Figure 90. Schematic illustration of the process to fabricate metallic fishnet structures by a combination of self-assembly, nanosphere lithography and electrodeposition.

2. PREPARATION OF NON-CLOSED PACKED MONOLAYERS OF PS BEADS

Monolayers of polystyrene (PS) particles were prepared on conductive substrates in the same procedure as described previously in Chapter 2 by the self-assembly of the PS particles on the water surface. For this part of the work, we investigated the effects of oxygen plasma etching on the size and positions of the PS particles. Figure 91 shows the SEM images of the PS particles before and after oxygen plasma etching at 70W for 60 s and 90 s.

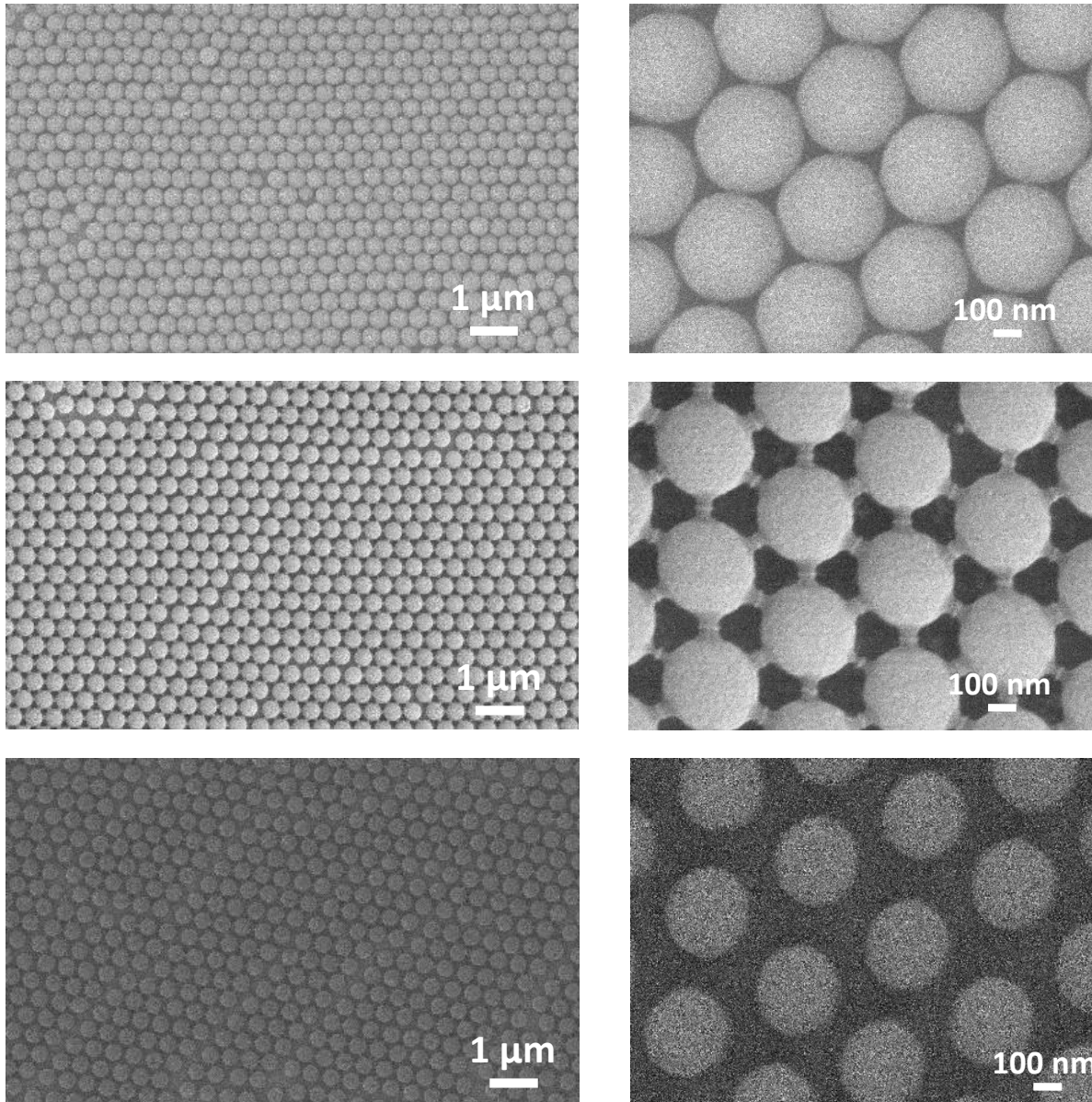


Figure 91. SEM images of a closed packed monolayer of 430 nm PS particles after oxygen plasma etching at 70W. (Top) Closed packed monolayer before plasma etching, (middle) after 60 s, (bottom) after 90 s.

Prior to the oxygen plasma etching step, the monolayers were sintered for 30 minutes at 90°C to ensure that the PS particles do not move as they are ‘shrunk’ by the plasma. Figure 92 shows the dramatic effect of this sintering step on the difference in the positional order of the PS particles after etching

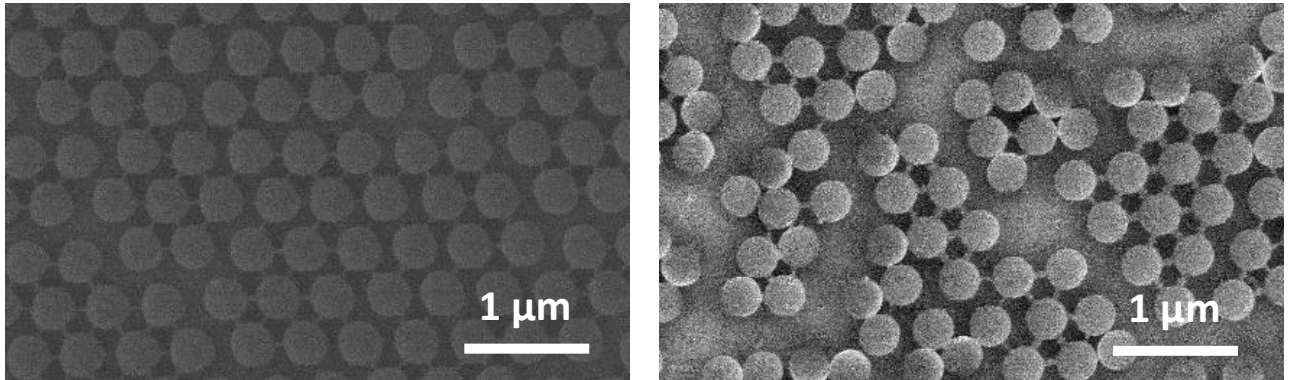


Figure 92. Comparison of the positional order of the PS particles (left) with and (right) without the short sintering step before plasma etching at 70W for 90 s.

It is clearly seen from Figure 92 that the monolayer that was sintered for 30 min at 90°C before the oxygen plasma etching maintained the initial position of the beads even as the beads were reduced in size. The monolayer sample that did not undergo the sintering step before etching is very disorganized once the beads were etched. In this case, it can be observed that the etched beads tend to roll into each other and group together in small random clusters. Hence, the short sintering step is vital to maintaining the positional order of the initial PS particles.

Having established the procedure to prepare the PS monolayers for oxygen plasma etching, three oxygen plasma etching conditions were investigated for four different etching times for the monolayers made of 430 nm PS particles. Figure 93 shows the results obtained for the average particle diameter after etching at 30 W, 50 W and 70 W for 30 s, 60 s, 90 s and 120 s. We can observe that the higher the power applied during the oxygen plasma etching process, the faster the PS particles are reduced in size. This is expected as the increase in plasma power increases the intensity of the oxygen plasma and therefore increases the rate of the etching process. We can also observe that as the duration of the etching time increases, the slope of the plots (which corresponds to the etching rate) also increases. This can be attributed to the change in temperature during the etching process and the particular equipment used for this step. Oxygen plasma etching generates heat that increases the temperature as the duration

of the etching process is increased. Furthermore, the equipment used for this oxygen plasma etching process does not have any component that can regulate the temperature inside the etching chamber during the entire process. Hence, the temperature during the etching process is not specifically regulated, and this increase in temperature as the process proceeds could result in the increased etching rates observed. This effect is not as pronounced at 30W, but is pretty evident at 70W (observing the change in the slope of the plots over time). The increased etching power results in an increase in the corresponding rate of the chamber heating up, which results in a faster rate of etching.

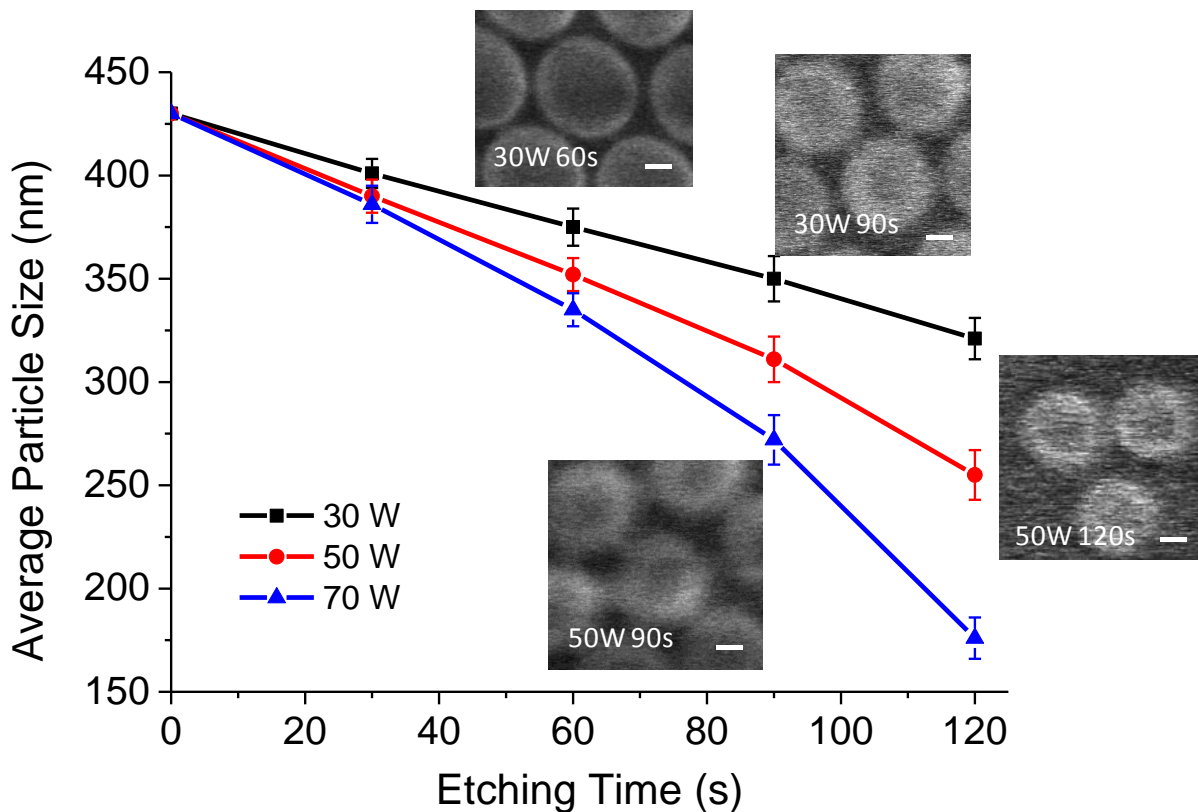


Figure 93. Evolution of PS particle size under three different etching conditions and four different periods of time (Scale bar = 100 nm).

With this series of experiments, we have established the relationship between etching power, time and the final size of the particles. This allows us to be able to estimate and fine tune the size of the non-close packed etched PS particles according to what we desire.

3. SEQUENTIAL ELECTRODEPOSITION OF METALS

Here, we will once again demonstrate the versatility of using electrodeposition to electrodeposit gold and nickel to our desired amounts. The process of electrodeposition is similar to what has been described in the previous chapters (Chapter 3 and 4). By monitoring change in current as the electrodeposition proceeds, we can accurately estimate the depth of the electrodeposited metal. The aim of this part of the work was to create a gold-nickel-gold structure that resembled a fishnet, and having the nickel layer positioned at a depth that is half the PS particle diameter.

We estimated the depth of electrodeposition of each metal in the same way as we did in Chapter 4. The only difference is that the templates are modified in a different way and that we intend to sequentially electrodeposit multiple layers of each metal into one single template, where as in Chapter 4, we only electrodeposited one layer of nickel followed by one layer of gold.

Here, we will electrodeposit one layer of nickel followed by one layer of gold and then another nickel layer of nickel followed by another layer of gold, to obtain a fishnet-like structure, with the position of the second nickel layer electrodeposited at a depth close to the middle of the PS particles (half D). The other requirement for electrodeposition is that the electrodeposited gold layers should be of similar thickness. This can be done by electrodepositing the gold layers for the same duration.

Hence, the main variable that is left to adjust is the thickness of the first nickel layer. This is the most important variable to determine as experimentally, this is the first electrodeposition step, and any mistake in the calculations of the thickness of this layer will affect all the subsequent layers to be electrodeposited, and definitely the final structure that is obtained. Figure 94 illustrates how the cross section of the samples should appear after electrodeposition. Figure 95 shows examples of samples electrodeposited with different number of layers (with similar thickness) of nickel and gold.

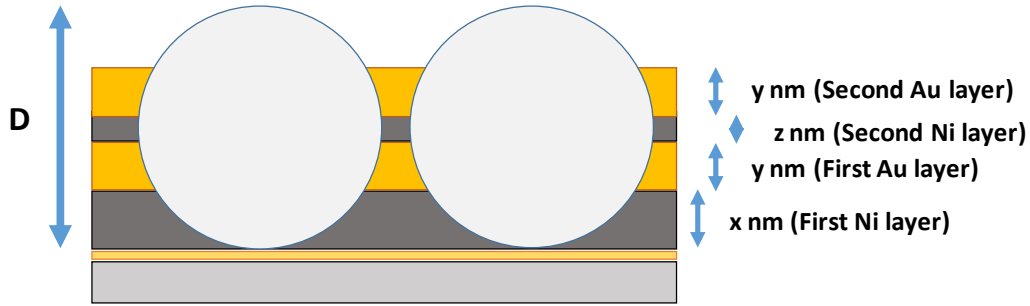


Figure 94 Illustration of the cross section of an electrodeposited sample

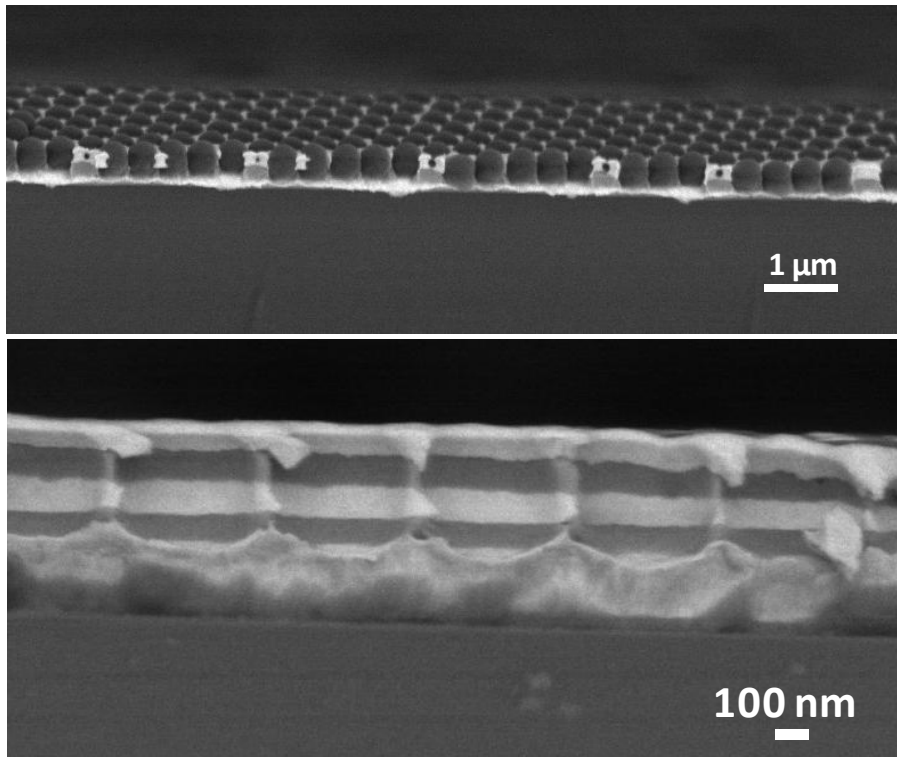


Figure 95. SEM images of (top) nickel-gold and (bottom) nickel-gold-nickel-gold deposited into a colloidal monolayer made of 430 nm PS beads with a similar thickness for each layer.

Using Figure 94 as a guide, and having experimentally determined the time required to electrodeposit each metal to a depth of half D , we can use the formulas listed in Table 12 to estimate the time required to electrodeposit each layer of metal. $t_{Ni,0.5}$ and $t_{Au,0.5}$ refer to the experimentally determined duration for the thickness of each metal to reach half D (obtained from the calibration step).

Table 12. General estimation of electrodeposition (ED) duration for each metal layer to a desired depth

	First Ni layer	First Au layer	Second Ni layer	Second Au layer
Desired thickness (nm)	x	y	z	y
Estimated time for ED (s)	$\frac{D - 2y - z}{D} \times t_{Ni,0.5}$	$\frac{y}{D} \times 2t_{Au,0.5}$	$\frac{z}{D} \times 2t_{Au,0.5}$	$\frac{y}{D} \times 2t_{Au,0.5}$

Note* D (nm) = $2x + 2y + z$

Applying a similar methodology as described previously in Chapter 4, we first electrodeposited nickel and gold separately into the templates to figure out the time required for both metals to be electrodeposited to half the bead diameter.

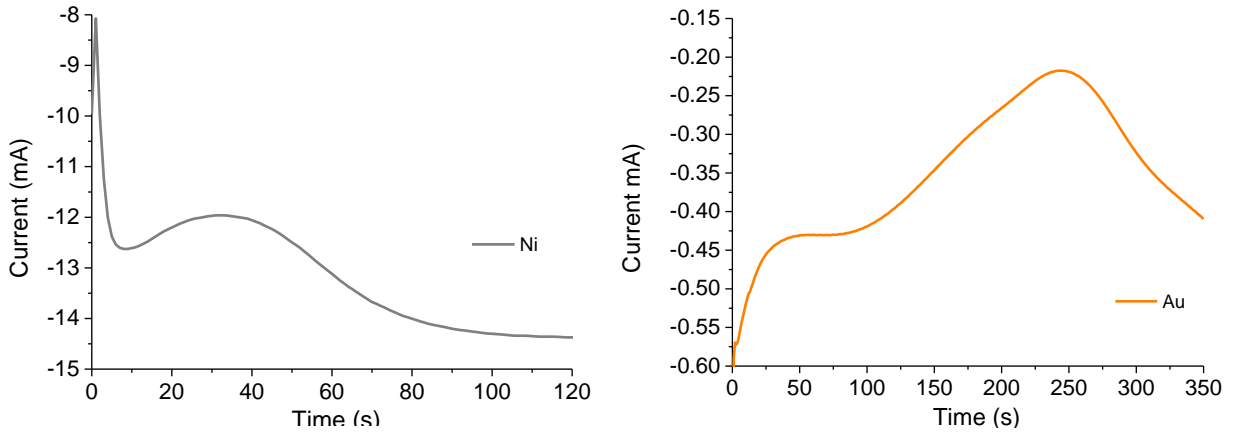


Figure 96. Electrodeposition current-time plots of (left) nickel and (right) gold into similar templates during the same session

From the experimental information obtained in Figure 96, we will demonstrate the feasibility of the using the calculations in Table 12 to fabricate a Ni-Au-Ni-Au structure with the following estimated proportions of $0.3D:0.15D:0.1D:0.15D$ (where $D = 430$ nm). Using $t_{Ni,0.5} = 32$ s and $t_{Au,0.5} = 244$ s, along with the y and z values of $0.15D$ and $0.1D$ respectively, we estimate the time required for the electrodeposition of the first layer to be 20 s, the first gold layer to be 71 s, the second nickel layer to be 6s and the second gold layer to be 71s (same as the first gold layer). Figure 97 shows the current-time plots of the electrodeposition of nickel and gold in sequential order.

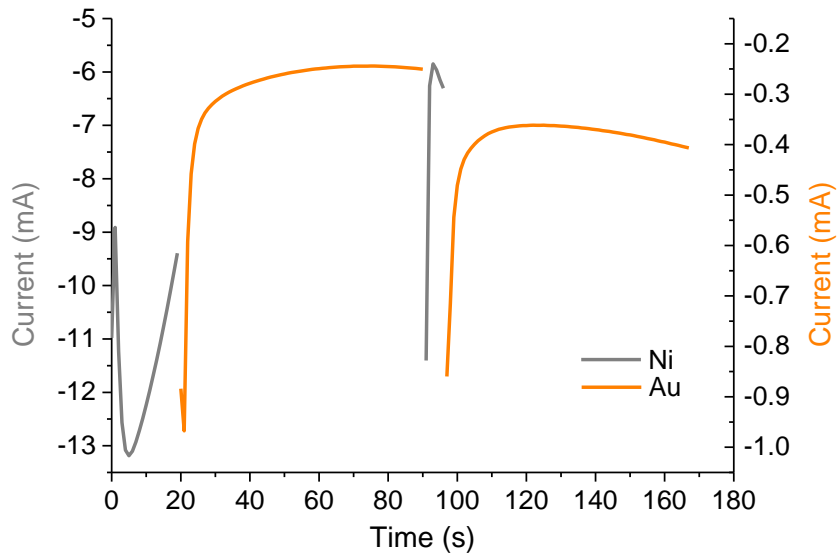


Figure 97. Profile of current change during the electrodeposition of Ni and Au over time in a monolayer of 430 nm PS beads at a fixed voltage of -1.0 V and -0.7 V respectively.

From Figure 97, we can observe that the current-time plots resemble the shape of the curve obtained when we electrodeposit only one metal through a template of spherical particles. We see that initially the current decrease (in absolute values) as the first nickel layer is electrodeposited through the template. This corresponds to the decrease in available surface for electrodeposition as nickel is electrodeposited into the template made of spherical particles. This trend continues with the first layer of gold, and we can observe the current minimum at the end of the electrodeposition of the first layer of gold at about 75 s. A current minimum is also observed in the short 6 s electrodeposition of the second layer of nickel. The subsequent plot for the second layer of gold show an increase in current (in absolute values) corresponding to the increase in surface area available for gold to be electrodeposited into the template, as it is now above a depth of half D .

To verify the predictions that the nickel and gold metal layers are being electrodeposited as we had expected, multiple samples were fabricated. Figure 98 shows the cross sectional SEM images obtained after each step of the electrodeposition process.

From Figure 98, we can clearly distinguish the different layers of nickel and gold electrodeposited into the templates under backscattered SEM. It can be observed that the metals fill up the pores evenly across the electrodeposited surface. The actual positions of each layers corresponds very well to our intended positions for each layer. This is especially

true for the positioning of the second ‘middle’ nickel layer. For Figure 98 (c) and (d), we can see that the second nickel layer lies exactly in the middle at the half D, which can be clearly deduced by the contact spots between the PS particles. In addition from Figure 98 (d), we can also see that the thickness of the two electrodeposited gold layers are comparable with each other, which is what we had expected based on their equal electrodeposition time. For this series of samples, the thickness of the first Ni, first Au, second Ni and second Au layers are about 110 nm, 90 nm, 37 nm, and 90 nm respectively.

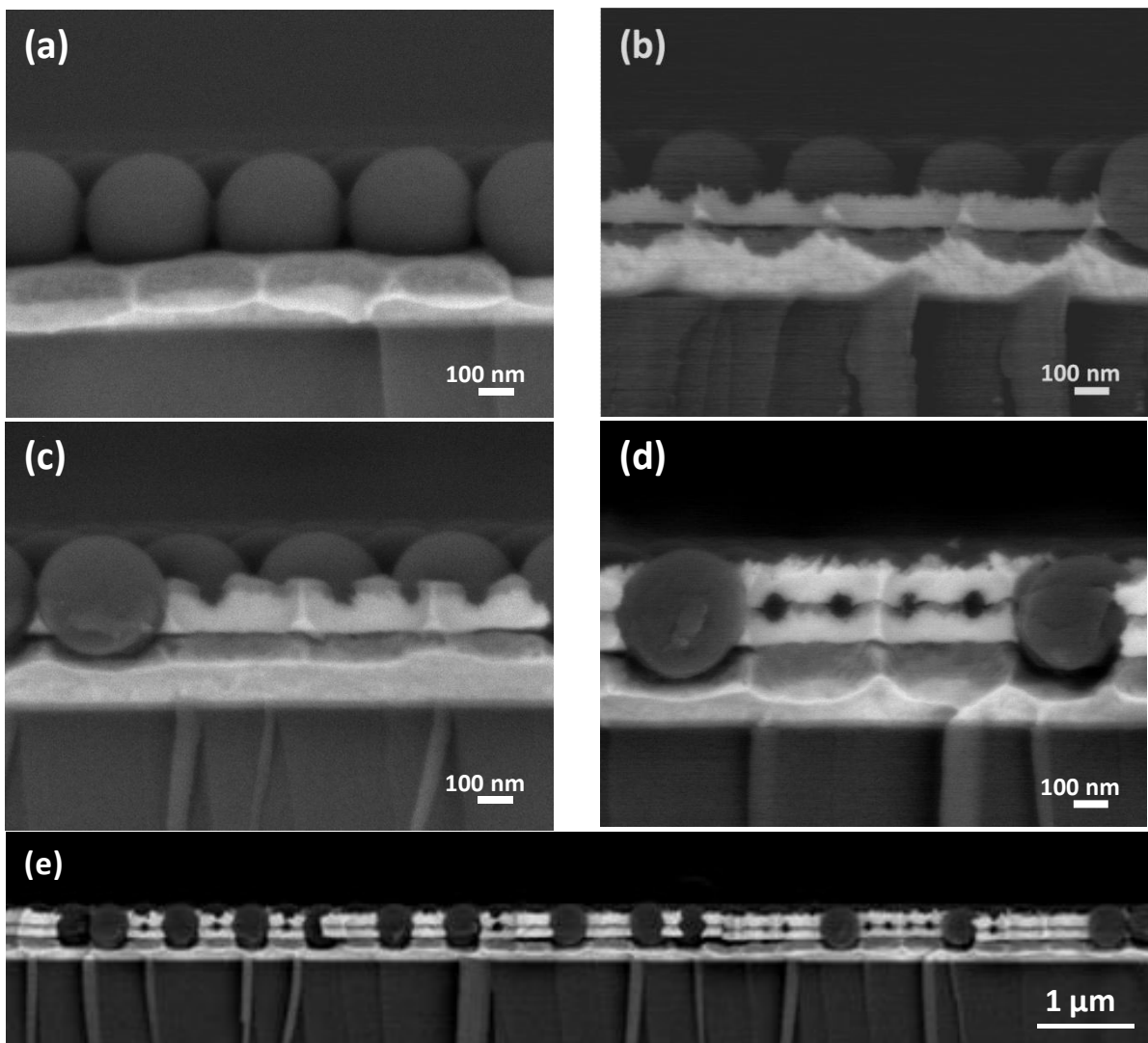


Figure 98. Backscattered SEM cross section images of the samples showing the different electrodeposited layers of Ni (dark) and Au (bright) into a 430 nm PS monolayer at the different stages. (a) After electrodeposition of the first Ni layer at -1.0 V (vs Ag/AgCl) for 20 s. (b) After electrodeposition of the first Au layer at -0.7 V (vs Ag/AgCl) for 71 s. (c) After electrodeposition of the second Ni layer at -1.0 V (vs Ag/AgCl) for 6 s. (d) After electrodeposition of the second Au layer at -0.7 V (vs Ag/AgCl) for 71 s. (e) Enlarged view of the final structure.

It is obvious that this set of samples were made with close-packed PS particle templates that were not etched. To verify that this method is applicable to etched non-close-packed PS particle templates, a similar process was repeated with etched templates. Figure 99 shows the SEM images obtained for two such samples fabricated.

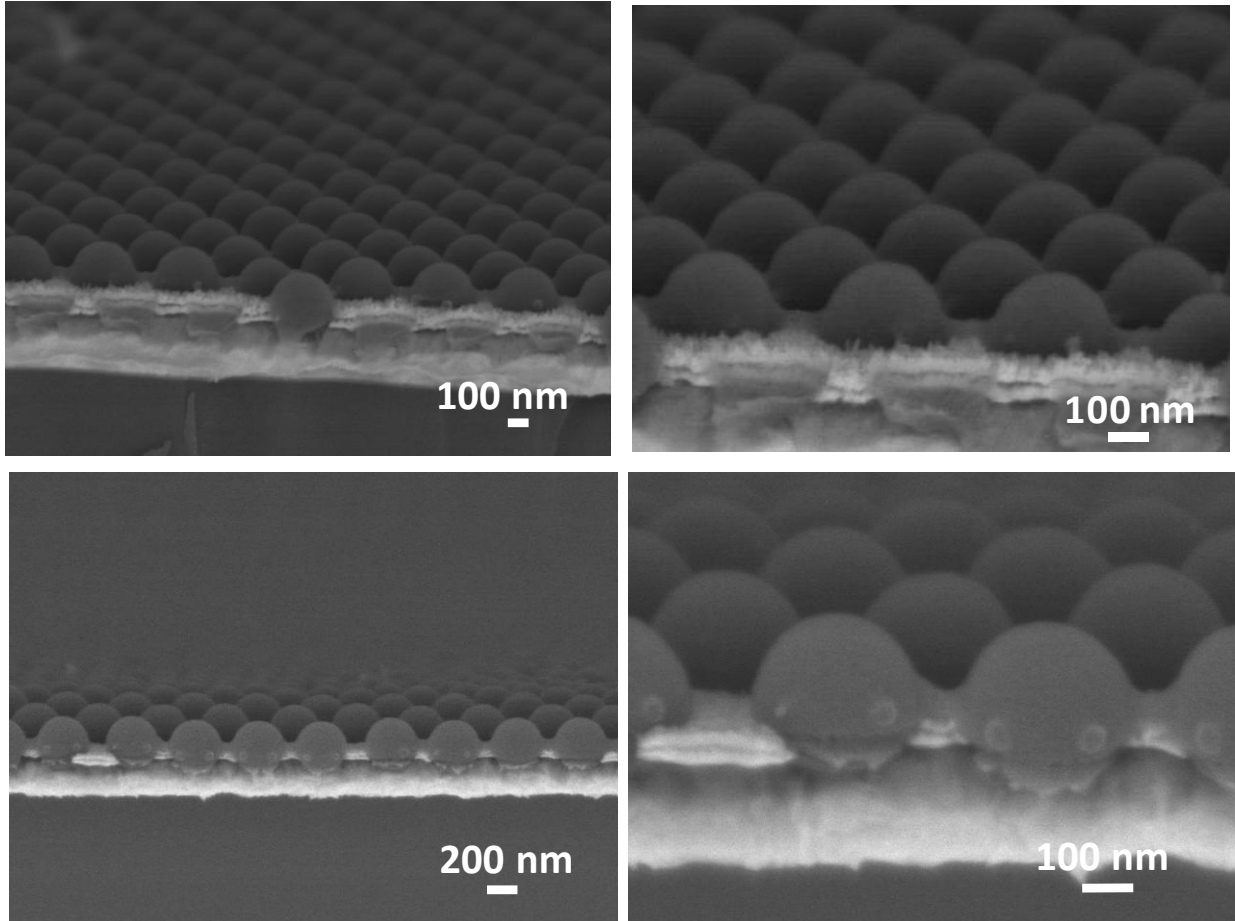


Figure 99. Sequential electrodeposition of nickel-gold-nickel-gold into non-close-packed etched PS template ($D = 340$ nm). (Top) gold-nickel-gold layers with thickness of 76 nm, 15 nm, 76 nm respectively. (Bottom) gold-nickel-gold layers with thickness of 25 nm, 10 nm, 25 nm respectively (Left) Enlarged and (right) close up view of the respective samples.

From Figure 99, we observe that we are still able to control the position of the different layers very accurately as we electrodeposit nickel and gold through the etched templates. This is evidenced particularly by the position of the second ‘sandwiched’ nickel layer which sits very close to height of half D (diameter of the template etched PS particle). Furthermore, the thickness of the gold layers can also be seen to be very similar in thickness. This proves that the method to estimate the thickness of the electrodeposited metal layers is transferrable between etched and non-etched templates as long as the building block (i.e. PS particles) are spherical in shape. In addition, from this set of SEM images (Figure 99), we observe the

electrodeposited layers are uniform across the electrodeposited area and we demonstrate that we can vary the thickness of the gold and nickel layers independently, which creates the possibility of making structures with tunable thicknesses at each layer level. We are able to electrodeposit just a very thin layer of nickel sandwiched between the two gold layers, as evidenced by the successful electrodeposition of an extremely thin nickel layer of about 10 nm over the active surface area, sandwiched between the two gold layers (Figure 99, bottom).

4. DISSOLUTION OF SACRIFICIAL NICKEL LAYERS

For the next step, our objective was to remove the sacrificial nickel layers from the electrodeposited nickel-gold-nickel-gold structure. 16 weight% HNO_3 (nitric acid) was used to dissolve the nickel layer. The sample was left in the acid for up to a few days (depends on the sample size) to ensure complete nickel dissolution.

To verify that the sandwiched nickel layer was completely removed, we first fabricated a simple gold-nickel-gold structure on a basic template and attempted to dissolve the ‘sandwiched’ nickel layer. Figure 100 shows the SEM cross section of a sample before and after nickel dissolution.

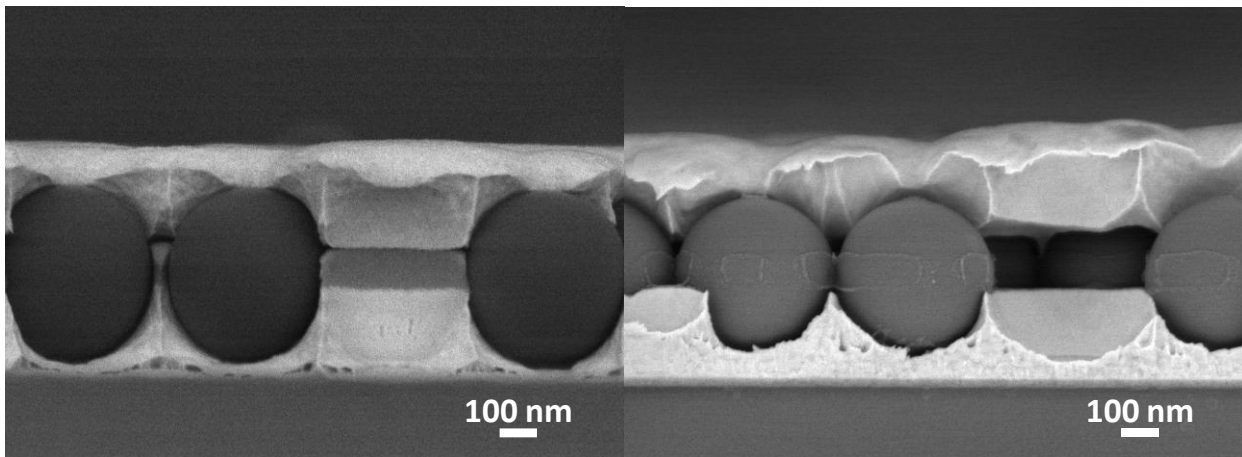


Figure 100. Back scattered SEM cross sectional images of an electrodeposited gold-nickel-gold structure (right) before and (left) after nickel dissolution.

Figure 100 shows very clearly that nickel is dissolved without any other noticeable effects on the gold layers or the particles. All the nickel in the sandwiched layer is totally removed as far as it was observed under the SEM. Figure 101 shows an enlarged view of the cross section after nickel dissolution.

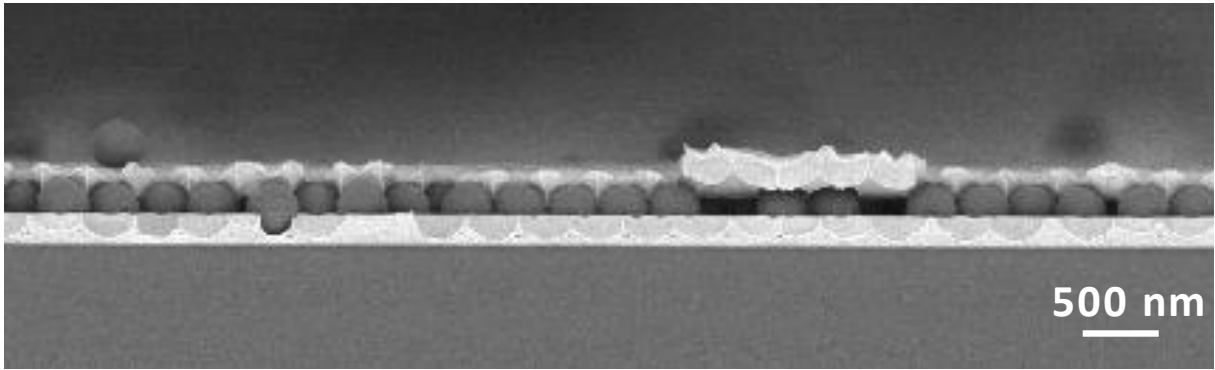


Figure 101 Cross section SEM view of electrodeposited gold-nickel-gold structure after nickel dissolution

Similar to the previous tests, once we have identified the feasibility of this nickel dissolution process, we proceeded to work with the actual samples containing electrodeposited nickel and gold in the etched PS templates.

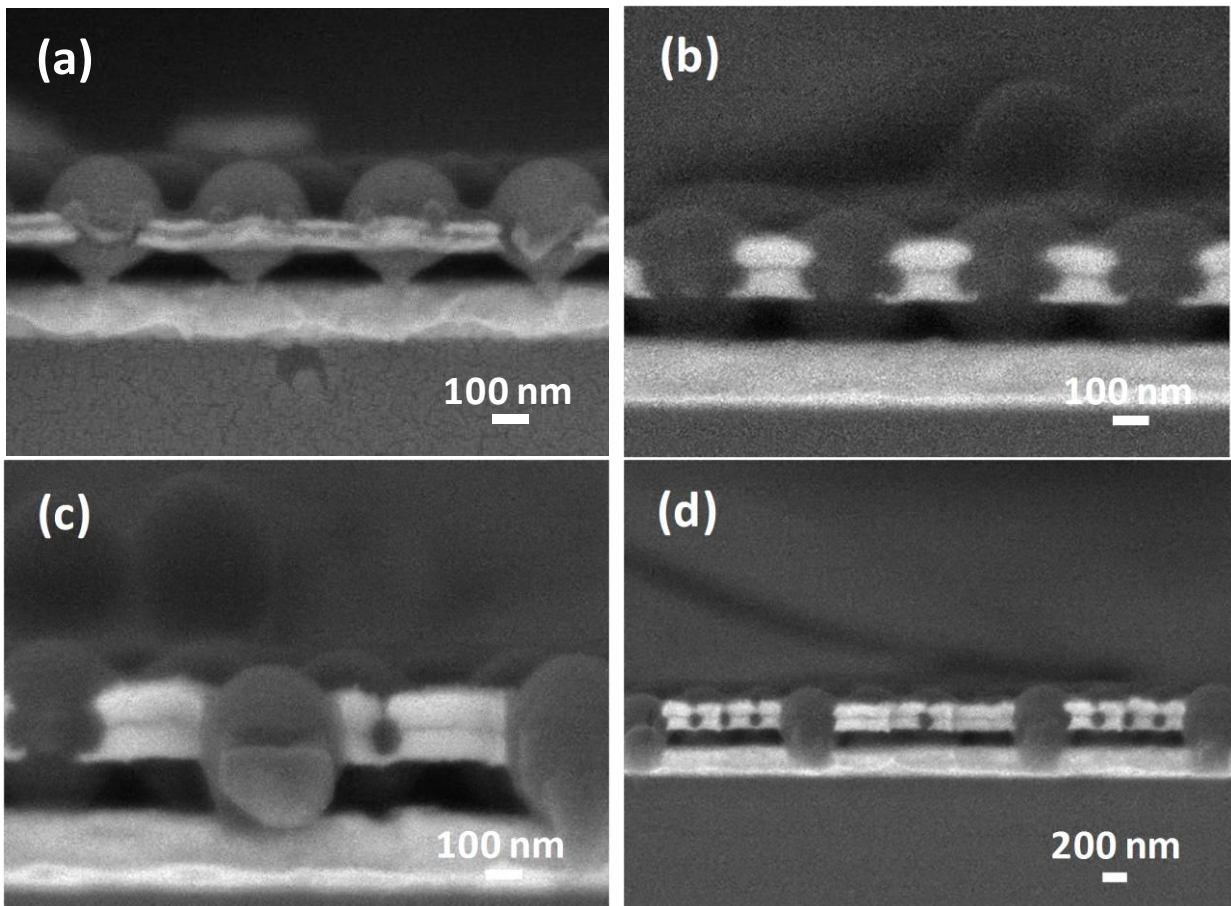


Figure 102. Gold-air-gold fishnet structures obtained after dissolution of nickel. Electrodeposited gold of increasing layer thickness of (a) 22 nm, (b) 56 nm and (c) 84 nm. All three samples have a spacer layer of about 10 nm between the gold layers. (d) enlarged view of (c).

From the results obtained in Figure 102, we can observe that the first nickel layer is completely dissolved, exposing the outlines of the PS particles at the back which can be clearly seen. We also observe that the structural integrity of the gold layers remain regardless of their thickness. Hence, we speculate that the PS particles serve as supports to these gold layers, preventing them from collapsing onto each other or onto the substrate.

5. TRANSFERRING THE FISHNET ONTO A TRANSPARENT SUBSTRATE

Thus far, all the previous procedures from the oxygen plasma etching step to the electrodeposition step and the subsequent nickel dissolution steps have all been conducted on conductive gold coated glass substrates. We have successfully demonstrated that up till this point, the fabrication process is entirely feasible with possibilities of tuning PS particle size, electrodeposition thickness and the simple step to dissolve of nickel. For a fishnet metamaterial to be useful in a practical sense, our next challenge was to devise a method to transfer the fishnet structure we have fabricated from the conductive gold coated glass substrate, onto a transparent substrate that could allow us to investigate the optical properties. To attempt this transfer, the following trials were made:

- 1) Transferring the fishnet onto PDMS (similar to the method used in Chapter 4 for the gold nanopillar arrays)
- 2) Transfer the fishnet onto water and re-scoop it up on a piece of glass

5.1 TRANSFER OF FISHNET STRUCTURES ONTO PDMS

The procedure for this trial was similar to the one used to transfer the gold nanopillar arrays described in chapter 4. The details of the procedure for the application of PDMS onto the substrates are the same as that described in Annex 5 for the nanopillar structures. Certain slight modifications had to be made to the conductive substrate to prepare for this transfer step at the end. Briefly, the entire process can be described as follow. First, a thin smooth nickel layer was electrodeposited over the entire gold coated glass substrate before any PS particles were transferred onto it. We call this the nickel plating step. Once the gold substrates were nickel plated, PS monolayers were transferred onto them and etched accordingly followed by electrodeposition of the nickel-gold-nickel-gold layers. When the electrodeposition was

complete, the entire sample was left in Tetrahydrofuran (THF) to remove the PS particles completely. Once the PS particles were completely removed, PDMS was applied to the top surface of the substrate. The assumption here is that the PDMS will completely infiltrate all the available spaces left behind after the PS particles were removed (i.e. they act as the new supports for the eventual gold layers after nickel dissolution). Once the PDMS infiltration is complete, the nickel layers are dissolved and the fishnet structures will be transferred onto the PDMS layers. Figure 103 shows the SEM image of a gold-air-gold fishnet transferred onto PDMS.

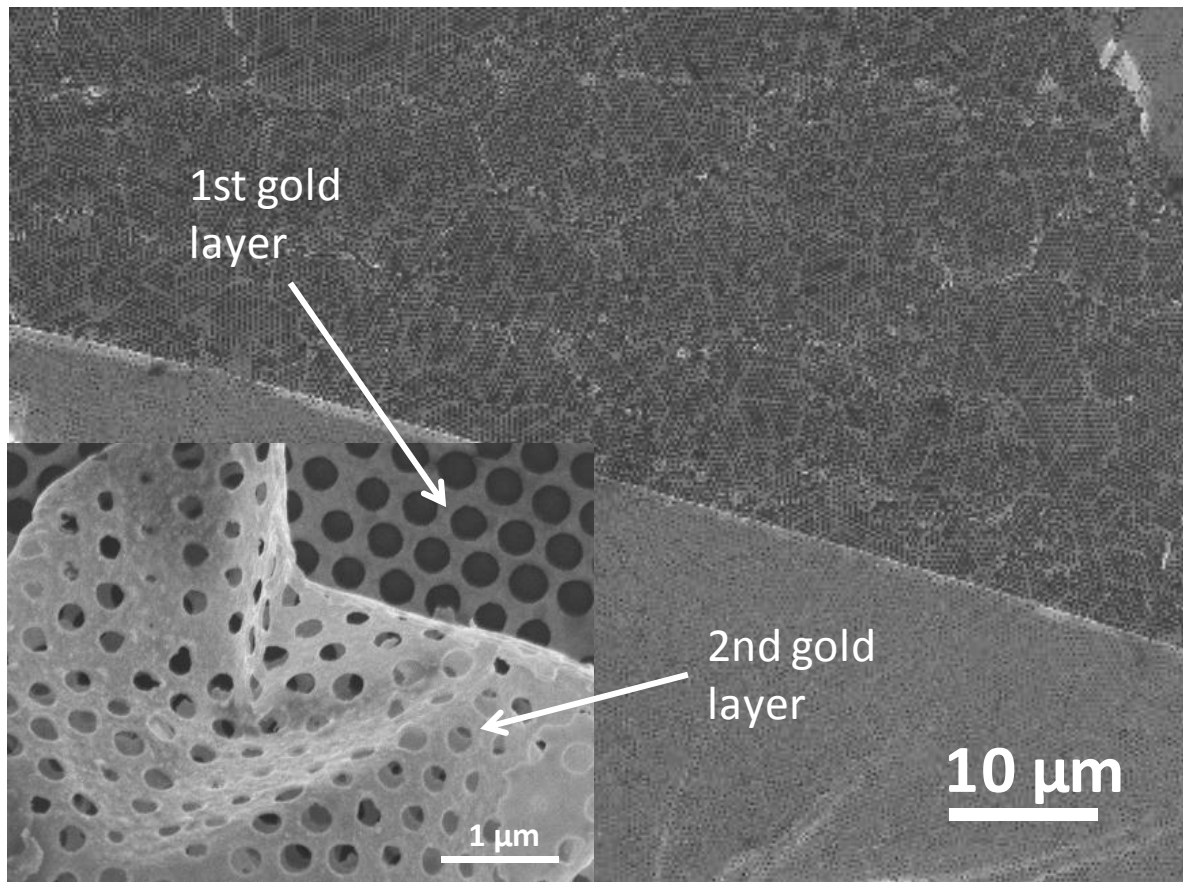


Figure 103. SEM images of the transferred gold layers onto PDMS. (Inset) Close up SEM image showing clearly the first gold layer in contact with PDMS and the second layer sitting above the first layer but it is ‘crumpled’.

From Figure 103, we can clearly see two layers of perforated gold films lying one on top of the other. It is observed that the top layer is folded in some regions and appear more ‘crumpled’ than the bottom layer which is flat spreads out very evenly. The top layer corresponds to the first electrodeposited gold layer while the bottom layer corresponds to the second electrodeposited gold layer (refer to Figure 94 for clarifications). This is because the

PDMS is applied onto the top of the electrodeposited sample before nickel is dissolved; hence the orientation of the gold layers are now inverted. However, since the gold layers are supposed to be symmetrical, there should be no difference if either one is on top or below. The main issue here is that the bottom gold layer spreads out very well due to the fact that it is completely in contact with the PDMS on one side. However, the top gold layer is only supported by the PDMS that infiltrated the pores which makes it very fragile, and easily disturbed and detached from the surface (as can be clearly observed in Figure 103 inset).

From Figure 103 inset, we can clearly see the pores in the gold films that correspond to the etched PS particles that were originally there. We can observe a good and regular ordering of the particles from these inverse images left in the perforated gold films. There are some tears that can be seen in the bottom gold layers which can attribute to the mechanical stress that the PDMS substrate is subjected to when it is peeled off the conductive substrate. This peeling off of the PDMS from the original conductive substrate is probably the main reason for the tears in the bottom gold layer as well as the detachment and subsequent folding for the top gold layer. These images suggests that we still need to devise a gentler and more refined technique to remove the fishnet structures that could better preserve the overall integrity of the fishnet structure during the transfer process. Nonetheless, with the fishnet transferred onto PDMS, we performed optical characterizations on them and the preliminary results are in the following section.

Optical Characterizations

With the structures transferred onto PDMS, we did preliminary optical measurements on them by taking their transmission spectra. Figure 104 shows the results of the measurements for three samples transferred onto PDMS with 30 nm, 60 nm and 90 nm gold layers each separated by a gap of about 15 nm.

From Figure 104, we can see that for the sample with the thickest gold layer (90 nm), it is almost opaque except for a small transmission peak centered at 504 nm. This transmission peak can be observed to be present for all the three samples measured, and is probably due to the positioning of the pores that exist in the gold films. The same etched 430 nm PS monolayer was used as the template during electrodeposition. When the thicknesses of the gold layers are reduced to 60 nm, we observe that a second transmission peak emerges around

785 nm and the overall transmission increases. Further reduction in the layer thickness of gold to 30 nm shows a further increase in overall transmission for all wavelengths and also the shifting of the second transmission peak to 801 nm and the emergence of a third peak (observed as a small shoulder at 714 nm). The overall increase in transmission as the gold layers become thinner is expected as more light is able to pass through the gold layers when they are thinner. However, to better understand our results, it is necessary to perform some simulations which will have to be done in the future.

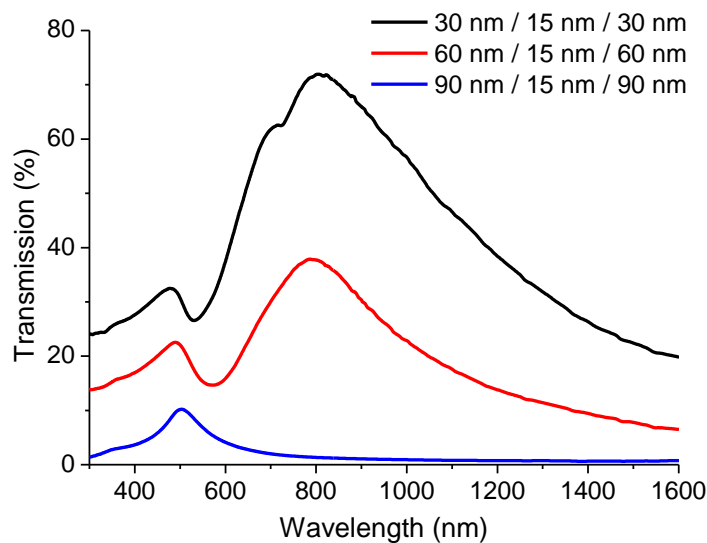


Figure 104. Transmission spectra of fabricated fishnet structures transferred onto PDMS with different gold layer thicknesses.

5.2 TRANSFER OF FISHNET STRUCTURES ONTO WATER AND RE-SCOOPING THEM OUT

The alternate idea to transfer the fishnet structure was to attempt to float the fishnet structure (after nickel dissolution) on a water surface. This procedure for this idea is similar to the previous method involving PDMS up until the electrodeposition of the gold and nickel layers. Instead of dissolving the PS particles, the PS particles are kept and all the nickel layers are dissolved. The entire substrate is submerged in just enough nitric acid to dissolve the nickel layers. Once the nickel has been dissolved, additional water is added into the beaker to increase the volume of the liquid and dilute the nitric acid at the same time. The challenge here is to very carefully bring the substrate up to the air water interface and attempt to separate the PS particles with the gold layers from the substrate they were sitting on. The idea

behind this approach was the expectations that the very thin gold films would float and the perforated gold films should hold the PS particles in position.

Unfortunately, successive attempts at using this approach have not been successful. It appears that after nickel dissolution, there is still a very strong physical adhesion force of the fishnet structure to original substrate. Only little flakes of the gold films have been re-scooped out onto glass substrates.

6. CONCLUSION

In this chapter, we have shown that it is possible to use a combination of colloidal templating, nanosphere lithography and electrodeposition to fabricate metal nanostructures with tunable configurations of particle spacing and layer thickness. These techniques are all very versatile and provides a very good level of control of the fabrication parameters. Particle of pore spacing can be easily configure by choosing PS particles of the appropriate size. Individual particle or pore size of the non-close packed templates can be easily adjusted by controlling the etching process by varying the etching power and time under oxygen plasma etching. We have demonstrated the effectiveness of electrodeposition in terms of the control that can be achieved by using it to electrodeposit gold and nickel layers with tunable thickness and very fine control. By using a simple calculation method, we are able to estimate the thickness of the electrodeposition process very accurately, and this has been shown by the consistent positioning of the electrodeposited ‘sandwiched’ nickel layer around the depth of half D (diameter of the template PS particles). Next, we have also demonstrated that the acid dissolution of nickel has no effect on the structural integrity of the remaining fishnet structure. The gold layers and PS particles are not adversely affected by the removal of nickel. The resulting structure after nickel dissolution is simply the same structure before nickel dissolution but without the nickel.

However, we have encountered difficulties in successfully transferring the entire fishnet structure onto an alternative transparent substrate without damaging it. As discussed, attempts using both approaches (transfer on PDMS and water) have not been entirely successful in preserving the overall structural integrity of the entire fishnet structure. While parts of the fishnet structure are maintained when it is transferred onto PDMS, obvious tears and folding of the gold layers can still be readily observed on other parts of the samples. In this aspect,

more work has to be done to investigate other possibilities and alternatives that could be used to transfer our fishnet structures. Certainly, this will not be the only challenge that needs to be tackled. Even with the successful transfer of the structures, we would still have to investigate and tune the resulting optical properties of the materials by re-evaluating the entire process again.

REFERENCES

- [1] R. Sambles, “Gold loses its lustre,” *Nature*, vol. 438, pp. 6–7, 2005.
- [2] V. G. Veselago, “The electrodynamics of substances with simultaneously negative values of ϵ and μ ,” *Sov. Phys.*, vol. 10, no. 4, pp. 509–514, 1968.
- [3] J. B. Pendry, A. J. Holden, D. J. Robbins, and W. J. Stewart, “Magnetism from conductors and enhanced nonlinear phenomena,” *IEEE Trans. Microw. Theory Tech.*, vol. 47, no. 11, pp. 2075–2084, 1999.
- [4] R. A. Shelby, D. R. Smith, and S. Schultz, “Experimental verification of a negative index of refraction,” *Science*, vol. 292, no. 5514, pp. 77–9, Apr. 2001.
- [5] J. Wood, “The top ten advances in materials science,” *Mater. today*, vol. 11, no. 1, pp. 40–45, 2008.
- [6] J. Valentine, S. Zhang, T. Zentgraf, and X. Zhang, “Development of bulk optical negative index fishnet metamaterials: Achieving a low-loss and broadband response through coupling,” *Proc. IEEE*, vol. 99, no. 10, pp. 1682–1690, Oct. 2011.
- [7] A. Mary, S. Rodrigo, F. Garcia-Vidal, and L. Martin-Moreno, “Theory of negative-refractive-index response of double-fishnet structures,” *Phys. Rev. Lett.*, vol. 101, no. 10, p. 103902, Sep. 2008.
- [8] S. Xiao, U. K. Chettiar, A. V Kildishev, V. P. Drachev, and V. M. Shalaev, “Yellow-light negative-index metamaterials,” *Opt. Lett.*, vol. 34, no. 22, pp. 3478–80, Nov. 2009.
- [9] G. Dolling, M. Wegener, C. M. Soukoulis, and S. Linden, “Negative-index metamaterial at 780 nm wavelength,” *Opt. Lett.*, vol. 32, no. 1, pp. 53–5, Jan. 2007.
- [10] U. K. Chettiar, A. V Kildishev, H.-K. Yuan, W. Cai, S. Xiao, V. P. Drachev, and V. M. Shalaev, “Dual-band negative index metamaterial: double negative at 813 nm and single negative at 772 nm,” *Opt. Lett.*, vol. 32, no. 12, pp. 1671–3, Jun. 2007.
- [11] G. Dolling, C. Enkrich, M. Wegener, C. M. Soukoulis, and S. Linden, “Simultaneous negative phase and group velocity of light in a metamaterial,” *Science*, vol. 312, no. 5775, pp. 892–4, May 2006.
- [12] J. Valentine, S. Zhang, T. Zentgraf, E. Ulin-Avila, D. A. Genov, G. Bartal, and X. Zhang, “Three-dimensional optical metamaterial with a negative refractive index,” *Nature*, vol. 455, no. 7211, pp. 376–9, Sep. 2008.
- [13] K. Lodewijks, N. Verellen, W. Van Roy, V. Moshchalkov, G. Borghs, and P. Van Dorpe, “Self-assembled hexagonal double fishnets as negative index materials,” *Appl. Phys. Lett.*, vol. 98, no. 9, p. 091101, 2011.

OVERALL CONCLUSION AND PERSPECTIVES

Through the course of the work done in this PhD thesis, we have attempted to design and fabricate several types of nanostructured materials through the use of bottom-up self-assembled colloidal crystals. The work has been most challenging at figuring out the process parameters to control and fine-tune the nanostructures, but it has also been equally rewarding when we successfully obtained the final product envisioned at the start of each process.

In Chapter 1, we have made a brief review of the general concepts related to the work discussed in this thesis, the idea and theory of photonics and plasmonics, as well as the general reported methodology of fabricating such devices from top-down and, especially on, bottom-up self-assembly approaches.

In Chapter 2, we attempted to incorporate a photonic crystal (an inverse opal TiO_2 layer) into a solid state dye sensitized solar cell (DSSC) in a controlled manner to enhance light trapping and improve the cell efficiency. We have successfully demonstrated that by stacking individual monolayers of the polystyrene (PS), we can control the exact thickness of the opaline layer and consequently, the thickness of the inverse opal (IO). We have shown that the bandgap can be tuned by changing the size of the particles used, and that it is important to ensure that the bandgap of the inverse opal matches the absorption of the dye used. We also determined that there is an optimum layer thickness of the inverse opal layer that results in the best cell efficiency. More work can be done to investigate other configurations of the IO coupled with different dyes, and to determine the best combination of dye and IO structure that could produce the best cell efficiency.

In Chapter 3, we showed that we could electrodeposit gold very accurately through a single monolayer of close-packed polystyrene beads up to a certain depth by adjusting the electrodeposition time. The depth of gold electrodeposited can be adjusted to a point where we were able to demonstrate omnidirectional absorption of light for different particle sizes. We have shown that when the beads were replaced with voids, the absorption was blue shifted and the intensity was slightly lowered. We have also elaborated the electrodeposition of gold on a planar gold substrate without any templates. By simply changing the electrodeposition voltage and keeping the other parameters constant, we have shown that a very rough textured gold surface can be fabricated which exhibits almost no specular reflection across the

wavelength range of 250 nm to 2500 nm. The next step for these gold nanostructures would be to incorporate them into suitable devices that can utilize their unique optical properties. In the near future, we have plans to attempt transferring these nanostructures by PDMS stamping onto suitable devices / materials (e.g. silicon) for testing.

In Chapter 4, we made use of sintered close-packed PS beads to electrodeposit and fabricate gold nanopillars. We were able to control the distance between the triangular tips of the adjacent pillars by adjusting the electrodeposition time. However, the distance between the tips of the pillars did not have any noticeable difference in the SERS effect measured between different samples. We also made use of the electrodeposition of a sacrificial nickel layer to electrodeposit symmetrical gold pillars which could be transferred onto a transparent material such as polydimethylsiloxane (PDMS). The embedded gold pillars in PDMS were then optically characterized and further subjected to stress by stretching the PDMS samples along one direction. It was observed that the different pillar geometries exhibited different plasmonic absorption peaks. Increasing the height of the pillars induced a blue shift of the absorption peaks. Furthermore, the peaks are also dependent on the spatial positioning of the gold nanopillars (i.e. the use of different size PS templates). The trend in the change of intensity and shift of the absorption peaks corresponded well with simulated data. More work can be done to optimize the individual parameters at each step of the fabrication process to achieve a higher level of control that could allow us to tune the shape, size and homogeneity of the entire nanostructured array.

In Chapter 5, we have attempted to fabricate a fishnet structured metamaterial by making use of bottom-up techniques. Preliminary images have shown that the method is feasible and works very well up until the electrodeposition of the different layers of metals. However, the most challenging hurdle that still remains is to devise a new method to remove or replace the sacrificial metal layers without damaging the inherent gold layers that have already been electrodeposited.

In summary, we have successfully studied the effect of adding individual layers of inverse opal structures on the efficiency of a solid state DSSC, demonstrated that electrodeposition of gold can be used to fabricate optically unique nanostructured surfaces and designed a process pathway to fabricate large area arrays of plasmonic gold nanopillars. While, we have met some of the initial objectives we set at the beginning, in light of the work that has been accomplished, more questions have arisen, and more work is still left to be done. The work

described here is just the tip of an iceberg of a myriad of possibilities to explore in the field of nanofabrication utilizing colloidal self-assembly and lithography.

“Learn from yesterday, live for today, hope for tomorrow. The important thing is to not stop questioning.”

— Albert Einstein, Relativity: The Special and the General Theory

ANNEX 1. SYNTHESIS OF SILICA AND POLYSTYRENE BEADS

A. SYNTHESIS OF SILICA BEADS BY THE STÖBER PROCESS

The Stöber process was used to synthesis silica nanoparticles fundamentally because of the ease and reproducibility of the process [1]–[3]. For silica nanoparticles between 100 nm to 400 nm, a one-step synthesis process is sufficient to obtain particles within this size range. For silica nanoparticles larger than 400 nm, a two-step process, which makes use of the silica nanoparticles synthesized in the one step process as seeds, enlarges the particles by a calculated chemical controlled growth process.

TEMPERATURE DEPENDENT ONE STEP SYNTHESIS OF SILICA NANOPARTICLES

A series of experiments (listed in Table 13) were carried out to determine the relationship between the reaction temperature and size of silica particles synthesized (while maintaining all other reaction parameter constant). Since the main aim of this part of the project was not to study the kinetics and growth of silica nanoparticles but rather to produce enough batches of monodisperse nanoparticles for the colloidal templating, the impact of the other various reaction conditions on the synthesis process were not investigated.

The procedure to synthesize the silica particles are as follows. First, the required amounts of distilled water, absolute ethanol (VWR Chemicals) and ammonia (30 % solution, Carlo Erba) were mixed together (using a magnetic stirrer) in a three neck round bottom flask kept in an oil bath at the desired temperature. The main neck of the flask was connected to a condenser cooled by flowing tap water, and the side necks were capped with a rubber caps to prevent evaporation of the solvents. After 30 minutes of equilibrating the temperature of the mixture, the required amount of tetraethylorthosilicate (TEOS, 98 % Aldrich) was added to the mixture in the flask. A cloudy white suspension can be observed after the addition of TEOS, and the reaction was left overnight to ensure that all the TEOS had been consumed by the reaction. The final suspensions was then kept in plastic bottles in their current forms without additional treatment.

Transmission electron microscopy was used to determine the final sizes of the silica particles obtained. Figure 105 shows some of the TEM images of the monodisperse particles obtained from the one step synthesis.

Table 13. Summary of the experimental conditions and final particle size of the monodisperse particles obtained.

Batch	Ethanol (ml)	Water (ml)	Ammonia (ml)	TEOS* (ml)	Temperature (°C)	TEM Average Particle size (nm)
T25	100	18	5	7.5	25	480 ± 12
T27					27	425 ± 11
T28					28	352 ± 7
T30					30	352 ± 8
T35					35	293 ± 6
T36					36	285 ± 7
T37					37	246 ± 10
T40					40	190 ± 8
T45					45	193 ± 7
T65					65	181 ± 9

*TEOS: Tetraethylorthosilicate

Referring back to Table 13, it can be observed that the reaction temperature has a very significant impact on the size of the silica nanoparticles obtained. The data was re-plotted in Figure 106 to illustrate the relationship between reaction temperature and the final particle size.

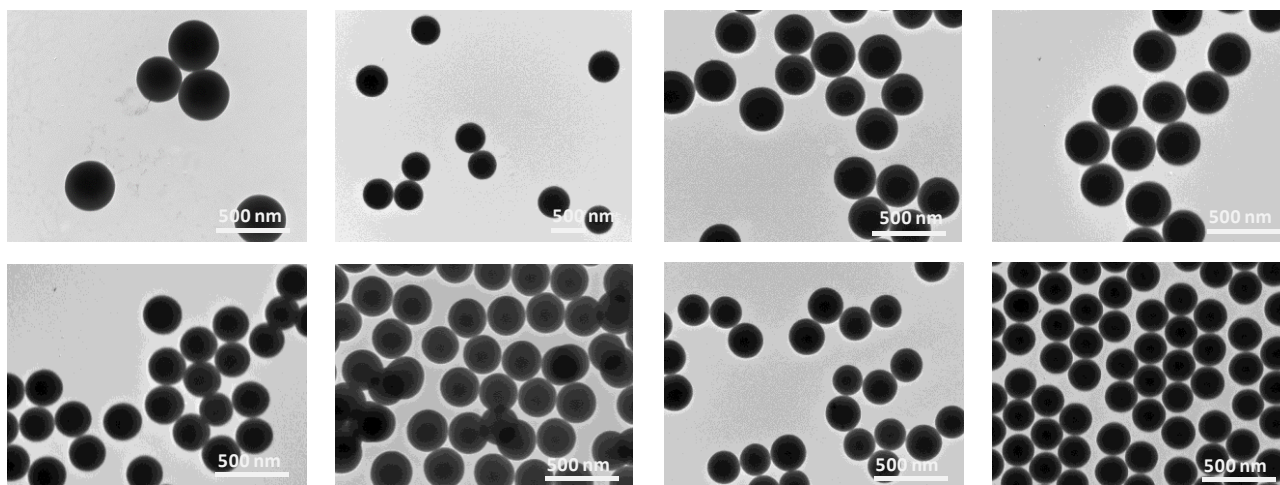


Figure 105. TEM images of monodisperse, spherical Silica beads synthesized at (top, left to right) 25 °C, 27 °C, 28 °C, 30 °C, (bottom, left to right) 35 °C, 36 °C, 37 °C and 40 °C.

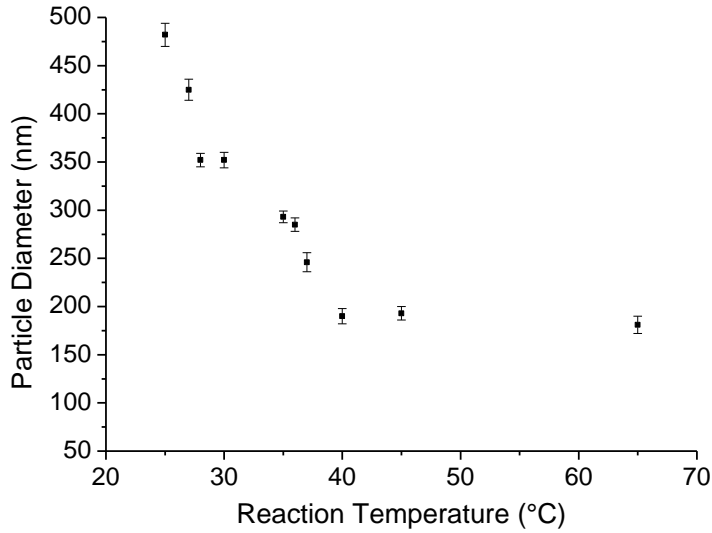


Figure 106. Effect of temperature on the size of silica beads synthesized

From Figure 106, it can be clearly seen that there is a decrease in the size of the silica nanoparticles synthesized as reaction temperature is increased (while keeping other reaction conditions constant). A general methodology for synthesizing monodisperse spherical silica nanoparticles up to about 480 nm was thus developed.

SEEDED GROWTH OF SILICA NANOPARTICLES

In the previous section, the procedure to synthesize silica nanoparticles from a single step process was described. If silica nanoparticles larger than 500 nm are desired, the silica nanoparticles obtained in the single step reaction can serve as seeds in a second growth step. By knowing the initial size and concentration of the seed particles, and the targeted size of the final particle, the amount of additional TEOS required to grow the silica seeds can be back calculated and estimated for the second growth step [4].

Assuming that the reaction kinetics is fast and the conversion of TEOS into silica is very fast and complete, we can write the relationship between the total volume of TEOS to be added and the volume of silica desired as follows,

$$V_{SiO_2} = \left(\frac{M_{SiO_2}}{M_{TEOS}} \right) \times \left(\frac{\rho_{TEOS}}{\rho_{SiO_2}} \right) \times V_{TEOS} = 0.122 \times V_{TEOS}$$

M and ρ refer to the molar mass and density respectively, and their corresponding values are given in Table 14.

Table 14. Standard values of molar mass and density of TEOS and silica.

M_{SiO_2} (g/mol)	M_{TEOS} (g/mol)	ρ_{SiO_2} (g/m ³)	ρ_{TEOS} (g/m ³)
60	208.3	2.2×10^6	0.83×10^6

If we consider that at each instant, there are n number of particles and each particle has a volume of V_p with a radius of r_p , we can then write the following relationships,

$$V_P = \frac{4}{3}\pi r_p^3$$

and

$$V_P = \frac{V_{SiO_2}}{n}$$

Hence,

$$r = \left[\frac{3}{4\pi} \times \frac{0.122 \times V_{TEOS}}{n} \right]^{1/3}$$

With this relationship, we can easily estimate the additional amount of TEOS required to be added to grow the silica particles to our desired sizes. This method allows for a relatively good control and estimation of the final silica particle size provided the size and concentration of the silica seeds are known. The growth step is simple and is done at 25 ± 1 °C. TEOS is added very slowly at a rate of 8 ml/h using a syringe pump.

Using this method and calculation; silica beads up to 1 μm have been successfully synthesized. Figure 107 shows the SEM pictures taken of the 1 μm sized beads grown from 480 nm seed particles.

Once the silica particles are prepared, an additional step was required to functionalize them for use in the Langmuir-Blodgett technique.

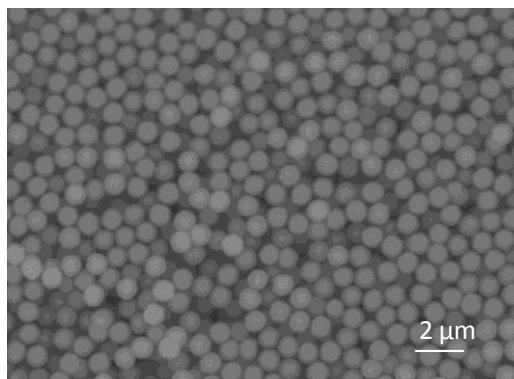


Figure 107 SEM photo of 1 μm monodisperse silica nanoparticles after the second growth step.

The synthesized silica suspensions that are obtained immediately after synthesis (either through the one step or two step synthesis) are left in the flask and excess APTES (Aminopropyltriethoxysilane, 99 % Aldrich) is added to the suspension in the flask at a ratio of about 20 APTES molecules per mm^2 of silica particle surface [4]. This new mixture is then left for two hours in an 80 °C oil bath. After two hours, the silica beads are cleaned by six cycles of centrifugation and redispersion in distilled water and are kept in distilled water for storage.

B. SYNTHESIS OF POLYSTYRENE BEADS BY EMULSION POLYMERIZATION

Emulsion polymerization is probably the most standard method used to synthesize polystyrene (latex) particles. First reported by Harkins [5] in 1947, this method has since been studied and revised extensively [6]–[8]. Figure 108 shows a schematic illustration of the micelle nucleation model for emulsion polymerization.

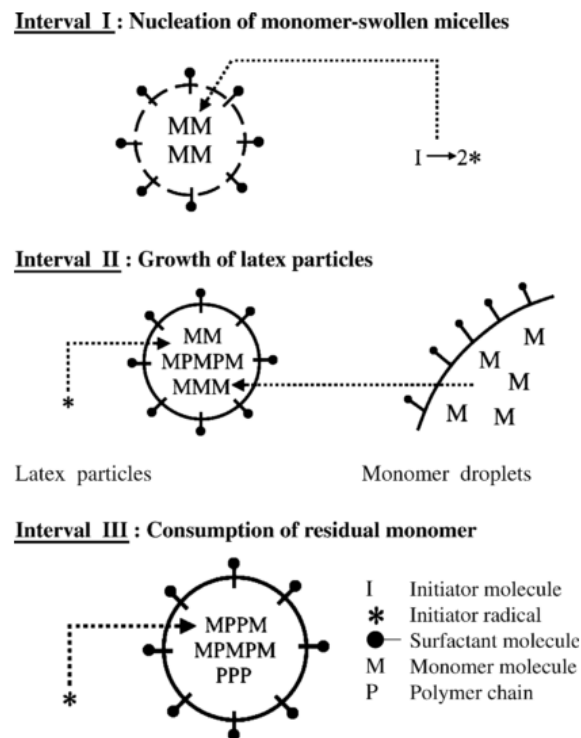


Figure 108. Schematic representation of the micelle nucleation model for emulsion polymerization. [6]

Typically an emulsion polymerization formulation consists of the monomer, surfactant, water and water soluble initiator. At the start of the reaction, the surfactant enables emulsified monomer droplets to be dispersed in the continuous aqueous phase. There exists only a very small fraction of the hydrophobic monomers dissolved in the aqueous phase or in micelles (if critical micelle concentration is exceeded). The majority of the monomers are contained within monomer droplets which act as monomer reservoirs. The addition of an initiator starts the polymerization process. According to the micelle nucleation model, the micelles which have an extremely large oil-water interfacial area captures the free radicals generated and this results in the generation of sub-micron latex particles. Monomer droplets in comparison have a small surface area and hence are not effective in capturing the free radicals when compared with the micelles.

Free radicals generated in the aqueous phase will first polymerize monomer molecules also dissolved in the aqueous phase, which increases the hydrophobicity of the resultant oligomeric radical. Upon reaching a critical chain length, these radicals will become hydrophobic enough to strongly favor entering a micelle. Once inside the micelle, the radicals will polymerize with the monomers within eventually transforming the micelle into a particle nuclei. These nuclei continue to grow by reacting with monomers from the monomer droplets or other micelles. There is an increased demand for surfactant as particle nuclei grow, and micelles that do not contribute to particle nucleation will disband to supply the surfactant required, in order to maintain sufficient colloidal stability. In addition, surfactant molecules can also desorb from the monomer droplets and diffuse across the aqueous phase to the particle surface. The polymerization reaction continues until all the monomers are consumed.

Emulsion polymerization was used to synthesize all the PS particles used in work mentioned in this thesis. The components required to synthesize the PS beads were styrene (99 %, Fluka), distilled water, sodium bicarbonate (NaHCO_3 , 99.5 %, Prolabo), potassium persulphate (KPS, 98 %, Prolabo), and sodium sulfonate (SSNa, Aldrich). All the reactions were carried out at 70°C (using an oil bath).

The procedure to synthesize the PS particles was adapted from [8] and slightly modified as follows. First, styrene, water, NaHCO_3 and SSNa were mixed together in a three neck round bottom flask that was placed in an oil bath maintained at 70°C. Rubber caps were used to seal the two side necks and the main neck of the flask was connected to a condenser cooled by flowing tap water. Then, nitrogen gas was bubbled through the mixture (using a syringe needle) for a minimum of thirty minutes or until the temperature appeared to have stabilized. After nitrogen bubbling, the initiator, KPS (dissolved in a 10 ml of water) was then added into the mixture to start the polymerization process. During the polymerization process, the tip of the syringe needle with nitrogen gas flow was positioned just above the surface of the mixture to maintain the nitrogen atmosphere. After about six hours, the initial colorless solution will have become a cloudy white suspension with a thin layer of transparent liquid sitting on the surface. This final suspension is allowed to cool down and the PS particles are cleaned six times by repeated centrifugation and redispersion with distilled water. Table 15 shows the list of the PS particles synthesized and varying amounts of each reagent added. Figure 109 shows some of the TEM images of the synthesized PS particles.

Table 15. List of PS particles synthesized

Batch	Styrene (ml)	Water (ml)	NaHCO ₃ (g)	KPS (g)	SSNa (g)	Average particle size (nm)
1	27	225	0.25	0.20	0.025	595±15
2				0.25		460±12
3				0.40		260±7

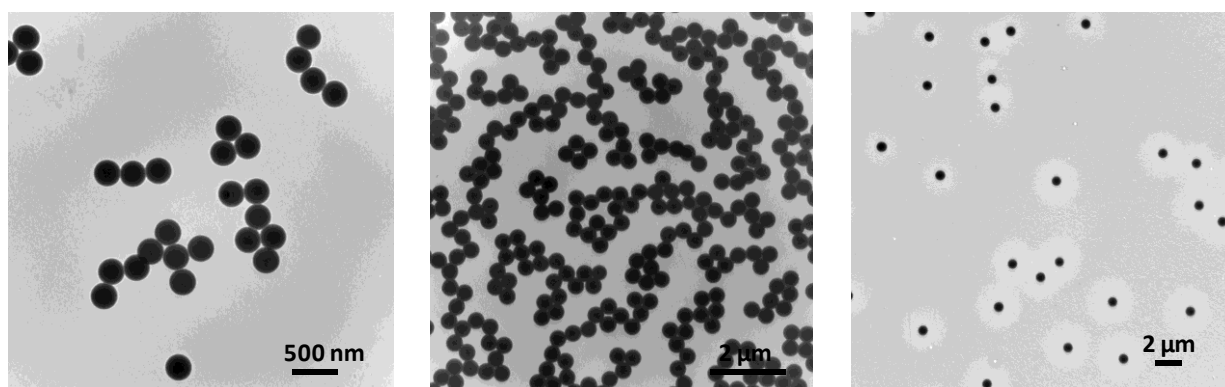


Figure 109. TEM images of the PS particles synthesized using different amounts of the initiator KPS: (left to right) 0.40 g, 0.25 g and 0.20 g of KPS.

ANNEX 2. PREPARATION OF COLLOIDAL CRYSTALS

A. VERTICAL DEPOSITION TECHNIQUE

Glass, gold-coated glass and fluorine-doped tin oxide (FTO) glass substrates used for vertical deposition were cleaned by ultrasound for 20 minutes each in acetone followed by ethanol and then in isopropanol. After the three rounds of ultrasound, the substrates were dried quickly by blowing air over the surface. Prior to using the glass substrates, they were treated with UV-ozone for 20 minutes.

Polystyrene (PS) suspensions of the desired concentrations (0.01 wt%, 0.02 wt%, 0.05 wt%, 0.08 wt%, 0.10 wt%, 0.20 wt%) were first prepared by mixing a known concentration of PS suspension with water. Next, 10 ml of the PS suspensions prepared was poured into a 22 ml cylindrical container. The clean glass substrates were then hanged vertically and partially submerged in the PS suspensions. These samples were subsequently placed in an oven set at 45°C (with 70% humidity) for at least four days before the samples were taken out.



Figure 110. (Left) Photograph to demonstrate how the glass slides were vertically supported. (Right) Photograph of a substrate coated with 595 nm PS beads after the vertical deposition process.

After four or more days, most or all of the water in the PS suspensions will have evaporated, and the glass substrates with the colloidal crystal layers can be removed from the glass containers. Figure 110 shows an example of the vertical deposition set up as well as a glass substrate with an opal layer deposited at the end of the vertical deposition process.

B. SELF-ASSEMBLY OF CLOSED PACKED MONOLAYER ON WATER SURFACE

Glass, gold-coated glass and fluorine-doped tin oxide (FTO) glass substrates were treated in the same way as described in the previous section (i.e. 20 minutes of ultrasound each in acetone, ethanol and isopropanol followed by 20 minutes of UV-ozone).

PS suspensions to be used for spreading are prepared by first determining the concentration of PS particles in distilled water (the synthesized PS particles are all stored in water). Next, a desired amount of the PS suspensions are diluted to between 10 to 15 wt% in distilled water. Once the diluted PS suspensions in water are prepared, an equal volume of ethanol was added to the PS suspensions so that the PS particles are suspended in a 1:1 mixture of water and ethanol.

For the self-assembly of monolayers of PS beads on water, a glass beaker was first thoroughly cleaned to ensure that there are no foreign particles in it. Next, about 400 ml of distilled water was poured into the container, and a piece of cleaned glass slide was inserted into the water at a 45° angle and stuck to the edge of the glass container using scotch tape. This glass slide is used as the surface for spreading the PS suspension onto the water surface. The container was left to stand for a while until there is minimal movement on the water surface. Next some surfactant solution (1 wt% sodium dodecyl sulfate, SDS, Fluka) was added onto the surface of the water (Note: The amount of surfactant added varied slightly with each experiment so it is difficult to state precisely the exact amount required. In addition, after each transfer of a monolayer onto a substrate, the surfactant concentration changes and needs to be corrected accordingly to the situation. Hence, hands-on experience is the key to mastering this procedure).

Once the surfactant concentration is adjusted properly (this is done by observing how small amounts of PS suspension spreads on the water surface, and slowly adding more surfactant until the PS suspensions spreads in an orderly manner), 15 µl of PS suspension is spread on the inclined glass slide using a micropipette. This procedure has to be done very slowly and steadily to ensure that the particles spread evenly onto the water surface. If the spreading is too fast, many tiny clusters of monolayers will form, and PS suspension will also dive into the water subphase at the glass-air-water interface (a cloudy white ‘explosion’ of PS suspension into water can be seen). On the other hand, if the spreading is too slow, the PS suspension could dry up before it reaches the glass-water interface which creates white clusters on the glass slide that could affect subsequent spreading using the same glass slide.

Figure 111 shows an example of how the self-assembled monolayers look like after spreading (Note: the diffraction of light can be clearly observed in the photograph).

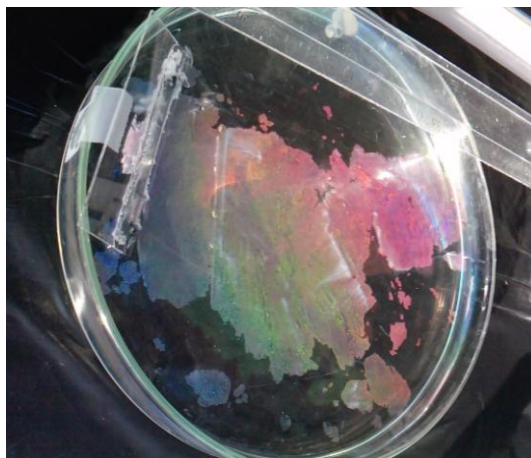


Figure 111. Self-assembled monolayers of PS particles on the water surface.

Once the monolayers are on the water surface and are large enough in surface area, a clean substrate is immersed into the water using a pair of tweezers (at a region where the water surface is clean, i.e. no particles floating on the surface), and it is carefully positioned under the self-assembled monolayer of interest. Then, very slowly and steadily, the substrate is lifted out of the water surface at an angle. If formed properly, the self-assembled PS monolayers will ‘stick’ onto the surface of the substrate like a form of coating. Once the substrate is removed, it is left to stand at an angle to allow for the excess water to dry off. Figure 112 shows examples of the substrates drying after the monolayers are transferred onto them. This process can also be repeated on the same samples to stack multiple PS monolayers.



Figure 112. Pictures of transferred monolayers consisting of 430 nm PS beads on substrates.

C. LANGMUIR-BLODGETT TECHNIQUE

Amino-functionalized silica particles are first transferred from water into absolute ethanol via three cycles of centrifugation and redispersion. Just prior to spreading, chloroform (VWR Chemicals) is added to the ethanol particle suspensions to achieve a final ratio of 1:4 (ethanol : chloroform)

Using a plastic pipette, the silica suspension is dropped randomly across the entire trough surface. The physical packing of the silica particles on the water surface is then performed by two mobile barriers. The surface pressure is carefully monitored throughout this process, and it will slowly increase as the mobile barriers gradually move closer and closer together (reducing the surface area available for the silica particles). Once the surface pressure reaches a predetermined value, typically between six to ten mN/m, the transfer of the close packed monolayer of silica beads onto solid substrates is performed as follows.

Glass, gold-coated glass and fluorine-doped tin oxide (FTO) glass substrates were treated in the same way as described in the previous section (i.e. 20 minutes of ultrasound each in acetone, ethanol and isopropanol followed by 20 minutes of UV-ozone). For the gold-coated glass substrates, an additional step of immersing the substrates in 1 mM cysteamine solution overnight was required (to increase their hydrophilicity) before they could be used.

Substrates are attached to a mobile arm positioned vertically on top of the middle of the trough. The substrates are quickly inserted vertically (down-stroke) into the water until about four fifths of the substrate is submerged. Then the substrates is very slowly lifted (up-stroke) out of the Langmuir trough. During the whole transfer cycle, the surface pressure is kept constant by the enslaved displacement of the barriers. Each cycle results in the transfer of a single monolayer of silica particles onto the exposed surfaces of the substrate (i.e. both sides). By repeating the process, multiple layers of silica beads can be deposited as desired on the substrate. Figure 113 shows a schematic illustration of the process.

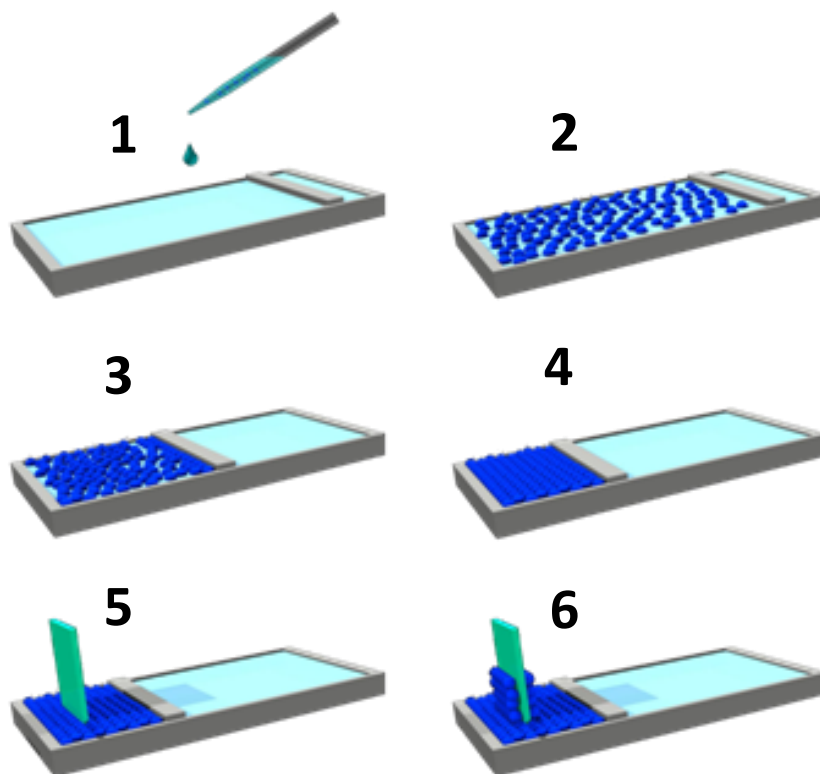


Figure 113. Schematic Illustration of the Langmuir Blodgett Technique. (1-2) Silica beads are spread on the water surface. (3-4) A mobile barrier is used to pack the floating beads on the water surface. (5) A solid substrate is immersed vertically into the trough. (6) The substrate is slowly removed vertically from the trough and a single layer of beads is transferred onto the surface of the substrate

ANNEX 3. FABRICATION OF SOLID STATE DSSCs

A. PREPARATION OF FLUORINE-DOPED TIN OXIDE (FTO) GLASS SLIDES

Fluorine doped tin oxide (FTO) glass pieces of 1.5 cm by 1.5 cm were cut and used as starting substrates for the fabrication of the solid state DSSCs. A piece of scotch tape was then wrapped around the FTO substrates leaving an area of 0.5 cm by 1.5 cm (from one of the edges) exposed. Next, the 'wrapped' FTO pieces were placed with the conductive side facing up and zinc powder (98 %, Aldrich) was applied to cover the exposed surface. Once the exposed surface was completely covered with Zn powder, concentrated hydrochloric acid (HCl, Alfa Aesar) was dropped onto the Zn powder to etch away the exposed part of the FTO surface. This reaction was very fast and took no longer than a minute. When the reaction ended, the etched FTO slides were rinsed in water to remove the excess acid and grey residue. Subsequently, the scotch tape was removed, and the etched surface can now be clearly distinguished from the surface protected with tape. These etched FTO slides are then cleaned by a placing them in acetone, then in ethanol and then in isopropanol for 20 minutes each under ultrasound. Once completed, the substrates were dried by an air gun and placed under UV ozone for another 20 minutes to prepare them for the subsequent spin coating step.

B. PREPARATION OF COMPACT TiO₂ LAYER

A commercial anatase nanoparticle paste (Dyesol 18NR-T) was diluted with anhydrous terpineol to a concentration of 0.05 M. 60 µl of this mixture was then spread over the conductive surface of a FTO substrate and spincoated onto it at 1000 rpm for 60s. After spincoating, the samples are heated at 450 °C on a heating plated for 30 minutes followed by 70 °C for 20 minutes. Next, 220 µl of TiCl₄ (Aldrich) was added to 100ml of distilled water and allowed to mix at 70 °C for 5 minutes. Once ready, the spincoated FTO substrates are immersed in the TiCl₄ solution for 30 minutes at 70 °C. After 30 minutes, the FTO substrates are removed from the solution and rinsed with water and blown dry. They are then placed on a heating plate set at 450 °C for 20 minutes and after that, at 70 °C for 20 minutes.

C. PREPARATION OF POROUS TiO₂ LAYER

The Titania paste required for the spincoating of the porous layer is prepared as follows: for every 1 g of Ti-nanoxide (SOLARONIX), 1.52 ml of absolute ethanol (VWR Chemicals) is used to mix with it. The amount of Ti-nanoxide used is calculated based on the number of samples that will be prepared. After adding the appropriate amount of ethanol to the Ti-nanoxide, the container is sealed and left overnight under stirring.

Before beginning the spincoating of the titania paste onto the FTO substrates (previously coated with the compact layer of TiO₂), the substrates are first dried again at 450 °C for 5 minutes then left to rest at 70 °C (to remove the moisture content in the substrates). Then, for each substrate, 80 µl of the titania paste (Ti-nanoxide in ethanol) is spread on top of the compact layer of TiO₂, and spincoated at 1000 rpm for 60 s.

After spincoating, the substrates are placed on the heating plate set at 250 °C for 5 minutes, then at 350 °C for 5 minutes, 450 °C for 15 minutes and finally 500°C for 15 minutes, before lowering to 70 °C for 20 minutes. Figure 114 shows how the appearance of the substrates change as the temperature is increased.



Figure 114. Changes in substrate appearance at (from left to right) 250 °C, 350 °C, 450 °C and 500 °C

The substrates were then immersed in a solution of 220 µl of TiCl₄ in 100 ml of water at 70 °C for 30 minutes (prepared in a similar way as described in the previous section). After 30 minutes, the substrates were rinsed with water and then blown dry and left on a hot plate at 450 °C for 20 minutes and then cooled to 70 °C for another 20 minutes before cooling down to room temperature.

D. FABRICATION OF INVERSE OPAL TiO₂ BY THE VACUUM INFILTRATION METHOD

Self-assembled polystyrene (PS) monolayers were transferred onto the layer of nanoporous TiO₂ coated substrates via the transfer of the monolayers from the water surface (refer to Annex 2B). This process was repeated depending on how many monolayers we wanted to stack together. Figure 115 shows some photos of the substrates after stacking four monolayers of 595 nm PS beads on the substrates.



Figure 115 Photos of opal templates deposited on TiO₂ coated (screen printed) FTO via the stacking of four monolayers of 595 nm PS beads (viewed from various angles).

Infiltration of the opaline templates was done by first clipping a clean glass slide on the top of the opal template and then it was partially dipped into the titania precursor solution (which consisted of 3.2 ml of trifluoroacetic acid (TFA, 99 % Sigma), 0.8 ml of hydrochloric acid (HCl, Alfa Aesar) and 4.0 ml of titanium (IV) isopropoxide (97 %, Aldrich) according to [9]) and the precursor would fill the pores very quickly by capillary action (the viscosity of the solution can be adjusted by adding some ethanol). The infiltrated samples were then left to dry overnight and the cover slides were removed the next day. Figure 116 shows the photos of the infiltrated samples left to dry overnight and the substrates after removal of the covering glass slide. The dry infiltrated substrates were then placed in the oven at 450°C for 3h to remove the PS beads and calcine the TiO₂ to an anatase phase (which was confirmed by X-ray diffraction).



Figure 116 (left) Infiltrated opals clamped with a glass slide and left to dry overnight. (Right) Infiltrated substrates before PS bead removal

E. INCORPORATION OF DYE AND HOLE TRANSPORT LAYER

The dye, D102, was used for sensitization of the device. 0.6 mg of the dye powder was required for every 5 ml of the dye solvent which was a 1:1 mixture of tert-butanol and acetonitrile. Depending the total volume of dye required, the corresponding amounts of dye powder and solvents were calculated. The mixture was mixed for 5 hours in a bottle wrapped with aluminum foil before it was used.

Prior to soaking the substrates in the dye, the substrates were again heated to 450 °C for 10 minutes and then kept at 70 °C for about 20 minutes before they were soaked in the dye solution for one hour (Figure 117). The substrates and dye were in petri dish covered by aluminum during the soaking process.

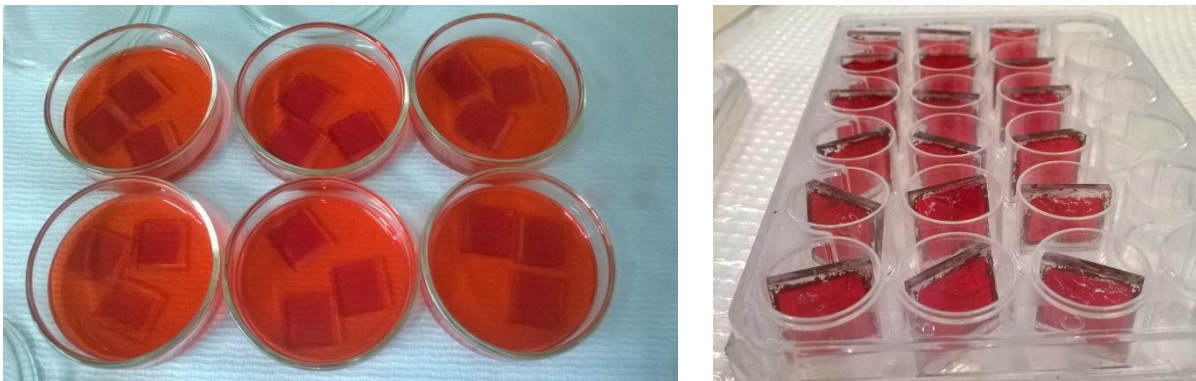


Figure 117. (Left) Soaking of substrates in dye D102. (Right) Substrates after removal from dye solution.

In the meantime, as the substrates were left in the dye, 'spiro' solution (which would become the hole conducting layer after spin coating) was prepared. The components of this mixture was in the ratio of 20 mg of spiro-MeOTAD : 100 μ l of chlorobenzene : 5.18 μ l Li salt : 2.45 μ l of tert- butylpyridine. About 40 μ l of this solution was needed for each substrate. Hence, the corresponding amount to prepare depended on the number cells intended for fabrication.

After one hour of soaking the substrates in the dye, the substrates are ready for the spincoating of the hole transport layer (i.e. spiro solution). About 40 μ l of the spiro solution was spread over the surface of a substrate, and it was left to stand for 60 s in normal atmosphere on the spincoater. At the end of 60 s, the spincoater was started, and it was spincoated at 3500 rpm for 20 s.

F. COMPLETING THE SOLID STATE DSSC

Using a mask, metal contacts made of 50 nm of silver followed by 50 nm of gold were then deposited on the surface to complete the device. Figure 118 shows an illustration and a photograph of the complete fabricated device

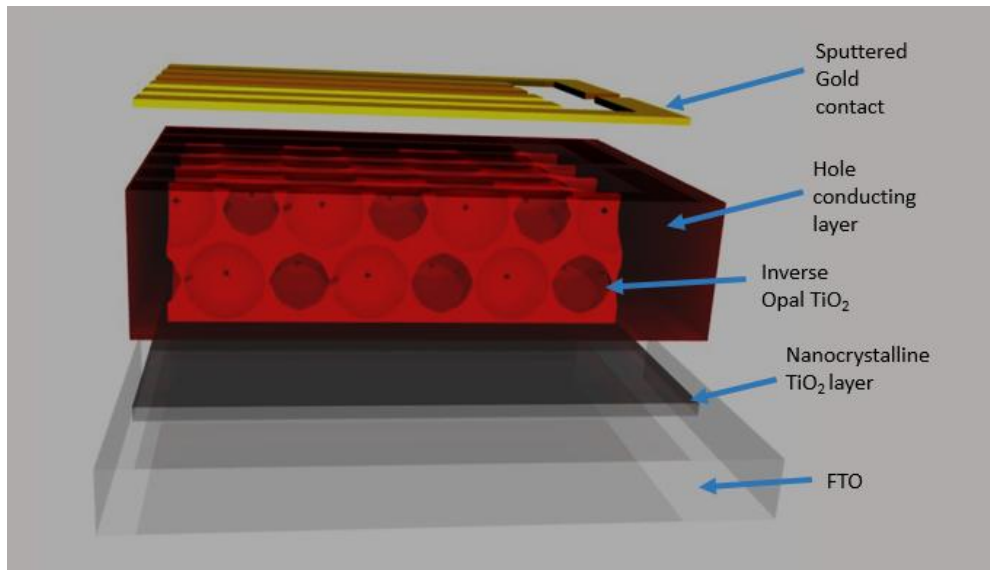


Figure 118. (Top) Sketch of the different layers in a completed solid state DSSC incorporating the inverse opal TiO₂ structure. (*Note: not to scale. Layers are separated for better clarity). (Bottom) Photo of an actual completed solid state DSSC.

ANNEX 4. ELECTRODEPOSITION OF METALS

The electrodeposition set-up (Figure 119) consisted of a three electrode cell (consisting of a working electrode (WE), a (2 cm × 2 cm × 0.4 cm) glassy flat carbon counter electrode (CE) and a Ag/AgCl (saturated KCl) reference electrode (RE)) connected to a potentiostat (Autolab PGSTAT-20). A home-made design for the electrode holders were used to ensure consistency and reproducibility of the results. The home-made design consisted of a Teflon cap with three holes and two customized metal electrode holders that could fit snugly into the holes. All the electrodeposition processes was carried out in a water bath set at 25±1°C. The intensity of the faradaic current generated during the electrodeposition processes were measured using an Autolab PGSTAT 20 potentiostat (EcoChemie) system monitored by a PC running the GPES 4.9 software.

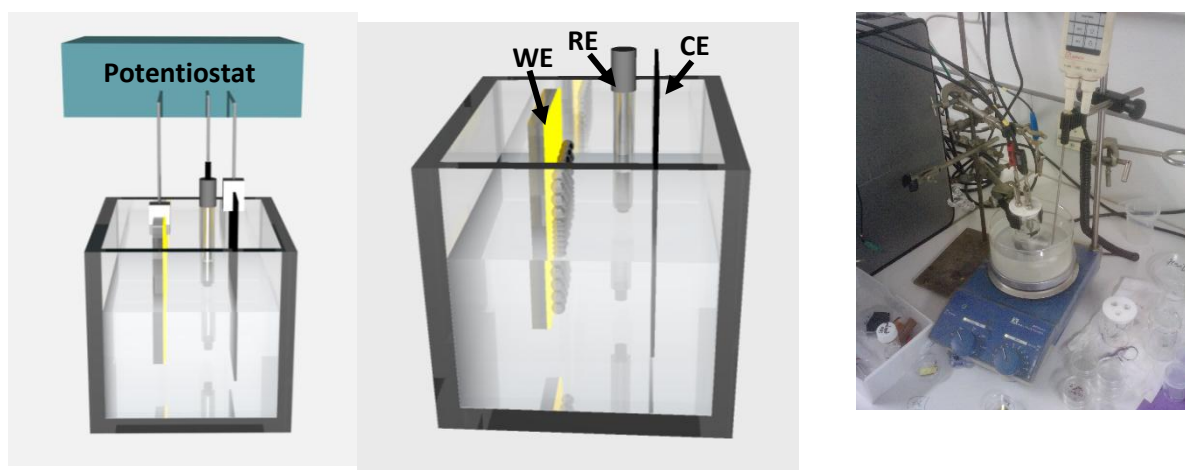


Figure 119 (left) Sketch of the electrodeposition set up and (right) picture of the experimental set up

A. PREPARATION OF SUBSTRATES

Generally, gold coated glass slides (with a 150±10 nm layer of gold) purchased commercially (AMC, France) were used as the substrates for electrodeposition (i.e. the working electrode, WE). These gold substrates were originally 5 cm by 2.5 cm and were usually cut to the size of 2.5 cm by 1.25 cm for the experiments. For the nickel plated gold-coated glass substrates mentioned in Chapter 4 and 5, they were basically these commercially bought gold-coated glass substrates with a layer of about 100 to 200 nm of nickel electrodeposited on them (nickel plating for 60s at -1.0 V vs Ag/AgCl).

For the non-templated electrodeposition of gold (described in Chapter 3), the gold substrates were used directly after cleaning in 20 minutes of ultrasound each in acetone, ethanol and isopropanol followed by 20 minutes of UV-ozone.

Templated gold substrates or nickel-plated gold substrates were prepared either by the Langmuir-Blodgett technique (for silica particles, refer to Annex 2C) or the water surface transfer technique (for polystyrene particles, refer to Annex 2B). After the transfer of the self-assembled layers onto the gold substrates, a short sintering step of 30 minutes at 90 °C was performed on the templated gold substrates with PS particles to fix the particles in place, otherwise the electrodeposition of the metals would occur under the particles and not through the template. For the templates with silica particles, this step was not necessary.

Prior to electrodeposition, transparent nail varnish was used to mark out the area for electrodeposition. Figure 120 shows an example of how the nail varnish was used to designate the electrodeposition area. It must be noted that not only the top surface, but the narrow sides have to be varnished as well to ensure that electrodeposition only occurs on the exposed surface. After varnishing the samples, they are left to dry for about five minutes before they can be put in the electrodeposition baths for the subsequent electrodeposition steps.

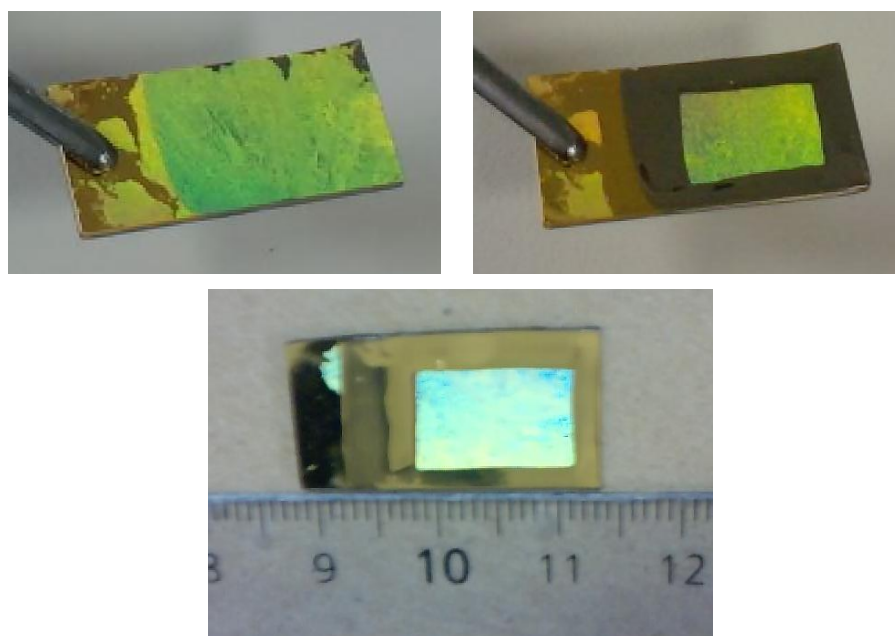


Figure 120. Preparation of templated substrates using nail varnish to designate the electrodeposition area. Photographs of (top left) before and (top right) after applying nail varnish onto the templated nickel-plated gold samples. (Bottom) Measurement of the size of the electrodeposition area on a templated gold sample.

B. ELECTRODEPOSITION OF GOLD (AU)

The electrodeposition of gold was done using a cyanide-free gold plating bath purchased from Metalor (ECF-63; gold concentration 10 g/L). The constant potential electrodeposition of gold was performed at -0.7 V (vs saturated Ag/AgCl (saturated KCl)), unless otherwise stated.

C. ELECTRODEPOSITION OF NICKEL (NI)

The electrodeposition of nickel was done using a nickel plating bath purchased from Coventya. The constant potential electrodeposition of nickel was performed at -1.0 V (vs Ag/AgCl).

ANNEX 5. FABRICATION OF GOLD NANOPILLAR STRUCTURES IN PDMS

Self-assembled monolayers of PS particles of various sizes (260 nm, 430 nm and 595 nm) were first transferred onto nickel plated gold-coated glass substrates (as described in Annex 2B). Next, the templates were sintered at the various conditions (90 °C, 95 °C, 100 °C, 105 °C, 110 °C, 115 °C for durations ranging from 30 s up to 10 minutes) to determine the optimum conditions that could adjust the pore size into one that is suitable for pillar growth.

Next electrodeposition of a sacrificial nickel layer was made followed by the electrodeposition of gold so that symmetrical gold pillar structures could be formed close to the middle of the template (i.e. the electrodeposited gold is centered at a depth of about half the diameter (D) of the PS particles). This is done by first using two templated samples to electrodeposit gold and nickel individually to figure out the time taken for gold, $t_{Au,0.5}$, and nickel, $t_{Ni,0.5}$, to reach the first current minimum (in absolute values) which corresponds to a electrodeposited depth of half D. With this experimentally derived time to reach a depth of half D, we can figure out the rate of electrodeposition and use it to calculate the estimated time required for the electrodeposition of the sacrificial nickel layer and the gold pillar layers for the actual structures.

For example, if we want the thickness of the gold layer to be one third of the diameter (D) of the PS particles, then the time required for the electrodeposition of gold should be about:

$$t_{Au,0.5} \times \frac{2}{3}$$

To position the gold layer such that it is centered at a depth of half D, the thickness of the nickel layer will then be one third of D. Hence, the time required for the electrodeposition of the sacrificial base nickel layer would be:

$$t_{Ni,0.5} \times \frac{2}{3}$$

Therefore, to fabricate the a symmetrical gold nanopillar structure by electrodeposition through the template, nickel is first electrodeposited for $t_{Ni,0.5} \times \frac{2}{3}$ followed by gold for $t_{Au,0.5} \times \frac{2}{3}$.

After the electrodeposition of the first nickel layer, the substrate is thoroughly rinsed with distilled water and thoroughly dried by blowing with air before it is used for the subsequent electrodeposition of gold. This rinsing and drying step is very important to prevent contamination between the two electrolytic baths. Furthermore, the rinsing also washes away excess bath solution that sticks onto the surface of the samples after removal from the electrolytic bath. If the excess bath solutions are not rinsed away, when it dries, crystalline salts from the respective bath solutions will form which will affect the integrity of the electrodeposited structures as well as the quality of the subsequent electrodeposition steps.

After completing the electrodeposition steps of nickel followed by gold, the samples are thoroughly rinsed with distilled water and dried.

Once dry, the samples are soaked in tetrahydrofuran (THF) for at least three hours to completely remove the PS particles as well as the nail varnish that was applied on the templates. After the PS template and varnish are removed from THF, the samples are thoroughly rinsed in ethanol to wash away all the residues, and then dried.

To prepare the PDMS, first the monomer and curing agent are mixed in the ratio of 10:1. Usually about 35 g of monomer and 3.5 g of curing agent is more than sufficient to cover a glass petri dish of 10 cm in diameter. Once the curing agent is added to the monomer in a beaker, it is thoroughly mixed using a spatula and the initially transparent mixture will become cloudy and white due to the presence of bubbles that get trapped during the mixing process. Next, the air bubbles in this viscous bubbly mixture is removed by placing the beaker in a desiccator connected to a vacuum pump. The mixture is left in the desiccator for about one hour to remove the air bubbles. After the removal of the air bubbles, the mixture will become transparent again and it will resemble a very viscous transparent liquid and it is now ready to be poured onto the electrodeposited substrates (after template removal).

The substrates are placed on a petri dish and spaced out evenly. Next, the viscous transparent mixture of monomer and curing agent is gently poured onto the substrates and eventually cover the entire surface of the petri dish. During this process, there will be some air bubbles

that get trapped in between the viscous liquid, the substrates and the petri dish. To remove these air bubbles and to ensure that the infiltration of the viscous liquid is as complete as possible, the petri dish is put into the desiccator for another one hour.

After one hour, the petri dish is visually inspected for any air bubbles. If none can be seen, the petri dish is then placed in an oven set at 70 °C for 90 minutes to start polymerisation process. At the end of 90 minutes, the petri dish is removed from the oven and a solid layer of PDMS is now formed over the substrates.

Once the PDMS is formed on top of the substrates, small cuts are made on the PDMS to expose a little corner of the nickel plated region of each sample (Figure 121). Then, to each of these exposed regions, a few milliliters of 16 weight% of nitric acid (HNO_3) are dropped onto them using a plastic pipette. The nitric acid will slowly dissolve the sacrificial nickel layers which would leave the gold pillars embedded in the PDMS layer and no longer connected to the original gold coated glass substrate (Figure 122). This process takes about a week because only a very small part of nickel is exposed to the acid, and the acid has to slowly eat its way through the nickel layer buried under the PDMS layer. It is a totally diffusion dependent process, and it becomes harder to dissolve the nickel under the PDMS that is further away from the exposed site.

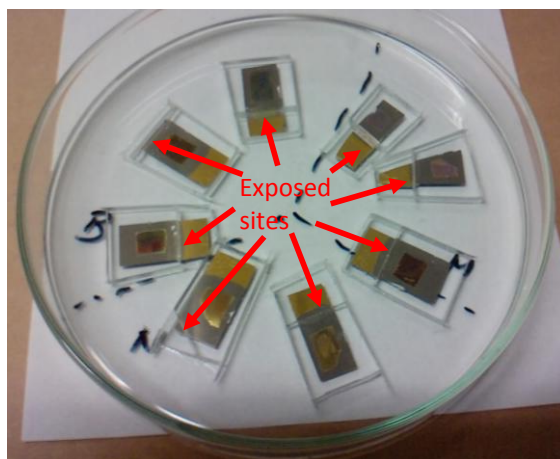


Figure 121. Photograph of the cuts made into PDMS to expose the nickel layers for acid dissolution. Nitric acid is then added to these exposed sites to dissolve the nickel layers without damaging the gold pillar arrays on the substrates.

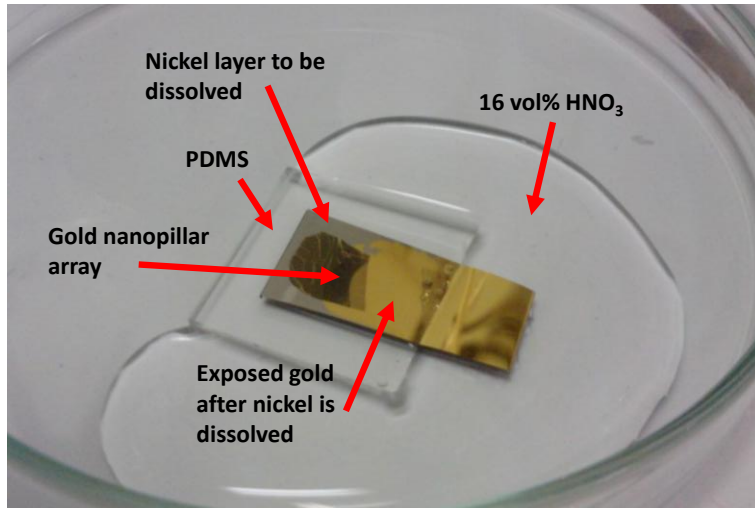


Figure 122. Photograph of a sample as nickel is being dissolved by nitric acid.

Once the nickel is dissolved, the original gold coated surface of the substrate can be observed very clearly (Figure 122). The petri dish is now thoroughly rinsed in distilled water to remove the nitric acid and the PDMS covering the substrates are very gently and carefully removed. Figure 123 shows the final samples that are obtained at the end of the entire process.



Figure 123. Photographs of gold nanopillar arrays after transferring onto PDMS

ANNEX 6. CHARACTERIZATION OF FABRICATED SAMPLES

All the UV–vis–NIR spectra presented in this thesis were recorded under normal incidence using a CRAIG 2020 microspectrophotometer for the wavelength range of 300-1600 nm.

All the incidence-angle dependence of the UV-vis-NIR reflection spectra were measured with Lambda 950 Perkin-Elmer spectrophotometer equipped with the Universal Reflectance Accessory (URA) for the wavelength of 200-2500 nm.

Unless otherwise stated, scanning electron microscopy images were taken with a JEOL 6700F microscope operating normally operated at 5 kV. For the SEM images in Chapter 3 section 3.3, they were taken with a Hitachi S2500 microscope operating at 25 kV. Gold conductive coatings were applied for all cross sectional images, as well as top down images that involved imaging silica or polystyrene particles. The SEM images of the electrodeposited nanostructures after the removal of the templates were taken without the application of any conductive coatings.

A Hitachi H600 transmission electron microscope (TEM) was used to image the silica and polystyrene particles synthesized.

REFERENCES

- [1] W. Stober, “Controlled growth of monodisperse silica spheres in the micron size range,” *J. Colloid Interface Sci.*, vol. 26, pp. 62–69, 1968.
- [2] K. Tadanaga, K. Morita, K. Mori, and M. Tatsumisago, “Synthesis of monodispersed silica nanoparticles with high concentration by the Stöber process,” *J. Sol-Gel Sci. Technol.*, vol. 68, no. 2, pp. 341–345, Oct. 2013.
- [3] N. Plumeré, A. Ruff, B. Speiser, V. Feldmann, and H. A. Mayer, “Stöber silica particles as basis for redox modifications : Particle shape , size , polydispersity , and porosity,” *J. Colloid Interface Sci.*, vol. 368, pp. 208–219, 2012.
- [4] S. Reculosa, “Synthèse de matériaux d’architecture contrôlée à base de silice colloïdale,” Thesis, University of Bordeaux 1, 2004.
- [5] W. D. Harkins, “A general theory of the mechanism of emulsion polymerization.,” *J. Am. Chem. Soc.*, vol. 69, no. 6, pp. 1428–44, Jun. 1947.
- [6] C. S. Chern, “Emulsion polymerization mechanisms and kinetics,” *Prog. Polym. Sci.*, vol. 31, no. 5, pp. 443–486, May 2006.
- [7] S. Shim, Y. Cha, J.-M. Byun, and S. Choe, “Size control of polystyrene beads by multistage seeded emulsion polymerization,” *J. Appl. Polym. Sci.*, vol. 71, no. 13, pp. 2259–2269, Mar. 1999.
- [8] J. W. Goodwin, J. Hearn, C. C. Ho, and R. H. Ottewill, “Studies on the preparation and characterisation of monodisperse polystyrene latices,” *Colloid Polym. Sci.*, vol. 252, pp. 464–471, 1974.
- [9] Z. Cai, J. Teng, Z. Xiong, Y. Li, Q. Li, X. Lu, and X. S. Zhao, “Fabrication of TiO₂ binary inverse opals without overlayers via the sandwich-vacuum infiltration of precursor.,” *Langmuir*, vol. 27, no. 8, pp. 5157–64, Apr. 2011.

“What we call the beginning is often the end. And to make an end is to make a beginning. The end is where we start from”

— Thomas Stearns Eliot

Title: Design and bottom-up fabrication of nanostructured photonic / plasmonic materials

Abstract:

The bottom-up self-assembly of colloidal particles is a versatile technique that allows the fabrication of large areas of colloidal crystals. The purpose of the present study is to develop highly reliable and reproducible process routes to fabricate nanostructured photonic and plasmonic materials that can be incorporated into different devices. Titania inverse opals with precise control of the layer thickness have been successfully incorporated into solid state DSSCs which showed improved performance of up to 105 %. Nanostructured gold surfaces that exhibited omnidirectional total light absorption have been fabricated by controlled electrodeposition of gold through colloidal monolayers of polystyrene beads. In addition, very rough gold surfaces that showed anti-reflective properties were also made. By tuning the pore size of the colloidal monolayer, plasmonic gold nanopillars with different lengths were fabricated by a sequential electrodeposition process. Using a non close-packed monolayer of PS beads combined with electrodeposition, fishnet metamaterials were fabricated.

Keywords: self assembly, colloidal crystals, inverse opal, dye sensitized solar cells, electrodeposition, gold, photonics, plasmonics, metamaterial

Résumé:

L'auto-assemblage de particules colloïdales est une technique polyvalente qui permet la fabrication de cristaux colloïdaux à de grandes échelles. Le but de notre étude est de développer des processus fiables et reproductibles pour fabriquer des matériaux photoniques et plasmoniques pouvant être incorporés au sein de différents dispositifs. Des opales inverses en dioxyde de titane composées d'un nombre précis de couches ont été intégrées au sein de cellules solaires à colorant « tout solide », ce qui a entraîné une amélioration des performances allant jusqu'à 105%. Des surfaces d'or nanostructurées présentant une absorption omnidirectionnelle et totale de la lumière ont été fabriquées par dépôt électrolytique d'or à travers une monocouche de particules de polystyrène. En outre, des surfaces d'or très rugueuses présentant des propriétés anti-réfléchissantes ont également été élaborées. En modulant la taille des interstices entre les particules de polystyrène, il a été possible de fabriquer par électrodéposition séquentielle des nanopiliers d'or de différentes longueurs. Enfin, l'utilisation d'une monocouche non compacte de particules comme moule a permis la réalisation de métamatériaux de type fishnet.

Mots clés: auto-assemblage, cristal colloïdal, opale inverse, cellules solaires à colorant, électrodéposition, or, photonique, plasmonique, métamatériau